

AGARD ADVISORY REPORT NO 345

**A Selection of Test Cases
for the Validation of Large-Eddy Simulations
of Turbulent Flows**

This Advisory Report was prepared at the request of the Fluid Dynamics Panel

Abstract

The two basic ways of computing turbulence have traditionally been direct numerical simulation (DNS) and Reynolds-averaged (RANS) modelling. In the former the full, time-dependent, Navier-Stokes equations are solved numerically, essentially without approximations. The results are equivalent to experimental ones. In the latter, only the stationary mean flow is computed, and the effect of the unsteady turbulent velocity fluctuations is modelled according to a variety of physical approximations.

It was realized early that direct numerical simulations were too expensive for most cases of industrial interest, while Reynolds-averaged modelling was too dependent on the characteristics of particular flows to be used as a method of general applicability.

Large-eddy simulations (LES) were developed as an intermediate approximation between these two approaches, the general idea being that the large, non-universal, scales of the flow were to be computed explicitly, as in DNS, while the small scales were modelled. The hope was that the small scales, which are removed from the flow inhomogeneities and particular boundary conditions by several steps of the turbulent cascade, would be universal (independent of the particular flow) and isotropic enough for a single simple model to be able to represent them in all situations.

The data contained in the present collection are intended for the validation of large-eddy simulations of turbulent flows, especially at the fundamental level of model development rather than at the level of complete codes. They therefore include relatively few 'complex' flows, consisting instead of 'building-block' experiments documented in as much detail as possible. These should also be useful for the validation of RANS and for the preliminary evaluation of experiments or turbulence theories. They include both laboratory experiments and direct numerical simulations.

Chapter 1 gives an overview of the present stage of large-eddy simulation, and of the similarities and differences between laboratory and numerical data. Its purpose is to describe the general organization of the data base, to summarize the different aspects of LES and of validation, and to give an idea of the quality and precision that can be expected from the data. Chapter 2 describes filtering methods and associated file formats.

Chapters 3 to 8 deal with the six flow categories, ranging from homogeneous to complex, in which the data have been classified. Each chapter includes an introduction discussing the data, their reliability, and how representative are they of the information presently available for those particular classes of flows. Each one is followed by a synoptic table of the data sets corresponding to its category.

These introductory chapters are complemented by data sheets, organized in the same group mentioned above, describing in detail each data set, the experimental or numerical procedures, the expected errors, and the initial and boundary conditions.

The data themselves are given in machine-readable form in the CD-ROM that accompanies the present report.

Abrégé

Les calculs d'écoulements turbulents sont couramment effectués par Simulation Numérique Directe (DNS) ainsi que par modélisation des équations de Navier-Stokes moyennées (RANS). La première méthode consiste à résoudre numériquement les équations de Navier-Stokes instationnaires, pratiquement sans approximation. Les résultats sont équivalents à des résultats d'expériences. La seconde approche permet seulement de calculer les états moyens stationnaires, alors que les fluctuations instationnaires sont modélisées moyennant un certain nombre d'approximations physiques.

Les simulations directes sont rapidement apparues trop coûteuses pour être utilisées dans la plupart des applications industrielles. D'autre part, les modélisations basées sur les moyennes en un point apparaissent souvent trop dépendantes des caractéristiques des écoulements pour permettre une application généralisée.

Ainsi, les Simulations des Grandes Echelles (LES) ont été développées et peuvent être considérées comme une approche intermédiaire entre la Simulation Numérique Directe et la Modélisation par Fermeture des Equations Moyennées. L'idée de base est de calculer explicitement les grandes échelles, de caractère non-universel (c'est à dire dépendant de l'écoulement considéré), et de modéliser les petites échelles. On peut en effet s'attendre à ce que les petites échelles deviennent indépendantes des inhomogénéités de l'écoulement et des conditions aux limites et suivent un comportement quasi-universel et suffisamment isotrope pour qu'un modèle relativement simple puisse les modéliser dans toutes les configurations envisagées.

Les informations regroupées dans la présente base de données sont destinées à la validation de calculs d'écoulements turbulents par Simulation des Grandes Echelles (LES), en particulier sur le plan fondamental de développement des modèles, plutôt que sur celui de la validation de codes complets. La base de données contient en effet relativement peu d'écoulements "complexes", mais est principalement constituée de données détaillées portant sur des écoulements "élémentaires". Ces dernières pourraient également servir à la validation des modèles RANS et à l'évaluation préliminaire des expériences de laboratoire. Elles peuvent être issues d'expériences physiques ou de calculs par Simulation Numérique Directe.

Le chapitre 1 présente un rapide panorama de l'état actuel de la Simulation des Grandes Echelles, ainsi qu'une discussion des similitudes et différences entre les données issues de mesures physiques et les données de calculs. L'objectif en est de décrire l'organisation générale de la base de données, de résumer les différents aspects de la simulation des grandes échelles et de donner un aperçu de la qualité et de la précision que l'on peut en attendre. Le chapitre 2 décrit la méthode de filtrage et les formats associés.

Les chapitres 3 à 8 sont relatifs aux six catégories d'écoulements retenues pour la base de données, s'étendant des écoulements homogènes aux configurations complexes. Chaque chapitre est précédé d'une introduction qui présente les données, décrit le degré de confiance que l'on peut leur accorder et discute leur niveau de représentativité pour le type d'écoulement considéré. Un sommaire présentant les diverses configurations d'écoulement sous forme de tableau récapitulatif est donné à la fin de chaque chapitre.

A la suite des chapitres de présentation, pour chacune des six catégories d'écoulement retenues, une série de fiches documentaires individuelles est fournie. Ces fiches présentent en détail chaque configuration, les méthodes d'obtention des données (à partir d'expériences physiques ou à partir de simulations numériques directes), les précisions et les conditions initiales et aux limites.

Les données elles-mêmes sont fournies sous la forme de fichiers universellement lisibles et archivées sur un disque CD-ROM accompagnant le présent rapport.

Acknowledgements

This collection of data sets is the result of the work of many people. First are the authors of the original data, who provided them gracefully, and in many cases re-processed them in several ways to make them more useful for the present purpose. In some instances new computations and experiments were performed, or previous ones were extended, to complete gaps in the existing information.

The compilation was the result of Working Group 21 of the Fluid Dynamics Panel of AGARD. The Working Group was chaired by J. Jiménez and organized into subcommittees which edited seven of the eight chapters into which this report is divided. The membership of these subgroups is reflected in the authorship of the different chapters, with the first author acting as chair. They can be found below in the table of contents. Other members of the Working Group, while not appearing as authors of full chapters, took responsibility for individual data sets at different stages of the work, and should be considered as full co-authors of the data base. They are Carlo Benocci, Michele Onorato and Jaap van der Vegt.

The different subgroups requested at times the help of outside experts, which was always generously provided. These outside consultants are acknowledged at the end of the individual chapters. The report and the data sets have been examined by external referees, leading on occasion to substantial revisions. They should, as usual, remain anonymous, but their contribution is, for that same reason, especially valuable.

Funding for this work was provided in the first place by AGARD and by the different AGARD national organizations. Individual members were also partially supported at times by other institutions, among them the Canadian Department of National Defence (Tavoularis), the Spanish Comisión Interministerial de Ciencia y Tecnología and the Centre for Turbulence Research in Stanford (Jiménez), and the U.K. Ministry of Defence and Department of Trade and Industry (Smith). Their contributions are gratefully acknowledged.

The working group would finally like to thank the executive of the Fluid Dynamic Panel, Dr. J. Molloy, for his help during the organization of Working Group, as well as the staff of the Canadian Communication Group for their advice on the practical aspects of printing and editing the report and the data base.

Several of the figures in the data sheets have been reprinted from previous publications, with permission from the respective authors and publishers. The sketches in the data sheets for HOM00, HOM04, HOM06, HOM21, HOM27, TBL10, TBL12, TBL20, TBL31, SHL00, SHL03, SHL10, SHL20, SHL30 (figure 2), SHL31 (figure 2), CMP01 and CMP20 are reprinted from the Journal of Fluid Mechanics. So is figure 4 in chapter 5, and figures 1 and 4 in chapter 8. Those in SHL01, SHL02 and CMP32 are reprinted from the AIAA Journal. The figures in SHL06 and SHL21 are from Physics of Fluids. HOM07 and HOM22 are from Springer publications. SHL22 first appeared in Experimental Thermal and Fluid Science, and CMP00 in the International Journal of Heat and Fluid Flow.

Table of Contents

PART I: DESCRIPTION OF THE FLOWS

1.-An overview of LES validation. <i>Jiménez.</i>	1
1.1 Introduction	1
1.2 Large eddy simulations	1
1.3 Numerical vs. laboratory experiments	2
1.4 The organization of the data base	3
2.-Data Filtering and File Formats. <i>Jiménez & Moser.</i>	5
2.1 Introduction	5
2.2 Inhomogeneous flows	6
2.3 Data formats	7
2.4 Correlation functions	7
3.-Homogeneous Flows. <i>Tavoularis, Jiménez & Leuchter.</i>	9
3.1 Introduction	9
3.2 Isotropic and grid turbulence and their distortions	11
3.3 Rotating turbulence and its distortions	14
3.4 Uniformly sheared turbulence and its distortions	15
3.5 SUMMARY OF HOMOGENEOUS FLOWS	18
4.-Interaction of Shock Waves with Grid Turbulence. <i>Leuchter.</i>	19
4.1 Introduction	19
4.2 Experiments	20
4.3 Comments on Experiments	20
4.4 SUMMARY OF SHOCK-WAVE/ GRID-TURBULENCE INTERACTIONS	22
5.-Pipes and Channels. <i>Moser, Cantwell & Purtell.</i>	23
5.1 Introduction	23
5.2 Pipes	24
5.3 Channels	24
5.4 Rotating channels	26
5.5 Simulations	27
5.6 SUMMARY OF PIPES AND CHANNELS	28
6.- Free Shear Layers. <i>Bonnet, Moser & Rodi</i>	29
6.1 Introduction	29
6.2 Mixing layers	30
6.3 Jets	35
6.4 SUMMARY OF SHEAR LAYERS AND JETS	36

7.-Two-Dimensional Boundary Layers.	<i>Smith & Jiménez</i>	37
7.1	Introduction	37
7.2	Zero pressure gradient	37
7.3	Adverse pressure gradients	39
7.4	Separation	39
7.5	Surface curvature	40
7.6	Relaxing flow	40
7.7	SUMMARY OF BOUNDARY LAYER FLOWS	41
8.-Complex Flows.	<i>Purtell, Moser & Rodi.</i>	43
8.1	Introduction	43
8.2	Flow in a square duct	43
8.3	Flow around a circular cylinder	44
8.4	Flow around a square cylinder	44
8.5	Incompressible flow over a backward facing step	46
8.6	SUMMARY OF COMPLEX FLOWS	48
9.-References		49

PART II: INDIVIDUAL DATA SHEETS

Data Sheets for Homogeneous Flows		57
HOM00:	Decaying Grid Turbulence, <i>Comte-Bellot & Corrsin</i>	59
HOM01:	Decaying Grid Turbulence, <i>Ferchichi & Tavoularis</i>	61
HOM02:	Decaying Isotropic Turbulence, <i>Wray</i>	63
HOM03:	Forced Isotropic Turbulence, <i>Jiménez, Wray, Saffman & Rogallo</i>	65
HOM04:	Grid Turbulence with Plane Strain, <i>Tucker & Reynolds</i>	67
HOM05:	Grid Turbulence with Transverse Strain, <i>Leuchter & Benoit</i>	69
HOM06:	Grid Turbulence with Successive Plane Strains, <i>Gence & Mathieu</i>	72
HOM07:	Return to Isotropy of Strained Grid Turbulence, <i>Le Penven, Gence & Comte-Bellot</i>	74
HOM10:	Rotating Decaying Turbulence, <i>Jacquín, Leuchter, Cambon & Mathieu</i>	76
HOM12:	Rotating Turbulence with Axisymmetric Strain, <i>Leuchter & Dupeuple</i>	79
HOM14:	Rotating Turbulence with Plane Strain, <i>Leuchter, Benoit & Cambon</i>	82
HOM20:	Transversely Sheared Flow, <i>Leuchter et al.</i>	85
HOM21:	Uniformly Sheared Flow, <i>Tavoularis & Corrsin</i>	87
HOM22:	Uniformly Sheared Flow, <i>Tavoularis, Karnik & Ferchichi</i>	89
HOM23:	Homogeneous Shear Flow, <i>Rogers & Moin</i>	91
HOM24:	Homogeneous Shear Flow, <i>Sarkar</i>	93
HOM25:	Homogeneous Shear Flow (High Shear), <i>Lee, Kim & Moin</i>	95
HOM26:	Uniformly Sheared Flow with Streamwise Plane Strain, <i>Sreenivasan</i>	96
HOM27:	Uniformly Sheared Flow with Uniform Curvature, <i>Holloway & Tavoularis</i>	98
HOM28:	Uniformly Sheared Flow with S-Shaped Curvature, <i>Chebbi, Holloway & Tavoularis</i>	100

Data Sheets for Shock-Wave/ Grid-Turbulence Interaction	103
SHW00: Homogeneous Turbulence Interacting with a Normal Shock, <i>Jacquin, Blin & Geffroy</i>	105
SHW01: Homogeneous turbulence interacting with a normal shock, <i>Barre, Alem & Bonnet</i>	107
Data Sheets for Pipes and Channels	109
PCH00: Fully Developed Turbulent Pipe Flow Simulation, <i>Loulou, Moser, Mansour & Cantwell</i>	111
PCH01: Turbulent Pipe Flow Experiments, <i>Durst, Jovanovic & Sender</i>	113
PCH02: Turbulent Pipe Flow Experiments, <i>Perry, Henbest & Chong</i>	114
PCH03: Turbulent Pipe Flow Experiment, <i>den Toonder & Nieuwstadt</i>	116
PCH04: Turbulent Pipe Flow Experiments (Superpipe), <i>Zagarola & Smits</i>	117
PCH05: Rotating Turbulent Pipe Flow Simulation, <i>Orlandi & Fatica</i>	118
PCH10: Fully Developed Turbulent Channel Flow Simulations, <i>Mansour, Moser & Kim</i>	119
PCH11: Fully Developed Turbulent Channel Flow Experiment, <i>Niederschulte, Adrian & Hanratty</i>	121
PCH12: Fully Developed Turbulent Channel Flow Experiments, <i>Wei & Willmarth</i>	122
PCH13: High Reynolds Number Channel Flow Experiment, <i>Comte-Bellot</i>	123
PCH20: Fully Developed Rotating Channel Flow, <i>Johnston, Halleen & Lezius</i>	124
PCH21: Fully Developed Rotating Channel Flow Simulations, <i>Piomelli & Liu</i>	125
PCH22: Fully Developed Rotating Channel Flow Simulations, <i>Andersson & Kristoffersen</i>	126
PCH23: Fully Developed Rotating Channel Flow Experiment, <i>Nakabayashi & Kitoh</i>	128
Data Sheets for Free Shear Flows	129
SHL00: Single Stream Plane, Incompressible Turbulent Mixing Layer, <i>Wynanski & Fiedler</i>	131
SHL01: Plane, Incompressible Turbulent Mixing Layer. Influence of initial conditions. Vel. ratio 0.6, <i>Bell & Mehta</i>	133
SHL02: Plane, Incompressible Turbulent Mixing Layer. Influence of Near Plate Wake., <i>Mehta</i>	135
SHL03: Plane, Incompressible Turbulent Mixing Layer. Natural and Forced., <i>Oster & Wynanski</i>	137
SHL04: Plane, Incompressible Turbulent Mixing Layer. Vel. ratio 0.54, <i>Delville, Garem & Bonnet</i>	139
SHL05: Time Developing Turbulent Mixing Layer Simulations, <i>Rogers & Moser</i>	141
SHL06: Plane, Incompressible Turbulent Mixing Layer. Influence of External Turbulence., <i>Tavoularis & Corrsin</i>	144
SHL10: No-shear Turbulence Mixing. (Vel. ratio 1.), <i>Veeravalli & Warhaft</i>	146
SHL20: Supersonic Plane Turbulent Mixing Layer, $M_c = 0.62$, <i>Barre, Quine, Menaa & Dussauge</i>	148
SHL21: Supersonic/Subsonic Plane Turbulent Mixing Layer. $M_c = 0.51-0.86$, <i>Samimy & Elliott</i>	150
SHL22: Supersonic Plane Turbulent Mixing Layer, $M_c = 0.525-1.04$, <i>Bonnet, Barre & Debisschop</i>	152
SHL30: Round turbulent jet, <i>Hussein, Capp & George</i>	154
SHL31: Plane turbulent jet, <i>Gutmark & Wynanski</i>	156
Data Sheets for Turbulent Boundary Layers	159
TBL00: Flat plate, zero-pressure-gradient TBL, <i>Smith & Smits</i>	161
TBL01: Turbulent Boundary Layer with No Pressure Gradient, <i>Spalart</i>	163
TBL10: Turb. B.L. in Adverse Pressure Gradient, <i>Marusic & Perry</i>	165
TBL11: Turb. B.L. in Adverse Pressure Gradient; Numerical, <i>Spalart & Watmuff</i>	167
TBL12: Turb. B.L. in Adverse Pressure Gradient; Experimental, <i>Watmuff</i>	169

TBL20: Closed Separation Bubble, <i>Alving & Fernholz</i>	171
TBL21: Mild Separation Bubble, <i>Na & Moin</i>	173
TBL22: Small Separation Bubble on Isothermal Wall, <i>Spalart & Coleman</i>	177
TBL30: Boundary Layer with Surface Curvature, <i>Johnson & Johnston</i>	179
TBL31: Relaxing Turbulent Boundary Layer , <i>Webster, DeGraaff & Eaton</i>	181
Data Sheets for Complex Flows	183
CMP00: Flow in a square duct – Experiments , <i>Yokosawa, Fujita, Hirota, & Iwata</i>	185
CMP01: Flow in a square duct – Simulation, <i>Huser & Biringen</i>	187
CMP10: Flow Around A Circular Cylinder , <i>Cantwell & Coles</i>	189
CMP20: Flow Around A Square Cylinder, <i>Lyn, Einav, Rodi & Park</i>	191
CMP30: Backward Facing Step - Simulation, <i>Le & Moin</i>	193
CMP31: Backward Facing Step - Experiment, <i>Jovic & Driver</i>	195
CMP32: Backward Facing Step - Experiment, <i>Driver & Seegmiller</i>	197

Chapter 1: An overview of LES validation

Javier Jiménez

School of Aeronautics, Universidad Politécnica, 28040 Madrid, Spain
and Centre for Turbulence Research, Stanford CA 94305, USA

1.1 Introduction

The two basic ways of computing turbulence have traditionally been direct numerical simulation (DNS) and Reynolds-averaged (RANS) modelling. In the former the full, time-dependent, Navier-Stokes equations are solved numerically, essentially without approximations. The results are equivalent to experimental ones, although with a different set of limitations and advantages which are briefly discussed below. In the latter, only time scales much longer than those of the turbulent motion are computed, and the effect of the unsteady turbulent velocity fluctuations is modelled according to a variety of physical approximations.

In a relatively recent development, the requirement of time-scale separation in RANS is sometimes relaxed, allowing the mean flow to evolve according to its natural instabilities. In these ‘URANS’ computations, the resolved flow is usually taken to be unsteady and two-dimensional, and a model is applied to account for the effects of turbulence. Two-dimensional flows behave very differently from three-dimensional ones, and this approximation is probably only reasonable in those cases in which two-dimensional large-scale structures dominate the real flow [53].

It was realized early that direct numerical simulations were too expensive to be used in most cases of industrial interest, being limited to relatively modest Reynolds numbers, while Reynolds-averaged modelling was too dependent on the characteristics of particular flows to be used as a method of general applicability. Large-eddy simulations (LES) were developed as an intermediate approximation between these two approaches, the general idea being that the large, non-universal, scales of the flow were to be computed explicitly, as in DNS, while the small scales were modelled. The hope was that the small scales, which are removed from the flow inhomogeneities and particular boundary conditions by several steps of the turbulent cascade, would be universal and isotropic enough for a single simple model to be able to represent them in all situations.

The data contained in the present collection are intended for the validation of large-eddy simulations of turbulent flows, especially at the fundamental level of model development rather than at the level of complete codes. They therefore include relatively few ‘complex’ flows, consisting instead of ‘building-block’ experiments documented in as much detail as possible. They should also be useful for the validation of RANS and for the preliminary evaluation of experiments or turbulence theories. The flows have been classified in six different categories, ranging from homogeneous to complex, for each of which there is a general introduction in chapters 3 to 8. These summaries de-

scribe the data, their reliability, and how representative are they of the information presently available for those particular classes of flows. The data themselves are given in machine-readable form in the CD-ROM that accompanies the present report. Those not interested in the introductions will find lists of the data sets for each particular type of flow in the synoptic tables at the end of the corresponding chapters.

Chapter 2 discusses data filtering and formats. The purpose of the present introduction is to describe the general organization of the data base, to summarize the issues involved in LES validation, and to give an overview of the quality and accuracy that can be expected from the data.

The present states of LES and of validation are briefly reviewed first. The differences and similarities between laboratory and numerical data are discussed in §1.3, and the data base itself is described in §1.4.

1.2 Large eddy simulations

In the pioneering work of [44], the separation of small (‘subgrid’) and large scales was loosely linked to averaging over computational grid elements, and was, therefore, intrinsically dependent on the numerical implementation. The large scale field was nevertheless described in terms of functions of continuous spatial variables, governed by differential equations. Schumann [188] formulated the scale-separation problem in a mathematically consistent way by interpreting the subgrid quantities as volume or surface averages, linked to a particular finite-volume discretization. This implied that the large-scale variables resulting from his approach were no longer functions of continuous space, and they have been difficult to interpret in terms of turbulence theory. Consequently, it has been the former interpretation that has prevailed, although the result is that a certain confusion of numerical and filtering concepts persists up to this day. The current formulation of large- versus small-scale quantities was introduced in [121]. The equations are written in terms of filtered variables,

$$\bar{u}(x) = \int g(x, x') u(x') dx', \quad (1)$$

where the kernel $g(x, x')$ is independent of the numerical discretization, and the filtered variables are considered to be defined over continuous space. Equations for \bar{u} are obtained by filtering the equations of motion. Whenever nonlinear terms, like \overline{uv} , are encountered, the resulting filtered quantities cannot be expressed in terms of \bar{u} and the extra subgrid stresses have to be modelled. Useful reviews of the state of the art at various times can be found in [177, 189, 148, 61, 75, 122, 147], where the later reviews

do not necessarily supersede the older ones.

There are many outstanding issues in LES which make the validation of the results, and of the models themselves, essential. The most obvious ones are those related to the physical modelling of the subgrid stresses, which is in many cases based on engineering approximations, justified by little more than dimensional considerations. Numerical issues are also important, since most models use as input the velocity gradients of the filtered field, which depend on the smallest scales resolved by the simulations, and which are therefore strongly influenced by numerical errors [71, 111]. It is clear that filtering, modelling, and numerical techniques are interrelated [169] but in which way is still unclear.

There are two ways to validate a given combination of the three factors mentioned above. The simplest one is *a-posteriori* testing, in which an experiment is simulated using a complete LES code, and the predictions of the desired variables (e.g. mean velocities,) are compared to the measurements. While agreement of this kind is probably the ultimate goal of any simulation, this testing can only be incomplete and is difficult to interpret.

In the first place, if the results are poor, it is difficult to decide what is wrong, since any one of the many components of the complex code may be responsible. But, even if the agreement is good, it may be due to compensating errors, or may only be good for the particular experiment chosen for the test. Moreover, since the information available on the experiments is seldom complete, some parameters have to be guessed (e.g. boundary conditions,) and this provides enough latitude as to sometimes mask modelling errors. In no case is much understanding gained on the causes of agreement or disagreement, or on possible simplifications and improvements.

There are well-known techniques for testing code integrity and numerical accuracy, independently of physical considerations, which are beyond our scope. An *a-priori* method for testing the filtering and modelling parts of LES, independently of the numerical factors, was introduced in [35]. Assume that the full flow field in a given situation is known. It is then possible to compute exactly the filtered field \bar{u} and the subgrid stresses. From \bar{u} , using only information that would be available to the LES code in a real situation, it is also possible to compute the stresses that would be predicted by the proposed model, and to compare them to the actual ones derived from the data.

True *a-priori* testing requires actual flow fields, which are usually only available from direct numerical simulations (see however [145]). It has proved to be impractical to include such fields in the present data base. A single DNS snapshot, at the moderate Reynolds numbers relevant to large-eddy simulations, requires several hundred Mbytes of data, and reasonable statistics imply at least $O(10)$ such fields. Including *a-priori* data even for the few simple flows which are presently available would have needed approximately 100 Gbytes of data, and several hundred CD-ROMs. The data in this collection are therefore not ap-

propriate for *a-priori* testing, although a few filtered fields have been included to be used as ‘standard’ initial and in-flow conditions in simulations.

The results of *a-priori* testing have proved disappointing in those cases in which it has been tried. The subgrid stresses predicted by most models turn out to be only poorly correlated with those measured from the filtered fields [35, 8], in spite of which some of those models are very successful in *a-posteriori* performance. The reason seems to be, at least in part, that only the mean stresses are needed to compute the mean flows, and that mean values and integral quantities are better correlated than instantaneous ones. Also a certain fraction of the shear stresses is carried by the resolved large scales and does not have to be modelled.

In selecting the present validation cases we have chosen an intermediate path between the data needed for *a-priori* testing, which we cannot provide, and those sufficient for *a-posteriori* verification, which we have argued to be incomplete. We have taken the view that LES, even if it is only an imperfect representation of true turbulence physics, should at least predict those quantities associated with the large scales of the flow. In particular, turbulent intensities and other Reynolds stresses have to be reasonably well modelled if the LES equations are to be correctly closed. It is shown in chapter 2 that the computation of the Reynolds stresses of a filtered field requires the knowledge of the two-point correlation function of the velocities in the full field. This is a high-dimensional quantity which has not been reported in most experiments, but an effort has been made to include it whenever available. In most cases, this is only true for numerical simulations, but at least one case (SHL04) corresponds to a laboratory experiment. From these correlations, it is possible for a modeller, using an arbitrary filter, to compute one-point, second-order statistics of the filtered field, and to compare them to the mean stresses predicted by his model.

An attempt to provide even more detailed data has been made in the case of some homogeneous flows in chapter 3. A lot of information on the structure of the velocity fluctuations is contained, for those flows, in the probability density functions (p.d.f.) of the velocity differences across a given distance. For large distances, this is a large-scale quantity, and should be predicted by any LES which preserves the structure of those scales. It is shown in chapter 3 that the p.d.f.s in filtered fields are the same as those in fully resolved ones, as long as the filter width is sufficiently smaller than the distance across which the velocity differences are measured, and it should be possible to use them to test which scales are well modelled by a given technique, and which ones are not. Again, results from numerical simulations and laboratory experiments are included.

1.3 Numerical vs. laboratory experiments

In this data base we have included both numerical (DNS) and laboratory experimental data. They are treated on the same footing as ‘true’, in the sense that both are only subject to ‘instrumental’ errors that can be reduced with reasonable procedural care.

However, the limitations and uncertainties of both types of data are different, and they should be taken into account when using them for validation.

The general magnitude of the experimental errors that can be expected from hot wire measurements is discussed in chapter 3 (§3.1.3), in the context of homogeneous flows. Chapter 6 (§6.1) extends the discussion to the cases of free shear layers and jets, where the errors tend to be higher because of the large relative turbulence intensities, especially near the low-speed edge of the flows. This latter chapter also examines the uncertainties in Laser Doppler velocimetry, which deals better with high turbulence intensities, but which has its own set of errors due to limited seeding densities and to particle lag. The latter effect is especially troublesome in supersonic flows involving shock waves. The errors in numerical simulations are briefly discussed in §3.1.3, and each data set description sheet contains, as far as possible, its own error estimation.

The absolute error magnitudes are roughly comparable for numerical and experimental data. Mean first-order quantities should be accurate to a few percent, but second order quantities, intensities and correlations, may be off by 10% or more. The cause of the errors is however different. While laboratory uncertainties are mainly instrumental, numerical ones tend to be statistical. Laboratory experiments work with long data records, often only approximately measured, while numerics have very small ‘measurement’ uncertainties, but deal with samples which are severely limited in size and number. In particular, the few full flow fields which are included in the data base represent single realizations of a random process, and can only serve as ‘typical’ initial conditions for computations. They are not necessarily representative of the average state of their flows, and it is not advised to use them in that capacity, such as for *a-priori* testing.

There are other important differences between experimental and numerical data. The former tend to be fairly unconstrained, with walls, entry and exit conditions relatively far away from the flow itself, but those conditions tend to be poorly documented. There are, for example, very few cases in which information is available on the state of the boundary layers on the side walls, or on the downstream boundary conditions.

Such information is important in simulations, and most numerical data are well documented in this respect, but their boundary conditions tend to be artificial and relatively ‘tight’ with respect to the interesting parts of the flow. In many cases, for example, the size of the largest scales of numerical turbulence is pushed to the limit in which it is of the same order as the numerical box, which has an impact both on their behaviour and on the statistical significance of the data.

This difference in boundary conditions means that the numerical simulations and the laboratory experiments represent different flows, even when they both try to approximate the same ideal situation. Decaying grid turbulence and numerical simulations of triply periodic boxes, for in-

stance, both try to approximate isotropic turbulence, but both approximations are imperfect and different from one another. The same is true of spatially growing mixing layers in finite wind tunnels, and of temporally growing ones in stream- and span-wise periodic boxes. Both are approximations to an infinite self-similar turbulent mixing layer, but different ones.

In this sense the numerical data sets are better suited to be used in model validation, because the LES are likely to share with them many of the limitations in box size and the artificial boundary conditions, and because the latter are usually better documented in DNS than in laboratory experiments. In a sense, both DNS and LES are simulating the same flows, which are slightly different from those in the laboratory. The ultimate goal of simulations should be, however, to reproduce the latter.

1.4 The organization of the data base

The present report consists of three parts. The first two are contained in the printed volume, and are the set of introductory chapters and the collection of data sheets for the individual sets. Both are organized into six categories, as follows:

Chapter 3: Homogeneous turbulence, including strain and rotation (HOM).

Chapter 4: Interaction of shock waves with grid turbulence (SHW).

Chapter 5: Pipes and channels (PCH).

Chapter 6: Free shear flows (SHL).

Chapter 7: Turbulent boundary layers, especially distorted and separating (TBL).

Chapter 8: More complex flows (CMP).

The introductory chapters should be consulted for a discussion of the individual sets. Each one contains a table with a summary of what is available, and under what name. Each data set has been given a name formed by the prefix in the previous list and by a two-digit number, and they are referred by that name throughout the data base.

Chapter 1 is the present introduction, and chapter 2 explains how to use the data to obtain filtered quantities, and describes some of the less obvious data formats.

The third part of the data base consists of the data themselves, which are contained in machine readable form in the CD-ROM that accompanies the printed volume. All the files from a given set are collected in subdirectories named after the chapter and set names (e.g. chapter7/TBL10). At the time of publication, the data are also available on-line by anonymous ftp from `torroja.dmt.upm.es`, in Europe, or from `http://thomasc.stanford.edu` in the USA. Both sites are privately maintained, and there is no guarantee of their permanence. They might, however, be enhanced with new data as they becomes available.

Chapter 2: Data Filtering and File Formats

Javier Jiménez

School of Aeronautics, Universidad Politécnica
28040, Madrid, Spain
and

Robert D. Moser

Dept. Theoretical and Applied Mechanics
University of Illinois
104 S. Wright St. Urbana, IL 61801 USA

Summary

The problem of providing filtered DNS or experimental data for comparison to LES results is discussed briefly. It is argued that the data base should include enough information to allow users to apply their own filtering operators, but that this is only practical for first- and second-order one-point statistics. The former requires the inclusion in the data base of unfiltered mean profiles or flow fields. The latter requires the full small-separation correlation tensor. The more complete information contained in the full spectral tensor is normally impractically large, except for the particular case of isotropic turbulence.

Data formats are also discussed, including those for the correlation tensor in spatially inhomogeneous flows.

2.1 Introduction

In Large Eddy Simulation (LES), only the largest scales of turbulence are simulated, leaving the smaller scales to be modelled. Therefore, statistical quantities computed from an LES must be interpreted as statistics of the large scales. For some quantities, such as the mean velocity and the statistics of multi-point velocity differences (for large spatial separation), there is no small-scale contribution, and LES should be able to predict those well. However, for many quantities, such as all the single-point moments of order higher than one, there is a small-scale contribution, and the large-scale values given by an LES will differ from those measured in an experiment or computed in a DNS. Thus, to properly compare an LES with a DNS or experiment, it is necessary to extract the large scale statistics.

Whenever possible, the data sets in this collection include either large-scale information in addition to the usual unfiltered statistics or, more often, enough information to allow the users to derive filtered values using their own filtering operation. The large scales in LES are defined by means of a spatial low-pass filter which, for a single homogeneous spatial direction, is defined through an appropriate kernel $g(x)$ by

$$\bar{u} = \int g(x - x') u(x') dx'. \quad (1)$$

The choice of kernel is complicated by the fact that, in many LES, the filtering operation is not explicit, but implied by the presence of a discrete grid, in which case the simulator may not even know which filter shape he is us-

ing, and therefore to which filtered quantities to compare.

There are nevertheless several sensible choices for the functional form of g , one of the most common being Fourier truncation, which corresponds to

$$g_s(x) = \frac{\sin(2\pi x/\delta)}{\pi x}, \quad (2)$$

and which is mostly used in spectral numerical codes. Its only parameter is the filter width δ .

Another popular choice is the box filter

$$g_b(x) = 1/2\delta \quad \text{for } |x| < \delta, \quad 0 \quad \text{otherwise}, \quad (3)$$

which is easier to apply to computations or measurements in physical, rather than spectral, space.

The spectral counterpart of the convolution (1) is multiplication in Fourier space. Denoting the transform of a function of x by its capitalised symbol

$$\bar{U}(k) = 2\pi G(k)U(k). \quad (4)$$

For the two examples given above

$$2\pi G_s(k) = \begin{cases} 1 & \text{if } |k| < 2\pi/\delta \\ 0 & \text{otherwise,} \end{cases} \quad (5)$$

and

$$2\pi G_b(k) = \frac{\sin(k\delta)}{k\delta}. \quad (6)$$

The transfer function is defined in the familiar way as

$$T(k) = 4\pi^2 |G(k)|^2, \quad (7)$$

and, if the co-spectrum of two arbitrary variables u and v is

$$C_{uv}(k) = \Re[U(k)V^*(k)], \quad (8)$$

the co-spectrum of the filtered variables is given by

$$C_{\bar{u}\bar{v}} = T(k) C_{uv}. \quad (9)$$

In the particular case of $u = v$, (9) is the power spectrum of u . The energy or Reynolds stresses of the filtered flow are given by the integral of (9), and differ from those of the original flow by an amount that depends on the form of the transfer function. LES results should be compared to the filtered intensities, rather than to the unfiltered ones.

Since different LES simulations are run with different filters, the only way that a data base can be made useful for a variety of users is to include full spectra and co-spectra rather than fluctuation energies or stresses. In isotropic flows, co-spectra vanish and the information on the energy spectrum is contained in a single function of the wavenumber magnitude $k = |\mathbf{k}|$, from which all other spectra can be deduced [16]. In anisotropic flows, some of the co-spectra do not vanish, and the spectra have to be given, as much as possible, as two- or three-dimensional functions of the wavenumber components.

For homogeneous flows, therefore, it is enough to include the appropriate spectra and co-spectra to allow users to derive any second order one-point statistical quantity. Note however that this information is more complete than the one needed for the computation of the one-point statistics, and that it may be rather large for anisotropic flows. It will be seen below that one-point information is given more compactly by the small-separation correlation function.

Note also that (9) applies only to second order statistics and cannot be used to filter higher order moments. To do so would require higher order correlation functions with impractical storage requirements in all but the simplest cases. Thus, while higher order moments and velocity p.d.f.s are useful in characterising turbulent flows, and while the data base includes them whenever possible, it is impractical to provide enough information for users to derive filtered values for arbitrary filters.

2.2 Inhomogeneous flows

For inhomogeneous spatial directions, the choice of filter is not so clear. The analog of (1) is

$$\bar{u} = \int g(x, x') u(x') dx', \quad (10)$$

with g now a more complicated kernel. It can be written in a form more closely related to the homogeneous case as

$$\bar{u} = \int g(x - x', x) u(x') dx', \quad (11)$$

where the dependence on the second argument can be considered parametric, and represents the variation of the filter width and shape with spatial location. Furthermore, even the filters in homogeneous spatial directions may depend on the inhomogeneous coordinate. For example, in polar coordinates for pipe flow, the filter width in the azimuthal direction (δ_θ) should depend on the radial direction (r). In particular, $\delta_\theta \sim 1/r$ away from $r = 0$, with some appropriate regularity condition at $r = 0$.

The question is what is needed to generate arbitrarily filtered statistics in this case. The physical space dual of the co-spectrum is the two-point correlation function

$$R_{uv}(x, x') = \langle u(x) v(x') \rangle, \quad (12)$$

where $\langle \cdot \rangle$ is the ensemble averaging operator, which is usually substituted by time averaging, or by averaging over a suitable homogeneous direction. The correlation is a function of two independent variables, x and x' , and it is clear

from (12), and from the fact that filtering and averaging commute, that the correlation of the filtered field can be obtained by filtering its correlation function over each of the two independent variables,

$$R_{\bar{u}\bar{v}}(x, x') = \int \int R_{uv}(\xi, \xi') g(x, \xi) g(x', \xi') d\xi d\xi'. \quad (13)$$

For $x = x'$, we recover the one-point second order statistics $R_{uv} = \langle uv \rangle$. Note that it will generally be necessary to subtract local mean values from (13) to obtain the covariance, or the fluctuating energy and Reynolds stresses. It is not generally true that the mean values of the filtered and unfiltered variables are the same, but first order statistics can be obtained by directly filtering the mean profiles,

$$\langle \bar{u} \rangle = \overline{\langle u \rangle}. \quad (14)$$

In the special case of homogeneous directions the correlation function depends only on a single variable, $x' - x$, but the double filtering operation in (13) still has to be performed to recover the second order statistics. If we assume that the filter is also spatially homogeneous in that direction

$$\langle \bar{u}\bar{v} \rangle = \int R_{uv}(\xi) h(\xi) d\xi,$$

where

$$h(\xi) = \int g(\xi') g(\xi' + \xi) d\xi'. \quad (15)$$

In summary, to generate the first and second order statistics for filtered flow fields, it is necessary to know the unfiltered profiles of the average velocities, and the full two-point joint correlation function for all the variable pairs whose Reynolds stresses do not vanish.

The latter object can be rather large. For an inhomogeneous one-dimensional flow field on a N -point mesh, each correlation function is a two-dimensional object with N^2 points. In the extreme case of a fully three-dimensional field with three inhomogeneous dimensions, the correlation would be a six-dimensional object with N^6 points. Homogeneous directions add only one dimension to the correlation function. The present data base contains no fully inhomogeneous flows, but there are several cases with two inhomogeneous and one homogeneous directions, which would require N^5 points for the full correlation function.

Fortunately not all the correlation function is needed if only one-point statistics are to be computed. As noted for homogeneous flows, the full correlation contains long range information which is not needed for filtering. If we make $x = x'$ in (13), and assume that the widest filter has half-width H , the integrand only differs from zero inside the square ($|\xi - x| < H$, $|\xi' - x| < H$). The correlation is only needed in the union of all those squares, which is a band of width $2H$ centred along the diagonal $x = x'$. For the particular example of two inhomogeneous directions (x, y) and one homogeneous direction (z), the domain needed is

$$R(x, x', y, y', z' - z).$$

$$|x' - x| < H, \quad |y' - y| < H, \quad |z' - z| < H. \quad (16)$$

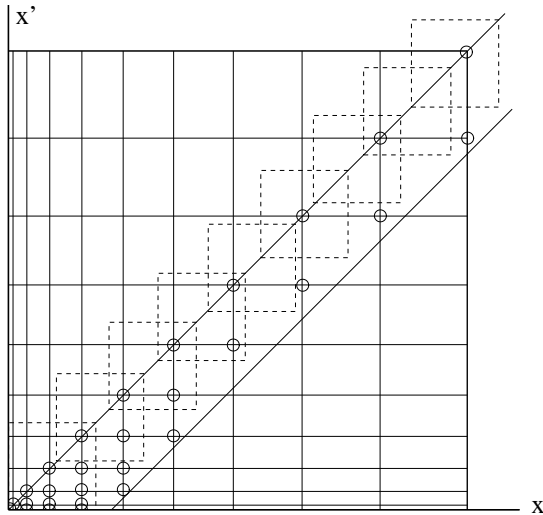


Figure 1: The two-point correlation function of a one-dimensional variable is defined in a two-dimensional mesh, symmetric with respect to the diagonal. Filtered one-point statistics are computed by convolution with square filters centred on the diagonal. Only correlation values inside a narrow band are needed for this operation, which can be reduced in half using the symmetry

Note that, for data defined on inhomogeneous grids, the bands in (16), even if they have a uniform geometric width, do not necessarily have a uniform number of points, and that the associated data structure needs to carry information on the beginning and the end of each x' interval (see figure 1).

The maximum filter width, H , is a parameter to be decided during the generation of the data base, and has been taken as uniform as possible, even for nonuniform flows. A reasonable order of magnitude is one tenth of the relevant flow dimension (such as the channel half-width, or the boundary layer thickness), corresponding to very coarse LES grids with 10-20 points across that dimension.

The previous discussion applies mostly to data originating from direct numerical simulations. In filtering laboratory experiments, it is generally only possible to filter in time, which is homogeneous in all the flows in this data base.

2.3 Data formats

As much as possible, files are self documenting and self contained. Small data sets are given as plain ASCII files, which can be manipulated, read and edited using standard editors. Many older editors and Fortran compilers do not admit formatted lines longer than about 132 characters, and those have been avoided as much as possible.

Moreover, since many smaller systems would not edit files larger than a few tens of Kbytes, and large formatted I/O operations are impractically slow in most computer systems, files larger that about 50 Kb are in binary 'flat' format, following the IEEE floating-point standard used by microprocessors. There are two implementation 'flavours' of this standard, which differ by the position in memory

of the bytes within a word. The data in this collection are in the 'big-endian' form (as used by DEC, IBM/Motorola and SGI processors), with the high-order byte in the low-address end. Utilities are included on the disk for converting to 'little-endian' form (as used by Intel processors).

Those utilities need to know the length of the floating point numbers in the file, which should therefore be fixed. Data in binary files only contain INTEGER*4 (four bytes per word) and REAL*4 (single precision floating) data, or their C equivalent, except as described next.

For the purpose of documentation, the first few Kbytes of each binary file are reserved for text data, in plain readable format, which can be isolated by the Unix head command or equivalent, or displayed by more. This header contains:

- A first line `HEADERLENGTH=4096\n`, giving the header length in bytes, followed by a *newline* (`\n`) character to allow for automatic stripping by user programs. The length in this example (4 Kb) is equivalent to about 50 text lines, and should be enough in most cases, but some files have longer headers.
- The file name.
- A short description of the data.
- Basic references, including the relevant chapter in the accompanying printed volume.
- A short description of the format.
- A short piece of code or pseudo-code that can be imbedded in a computer program to read the data in the rest of the file.

Note that the byte-swapping utilities that translate between the two-floating point formats will read the 'HEADER-LENGTH' line and copy the header accordingly. Thus these utilities can be used on the included binary files directly.

2.4 Correlation functions

The most complicated format is that for the correlation function in inhomogeneous flows since, as discussed in the previous section, only a band of the multidimensional array is needed, and the width of that band is variable. The following is a possible data organisation within a Fortran program, which has been followed as much as possible. Also included is pseudo-code to be used in generating and using the correlation function. It is assumed that the different components of the tensor are included in the code as the last running index of the array `couv`. Since different flows have a different number of non-zero components, these are identified in the file header.

The following are the declarations

```
c -----
c assumes two inhomogeneous directions,
c x and y, and one homogeneous one z.
c nx, ny are grids sizes
```

```

c  nz = H/dz is the max. filter width
c  m = number of tensor components.
c      1: u'u'
c      2: u'v'
c      3: v'v'
c      etc.
c
c  xmx(i)-> index in x(*) of the highest
c           ii in R(x(i),x(ii),...)
c  x0(i) -> index in couv of
c           R(x(i),x(i),...)
c  ymn(j)-> index in y(*) of the lowest
c           jj in R(...,y(j),y(jj),...)
c  ymx(j)-> index in y(*) of the highest
c           jj in R(...,y(j),y(jj),...)
c  y0(j) -> index in couv of
c           R(...,y(j),y(j),...)
c
c the dimensions ntx, nty of the list
c  couv should be large enough to
c  contain the whole band for each
c  variable
c -----
c  parameter (nx, ny, nz, ntx, nty)
c  real      x(nx),y(ny),dz
c  integer  xmx(nx),ymn(ny),ymx(ny)
c  integer  x0(nx),y0(ny)
c  real  couv(ntx,nty,-nz:nz,m)
c  ...

```

The x variation of the correlation $R_{uv}(x, x' \dots)$ is stored along the first index, ix , of the list-organised array `couv`. The i -th line of the function, corresponding to $x = x(i)$, is stored starting from the element $ix = x0(i)$, which contains the information for $x' = x$, and ending at $ix = x0(i) + xmx(i) - i$. Note that we have used the symmetry of the correlation tensor with respect to $x \leftrightarrow x', y \leftrightarrow y', z \leftrightarrow z', u \leftrightarrow v$ to avoid storing data for $x' < x$. For the y direction, we cannot use this symmetry, which makes the indexing of the y direction slightly different. Here we have the j -th line of the function corresponding to $y = y(j)$ stored starting from the element $iy = y0(j) + ymn(j) - j$, which contains the information for $y' = y(ymn(j))$, and ending at $iy = y0(j) + ymx(j) - j$. Finally the third index for the z direction, which is assumed to be homogeneous with uniform grid spacing dz is simpler. For a grid spacing dz , the correlation for $z' - z = dz * k$ is stored with index k . Thus, the information for the correlation $R_{uv}(x(i), x(ii), y(j), y(jj), z' - z) = R_{vu}(x(ii), x(i), y(jj), y(j), z - z')$, where $ii \geq i$, is found in

```

      if (ii.le.xmx(i) .and. jj.ge.ymn(j)
&      .and.
&      jj.le.ymx(j) .and. abs(k).le.nz)
&      then
          R= couv(x0(i)+ii-i,y0(y)+jj-j,k,m)
      else
          R= 0.
      endif

```

where the correlation is set to zero for points outside the stored band. For a homogeneous spatial direction, there may also be a statistical symmetry whereby $R_{uv}(\dots, z' - z) = \pm R_{uv}(\dots, z - z')$, where the plus or minus sign depends on the velocity components being correlated. In this

case, only data for $z' - z \geq 0$ need be stored. Use of such symmetries is described in the header of the correlation files.

Note that nz is not the full extent of the computational grid in the z direction, but the expected width of the widest filter. In some cases, especially in experiments collected with sparse fixed sensor rakes, the spacing between the data available in some directions may be larger than the widest expected filter, in which case $nz = 1$, and no filtering of the statistics is possible in that direction.

Note finally that the collection of reliable correlation functions requires large amounts of data which are not always available, and that users should be aware of the possibility of larger error bars in these quantities.

Acknowledgements

This chapter is the result of discussions with many people, mostly practitioners of LES or DNS and therefore either providers of data or potential users of them. Many of those discussions took place during the 1996 summer school of the Centre for Turbulence Research in Stanford, whose hospitality is gratefully acknowledged. Many of the ideas on the use of the correlation function are due to Daniele Carati. Alan Wray provided generous help that was essential in the design of the data formats.

Chapter 3: Homogeneous Flows

Stavros Tavoularis

Department of Mechanical Engineering
University of Ottawa, Ottawa, Canada K1N 6N5
and

Javier Jiménez

School of Aeronautics, Universidad Politécnica
28040, Madrid, Spain
and

Otto Leuchter

ONERA, 92190 Meudon, France

3.1 Introduction

3.1.1 The basic configurations

By definition, turbulence is *homogeneous* if its statistical properties (with the occasional exclusion of the first moments) are invariant under translation of the origin of the coordinate system. This implies that, ideally, such a flow should be unbounded. Simple analysis further shows that non-trivial turbulence cannot be both homogeneous and *stationary* (i.e. with statistical properties which are invariant under shifts of the time origin). Neither experiment nor computation produces exactly homogeneous flows, but both introduce a number of approximations. Notwithstanding such limitations, it is convenient to maintain this term in order to distinguish some relatively simple flow configurations from more complex ones. In the following, the term ‘homogeneous’ will denote several classes of approximately homogeneous flows, which approximate, to some degree, the theoretical notion of unbounded, exactly homogeneous turbulence. Furthermore, there is a difference between experimental and simulated homogeneous turbulence: in experiments, usually conducted in steadily operating wind-tunnels, turbulence is, at best, *transversely* homogeneous but changes statistically along the direction of the mean stream; in DNS, turbulence is nearly homogeneous within the computational domain but it is allowed to change, statistically, with time. The usual convention is that wind-tunnel turbulence can be considered as *nearly* homogeneous in a frame convected with the mean speed, if its statistical properties do not vary appreciably within a volume which is small compared to the dimensions of the apparatus, but large compared to the size of the most energetic turbulent eddies. Then, one can follow the temporal evolution of this flow in terms of the mean convection time, which is proportional to the streamwise distance from an actual or effective flow origin.

Turbulence can only be homogeneous if its production rate is uniform in space; similarly, transversely homogeneous turbulence can only be preserved if its production rate is uniform on a transverse plane. The simplest possible case occurs when the turbulence production rate vanishes everywhere, in which case the turbulent kinetic energy would *decay*. Another relatively simple configuration is the (rec-

tilinear) *homogeneous shear flow*, also known as *uniformly sheared flow*. Various relatively mild distortions from these ‘pure’ configurations, such as uniform strain and/or streamline curvature, can also be included within each class. Geometrical distortions of the flow domain or additional strain rates may introduce additional production terms in the Reynolds stress balance equations, or affect production implicitly by modifying the turbulent shear stress. Of special interest in many applications, including flows in turbomachinery and planetary flows, are the effects of rotation. Rotation introduces centrifugal and Coriolis accelerations, which affect the turbulent kinetic energy and the turbulence structure. Rotation, curvature and buoyancy have been identified as analogous mechanisms, so, with proper care, knowledge of the effects of one mechanism may be used to understand the effects of the others.

Homogeneous turbulence has been studied by all available means for as long and as intensely as any other class of flows. Its obviously appealing features are the relative simplicity of the statistical equations of motion and the lack of interfering factors, such as wall and entrainment effects. In particular, its subclass of homogeneous and *isotropic* (i.e. one whose statistical properties are invariant under rotations and reflections of the coordinate system) turbulence is mathematically the simplest possible turbulence that can be devised. On the other hand, the argument has also been made that lack of production and preferential orientation of the turbulent eddies complicates rather than simplifies the turbulence structure. Another drawback of homogeneous flows is that they do not occur in nature or in technology, which reduces their direct applicability. Despite these limitations, homogeneous flows continue to play a very important role in the advancement of turbulence research and maintain a firm position as test cases for the adjustment and verification of new theories and models.

3.1.2 The reported parameters

Although, ideally, all measured and computed values of each parameter should correspond to the same or equivalent mathematical definitions, in practice, discrepancies have been introduced in the literature, either by the use of different definitions or by different types of approximation to the original definition. To avoid any confusion, it

seems worthwhile to summarize the definitions and measurement/computation procedures used for the main parameters reported in the present chapter.

Experiments

The mean and r.m.s. velocity components are routinely computed by time or ensemble averaging of the corresponding fluctuating signals. The integral length scales are formally defined as the integrals of the corresponding two-point correlation coefficients; for example, the streamwise integral length scale, which is by far the most commonly reported, is defined as

$$L = \int_0^{\infty} R_{uu}(r, 0, 0) dr.$$

In practice, however, this scale is usually computed by integrating the streamwise auto-correlation coefficient to its first zero, or to near zero values, in combination with Taylor's frozen flow approximation. Occasionally, integral length scales have been estimated from one-dimensional spectra (see below). The measurement of the Taylor microscale, λ , could also be a source of confusion. The original definition [16] of the Taylor microscale, λ_g , involves a limiting process of a two-point correlation in a direction normal to the direction of the correlated velocity components, for example, as

$$\lambda_g = \left[\frac{2\overline{u^2}}{(\overline{\partial u / \partial y})^2} \right]^{1/2}$$

A different approach, used most often by experimenters, is to estimate this microscale from the streamwise velocity time series as

$$\lambda = \left[\frac{\overline{u^2}}{(\overline{\partial u / \partial t})^2} \right]^{1/2} \overline{U}$$

Although in isotropic turbulence the two definitions coincide, in shear flows the latter definition produces substantially larger microscales than the former one does [207]. Another approach that has occasionally been used is to compute λ from the turbulent kinetic energy dissipation rate, ϵ , estimated as the balance of other measurable terms in the kinetic energy equation. In the latter case, the assumption of local isotropy is also employed (see below). The turbulence Reynolds number for isotropic turbulence is unambiguously defined as $Re_\lambda = u' \lambda_g / \nu$. In non-isotropic flows, however, the use of different definitions and estimation methods for the microscale and the turbulence scale (for example, the use of the r.m.s. streamwise velocity or the r.m.s. turbulence kinetic energy) has created substantial ambiguity in the meaning of Re_λ . It is advisable to consult with the original source of experimental or numerical data for the appropriate definition.

Direct numerical simulations

Quantities used in these simulations follow the definitions in [16]. The r.m.s. one-component velocity is computed from the three-dimensional energy spectrum, $E(k)$, as

$$u'^2 = \frac{2}{3} \int_0^{\infty} E(k) dk.$$

The instantaneous energy dissipation rate, ϵ , is computed as

$$\epsilon = \nu \omega'^2 = 2\nu \int_0^{\infty} k^2 E(k) dk.$$

The integral length scale is computed as

$$L = \frac{\pi}{2u'^2} \int_0^{\infty} k^{-1} E(k) dk,$$

and the Taylor microscale, λ , is defined from $\lambda^2 = 15\nu u'^2 / \epsilon$. The microscale Reynolds number is defined as $Re_\lambda = u' \lambda / \nu$, and the large eddy turnover time as $T = L / u'$.

3.1.3 The uncertainty of the reported results

Hot-wire measuring uncertainty

Because all presently reported measurements in homogeneous flows were taken with hot-wire anemometers, their uncertainty stems mainly from the construction and use of that instrument. However, a general characterization of modern hot-wire uncertainty [30] might not apply to all reported experimental results, which span several decades and are concurrent with such important technological advances as the integrated circuit, the fast Fourier transform and the digital data acquisition and processing. Some of the classical hot-wire measurements were obtained with entirely analog means, including analog linearizers, r.m.s. meters, correlators and delay lines, and also utilized homemade probes and instrumentation. On the other hand, homogeneous flows are relatively free of sources of large hot-wire uncertainty (e.g. large turbulence intensity, composition and temperature variations and flow reversal) and careful experimenters have, over a long time, produced reliable measurements, particularly those of velocity moments and other parameters depending primarily on the energy-containing and inertial-subrange ranges of turbulent scales.

Hot-wire uncertainty has systematic and random components, both of which, according to the latest international conventions, are considered at a standard deviation level. The combined uncertainty of a measurement at a given confidence level, usually the 95% level (i.e. with 20:1 odds that the true value would be within the interval whose boundaries are the reported value plus/minus the reported uncertainty; for large samples, the value of this uncertainty is equal to twice the rms uncertainty, which has been customarily reported in the past), can be estimated by properly combining all existing uncertainties and taking into account possible correlations among the different uncertainties [36, 37]. Among the main sources of systematic uncertainty are drifts in the velocity or temperature of the

flow-producing facility, imperfections in the fabrication of the probe, dirt accumulation and aging effects, misalignment with the flow direction, hot-wire length and spacing effects (spatial resolution), differences between calibration and test conditions, inadequacy of the calibration relationship, instrumentation offsets and human errors. These effects are usually impossible to trace backwards from published results and the best available means of estimating the resulting uncertainty would be to consider combinations of some typical uncertainties, while relying on the experimenter's experience to exclude others. Random uncertainty may be traceable in the form of scatter and includes instrumentation noise, inadequate sample size uncertainty and random occurrences of systematic errors, for example, effects of a fluctuating temperature on velocity measurement and varying misalignment during probe traversing.

An updated analysis of cross-wire uncertainty, conforming to current standards, has been performed in [81] and applied to the measurements of [33]. It accounts for curve-fitting uncertainty of calibration data to King's law and uncertainty in the determination of sensor and probe body orientations, which are the main contributors to the uncertainty of first and second moments, while it proves that electronic noise and finite sample uncertainty are higher order effects, at least when modern instrumentation and methods are used. As typical estimates of measuring uncertainty in homogeneous flows, one could use the following results of this study:

Mean streamwise velocity component: $\pm 2\%$.

Mean transverse and spanwise velocity components: $\pm 3\%$ of the mean streamwise component.

Streamwise Reynolds stress: $\pm 4\%$.

Transverse and spanwise Reynolds stresses: $\pm 8\%$.

Dominant Reynolds shear stress (for shear flows): $\pm 8\%$.

Shear stress correlation coefficient: ± 0.03 .

Turbulent kinetic energy: $\pm 3\%$.

The uncertainty of the streamwise mean velocity and streamwise mean stress decreases substantially if these parameters are measured with single wires. The typical uncertainty in other measured properties is more difficult to estimate, in view of the wide diversity in measuring instrumentation and procedures. Integral length scales would likely have an uncertainty comparable to that of the corresponding stress. The directly measured Taylor microscale is very sensitive to the spatial and temporal resolution of the hot-wire probe and it is more likely to be systematically overestimated, often by a relatively large percent, in which case a correction must be applied to the measurements.

Uncertainties in numerical simulations

There are virtually no *measurement* uncertainties in modern direct numerical simulations. The numerical errors in a high-quality spectral code may easily be below the 10^{-3} level. This does not mean, however, that the results are

accurate to that precision. The relation of numerical with physical experiments has been discussed in chapter 1. Here we briefly discuss the reliability of the simulations.

The main uncertainty in the *results* of numerical simulations is statistical. Computations are seldom run long enough to reach totally converged statistics. In steady-state forced experiments, like those in HOM03, the running time is equivalent to a few eddy-turnover times. In unsteady cases like HOM02 or HOM23-25, they correspond to single realizations. Moreover, the computational boxes are only big enough to contain a few large eddies.

If we assume that the smallest uncorrelated eddies in a turbulent flow have diameters of the order of 10η , a large simulation, like the 512^3 forced case in HOM02, contains roughly 5×10^5 uncorrelated eddies. Since the statistics are compiled over a few flow fields, the sample is equivalent to a few million eddies. The uncertainties of small-scale sensitive quantities, like vorticities or gradients, can therefore be expected to be small, of the order of 10^{-3} .

On the other hand, the ratio of the box size to the integral length is typically about 3, which implies that the total number of large eddies in the samples is $O(100)$, and that the statistical uncertainty of large-scale properties, such as energy densities or Reynolds stresses, is of the order of 10%.

An exception is HOM02, which was specifically designed to improve the large-scale statistics and can probably be trusted to the level of 3–5%, even for those quantities.

3.2 Isotropic and grid turbulence and their distortions

3.2.1 Experiments

Decaying grid turbulence

Since the earliest known experiments on grid turbulence in 1934 [191], a large number of experimental studies have been conducted, involving stationary grids, screens and perforated plates, swept grids, oscillating grids, grids with injection, nozzle-type grids, and, most recently, grids with randomly rotating rods carrying winglets, thus resulting in very large Re_λ [154]. The most widely used published data are those by Comte-Bellot and Corrsin [40, 41]. These results, presented here as case HOM00, are well documented, particularly on spectral statistics, and have been used almost exclusively in the development of DNS, LES and turbulence models, thus providing a bridge to the computational and theoretical literature. They achieved a particularly good isotropy (with the r.m.s. velocities equal to each other within less than 5%) by passing the grid turbulence through a slight (1.27:1) contraction. These and many other experiments in the incompressible regime have established that the kinetic energy of grid turbulence decays with distance from an effective origin, and can be fitted by a power law with an exponent in the range between 1.2 and 1.3. The analytical/numerical prediction of a proper decay exponent remains a major challenge.

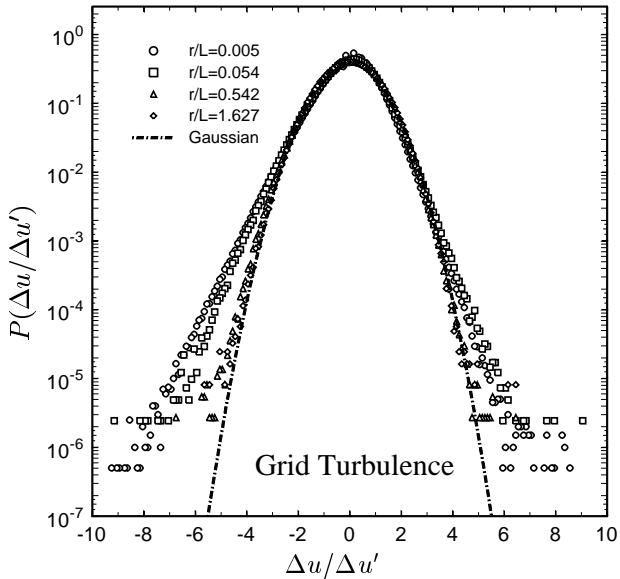


Figure 1: P.d.f. of longitudinal velocity differences in grid turbulence.

The Comte-Bellot/Corrsin results will be supplemented with some recent measurements [59] of probability density functions (p.d.f.) of velocity differences in decaying grid turbulence, presented as case HOM01. These include p.d.f. of both streamwise and transverse velocity differences over distances corresponding to the inertial subrange of the energy spectrum, which would be particularly useful to LES development. As typically shown in figure 1, these p.d.f. are skewed when the distance between points is much smaller than the integral length scale, L (compare these results to the skewness of the velocity derivative [206]) and approach the Gaussian p.d.f. as this distance becomes comparable to L , indicating that the two velocities become statistically independent.

Grid turbulence subjected to plane straining

From its inception, grid turbulence has also served as the initial state from which turbulence is allowed to develop to a distorted, more complex, state. The development of grid turbulence in distorted ducts was first studied in conjunction with the development of the Rapid Distortion theory [136, 214], but the experiments that have been referenced the most are those by Tucker and Reynolds [216], which include a case of lateral distortion in a duct with a rectangular cross-section of constant area but varying height-to-width ratio, such that there was no streamwise mean strain rate. These results will be presented here as case HOM04. More recently, several studies dealing with the adjustment of turbulence energy and structure following application of one or more plane strain rates and their removal have been published. This was achieved by passing grid turbulence through distorting ducts with elliptical [67, 68, 124] or rectangular [116] cross-sections. As representative results for the application of a single plane strain, we have selected case HOM05 [124] and, for two successive plane strains, case HOM06 [67]. HOM05 has

the distinct feature of presenting the development of the correlation coefficient $\overline{vw}/v'w'$ under the influence of a transverse strain; it reaches values comparable to those of $\overline{uv}/u'v'$ in shear flows. HOM06 documents the adjustment of anisotropic turbulence to an additional plane strain. Finally, as a representative study of the recovery of turbulence towards isotropy after the removal of plane strain, we present case HOM07 [116]. This work documents that the rate of return towards isotropy depends on the initial energy partition to its components: it is faster when the turbulence is initially nearly axisymmetric and slower when one of the two transverse components is substantially larger than the other one.

3.2.2 Direct numerical simulations

Because of its simplicity, isotropic turbulence has historically been the subject of some of the the largest numerical simulations at any given time. It is usually modelled as a periodic cubic numerical box, without solid boundaries, using spectral numerical schemes similar in spirit or in detail to the one described in [176]. We will restrict ourselves to incompressible flows. High quality compressible turbulent codes have only recently appeared, although they already include fairly large calculations [170, 106]. Because of the possibility of discontinuities, the latter codes are usually not spectral, and rely on high-order finite-differences or finite-volumes techniques.

There is general agreement that the large scales of isotropic incompressible equilibrium turbulence are essentially independent of the Reynolds number, which would seem to imply that a single simulation, at sufficiently high Reynolds number, should be enough to characterize this flow. This has turned out to be an oversimplification. In the first place non-equilibrium effects are important, and several simulations have centred on the differences between forced and decaying turbulence, and on the influence on the latter of the form of the initial energy spectrum [202]. Another complication is the intermittent behaviour of turbulence [17], which is known to depend on Reynolds number, and which has motivated a number of simulations of forced turbulence, which at present include the highest Reynolds number simulations available.

Decaying flows

Experimental realizations of decaying turbulence are usually approximated by the spatial damping of properly manipulated grid turbulence, with the best known example being [41]. This experiment has historically become one of the first benchmarks against which to test new sub-grid scale LES models, particularly their ability to match the time evolutions of the turbulence kinetic energy and of the energy spectrum. Because neither grid turbulence nor numerical simulations are perfectly isotropic, increasingly detailed simulations of temporally decaying, spatially-periodic, numerical analogs of [41] have been undertaken periodically, so as to serve as comparison with LES and to remove one of the possible sources of disagreement [141]. The challenge is to include enough of the large scale spec-

trum while retaining adequate resolution of the small scales at the Reynolds numbers of the experiments.

A new simulation of this flow is included in the data base as case HOM02. It was carried at a numerical resolution of 512^3 ($k_{max} = 241$), using the code in [176]. The flow was initialized with random phases at an initial $Re_\lambda = 945$, and was allowed to decay to $Re_\lambda \approx 60$. Only results with Re_λ below about 105 are included in the data base, as corresponding to a flow that had sufficient time to relax from the initial conditions.

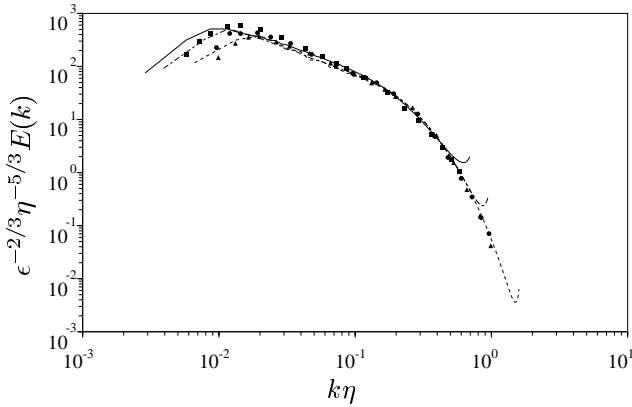


Figure 2: Evolution of the three-dimensional energy spectra of decaying isotropic turbulence at comparable times. Lines are simulations from case HOM02. Symbols represent measurements from HOM00. — and ■, $Re_\lambda = 71.5$; --- and ●, 65.1 ; ---- and ▲, 60.7 .

An important issue in simulations is the specification of initial conditions. Most simulations of turbulence are initialized with a random flow field having a given spectrum but uncorrelated phases. It is easy to show that such a field does not dissipate energy significantly until the velocity develops short term correlations. The skewness of the velocity derivative, which is an indicator of non-linear interactions is, typically, initially zero, it increases rapidly to a maximum, and then it decreases slowly as the Reynolds number of the decaying turbulence decreases. Different initial conditions result in different initial transients, which model only poorly the development of turbulence closely behind the grid; this is one of the major causes of disagreement between experiments and simulations. The data set in the present data base includes a flow field, filtered to a resolution 128^3 , with an energy spectrum corresponding to a Reynolds number somewhat larger than the most upstream station in [41], but with fully developed correlations. This field develops numerically into flows with spectra which follow closely those in the experiment (figure 2). This case may be concluded to have fairly realistic initial conditions and is recommended for comparisons with LES attempting to simulate decaying isotropic turbulence.

Forced flows

One of the main motivations for the simulations of forced isotropic turbulence has been the study of intermittency. It has been known for a long time that the original Kol-

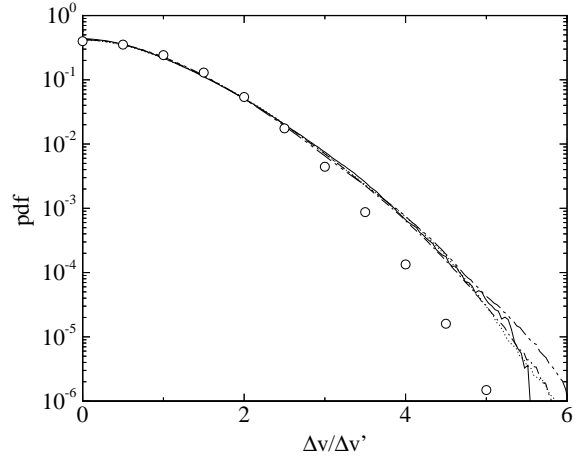


Figure 3: P.d.f. of transverse velocity differences for $\Delta x/L = 1/3$, and: —, $Re_\lambda = 62$; ·····, 95 ; — · —, 142 ; - - - -, 168 . ○, Gaussian.

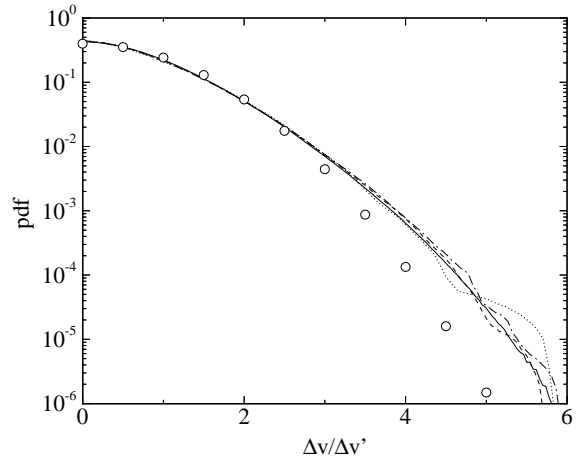


Figure 4: P.d.f. of transverse velocity differences for $\Delta x/L = 1/3$, and $Re_\lambda = 142$. Velocities are low-pass filtered with Gaussian spectral windows $\exp(-k^2 H^2)$, with: —, $H/L = 0$; - - - -, 0.025 ; — · —, 0.05 ; ·····, 0.1 . ○, Gaussian.

mogorov hypothesis [109], according to which all turbulent velocity differences within the inertial range should be statistically similar, is not precisely satisfied. It was found first that the p.d.f. of velocity derivatives are non-Gaussian and Reynolds number dependent [17], and it has become clear since then that non-Gaussian behaviour is also displayed by two-point velocity differences: their statistics change gradually from Gaussian to non-Gaussian as the separation distance is decreased from the integral length scale to the Kolmogorov microscale [101]. In fact, the dependence of the structure functions (moments of the velocity differences) on separation distance has been used as a test for the different theories on intermittency [110].

There is experimental evidence that the p.d.f. of the velocity differences are only functions of the separation distance, normalized with the integral length scale of the flow, and therefore essentially independent of Reynolds number, as long as the separation distance is within some 'ex-

tended' inertial range [101, 77]; the same result has also been found by numerical simulations (figure 3). Moreover, for separations large compared to the Kolmogorov microscale, these p.d.f. are independent of the details of the small turbulent scales, and, thus, could be measured with probes which are too large to resolve the dissipative length scales. From this, one may conclude that, in numerical simulations, the p.d.f. of velocity differences should be insensitive to spatial filtering of the velocity field, at least as long as the filter width is narrower than the separation distance (figure 4). A 'good' LES should also be able to reproduce intermittent p.d.f. at the resolved scales.

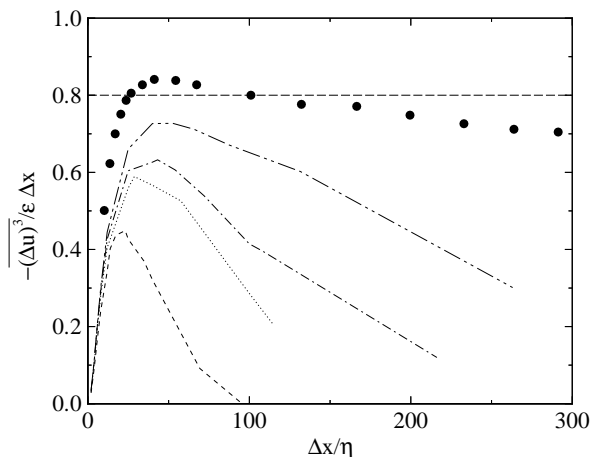


Figure 5: Normalized third order structure functions for the forced simulations in the data base. For an asymptotic inertial range, the function should be equal to 0.8. Lines are as in figure 3. Symbols are jet at $Re_\lambda = 852$ from [5]

The study of the phenomenon of intermittency has motivated several simulations of forced cubic periodic turbulent boxes [219, 181, 34]. The numerical codes are generally the same as those used for decaying turbulence, but the flow is driven by energy input at its large scales so as to achieve a statistically stationary state. The forced simulations have achieved somewhat higher Reynolds numbers than the decaying simulations, because they bypass the initial transient in the formation of the turbulent structure, during which some decay is inevitable. Forcing also improves the statistics at a given Reynolds number, because the flow can be observed for as long as the simulations run. On the other hand, forcing introduces an unnatural behaviour of the large scales.

The data base includes a set of simulations (HOM03) at various Reynolds numbers, all of which were obtained with the same code and forcing scheme [176], and at the same resolution in Kolmogorov units. The reported simulations are in the range $36 \leq Re_\lambda \leq 168$. In general, only statistical averages are given, both because initial conditions are irrelevant for driven flows, and because the fields are too large in most cases for inclusion. However, a single flow field from the $Re_\lambda = 95$ simulation has been included, filtered to 32^3 resolution, to be used as initial conditions in LES experiments. A version of this field, at 128^3 resolution, has been used as the initial condition for the DNS

computation of rotating turbulence in HOM13.

These simulations achieved Reynolds numbers which are among the largest available at the moment. In some cases, Re_λ is large enough for the dissipation to reach its asymptotic value, and for most scaling laws to settle to their large- Re_λ behaviours [94]. It should be realized, however, that the spectra of these simulations do not actually contain an equilibrium inertial range. This can be seen in figure 5, which tests the validity of the Kolmogorov '4/5' law, which should hold in the self-similar range of scales for which neither viscosity nor forcing are important. According to Kolmogorov's hypothesis, the quantity plotted in the figure should be equal to 4/5 in the inertial range. Nevertheless, none of the plotted curves reaches that value, although the simulations with the highest Re_λ show a tendency to approach it. The same conclusion follows from the analysis of the energy spectra [93], which suggests that an inertial range would not appear until Re_λ becomes at least 600.

3.3 Rotating turbulence and its distortions

3.3.1 Experiments

All measurements reported here were taken in the same basic facility, at ONERA, France. Rigid body rotation (about its streamwise axis) was imposed on an air stream by passing it through a rotating cylindrical duct equipped with a relatively long, fine-mesh, honeycomb. Turbulence was produced by a grid, positioned near the exit of the rotating duct, and then it was let to develop in a non-rotating downstream section.

The simplest configuration occurs when the downstream duct is also cylindrical, in which case the rotating turbulence is left to decay. This is presented here as case HOM10 [92], which largely supersedes an earlier study in a similar configuration [223] and is closer to being homogeneous (away from the walls) than any previous attempt to produce rotating turbulence using a variety of different configurations. The mean speed, U , in the duct was fixed and different conditions were achieved by changing the grid (three different mesh sizes, M) and the rate of rotation Ω (five different rates, including the reference case of no rotation), within the range of *grid Rossby numbers*, $Ro_M = U/2\Omega M$, from 95.4 to 4 (excluding the no rotation case). Measurements include the decay rates, integral length scales and energy spectra of the streamwise and transverse velocity components. The effects of rotation on the turbulence have been characterized by the value of the *turbulent Rossby number*, $Ro_q = (1/\Omega)/(q^2/\epsilon)$, which can be connected to the grid Rossby number through the turbulent kinetic energy equation. The results show that the effects of rotation on the turbulence structure and decay rate become measurable only for $Ro_q < 1$. The main effects are an overall decrease of the decay rate of the kinetic energy and an enhancement of anisotropy, with the transverse components losing energy through dissipation slower than the streamwise one does. At any rate, the effects of rotation in these experiments are far from spectacular, so one would expect that they can only be predicted by refined theoretical or numerical studies.

In subsequent studies, rotating grid turbulence, generated as above, has been subjected to different distortions by passing through ducts with varying cross-sections. Case HOM12 is a combination of rigid body rotation and axisymmetric straining, achieved with the use of an axisymmetric contraction as the downstream duct [128, 127]. Two ducts, with the same contraction ratio but different lengths, were used. Compared to non-rotating grid turbulence subjected to the same axisymmetric strain, rotating turbulence displays: a) a non-uniformity of the radial distribution of the mean velocity, although sufficiently weak to ensure approximate homogeneity of the turbulence near the axis, b) a reduced decay rate, especially that of the streamwise component, and c) a reduction of the Reynolds stress anisotropy, mainly as a result of reduced streamwise energy component decay.

Finally, case HOM14 presents the development of grid turbulence in solid body rotation subjected to plane strain [124, 126]. This was achieved with the use of a duct having an elliptical cross section with a constant cross-sectional area but periodically varying axis ratio and orientation. Compared to a corresponding undistorted grid turbulence with the same decay time, this flow maintained substantially higher energy levels and appeared to reach a plateau of kinetic energy, implying a balance between the production and dissipation rates. The Reynolds stress anisotropy exhibited an oscillatory pattern.

3.3.2 Direct numerical simulations

The numerical simulation of rotating turbulence, like those of decaying turbulence and homogeneous shear flow, suffers from the non-equilibrium problem, in which both large and small scales are important. All available simulations of three-dimensional rotating turbulence correspond to the spin-up problem, in which rotation is suddenly imposed to a non-rotating periodic box, containing either a fully developed or a random-phase field [211, 140]. This is different from the experimental configurations, in which turbulence is created, by a mechanical device, in a previously rotating fluid. Therefore, experiments and simulations of rotating turbulence can be expected to be comparable, if at all, only after a decay time which is sufficiently long to erase the effect of the initial conditions. This requires a high numerical resolution and a wide range of scales, which have only recently become possible. Unfortunately, no appropriate simulation on rotating turbulence was available at the time of publication of this report.

3.4 Uniformly sheared turbulence and its distortions

3.4.1 Experiments

By this term, one commonly understands a rectilinear flow with a uniform transverse mean velocity gradient, such that the shearing action is in the streamwise direction. The exception to this rule is one experiment [151], to be presented here as case HOM20, in which the mean streamwise velocity was constant and the shearing occurred on transverse planes. This was achieved by superimposing equal

rates of rigid body rotation and plane strain on grid turbulence in a duct with a rotating, cylindrical, upstream section and a non-rotating, elliptical, downstream section having a constant cross-sectional area but varying eccentricity and orientation. The mean shear rate in these experiments was comparable in magnitude with typical values in the streamwise shearing experiments, and the flow maintained a good homogeneity. There was a consistent development of anisotropy and the shear stress correlation coefficient reached values comparable to those in other shear flows. Unfortunately, the development time in the test section was relatively small (the maximum *total strain* was 2.25), so that the Reynolds stresses were still decreasing at the end of the duct, which indicates that production by the mean shear was still not the dominant process. Despite these limitations, however, these experiments have some advantages over the other shear flow configurations: decoupling of the shear and turbulence generation mechanisms, well defined entrance conditions (grid turbulence) into the sheared section and turbulence measurements in the flow development region.

The remaining cases in this section correspond to conventional uniformly sheared flows. The idealized concept of homogeneous sheared turbulence, attributed to von Karman, was realized experimentally and carried to maturity at the Johns Hopkins University in the 1960s and 70s. In these and all subsequent studies, the shear was generated by passing the flow through a device with a variable resistance and some care was taken to homogenize the initial length scales. The first detailed study with a reasonable transverse homogeneity had a relatively low mean shear [32] and is known to suffer from insufficiently developed turbulence structure; one should avoid using this work, despite its frequent past use in many computational studies and turbulence models. Higher shear experiments [74, 207, 208, 210] have resolved this problem. Two sets of independent experiments will be presented here: case HOM21 [207, 208], as representative of the Johns Hopkins experiments and case HOM22 [210], as representative of the University of Ottawa experiments. Some recent [43] experiments at very high shear rates, showing a dependence of the turbulence structure upon the mean shear and similar to DNS results [117, HOM25], are not detailed enough for the present purposes.

Case HOM21 largely supersedes all earlier [74] experiments in the same facility and is the best documented uniformly sheared flow experiment. The published results [207, 208] include ample information about the fine structure as well as spectra and p.d.f., however, in the present database, we present only the most essential statistics, namely the development of Reynolds stresses, integral length scales and microscales and some two-point correlations. Case HOM22 includes flows with different values of the mean shear and initial length scale and is, thus, suitable for detecting any possible sensitivity of LES results to those parameters. Some recent measurements [59] of p.d.f. of velocity differences in the same flow, have also been presented as case HOM22. These include p.d.f. of both streamwise and transverse velocity differences over distances cor-

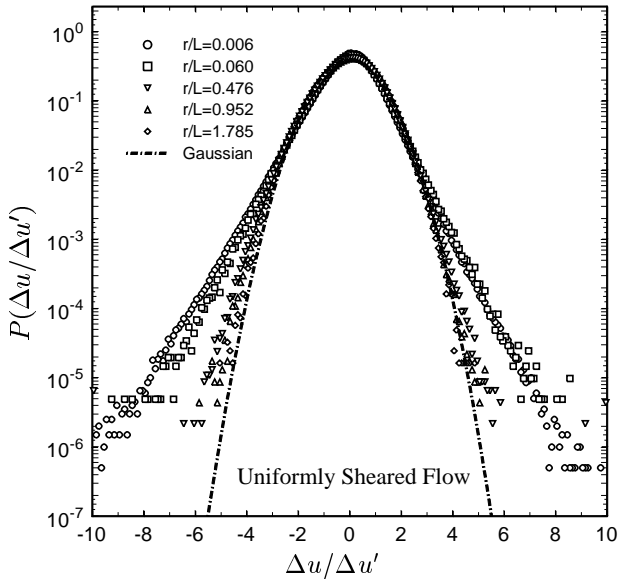


Figure 6: P.d.f. of longitudinal velocity differences in uniformly sheared turbulence.

responding to the inertial subrange of the energy. As typically shown in figure 6, these p.d.f.s are non-Gaussian and skewed when the distance between points is much smaller than the integral length scale, L , and approach the Gaussian p.d.f. as this distance becomes comparable to L , indicating that the two velocities become statistically independent. Although, qualitatively, the p.d.f. in shear flow resemble those in isotropic turbulence, quantitatively, there are distinct differences between the two sets, only part of which can be attributed to differences in Re_λ . There are also differences in the p.d.f. of velocity differences between points separated in the streamwise direction from those separated in the transverse direction. These differences appear to contradict local isotropy.

Geometrical distortions of uniformly sheared turbulence seem to be fruitful environments for testing theoretical hypotheses and adjusting computational schemes. It is, therefore, somewhat surprising that only relatively few studies of this type exist. The application of streamwise strain to uniformly sheared turbulence, by passing it through two-dimensional contractions, will be presented as case HOM26 [204]. The effects of centrifugal actions / streamline curvature will be presented as cases, HOM27 and HOM28 [82, 33], in which fully developed uniformly sheared turbulence was passed through curved ducts with a constant or abruptly changing radius of curvature. There have been no corresponding DNS for these types of experiment, but the geometries appear to be quite suitable for LES studies. In particular, these experiments document both the rate of adjustment of uniformly sheared flow structure to additional strains as well as the quasi-self-similar asymptotic structure that such flows achieve under the prolonged influence of a uniform additional strain.

3.4.2 Direct numerical simulations

As noted in [176], spectral simulation codes for isotropic turbulence can be easily adapted to homogeneous shear flow by a simple transformation of the set of wavenumbers. This approach has been used in a number of simulations. The transformation is equivalent to distorting the computational grid with the mean shear, and it is customary to compensate this distortion at regular intervals by re-interpolating the flow field into the original orthogonal grid. As a consequence, in these simulations, most quantities are only available at the discrete interpolation times.

In the present data base, we have included three different data sets, all of them incompressible, in which the flow is triply periodic in a parallelepiped and the mean shear is in the x_2 direction. An equivalent compressible flow simulation at moderate Mach numbers can be found in [187].

The first set, HOM23 [178], contains three different flow simulations, with different combinations of viscosity and shear. The same simulations contain a passive scalar field, subjected to an imposed, constant, mean scalar gradient. Two more simulations are dynamically identical to the cases mentioned above (U), but with different Schmidt numbers for the scalar.

The second set, HOM24 [187], has a Reynolds number comparable to that in the highest value case above, but uses a different numerical scheme and a different initial spectrum. It is included to allow a comparison between different numerical experiments at comparable conditions.

The third case, HOM25 [117], has a much higher dimensionless shear rate than the other two. The structure of this flow was found to be different from those at low shear rates and exhibited longitudinal velocity streaks similar to those in the near-wall region of boundary layers and pipes (see also [43]).

The simulations in the two first data sets were started from initially random-phase Fourier modes with a given power spectrum, while that in the third set was started from fully-developed isotropic turbulence, computed in a previous decaying turbulence simulation. The difference in the subsequent development is seen in figure 7(a), which shows the evolution of the turbulence Reynolds number for all simulations. While for the random-phase initial conditions Re_λ shows an initial decrease, for the fully developed initial conditions there is no initial relaxation period.

Figure 7(b) shows the evolution of the dimensionless shear rate, $S^* = Sq^2/\epsilon$, together with experimental results from [210]. It is clear that the long-time numerical values differ from each other and from the experimental ones. One should keep in mind, however, that, in these simulations, most of which used a 128^3 grid, the statistics are taken over a relatively small ensemble of flow structures and without the benefit of time averaging. Therefore, the oscillations in individual evolution curves are most likely due to the numerical and statistical uncertainties. On the other hand, the dimensionless shear rate in the simulations presents an increasing trend, which is beyond the uncertainty, and

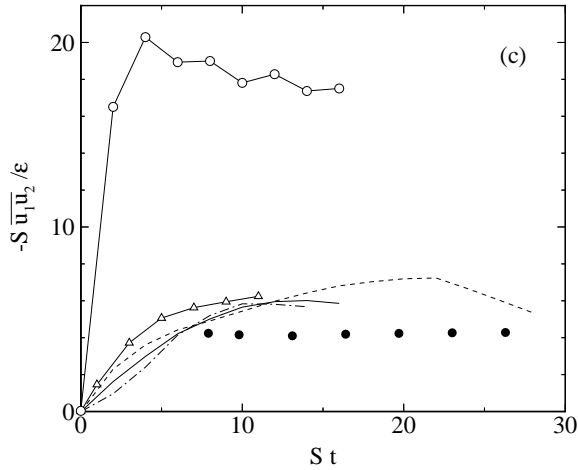
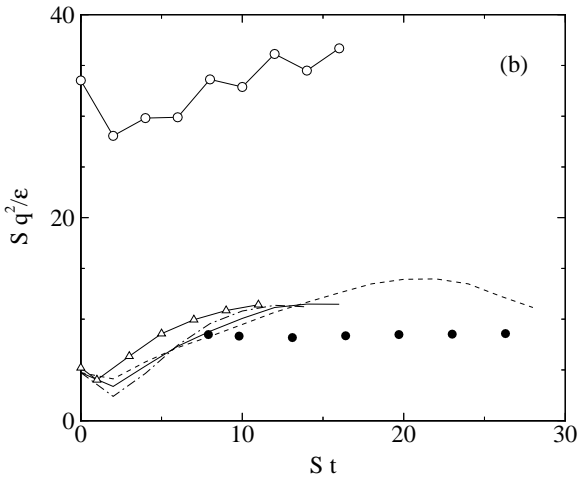
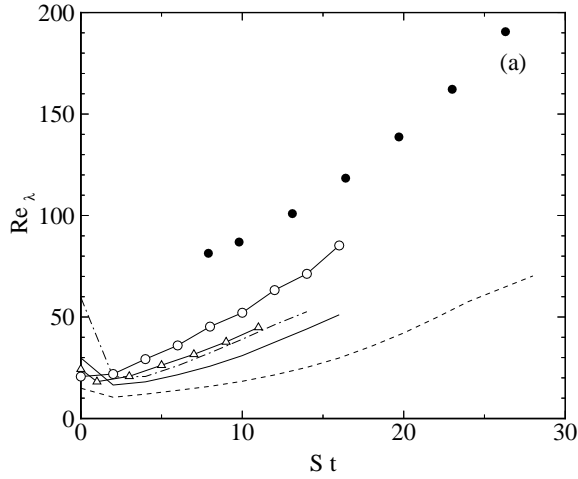


Figure 7: Evolution of flow parameters for the shear flow numerical data sets. (a) $Re_\lambda = (5q^4/3\epsilon\nu)^{1/2}$, where $q^2 = \overline{u_i u_i}$. (b) Dimensionless shear, Sq^2/ϵ . (c) Similarity parameter, $-S\overline{u_1 u_2}/\epsilon$. Symbols; — : HOM23-U. - - - : HOM23-W. - · - : HOM23-X. —△— : HOM24. —○— : HOM25. • : Experiments from [210].

which is not present in the experiments. Such differences should not necessarily be disconcerting because the simulations and the experiments represent somewhat different kinds of flows [207], subjected to different initial conditions. Even so, it is still interesting to determine whether the simulations and the experiments attain the same self-similar asymptotic regimes. As seen above, both types of flows have growing Reynolds numbers, which is an indication that the turbulence structure is dominated by the mean shear. A quantitative test can be derived from the simplified energy equation,

$$\partial k / \partial t + S \overline{u_1 u_2} = \epsilon,$$

which shows that self-similar growth requires that production be proportional to dissipation, i.e. that

$$S \overline{u_1 u_2} / \epsilon = \text{const.}$$

This quantity is plotted in figure 7(c), which suggests that, unlike the experiments, most simulations reach their self-similar stage only towards the end of computational time. Extension of the computation to longer times is prevented both by the growth of the longitudinal integral scale, which interferes with the finite size of the computational box, and by the increase in Re_λ , which degrades the resolution for a given computational grid. The numerical aspects of each simulation are discussed in the respective papers. In general, all of them are discontinued when the longitudinal integral scale becomes of the order of 10% of the length of the box, or when the resolution falls below $k_{max}\eta \approx 1$, which is generally considered to be an adequate limit.

3.5 SUMMARY OF HOMOGENEOUS FLOWS

ISOTROPIC AND GRID TURBULENCE AND THEIR DISTORTIONS

HOM00	Decaying grid turbulence	E	Comte-Bellot & Corrsin [41]	pg. 59
HOM01	Decaying grid turbulence	E	Ferchichi & Tavoularis [59]	pg. 61
HOM02	Decaying isotropic turbulence	N	Wray	pg. 63
HOM03	Forced isotropic turbulence	N	Jiménez & Wray [94, 93]	pg. 65
HOM04	Grid turbulence with plane strain	E	Tucker & Reynolds [216]	pg. 67
HOM05	Grid turbulence with transverse strain	E	Leuchter & Benoit [124]	pg. 69
HOM06	Grid turbulence with successive plane strains	E	Gence & Mathieu [67]	pg. 72
HOM07	Return to isotropy of strained grid turbulence	E	Le Penven, Gence & Comte-Bellot [116]	pg. 74

ROTATING TURBULENCE AND ITS DISTORTIONS

HOM10	Rotating decaying turbulence	E	Jacquin, Leuchter <i>et al</i> [92]	pg. 76
HOM12	Rotating turbulence with axisymmetric strain	E	Leuchter & Dupeuple [128, 127]	pg. 79
HOM14	Rotating turbulence with plane strain	E	Leuchter & Benoit [124]	pg. 82

SHEARED TURBULENCE AND ITS DISTORTIONS

HOM20	Transversely sheared flow	E	Leuchter <i>et al</i> [151, 125]	pg. 85
HOM21	Uniformly sheared flow	E	Tavoularis & Corrsin [207]	pg. 87
HOM22	Uniformly sheared flow	E	Tavoularis & Karnik [210]	pg. 89
HOM23	Homogeneous shear flow	N	Rogers & Moin [178]	pg. 91
HOM24	Homogeneous shear flow	N	Sarkar [187]	pg. 93
HOM25	Homogeneous shear flow (high shear)	N	Lee, Kim & Moin [117]	pg. 95
HOM26	Uniformly sheared flow with streamwise plane strain	E	Sreenivasan [204]	pg. 96
HOM27	Uniformly sheared flow with uniform curvature	E	Holloway & Tavoularis [82]	pg. 98
HOM28	Uniformly sheared flow with S-shaped curvature	E	Chebbi, Holloway & Tavoularis [33]	pg. 100

E: experimental cases. N: numerical ones. Consult individual data sheets for more details

Chapter 4: Interaction of Shock Waves with Grid Turbulence

Otto Leuchter

ONERA

F - 92190 Meudon, France

4.1 Introduction

Interactions between shock waves and turbulence occur in a variety of flow configurations of practical relevance. Typical examples are shock wave/boundary layer interactions and shock wave/free shear layer interactions encountered in external and internal aerodynamics. Complex linear and nonlinear mechanisms come into play in such situations, resulting in a drastic change of the turbulence structure and the statistical properties of the flow. The theoretical background of these structural changes is the existence of complex interactions between the basic modes of compressible turbulence known as vorticity, acoustic and entropic modes. Fundamental questions arise in this context, concerning the amplification of the turbulence passing through the shock wave, the change of anisotropy of the Reynolds stresses and the associated length scales, and the way the shock-impacted turbulence adapts itself to the new flow conditions downstream of the interaction.

The basic physics of such complex interactions are most conveniently investigated in reasonably simplified flow configurations. A typical example is that of homogeneous quasi-isotropic turbulence subjected to sudden compression by a normal shock wave. This type of flow was originally investigated in shock tubes [79, 105, 84, 26], and more recently in stationary wind tunnel flows. [91, 13]. The relevant parameters in these investigations are the shock strength (i.e. the shock-normal Mach number), and the initial state of the turbulence interacting with the shock wave, as defined by the turbulent energy level, the ‘compressibility’ content, the Reynolds stress and length scale anisotropy, and the turbulence Reynolds number. For a general review of compressibility effects on turbulence one can consult [120].

Direct numerical simulations (DNS) of decaying turbulence passing through a shock wave have been performed by various authors (see e.g. [119, 180, 73, 118, 138]). This type of approach is commonly restricted to Reynolds numbers that are too low to be representative for practical applications. Large-eddy simulations (LES) are expected to go beyond this bound and become more relevant for real-world applications. Nevertheless, DNS computations, even at fairly low Reynolds numbers, do provide interesting insights into the physics of the complex mechanisms which govern the interactions. For instance, the effect of upstream compressibility (i.e. dilatational velocity fluctuations) on the turbulence amplification (hard to evaluate experimentally!) has been brought to light clearly in the work of Hannappel and Friedrich [73]. Besides the basic observation that initially isotropic turbulence becomes axisymmetric when passing through the shock wave, the

authors observed that upstream compressibility produces higher vorticity components parallel to the shock wave, whereas the axial component is convected through the shock wave without major alterations. Simultaneously, the decrease of micro-length scales relative to the transverse velocity fluctuations is less pronounced in the presence of upstream compressibility, and the increase of the dissipation length scale is slightly reduced. The important role played by the acoustic and entropic fluctuations upstream of the shock/turbulence interaction has also been highlighted in the recent work by Mahesh *et al.* [137, 138]. The effect of shock strength was discussed by Lee *et al.* [118].

As mentioned before, experiments in this field can be divided into two main classes. The first covers experiments performed in supersonic wind tunnels, where a (normal) stationary shock wave is produced by means of a suitable shock generating device. The turbulence is usually created in the sonic region of the supersonic nozzle using a grid-type turbulence generator. Homogeneous (quasi-isotropic) turbulence is achieved at the position where the flow impacts the shock wave. The measurements are made at a given axial distance with respect to the position of the shock wave. Unambiguous statistics are determined as a function of the distance between the measurement point and the shock wave, for a given upstream state of the turbulence. These experiments are easy to compare with numerical simulations considering homogeneous turbulence flowing through a stationary shock wave.

The second family of experiments reported in the literature on free turbulence/shock wave interactions considers traveling shock waves moving through a homogeneous turbulent field. The experiments are performed in shock tubes, where the interacting shock wave results from the reflection of an incident shock wave that first passes through a turbulence-generating grid, entraining a transversely homogeneous turbulent flow of constant velocity. The flow remains subsonic provided that the incident shock wave is sufficiently weak. The strength of the reflected shock wave (and accordingly the flow velocity behind it) can be controlled to a certain extent by replacing the reflecting solid wall with a porous end wall. A remarkable facility based on this principle has recently been constructed at CUNY by the group of Andreopoulos (see [25, 26, 27]), allowing turbulence measurements with good space and time resolution.

Useful information can be gained from this type of experiment about the basic mechanisms involved in shock wave/turbulence interactions. Statistical measurements performed at a fixed position in the shock tube are not easy

to interpret, however, in terms of statistical measurements made in stationary wind tunnel experiments, or in terms of statistical results obtained from numerical simulations considering stationary shock waves (as e.g. in [73] or [118]). This is primarily due to the fact that during the useful period of measurements, the distance between the probe and the upstream-propagating shock wave increases, while the state of the turbulence encountered by the shock wave is continually varying. These intrinsic difficulties are further aggravated by the relatively short time available for the measurements, which (for a given dimension of the shock tube) is a decreasing function of the shock intensity. Therefore, shock tube experiments are generally run with relatively low shock intensities compared to those achievable in wind tunnels. This is also done to ensure subsonic flow behind the incident shock wave and to avoid choking of the turbulence grid.

The following description of possible test cases for LES with stationary shock waves will be restricted to wind tunnel experiments in supersonic flow.

4.2 Experiments

To our knowledge, there are two recent and reasonably well-documented experiments in wind tunnels with stationary shock waves. The first was carried out at ONERA-Meudon in a supersonic wind tunnel in which the turbulence was created by means of a grid located at the nozzle entrance. The grid itself constitutes the sonic throat of the nozzle and provides a Mach number of 1.4 at the location of the normal shock wave. The shock position is controlled by a second throat and by suction of the boundary layer at the wall of the wind tunnel. The measurements are by Laser-Doppler Anemometry (LDA).

The most salient feature of this experiment is the sharp change in the energy decay through the shock wave and the absence of any significant amplification of the turbulent energy. Based on recent DNS results, it may be conjectured that low amplification of the turbulent kinetic energy through the shock wave could be due to intrinsic compressibility effects in the sense that the thermodynamic pressure fluctuations store energy at the expense of turbulent kinetic energy and alter the interaction mechanism [63].

The second experiment was performed at CEAT-Poitiers, in a similar facility. A multi-nozzle turbulence generator (constituted by 625 adjacent conical nozzles) was used here instead of a turbulence grid, providing supersonic flow at Mach number 3 in front of the shock wave, with a significantly lower turbulence intensity level than in the ONERA experiment (and consequently lower Reynolds number). From this point of view (and also with regard to differences in the measuring techniques used), the two experiments may be considered as complementary. A normal shock wave is created in the central part of the test section by means of a Mach effect produced by the interaction of two oblique shock waves of opposite inclination. This particular arrangement causes the axial mean velocity to be linearly increased behind the shock wave, at a rate $\Delta U/\Delta X$ of approximately $5.4 \times 10^3 \text{ s}^{-1}$ (corresponding

to a variation of one percent per millimeter in the upstream velocity). Hot-wire techniques and LDA were used for the measurements.

The measurements showed that the streamwise velocity fluctuations are increased through the shock wave, in agreement with Ribner's theory, whereas the longitudinal integral length scale is decreased. Like in the ONERA experiment, the amount of compressibility in the upstream part of the flow could not be quantified by the techniques used for the measurements.

4.3 Comments on Experiments

No direct information is included in the data base concerning velocity spectra, since spectral analysis was not possible with the LDA measurements. Only in the second experiment (CEAT-Poitiers) was spectral analysis performed on hot-wire signals which may be assumed to represent mass flux fluctuations. The lack of turbulent kinetic energy spectra is a serious limitation regarding the assessment of numerical simulations, since initial spectra can only be estimated analytically from the statistical quantities reported in the data base.

A further significant limitation of both data sets arises from the lack of information on one-point statistics (as well as spectral distributions) concerning the additional modes of fluctuation (entropic and acoustic modes). As evidenced by DNS (see above), these modes have a strong influence on the interaction mechanism, and must therefore be accounted for in the generation of compressible initial conditions for LES, as well as in subgrid models. Due to metrological difficulties, no direct information on the relative importance of such fluctuations could be included in the data base. The increased energy decay downstream of the shock wave, and the absence of any noticeable amplification of the turbulent energy observed in the ONERA experiment, could possibly be attributed to a relatively high level of irrotational fluctuations produced by the specific turbulence generating device used for that experiment. The difference between the two experiments regarding the turbulent energy amplification may be explained by a possibly lower level of dilatational fluctuations in the CEAT experiment, due to a "milder" turbulence generating procedure and a significantly lower Reynolds number.

LDA measurements in compressible flows with shock waves are usually contaminated by uncertainties due to the finite particle response. Particle drag affects the mean velocity recovery immediately behind the shock wave and produces spurious turbulence in the case of polydispersed particles, the extent and level of which depend on the actual size distribution of the particles. Basic studies of the behavior of particles flowing through a shock wave in laminar flow (see for example [123, 212]) have demonstrated the possibility of quantifying these effects, using current laws for the particle drag and estimated (or measured) forms of particle distribution. For both experiments, the recovery distance can be estimated to be of the order of a few millimeters, for particles of sub-micron size commonly used in the experiments.

For the ONERA experiment, the mean flow and turbulence data given in the data base represent average values of several axial explorations performed at different vertical positions in the plane of symmetry of the nozzle. These measurements reveal satisfactory transverse uniformity of all flow parameters recorded in the data base. A moderate negative mean gradient of the axial mean velocity is observed upstream of the shock wave, with a more or less pronounced corrugated variation of the velocity, presumably due to steady Mach waves originating from the turbulence generator [20].

For the CEAT experiments, the reported measurements were performed by single explorations on the axis of the flow. Separate measurements have revealed satisfactory transverse uniformity of the velocity in the central region of the flow interacting with the shock wave [2].

The CEAT data set also includes information about the behavior of integral length scales relative to mass flux fluctuations, deduced from autocorrelations of hot-wire signals via Taylor's hypothesis. This procedure yields only approximate estimates of the length scale downstream of the shock wave, due to the fact that the mean velocity is not constant. However, the associated uncertainty of the length scale estimation remains acceptably small, of the order of a few percent. The data indicate a larger decrease of the lengthscale than that found in the DNS of Lee *et al.* [118] for the same Mach number, and nearly the same Reynolds number (but for a higher level of the turbulence Mach number). The comment on the crucial limitation of DNS regarding the level of the Reynolds number (see above) also applies to that experiment.

It is emphasized that the present compilation is to be considered as a first attempt to create reliable data bases on the topic of (stationary) turbulence/shock wave interactions. In spite of severe limitations with regard to LES assessment (as outlined before), it is expected that the data selected for this purpose will provide useful information for first checks on numerical simulations of compressible turbulent flows involving shock waves.

4.4 SUMMARY OF SHOCK-WAVE/ GRID-TURBULENCE INTERACTIONS

SHW00	Stationary shock on grid turbulence	E	Jacquin, Blin & Geffroy [91]	pg. 105
SHW01	Stationary shock on grid turbulence	E	Barre, Alem & Bonnet [13]	pg. 107

E: experimental cases. N: numerical ones. Consult individual data sheets for more details

Chapter 5: Pipes and Channels

Robert D. Moser

Department of Theoretical and Applied Mechanics
University of Illinois at Urbana-Champaign
Urbana, IL 61801, USA

and

Brian Cantwell

Department of Aeronautics and Astronautics
Stanford University
Stanford, CA 94305, USA

and

L. Patrick Purtell

Mechanics and Energy Conversion Division
Code 333 - Office Naval Research
800 N. Quincy St.
Arlington, VA 22217-5660

5.1 Introduction

Fully developed pressure gradient driven turbulent flows in pipes and channels are ideal model flows for simulations of wall-bounded turbulence. Since the flow is fully developed, it is homogeneous in the streamwise direction. Thus, periodic boundary conditions may be used in that direction, avoiding the problems associated with inflow and outflow boundary conditions. Further, by assuming homogeneity in the spanwise direction in the channel and imposing periodicity, or by using the natural angular periodicity in the pipe, one can use transform methods to invert the elliptic operators that occur in time discretizing the Navier-Stokes equations. This greatly simplifies the numerical procedures. Finally, since the flow is statistically stationary, by making an ergodicity assumption, statistical quantities can be easily computed by averaging in time.

For these reasons, fully developed channel flows have long been simulated numerically, both by LES (e.g. in [149, 167]) and DNS [108, 139, 135, 182, 104]. The pipe flow is less often simulated due to the need to use cylindrical coordinates, and deal with the coordinate singularity at the centre-line. A variety of researchers have reported success in simulating channel flows using a variety of LES models.

There have been many of DNS's of the channel flow at low Reynolds number, starting with the simulation of Kim, Moin & Moser [108], which was at $Re_\tau = 180$ to match the oil-channel experiments of [55, 112]. These low-Reynolds-number simulations are not included in this data base, though they have been used extensively in the past (especially [108]) for comparison to LES. The reason is that the Reynolds numbers are so low as to make LES a questionable endeavour. However, there are three simulations available at higher Reynolds numbers ($Re_\tau = 300, 395$ and 590) [139, 164]. The simulations at 395 and 590 reported by Mansour, Moser & Kim [139] are included here as case PCH10. There are also two fully developed pipe flow DNS available [132, 56], both at the same $Re_\tau = 380$ (based on diameter), which is also really too low for meaningful LES.

However, since these are the only cases for which detailed DNS data are available, one of the pipe simulations is included here [132]. Furthermore, a numerical simulation of a rotating pipe [160] is included to provide a case with an extra complication.

In addition to being attractive flows to simulate, the channel and pipe are also experimentally attractive, and for many of the same reasons. For providing data that is consistent with the idealizations inherent in a numerical simulation (LES or DNS), the pipe is the preferred geometry, since the complication of experimental side walls is avoided. Channel flow experiments are usually done in rectangular channels with large aspect ratios (12 or higher is common), to avoid large side wall effects. On the other hand it is often easier to make measurements in a channel, due to the planar boundaries. Several sets of experimental data are included for both pipes and channels. For channels, there have been many experiments over the years (e.g. [114, 39, 55, 95, 222, 158]). Two recent experimental studies using the best currently available measurement techniques were selected [222, 157]. The Niederschulte experiment [157] (case PCH11) is at $Re_\tau = 921$ ($Re_b = 18,339$) provides very well resolved profiles, down to very close to the wall. The Wei & Willmarth data [222] (case PCH12) has less well resolved profiles, but includes a range of Reynolds numbers ($Re_\tau = 708$ to 1655). In addition, data from the classical experiment of Comte-Bellot [39] are included as case PCH13. These remain the highest Reynolds number channel flow data available ($Re_\tau = 2340$ to 8160). However, the measurements of Comte-Bellot were made with relatively long hot wires (see the relevant data sheet on page), so great care is required in using these data. In particular, the near-wall data are not reliable. Experimental pipe flow data from 4 sources ([54, 166, 213, 228]) are included here as cases PCH01 through PCH04. They span a range of Reynolds number from 7500 to 35×10^6 with a variety of data available.

Finally, channel flows and pipes have been simulated and

measured experimentally with a variety of complicating features such as rotation and curvature. These flows provide an opportunity to address these complications in a flow with very simple geometry. Thus several rotating flows are included in this section. They include the axially rotating pipe simulation by Orlandi [160] (PCH05), and both experimental ([97, 156], PCH20 and PCH23) and numerical ([168, 113], PCH21 and PCH22) rotating channels.

The pipe, channel and rotating channel flows are discussed in more detail below. The cases included in this section are listed in table 1.

5.2 Pipes

Perhaps no other flow has been studied as much as turbulent flow in a pipe. Aside from its obvious practical importance in a vast variety of industrial applications, pipe flow has drawn the interest of researchers because of its geometrical simplicity and because of the apparent ease with which it can be studied experimentally.

The laminar parabolic pipe profile is known to be stable to small disturbances and so the creation of turbulent pipe flow is usually attributed to transition in the pipe entry boundary layer. As the layer develops along the wall small disturbances become amplified producing turbulent spots which convect downstream eventually merging to produce turbulent flow across the full width of the pipe.

Lindgren [131] and later Wygnanski & Champagne [224] showed that this picture is a little too simplistic. Below a pipe Reynolds number of about 3200 (based on diameter) a variety of mechanisms play a role in transition depending on whether the entry flow is smooth or disturbed. Below a Reynolds number of 2300 even large disturbances at the pipe entrance will decay and the flow will relaminarize. Above a Reynolds number of about 3200, turbulence initiated by a disturbed entry condition will be maintained. Considerations of the transition process are particularly important in the context of direct numerical simulations which, due to computer hardware limitations, are necessarily limited to relatively low Reynolds numbers. Since most simulations are time developing the flow must be initiated with disturbances which are large enough to excite nonlinear amplification mechanisms and the simulation Reynolds numbers must exceed the $Re = 3200$ threshold.

A number of criteria have been proposed to test whether a pipe flow is fully developed. Probably the most rigorous is the requirement that fully developed flow corresponds to a state where the turbulence intensity in the pipe is independent of significant changes in the entry conditions. The equivalent criterion for a temporal simulation is that the turbulence level of the simulation at late times must be independent of the turbulence level used to initiate the flow. While this criterion is probably the most rigorous, it is rarely used for practical reasons of computational cost or facility limitations. Experimentally, fully developed flow is generally accepted to occur beyond an entry distance of 100 to 150 diameters. Simulations are as-

sumed to be fully developed once time averaged statistical quantities converge and good agreement with experimentally measured mean velocity profiles has been reached. In this respect simulations are not carried out for the express purpose of generating mean velocity data but rather they are undertaken to provide information about pressure and higher order velocity statistics which may be difficult or impossible to obtain experimentally.

Although experiments on pipe flow have a long history going all the way back to the classical work of Osborne Reynolds there remains today intense interest in this flow. Most recently basic logarithmic scaling laws for the mean velocity near the wall, which were once universally accepted, have been called into question by Barenblatt [9] who proposes to replace the Reynolds number invariant logarithmic profile with a Reynolds number dependent power law profile which asymptotes to a logarithmic envelope. The distinction between the two profiles goes to our most fundamental understanding of the dependence of turbulent flows on Reynolds number when the Reynolds number is very large. At the time of this writing, this controversy has not been resolved one way or another and there are strong feelings on both sides.

Eventually, when the dust settles a key role in deciding the outcome will have been played by the pipe data enclosed with this data base. In particular, the recent measurements of Zagarola (Case PCH04) when combined with the measurements of Henbest (Case PCH02), Durst (PCH01) and Toonder (PCH03), provide a range of nearly five orders of magnitude in the Reynolds number with a useful amount of redundant overlap between cases. The simulation data base of Loulou (Case PCH00) provides fundamental information about flow statistics particularly near the wall where measurements of skewness and flatness have been the subject of debate. The rotating pipe case of Fatica (Case PCH05) is included to provide data on the effect of rotation on turbulence in a well defined geometry.

5.3 Channels

The idealized turbulent flow between two parallel plates driven by a mean pressure gradient parallel to the wall is perhaps the easiest wall bounded flow to understand. It is homogeneous in the streamwise and spanwise directions. Also, integrating the mean streamwise momentum equation from wall to wall yields

$$\tau_{\text{tot}} = -\overline{uv} + \frac{1}{Re} \frac{\partial U}{\partial y} = y \frac{\partial P}{\partial x}$$

where τ_{tot} is the total mean shear stress, y is the coordinate normal to the walls ($y = 0$ at the channel centre), U is the mean velocity and $\frac{\partial P}{\partial x}$ is the mean pressure gradient. Thus, we have an analytic expression for the mean shear stress. This provides a sanity check on both experimental and computational data, and in experiments, it allows the wall shear stress to be unambiguously determined, either by measuring the pressure gradient or the Reynolds stress far from the wall where the viscous stress is negligible. The Reynolds stress and equilibrium total stress are plotted from both the simulations [139] (PCH10)

	Re_b	Re_τ	Ro_b	Comments
PIPE FLOWS				
PCH00	5600	380		Spectral Method
PCH01	7442–20800	490–1200		
PCH02	29300–80500	1610–3900		Includes roughness
PCH03	24580	1382		
PCH04	31000– 35×10^6	1700– 10^6		Superpipe
PCH05	4900	340	0–2	Finite Difference
CHANNEL FLOWS				
PCH10	6875–10935	395–590		Spectral Method
PCH11	18400	921		
PCH12	13145–35353	708–1655		
PCH13	57000–230000	2340–8160		Analog Hot Wire
ROTATING CHANNEL FLOWS				
PCH20	5500–17500		0–0.21	
PCH21	2850	177	0.144	Spectral Method
PCH22	2900	194	0–0.5	Finite Difference
PCH23	850–5000	67–300	0–0.055	

Table 1: Comparative listing of cases in this chapter of the database. Consult data sheets of individual cases for more details, also see Table 2. Re_b is Reynolds number based on bulk (average) velocity and channel half-width (diameter for pipe), Re_τ is based on friction velocity and half-width (diameter), and the rotation number $Ro_b = 2\Omega\delta/U_b$, where δ is half-width and U_b is bulk velocity.

and the experiments [157, 222, 39] (PCH11, PCH12 and PCH13) in figure 1. For large y , all the data should lie just slightly above the equilibrium line, by the amount of the viscous stress. Note however that the data of Niederschulte (PCH11) and Comte-Bellot (PCH13) lie below the line (greater stress), while some of the Wei & Willmarth data (PCH12) lie above the line. This must all be considered to be error; however, the cause of the error is not obvious. Regardless of the cause, these errors provide some guidance as to the accuracy of the second order statistics in the channel flows.

Near the wall, the channel flow has the usual features of a wall bounded turbulent flow such as a boundary layer. In particular, the mean velocity exhibits an approximate log-layer and viscous sublayer. In analyzing this in detail however, one must account for the fact that there is actually a mild favourable pressure gradient in this flow. The r.m.s. velocity profiles near the wall are also similar to those of other wall-bounded flows. Shown in figures 2 and 3 are the mean velocity and r.m.s. streamwise velocity from the channel flow cases included here.

Despite the range of Reynolds numbers, and the three independent sources of data, the mean velocity profiles in wall coordinates collapse remarkably well for the cases PCH10, PCH11 and PCH12. Absent among these cases are the variation of log-layer intercept with Reynolds number that is common at very low Reynolds number. The exceptions to the good data collapse are the $Re_\tau = 708$ profile from PCH12, which lies slightly below the others in the log region and the $Re_\tau = 2340$ and 8160 profiles from PCH13,

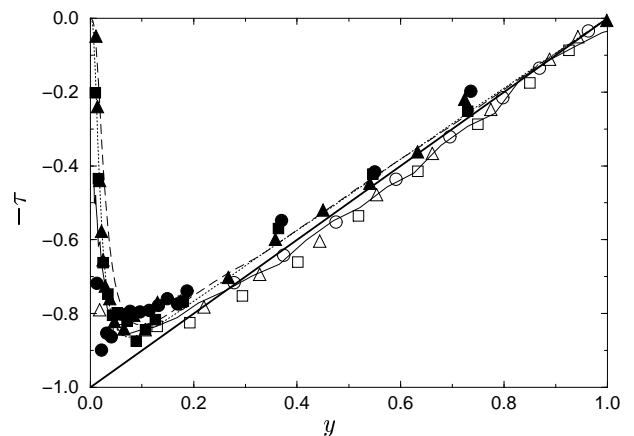


Figure 1: Total stress (equilibrium, dark diagonal line) and Reynolds shear stress on one wall of the turbulent channel cases • PCH12 at $Re_\tau = 1655$, ■ PCH12 at $Re_\tau = 1017$, ▲ PCH12 at $Re_\tau = 708$, — PCH11 at $Re_\tau = 921$, PCH10 at $Re_\tau = 590$ and ---- PCH10 at $Re_\tau = 400$.

which lie above the others. In neither case is this consistent with an overall Reynolds number effect. This would seem indicative of the accuracy of the mean profiles in this cases.

In the rms streamwise velocity profiles, the near-wall peak value is expected to be a weakly increasing function of Reynolds number [198, 174], and this is certainly true of the data from PCH12. However, the peak in the PCH11 case ($Re_\tau = 921$) is lower than the $Re_\tau = 708$ peak from

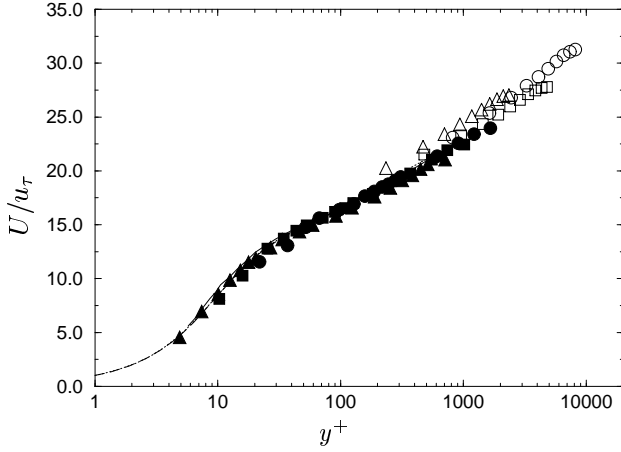


Figure 2: Mean velocity profiles from the turbulent channel cases. Symbols are as described in figure 1.

PCH12, and the peaks from the two PCH10 computations ($Re_\tau = 395$ and 590) are higher than the $Re_\tau = 921$ and $Re_\tau = 708$ cases from PCH11 and PCH12 respectively. Thus, the data from the three cases are not consistent with each other regarding the r.m.s. u peak, and certainly are not consistent with a monotonic increase with Reynolds number. This suggests the level of uncertainty in the r.m.s. velocity fluctuations. Note that the near-wall data of Comte-Bellot (PCH13) is not plotted here because they are not considered reliable near the wall.

5.4 Rotating channels

Rotation, like curvature and buoyancy [23], can have a fundamental influence on the stability of shear layers.

Consider a unidirectional shear flow, characterized by a velocity $U(y)$ in the streamwise direction x , and rotating about the spanwise direction z , with angular velocity Ω . The fundamental parameter describing this flow is the ratio S of rotation and shear vorticity $-dU/dy$

$$S = -\frac{2\Omega}{dU/dy}$$

or, in nondimensional terms, the rotation number $Ro = 2|\Omega|\delta/U_o$, where δ is typical length scale, and U_o the velocity scale.

This parameter can be related to the flow stability through an equivalent gradient Richardson number [23]:

$$B = S(S + 1)$$

The role of the rotation is found to be destabilizing [97] [215] when:

$$-1 < S < 0$$

or

$$B < 0$$

In laminar flows, as reviewed in [113], the effect of the rotation is to retard or suppress laminar-turbulent transition for $S > 0$ (stabilizing), or to move it to lower Reynolds numbers for $-1 < S < 0$ (destabilizing). Restabilization can be expected for $S < -1$.

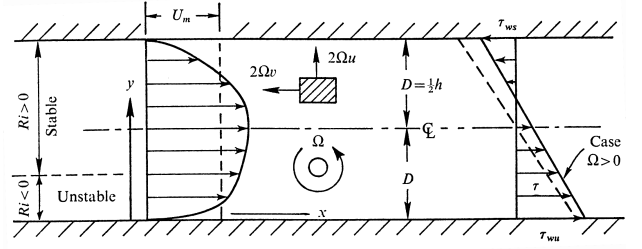


Figure 4: Diagram depicting the configuration of the rotating channel from [97]

In turbulent flows, the study of a two-dimensional boundary layer in rotation about the spanwise axis [97] leads to the conclusion that rotation can either increase the level of turbulence, for $S < 0$, or decrease it, for $S > 0$, through its interaction with the wall-layer streak bursting process.

In view of the fundamental importance of the phenomenon, as well as its practical interest (rotating machines), turbulence models should be able to reproduce and predict this behaviour.

An interesting case of flow rotation is that of a rotating two-dimensional developed channel flow (*rotating channel* for short), where the two aforementioned effects are both present: in fact turbulence is increased on the unstable (pressure, leading) side, and decreased on the stable (suction, trailing) side (see figure 4). Therefore, they can be both studied and simulated in a single flow. Availability of reliable experimental data [97] and matching Direct Numerical Simulations [113, 4, 168] makes it a very suitable test case for model validation, and it has been used as such by several researchers [168, 107, 153, 205, 203, 7].

5.4.1 Experiments

Because of the difficulty in setting up this flow configuration, experiments are rare. However, data from two are included here: The classical work of Johnston et al. [97] and the more recent work at lower Reynolds numbers of Nakabayashi and Kitoh [156].

The experiments of Johnston et al. illuminated the overall characteristics of the flow, except for the low Reynolds number effects explored by Nakabayashi and Kitoh. Three main phenomena were in evidence:

- the reduction of wall bursting on the stable side, leading to a reduction in turbulence level. An opposite effect should be expected on the unstable side, but it was not visually noted.
- The development of four roll cells for $Ro_b > 0.05 - 0.10$. These structures originate on the unstable wall and play a very important role, interacting with the bursting phenomenon and transporting high turbulence fluid from the wall layer to the core flow. The roll cells are assumed to be a realization of a Taylor-Gortler instability.

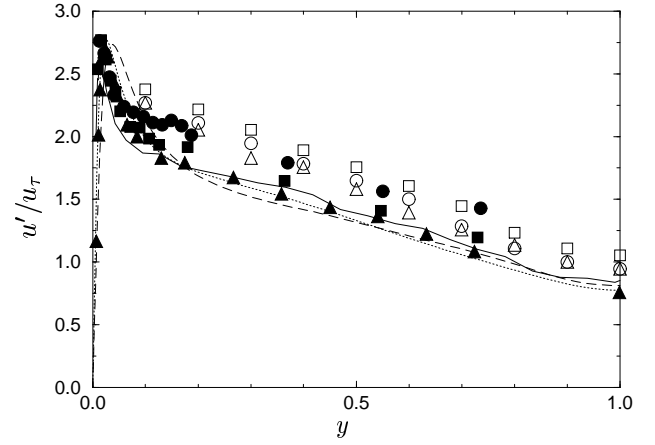
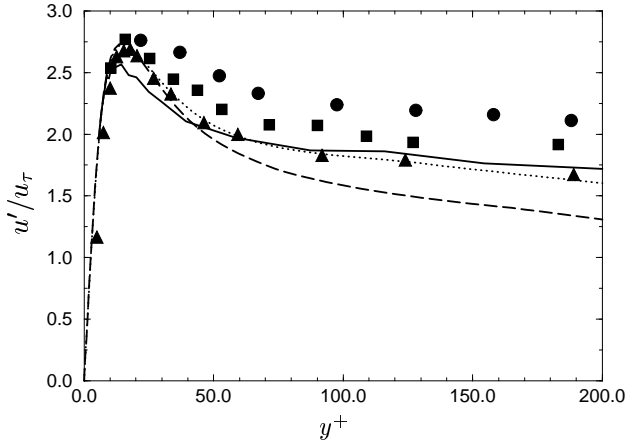


Figure 3: Streamwise rms velocity profiles from the turbulent channel cases. Symbols are as described in figure 1.

- Full relaminarization at $Re_b = 10000 - 12000$ and $Ro_b = 0.21$, associated with a region of negative rate of turbulence energy production.

Velocity profiles show increasing asymmetry with growing Ro .

At the same time, the evolution of friction velocity u_τ with Ro_b shows an increase of turbulence level on the unstable wall and a corresponding decrease on the stable wall, with respect to the friction velocity u_{τ_0} measured in absence of rotation. Two main effects are evident from the data: the saturation of u_τ at high Ro on the unstable side, which is attributed to the development of the roll cells, and the strong drop of u_τ on the stable side, corresponding to the relaminarization.

Overall, the available information in [97] offers a complete qualitative description of the flow, which the predictions should match, and enough quantitative data to assess their quality. However, it should be kept in mind that neither DNS nor the most recent LES predict the full relaminarization nor the corresponding drop of u_τ on the stable side. Therefore the possibility remains that this behaviour might be due to the test section and, notably, to its short length which would prevent full development (equilibrium) of the flow. For validation purposes, it would be preferable to base the comparison on the mean velocity profiles and the surface velocities measured before relaminarization.

5.5 Simulations

Because of its simple geometry but complex and interesting flow, the rotating channel has been the subject of several DNS studies. Two are included here: Kristoffersen and Andersson [113] and Piomelli and Liu [168].

5.6 SUMMARY OF PIPES AND CHANNELS

PIPES				
PCH00	Pipe	N	Loulou <i>et al</i> [132]	pg. 111
PCH01	Pipe	E	Durst <i>et al</i> [54]	pg. 113
PCH02	Pipe	E	Perry <i>et al</i> [166]	pg. 114
PCH03	Pipe	E	Eggels <i>et al</i> [56]	pg. 116
PCH04	Super pipe	E	Zagarola [228]	pg. 117
PCH05	Rotating pipe	N	Orlandi & Fatica [160]	pg. 118
CHANNELS				
PCH10	Channel, $Re_\tau = 400 - 590$	N	Mansour <i>et al</i> [139]	pg. 119
PCH11	Channel, $Re_\tau = 921$	E	Niederschulte [157]	pg. 121
PCH12	Channel, Re_τ dependence	E	Wei & Willmarth [222]	pg. 122
PCH13	Channel, High Re	E	Comte-Bellot [39]	pg. 123
ROTATING CHANNELS				
PCH20	Rotating channel	E	Johnston <i>et al</i> [97]	pg. 124
PCH21	Rotating channel	N	Piomelli & Liu [168]	pg. 125
PCH22	Rotating channel	N	Anderson & Kristoffersen [4]	pg. 126
PCH23	Rotating channel	E	Nakabayashi & Kitoh [156]	pg. 128

E: experimental cases. N: numerical ones. Consult individual data sheets for more details

Chapter 6: Free Shear Flows

Jean-Paul Bonnet

Laboratoire d'Etudes Aérodynamiques,
C.E.A.T. Univ. Poitiers
43, route de l'Aérodrome
F-86036 Poitiers cedex, France
and

Robert D. Moser

Department of Theoretical and Applied Mechanics
University of Illinois at Urbana-Champaign
Urbana, IL 61801, USA
and

Wolfgang Rodi

Inst. for Hydromechanics
University of Karlsruhe
D-76128 Karlsruhe, Germany

6.1 Introduction

There are a large number of experimental studies of free shear layers, particularly in subsonic flows. Over 200 papers could be cited. However, for the purposes of LES validation, emphasis will be given to studies in which initial conditions and streamwise evolution are available. Since the review of Birch and Eggers [19], and the detailed compilation by Rodi [175], several review papers have been devoted to these flows (see for example Ho and Huerre [80], Fiedler *et al.* [62]). In the present data-base we focus our attention on nominally 2D flows (except for the data on axisymmetric jets).

Free shear layers are of interest for several industrial purposes such as afterbody or propeller characteristics, mixers, burners etc., and constitute a basic flow geometry which is an ingredient in several more complex flows. The understanding of the physics of such flows, as well as the ability to predict them computationally, is the key to controlling the mixing processes, pollutant dispersion, noise generation, vibrations, and flow control. Even for cases that are 2D in the mean, these flows rapidly undergo transition to 3D, though they are often dominated by large scale, quasi-2D organized structures, generally arising from the Kelvin-Helmoltz instability. They are also often associated with smaller scale eddies with different orientations. The consequences of the complexity of flow structures on the choice and validation of prediction methods is discussed in Fiedler *et al.* [62]. In this regard, LES is well suited for free shear flows.

The computation of these flows may be simpler than most of the other flows addressed in this data base. Except for the splitter plate used to generate inlet conditions, the flows develop without solid boundaries and the resulting regions of low Reynolds number. These characteristics generally simplify the computations. However, some complexities are still present such as the influence of initial conditions, wall proximity, external turbulence level, etc. In general (except for the grid and shear-free mixing layers), the flows

are created from boundary layers that should be correctly computed or prescribed as initial conditions. This is not always simple, particularly when abnormal boundary layers, such as those that are tripped, are used to generate the flow. On an other hand, transition can occur during the flow development, the computation of which is always complex. As mentioned above, the different kinds of flow structures should be well reproduced. Lastly, the streamwise evolution towards the asymptotic states is a process that should also be correctly computed; the comparisons between computations and experiments should not be restricted to the asymptotic, self-similar part of the flows. Particularly, experimental results obtained from momentum integration (such as turbulent shear stress), energy or shear stress balances are based on the presumption of self similarity, which may be absent or difficult to prove.

There are several specific experimental difficulties that arise when measuring free shear layers using Hot Wire Anemometry (HWA) as well as Laser Doppler Velocimetry (LDV). A major problem arises when one part of the flow is at rest. In particular, this occurs in one stream mixing layers (test case SHL00), or jets in still air (SHL30 and SHL31). For these configurations, stationary hot-wires are problematic because the turbulence intensity is high (say 30%) even at the centreline and exceeds 100% towards the edge because the mean velocity becomes very small. However, recent advances in the flying hot wire technique solve this problem. A review of this complex method can be found in [30]. Results obtained with flying hot wires in jets are described later in this text. These kind of problems are not encountered when using burst spectrum analyzers with a Bragg cell in LDV measurements.

Difficulties also occur when using HWA in supersonic mixing layers, particularly when one side is subsonic, while the other side is supersonic. This is the case for the three supersonic cases SHL00 to SHL02. For these flow configurations, the hot-wire has to operate in subsonic, transonic and supersonic regimes. For a complete survey, the re-

sponse of the HWA will differ depending on the regime. For Mach numbers less than typically 0.8, or greater than 1.2, the sensitivity of the HWA's are well known. However, in the transonic regime ($0.8 < M < 1.2$), special calibration is required. For test case SHL00, a specific calibration procedure has been used [11]. In supersonic flows the frequency response of the HWA can also be a limitation of the method. However, for test case SHL00, it can be assumed that the frequency response is sufficient, as stated in the description of the supersonic test cases.

When LDV is used, the size of the seeding particles is of concern, particularly in high speed, supersonic flows. Johnson [96] gives some estimates of -3dB cutoff frequency for Mach 3 flows. As an example, for $1\mu\text{m}$ diameter, the cutoff is estimated to be approximately 22kHz. This covers major portion of the fluctuations in the test cases SHL20 – 21 as noted by Samimy and Lele [184] based on DNS results¹. In the test case SHL02, the particles are smaller, so the cutoff frequency is expected to occur at around 86 kHz. For the same 50kHz frequency response requirement, the particle lag is apparently negligible.

Finally, for LDV measurements, a seeding bias can occur, in addition to the velocity bias generally taken into account in the data processing ([57]). The seeding bias is dependent on the seeding location. When flows have a marked organization with large scale structures, for example, the LDV results may depend on the location where the particles are injected. Particularly for supersonic mixing layers, results can be different if the flow is seeded in the supersonic (upstream) part or in the subsonic part, or in both parts. The influence of different seeding locations was addressed for test case SHL22. Dual seeding is generally applied, without definitive justification because it is always difficult to exactly balance the seeding rate between the two sides.

6.2 Mixing layers

6.2.1 Spatially Evolving Mixing Layers

Except for the shearless mixing layer, the mean shear of these flows is constant or behaves according to well known laws, and the flows evolve towards an asymptotic, self similar state. The most obvious diagnostic for similarity is the spreading rate. The spreading rate can be defined according to several different measures: evolution of any of a number of characteristic thicknesses (e.g. vorticity thickness, velocity thickness, total pressure-based thickness for flows mixing two gases, visual thickness from flow visualizations, etc.), or evolution of similarity parameters. Although different in detail, all these parameters are linked together through simple relationships [173]. For mixing layers with one side at rest, the evolution of the conventional thickness b (corresponding to the distance between the locations where the velocity reaches 10 and 90% of the external velocity) is $db/dx \simeq \sigma_0^{-1}$. The reference parameter σ_0 is the spreading parameter. Some scatter exists on the reference value but a general consensus of $\sigma_0 \simeq 11$

is accepted [130].

It is well known that, for subsonic, plane, single gas two-stream mixing layers, the spreading rate is a function of the velocity ratio, r . As an example, the following relationship, known as the Abramovich-Sabin rule, is generally accepted for incompressible iso-density flows [1, 183]:

$$d\delta_\omega/dx = \sqrt{\pi}/\sigma_0 \cdot \lambda \simeq 0.16\lambda$$

where δ_ω is the vorticity thickness and $\lambda = \frac{1-r}{1+r}$ with $r = U_2/U_1$, ratio of external velocities (the subscript 1 corresponds to the high speed side). In case of variable density flows, the spreading rate can be estimated from [29]

$$d\delta_\omega/dx \simeq 0.18\lambda$$

In this case, $\lambda = \frac{(1-r)(1+s^{1/2})}{2(1+rs^{1/2})}$ where the density ratio is accounted for ($s = \rho_1/\rho_2$). For supersonic flows, the spreading rate depends on the value of the Mach number. When this parameter increases, a dramatic decrease of the spreading rate is observed. The convective Mach number is generally used as the relevant parameter [21, 163, 49, 120, 195]. In the case of flows with the same gas on the two sides, as in case for the present data base, the convective Mach number is expressed as:

$$M_c = \frac{U_1 - U_2}{a_1 + a_2}$$

(a_1 and a_2 are the speeds of sound of the two external streams). In this case, the spreading rate can be estimated from:

$$d\delta_\omega/dx \simeq 0.18\lambda\Phi(M_c)$$

Discussions on the function $\Phi(M_c)$ can be found in [195].

In pursuing LES validation, it should be recalled that some scatter is observed among the different experimental results. These discrepancies can be attributed to several parameters [29, 88, 89, 28]. Oster and Wygnanski [161] proposed a ‘‘partial random list of possibilities’’ for these discrepancies: (i) turbulence in the free streams, (ii) oscillations in the free stream due to wind tunnel defects, (iii) aspect ratio, (iv) length of the test section, (v) residual pressure gradient, (vi) vibration of the splitter plate, (vii) structure of the boundary layers at the splitter plate, (viii) curvature and angle of the two streams at the splitter plate outflow and (ix) Reynolds number.

Some of the issues discussed above are difficult to model, such as (ii), (v) or (vi) (this last characteristic must be addressed to compute case SHL03). From LES, parametric studies can however be used to determine the sensitivity of the flows to these parameters. Most of the other parameters vary from one test case to the other. For example, the external turbulence level is different among the test cases. The external turbulence level is known to play an important role (producing high spreading rates) if, expressed in percent, larger than $0.5\lambda = 0.5(1-r)/(1+r)$, for subsonic, two stream mixing layers (0.5% for one-stream mixing layers) [165]. The state of the boundary layers present at the trailing edge of the splitter plate used to generate most of these

¹M. Samimy, private communication

flows play an important role. Depending on whether these boundary layers are laminar, transitional or turbulent, the length of the developing part of the shear layers (i.e. the distance required to establish self-similar profiles) can be different. The influence of the initial conditions on the spreading rate is not so clear. However, provided the external excitation has a broad band spectrum (ideally white spectrum), the flow can be considered as “well balanced” and the consensus obtained on the dependence of $d\delta/dx$ and, more sensitively, on $\overline{u'v'}$ on r can be accepted within perhaps $\simeq 5\%$. With the different test cases provided, the ability of an LES to predict this effect can be tested. The influence of the Reynolds number can also be investigated. This is of relevance when the shear layers are initially laminar but can also be important when transitional flows are considered. Lastly, the compressibility effects due to high velocities can also be addressed through the data provided.

The present data-base includes several configurations that offer a combination of the most relevant parameters cited above. It should be noticed that, despite quite different experimental conditions present in this data base (turbulent/laminar initial conditions, subsonic or supersonic flows), the velocity ratio of $r = 0.6$ is a common value, thus many of the effects discussed above can be addressed independently of the velocity ratio.

Several experimental results were not available from numerical files but only from the literature. In these cases, as described in the corresponding ‘read-me’ files, the data are obtained from digitizing printed documents.

6.2.2 Subsonic Plane Mixing Layers

First, subsonic plane mixing layers are considered. The velocity ratio is variable from a value of 0 (one side at rest) up to 0.8. Initial conditions are not available for each flow but, if not, the geometry is simple enough to be modelled. Thus, the influence of velocity ratio can be tested. For some of these data, both laminar and turbulent initial conditions are available. The streamwise evolution is available in the case of two stream flows. Table 1 presents some characteristics of the different mixing layers.

The first set of data is devoted to single stream flow (one side at rest), while the others are concerned with two-stream flows. The spreading rates expressed in terms of σ_0 are in good agreement except for SHL00 and some cases of SHL02. These points will be briefly addressed below.

- The first case, SHL00, represents the basic results of single stream mixing layers [226]. No initial conditions are available, and the effect of the tripping wire is not clearly quantified, nor is the presence of the wall at the exit plane. The spreading rate obtained is known to be too high (i.e. the value of σ is too low when compared to the rest of the literature). This point can be a challenge for computations. The trip wire is generally considered to be a source of artificial excitations. The effect of the trip has been analyzed in detail and confirmed by the experiments

Ref	r	λ	$db/dx,$	$d\delta_\omega/dx$ or σ	σ_0
SHL00	0	/	(σ_0)	/	9.
SHL01 (tripped)	0.6 -	0.25 -	(δ_ω)	0.023 0.019	10.9 13.2
SHL02	0.5	0.33	(δ_ω)	0.0318	10.4
-	0.6	0.25		0.0235	10.6
-	0.6	0.18		0.0168	10.5
-	0.7	0.11		0.0124	8.95
-	0.8	0.053		0.0073	7.2
SHL03	0.3	0.54	(b)	0.05	9.72
-	0.4	0.43		0.041	9.55
-	0.5	0.33		0.032	11.48
-	0.6	0.25		0.022	10.3
SHL04	0.54	0.3	(δ_ω)	0.05	10.6
SHL06	0.47	0.36	(σ)	32	10.6

Table 1: Overall characteristics and spreading rates of the test cases.

of Blatt [6] and should be taken into account for the simulations. Very detailed measurements are available in the self similar region (including turbulent energy budgets).

- In SHL01, for a single velocity ratio, the influence of the nature of the boundary layers at the trailing edge can be tested since two cases are available, that is with a laminar or turbulent (tripped) boundary layer [18]. In the case of laminar boundary layers, the layers are probably pre-transitional. Only integral parameters and mean velocity profiles are given (no turbulence data) in the boundary layers. Within the mixing layers, Reynolds stresses are provided for the developing and asymptotic regions.
- When the velocity ratio approaches one, the flow can exhibit a behaviour similar to a wake flow near the trailing edge. This wake effect vanishes downstream when the mean shear stress becomes predominant. Case SHL02 exhibits this feature in flows with velocity ratios r varying from 0.5 to 0.9 [144]. In this set of data, 5 velocity ratios are available. The boundary layers on the flat plate are turbulent (tripped) and no turbulence data are provided. Two components of velocity fluctuations are given for several distances from the trailing edge. The spreading rates measured with the velocity ratio close to one are quite far from the usual value due to wake effects. In this case, the minimum development length necessary to reach similarity ($\simeq 600 \cdot (\Theta_1 + \Theta_2) / \lambda$ [85]) is probably not obtained (Θ is the boundary layer momentum thickness, subscripts 1 and 2 refer to the two sides of the splitter plate).

²A. Roskho, private communication

- The presence and role of large scale motions can be more clearly observed when the flow is forced with a frequency close to the most unstable one. Data from such forced flows are available in SHL03 [161]. In this case, four velocity ratios (from 0.3 to 0.6) are available, but $r = 0.6$ is best documented and is therefore to be preferred. No boundary layer data are provided. Detailed turbulence data (Reynolds stresses) are provided for the closest downstream station. A special set of data is provided when the trailing edge is flapping, for the same velocity ratios. Frequency spectra are provided. In view of the computation of this flow, it should be recalled the the perturbation velocity normal to the mixing layer plane is frequency dependent. Indeed, the amplitude of the movement of the splitter plate is kept constant while the frequency is varied, then the perturbation velocity varies according to the frequency³.
- In the data set SHL04, a single configuration ($r = 0.6$, turbulent initial boundary layers) is available with very detailed data [46]. For this case, the usual statistics are provided with the streamwise evolution and initial conditions. In addition, higher moments (skewness and flatness) are provided. From an ER-COFTAC data base, large records of instantaneous hot wire velocity measurements are available (not included in the present data base). Detailed characterization of the turbulent boundary layers are given at the trailing edge (longitudinal velocity fluctuations). All the terms of the Reynolds stress tensor are provided for several downstream locations. Estimation of turbulent dissipation is also provided. High order moments are available. Some frequency spectra are given and in the similarity region, the turbulent kinetic energy budget is established. In addition, the PDF of velocities (including velocity differences of two velocity components) are given for three locations of the reference probe, namely on the axis, near the external part and for an intermediate location. Joint PDF's are considered for space or time separations.
- The influence of free stream turbulence is addressed by the test case SHL06 [209]. In this configuration, the initial conditions are quite different (no splitter plate) and are *a priori* well suited for simulations. In this experiment, the flow is created by two grids of different size. The mixing layer with a velocity ratio of 0.47 develops inside a stream with a significant turbulence level (typically 4%). No details are given on the typical scales of the grid turbulence. In this case, the most sensible initial conditions would be from two different simulations of grid turbulence. However, there is no splitter plate and the details of the initial flow are not known. The flows outside the mixing layer can be modelled as conventional grid-generated turbulence. Three downstream regions are tested with two velocity fluctuation com-

ponents. One and two point correlations are available (for 2 velocity component) at one station.

6.2.3 Temporally Evolving Mixing Layer

Case SHL05 includes three direct numerical simulations of time developing mixing layers as simulated by Rogers & Moser [179]. A time developing mixing layer differs from its spatially developing counterpart in that the layer has uniform thickness (on average) in the streamwise direction, is homogeneous in the streamwise direction and grows in time. It is computationally much more tractable than the spatially evolving mixing layer common to experiments. Asymptotically for small λ , a spatially evolving mixing layer when observed in a reference frame moving downstream at velocity $U_c = (U_1 + U_2)/2$ is equivalent to a time-developing mixing layer. However, for the purposes of comparison to LES, it is preferable to compare a time developing mixing layer LES to these time-developing DNS's.

The time developing nature of the simulations have several important consequences relevant to the comparison of LES to the DNS simulations.

First, since the flow evolves in time, it is not possible to do time averaging to obtain converged statistical quantities. Instead, averaging is done in the homogeneous spatial directions (i.e. the streamwise and spanwise directions). Thus the statistical sample available is limited, and in general is not adequate to obtain converged statistics. For example, in figure 1, profiles of the r.m.s. streamwise velocity fluctuations are shown for several times taken from a period during which the mixing layer is approximately self-similar. The profiles have been scaled using self-similar scaling (see [179]), so they are directly comparable. Notice that near the centre, the profiles are rather noisy, and differ in detail from each other. This is a consequence of the poor statistical sample. In addition, there is a small systematic variation among the profiles, due to the imperfection of the self-similarity.

Since LES is only able to reproduce the actual turbulent flow in a statistical sense, it is really only sensible to compare converged LES statistical results with converged statistics from the DNS. In principal, this would involve averaging over an ensemble of DNS and LES simulations started from an ensemble of initial conditions drawn from some distribution. Unfortunately, this is not feasible. The next best approach is to compare the statistics computed from an LES and a DNS begun from identical (filtered for LES) initial conditions. In this way, the flows to be compared will begin with identical large-scale features, which are presumed to be responsible for the variability in the one-field statistics. While one might hope that the evolution of the largest eddies would be well represented in an LES, it is inevitable that their evolution will eventually diverge from that of the DNS due to uncertainties in details of the unresolved small scales. The rate of this divergence has not been quantified. Therefore, even when starting with identical initial conditions in the best possible LES, an exact match of the statistical quantities is not expected. Figure 1

³A. Glezer, private communication

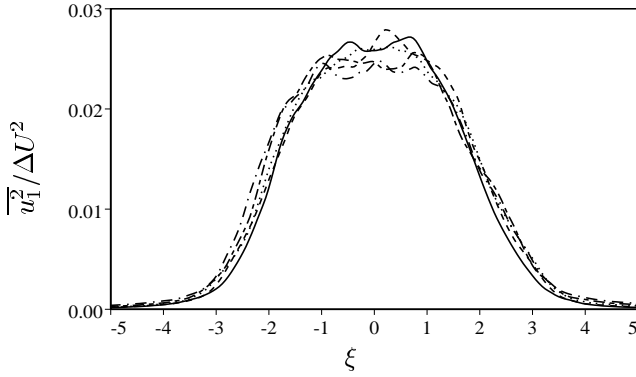


Figure 1: Profiles of $\overline{u_1^2}/\Delta U^2$ in self-similarly scaled coordinates at five times during the self-similar period of Case 1 (— $\tau = 105.2$, ---- $\tau = 116.7$, $\tau = 128.6$, -.-. $\tau = 141.0$, - - - $\tau = 150.8$).

gives an indication of the magnitude of the expected variation.

A turbulent time developing mixing layer is expected to develop towards a self-similar evolution, and indeed two of the flows included in case SHL05 have a self-similar period. This similarity was used by Rogers & Moser [179] to improve statistical sample by scaling statistical quantities self-similarly and averaging in time. However, this self-similar averaging poses a problem for LES comparison, since generally the filter width in the LES would be constant while the similarity length scale (layer thickness say) is growing.

Another consequence of the time-developing nature of this flow, is that the flow evolution is dependent on the details of the initial conditions. There are three separate flows included in SHL05, which differ only in the details of the initial conditions, and as discussed in [179], the evolution of these flows is quite different. By using the same initial conditions in an LES, one can compare to the DNS, and be assured that the cases being simulated are the same, so this dependence on initial conditions need not result in increased uncertainty in the comparison. However, when selecting flows for LES tests, it is desirable to use those that are realistic and that evolve like the physical flows of interest. It is difficult to construct appropriate initial conditions for this purpose since it is generally not possible to characterize the initial and inlet conditions of a physical flow (experiment or practical device) with sufficient detail.

The simulations in SHL05 were begun with initial conditions designed to model a mixing layer forming from a splitter plate with turbulent boundary layers. To this end, turbulent fluctuations were taken from a direct numerical simulation of a boundary layer [198] and used as initial conditions. In addition, the effect of the splitter plate tip as a site of receptivity to (two-dimensional) acoustic disturbances was modelled by adding some extra disturbance energy to the two-dimensional modes (see the data sheet). The turbulence in the initial conditions is thus realistic, but the model of the splitter plate tip receptivity may not be. Despite this, we see (figure 2) that the turbulence statis-

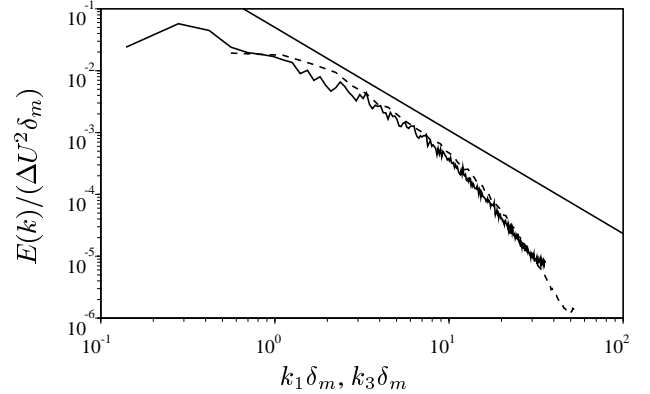


Figure 3: One-dimensional energy ($u_i u_i$) density spectrum at the mixing layer centreline of Case 1 ($\tau = 170.5$). — versus k_1 , ---- versus k_3 .

tics of two of the flows (Case 1 and Case 2) agree quite well with the experimental measurements of Bell & Mehta [18] in a mixing layer evolving from turbulent splitter plate boundary layers. In case 3, the transverse velocity variance is much larger than in these experiments, but there is considerable variation among experiments regarding this statistic. Further, the growth rates ($\frac{1}{\Delta U} \frac{d\delta_w}{dt} = 0.014, 0.014$ and 0.017 for cases 1 through 3 respectively) are in the range of experimentally observed growth rates for this flow (0.014 to 0.022, [179, 49])

Once the mixing layers have become fully developed, two of the flows (cases 1 and 2) do not exhibit convincing evidence of the large scale spanwise rollers commonly observed in turbulent mixing layers, while case 3 does. Furthermore, the character of the scalar mixing in cases 1 and 2 is different from that commonly observed in experiments. In particular, the probability density functions (PDF's) of the scalar fluctuations are 'marching' in cases 1 and 2, while they are 'non-marching' in case 3 and virtually all experiments in which it has been measured (see [152, 102]). This difference in scalar mixing is thought to be related to the lack of rollers in cases 1 and 2 (see [179]). Thus, with regard to the qualitative issues of structure and scalar mixing, it appears that case 3 is most representative of experiments, while for the statistics, cases 1 and 2 appear most representative. In all cases, it appears that the flows are sufficiently realistic to use as test cases for LES.

The numerical simulations of the flows in SHL05 were performed using the highly accurate numerical method of Spalart, Moser & Rogers [200]. The resolution was varied in time to maintain accuracy, and spectra and various other diagnostics were monitored to ensure the resolution was adequate. For example, streamwise and spanwise spectra from case 1 are shown in figure 3. Thus, the uncertainties in the data for SHL05 are dominated by the statistical sample issues discussed above, with no significant uncertainties introduced by numerical errors.

6.2.4 Turbulence Mixing

Lastly, a special incompressible case is addressed. It is

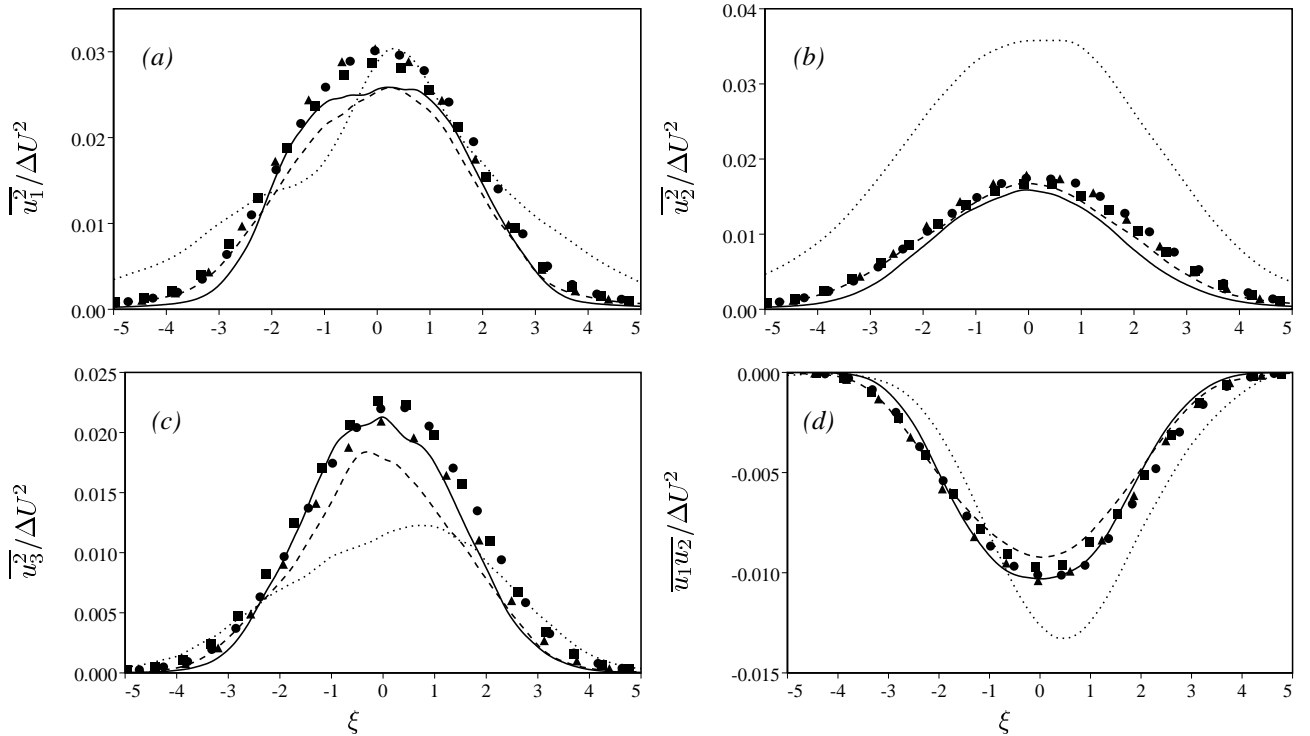


Figure 2: Comparison of the time-averaged (in scaled coordinates) simulation results for the components of the Reynolds stress tensor for the — Case 1, ---- Case 2, and Case 3 simulations with the experimental data (symbols) of Bell & Mehta (1990) at three downstream locations (\blacksquare $x_1 = 108.1\text{cm}$, \bullet $x_1 = 128.4\text{cm}$, \blacktriangle $x_1 = 189.4\text{cm}$).

shearless turbulence mixing. This case is of particular interest, since the key point is the mixing process between two different turbulent flows (turbulence levels, scales). Only a few experimental studies have been devoted to such flows [146, 76]. The more detailed study used for the test case SHL10 is the *turbulence* mixing [217, 218]. Due to a special grid arrangement, two streams with the same mean velocity but with different turbulent characteristics merge. Hence, the process of turbulence mixing is addressed. Very detailed turbulent measurements (3 velocity components) are available for three downstream locations: high order moments, spectra, Reynolds stress budgets.

6.2.5 Supersonic Plane Mixing Layers

For supersonic flows, the present data-base concentrates on three experiments which are comparable in their physical dimensions. Thus, the wall proximity and aspect ratios are equivalent. These flow characteristics are sometimes evoked in order to explain discrepancies between experiments, but these arguments cannot be invoked here. It should be noticed that, within the experimental uncertainties, the normalized spreading rates of the three test cases agrees with the function $\Phi(M_c)$ reported in [195]. No direct evidence of two-dimensionality is given, and the aspect ratio of the mixing layers is small, typically between 4 and 10, depending on the definition of the thicknesses. Reynolds number effects can be considered, since SHL20 has a Reynolds number that is less than that of the other two test cases. In all cases, the boundary layers at the trailing edge are fully turbulent on the supersonic side. The boundary layers on the subsonic side are not well quali-

fied, although they are of very small thickness. In SHL20, the influence of the subsonic boundary layer has been investigated and no important effect was observed, providing its thickness is small compared with the supersonic one. A convective Mach number of 0.6 is available in each of the three cases. For that value of M_c , redundant data are available for the evolution of basic statistical quantities (mean and velocity fluctuations) and, in light of the difficulties inherent in the measurements, this redundancy can be useful.

In addition, these three experiments are complementary, with regard to data for velocity and temperature fluctuations. Data sets SHL20 [11] are obtained with hot-wire anemometry (constant current); they thus provide one component of velocity and temperature fluctuations. They provide a test of the relationship between temperature and velocity fluctuations, the so-called Strong Reynolds Analogy [150, 65]. Special care was taken calibrating for the transonic regime. The frequency range of the hot wire anemometer seems adequate. The velocity results presented in SHL21 [58, 185] and SHL22 [45, 12] are obtained by means of Laser Doppler Velocimetry, using two different systems. Dual seeding in both sides is used without precise analysis of seeding bias, although some comparisons between different seedings are provided in SHL22. The effects of particle lag has been addressed in SHL21. SHL21 also has some pressure transducer measurements, while SHL22 includes some constant-temperature anemometry results. This variety of experimental methods provide complementary results. Data sets SHL20 and SHL22 provide characterization of the boundary layers on the supersonic side or immediately after the trailing edge. For cases SHL21

and SHL22, several values of M_c are available, ranging from 0.6 to 1, i.e. from the medium to highly compressible. In both cases, the flow developments are provided from the trailing edge up to the beginning (SHL20) or established similarity region (SHL21 and SHL22).

6.3 Jets

Free jets are an important subclass of free-shear layers that are of great practical significance. Jets into stagnant surroundings are particularly suited for basic studies because of the self-preserving nature of the far-field, in which the spreading rate, the velocity-decay constant and similarity profiles define entirely the statistical flow quantities. These jets are important test cases for simulation procedures for turbulent flows, whether turbulence models or large-eddy simulations and, in spite of their geometrically simple configuration, they pose a difficult task as most widely used turbulence models like the $k-\varepsilon$ model or the basic Reynolds-stress-equation models cannot predict the plane and the round jet with the same set of empirical constants. These two cases were therefore chosen, and the data provided are for the self-preserving downstream regions of the plane two-dimensional and the axisymmetric jet issuing into nominally infinite stagnant surroundings.

Rodi [175] reviewed the measurements carried out in these flows up to 1971 - some of these measurements were published later. For the round jet, the only data sets including turbulence measurements in the self-similar region were those of Wygnanski and Fiedler [225] and of Rodi [175]. In both cases the measurements have been obtained with stationary hot-wires. Both obtained a spreading rate of the jet half-width $dy_{1/2}/dx = 0.086$ which is in agreement with earlier measurements of the mean flow. The measurements of Wygnanski and Fiedler were much more extensive and have been the standard round-jet data for a long time. Less ideal features are that the centre-line velocity decay rate changes at $x/D \approx 50$ and that in the downstream self-preserving region only 65% of the initial jet momentum is left according to the velocity measurements. Nearly two decades later, almost concurrent detailed measurements with more suitable measurement techniques were carried out by Hussein, Capp and George [90] - called HCG - and by Panchapakesan and Lumley [162] - called PL. HCG used flying hot-wires and a burst-mode LDA technique and, for comparison also the stationary hot-wire technique. PL also measured with a flying hot-wire which moved on a shuttle. The flying hot-wire and LDA techniques are conceptually superior for flows with high turbulence intensity and indeed HCG found significant differences between their measurements obtained with the stationary and the flying hot-wire. On the other hand, the latter results agreed well with the LDA measurements. PL measured at $Re = 1.1 \times 10^4$ while the HCG jet had a Reynolds number of $Re = 9.55 \times 10^5$. Both sets of measurements yielded similar spreading rates of $dy_{1/2}/dx = 0.094$ to 0.096 , which are higher than those from the older measurements. The difference stems most likely from the use of larger enclosures into which the jets discharged and the fact that entrainment was allowed from

upstream, i.e. the jet did not emerge from a solid wall. This yielded better momentum conservation. HCG report that in the self-preserving region the momentum flux is 85% of the initial flux and PL report an even higher value of 95%. Finally the HCG data were chosen as case SHL30 because of the higher Reynolds number and also because two different advanced measurement techniques gave virtually the same results. HCG report the balances of turbulent kinetic energy and of the individual stresses for which the dissipation rate was determined with the assumption of locally axisymmetric turbulence; also in the diffusion term the triple correlation $\overline{vw^2}$ was not measured but assumed to be equal to $\overline{v^3}$. These assumptions introduce considerable uncertainties, leading to a fairly high pressure-diffusion term near the axis; also, the diffusion does not seem to integrate to zero. Here perhaps the PL results for the kinetic energy balance are more reliable; they determined the dissipation rate from the balance, neglecting the pressure diffusion.

For the plane jet, detailed results newer than those reviewed already in [175] (but some published later) could not be found. As all the older measurements have been obtained with stationary hot-wires, the reliability of at least the higher moment-measurements must be cast in doubt, in view of the findings of HCG and PL for the axisymmetric jet. The measurements reviewed by Rodi all show good agreement about the spreading rate ($dy_{1/2}/dx \approx 0.1$) and the velocity decay. The most extensive and complete set of measurements is that due to Gutmark and Wygnanski [72] which was therefore chosen as case SHL31. The measured shear stress agrees fairly well with the distribution calculated from the mean velocity, and the normal stresses are in reasonable agreement with the measurements of Heskestad [78]; for the v' and w' components this is true also for the other measurements, but the latter are up to 20% smaller for the longitudinal fluctuations u' . There is hence some uncertainty about this quantity. There are even greater uncertainties about the measurements of triple correlations and the terms in the kinetic energy balance. The pressure diffusion was determined as the out-of-balance term and reaches unusually high values. Probably more reliable is the energy balance obtained by Bradbury [22], but his jet had a co-flowing stream at 0.16 of the jet exit velocity and was hence not exactly self-preserving.

Acknowledgements

Professor A.J. Smits is gratefully acknowledged for his input to the experimental uncertainty section.

6.4 SUMMARY OF SHEAR LAYERS AND JETS

INCOMPRESSIBLE PLANE MIXING LAYERS				
SHL00	Single stream incomp. M. L.	E	Wyganski & Fiedler [226]	pg. 131
SHL01	Incompressible M. L., $r = 0.6$	E	Bell & Metha [18]	pg. 133
SHL02	Incomp. M. L., $0.5 \leq r \leq 0.9$	E	Metha [144]	pg. 135
SHL03	Forced incompressible M. L.	E	Oster & Wygnanski [161]	pg. 137
SHL04	Incomp. M. L., $r = 0.54$	E	Delville & Bonnet [47]	pg. 139
SHL05	Temporal incomp. M. L.	N	Rogers & Moser [179]	pg. 141
SHL06	Two turb. free streams, $r = 0.47$	E	Tavoularis & Corrsin [209]	pg. 144
TURBULENCE MIXING				
SHL10	No-shear turbulence mixing	E	Veeravalli & Warhaft [217]	pg. 146
COMPRESSIBLE MIXING LAYERS				
SHL20	Supersonic M. L., $M_c = 0.64$; $Re_\theta \simeq 1.6 \times 10^4$	E	Barre, Mena, Quine & Dussauge [11]	pg. 148
SHL21	Supersonic M. L., $M_c = 0.52$; $0.69; 0.87; Re_\theta \simeq 4. \times 10^4$	E	Elliott & Samimy [58]	pg. 150
SHL22	Supersonic M. L., $M_c = 0.52$; $0.535; 0.58; 0.64; 1.04; Re_\theta \simeq$ 8×10^4	E	Debisschop, Barre & Bonnet [45]	pg. 152
JETS				
SHL30	Round jet	E	Hussein <i>et al</i> [90]	pg. 154
SHL31	Plane jet	E	Gutmark & Wygnanski [72]	pg. 156

E: experimental cases. N: numerical ones. Consult individual data sheets for more details

Chapter 7: Two-Dimensional Boundary-Layers

Peter D. Smith

Aero-Structures Department, DERA Farnborough,
GU14 0LX, United Kingdom
and

Javier Jiménez

School of Aeronautics, Universidad Politécnica
28040, Madrid, Spain

Summary

The chapter starts with the simplest boundary layer flow: incompressible, two dimensional flow over a smooth flat surface with no imposed pressure gradient. Then the effects of adverse pressure gradients are introduced followed by separation from a smooth surface. The complicating effects of surface curvature are then discussed. The chapter ends with the case of a boundary layer which has experienced both pressure gradients and surface curvature and then relaxes back to an undisturbed state.

7.1 Introduction

Turbulent boundary layers have been investigated experimentally for at least the past 75 years. As a result a vast body of data exists. For the first half of this period measurements were, in the main, confined to the mean flow by the lack of suitable instrumentation and are therefore inadequate for LES validation.

Data measured prior to 1980 was extensively evaluated and documented for the Stanford conference which had the aim of detailing experimental data which could be used in Reynolds averaged turbulence model development. The Stanford database is available on the worldwide web at <http://www-safml.stanford.edu/~antwell/>.

The Stanford conference was followed a decade later by the Collaborative Testing of Turbulence Models (CTTM) project organised by Bradshaw et al. The database used in the CTTM project is available from the Journal of Fluids Engineering databank as item DB96-243 at <http://scholar.lib.vt.edu/>.

More recently a database of experimental and DNS results has been set up by the ERCOFTAC collaborative venture and is available at <http://fluindigo.mech.surrey.ac.uk/>.

Wherever possible the data described below is in addition to that contained in the above databases and has been selected with the particular requirements of LES validation in mind. Lack of space together with the current state of development of LES have restricted the choice of data to two-dimensional, incompressible flows which nevertheless contain a wide range of turbulence behaviours which must be correctly simulated.

7.2 Zero pressure gradient

As the simplest form of boundary layer, the flow with zero pressure gradient over a smooth flat surface has been extensively studied experimentally. As noted above much of the early data is confined to measurements of only the mean flow quantities. The first major review of the data was undertaken by Coles [38] in 1962. Since then of course the volume of data has increased enormously and its range now covers $0.5 < R_\theta \times 10^{-3} < 220$, where R_θ is the Reynolds number based upon momentum thickness. In the above range the low values are achievable by Direct Numerical Simulation whilst the highest values are achieved by making measurements on the walls of large industrial wind tunnels.

For the present purpose of recommending datasets which can be used for LES validation, this huge volume of data presents problems, since as explained below it is necessary to cover the Reynolds number range and no experiment or set of experiments has emerged as ‘best buy’. Fortunately Coles’ pioneering work has been carried forward in two very recent publications, a major review by Fernholz & Finley [60] and an AGARDOGRAPH edited by Saric [186]. What follows is an attempt to précis this work. This précis should be used merely as an introduction and anyone attempting to simulate zero pressure gradient flow is strongly advised to refer directly to the original reviews.

7.2.1 Mean flow behaviour

The turbulent boundary layer equations differ from the laminar ones only in the additional turbulent shear stress term $-\rho \overline{u'v'}$. An immediate result is that a turbulent boundary layer has *two* characteristic length scales, rather than one. A measure of the boundary thickness, such as δ , is the appropriate length scale in the outer part of the layer, away from the wall, and is thus termed the *outer* length scale. The viscous length, ν/u_τ , where u_τ is the friction velocity, is the appropriate length scale near the wall, and is termed the *inner* length scale. In contrast the laminar zero pressure gradient boundary layer has a single length scale, $\sqrt{\nu L/U_\infty}$, so that it is possible to obtain a full similarity solution for laminar boundary layers but not for turbulent boundary layers. For turbulent boundary layers, separate similarity laws for the inner and outer flows must be sought. The ratio of the outer and inner length scales δ^+ ($= \delta u_\tau / \nu$), increases with increasing Reynolds number and therefore the shape of the mean velocity profile must also

be Reynolds number dependent.

The viscous sublayer

In zero pressure gradient, very near the wall the x momentum equation has the solution.

$$\frac{U}{u_\tau} = \frac{yu_\tau}{\nu}$$

That is, very close to the wall, the velocity varies linearly with distance from the wall.

The law of the wall and the defect law

For the near wall flow Prandtl argued that the viscosity, wall shear stress and distance from the wall are the important parameters. Dimensional analysis then gives

$$\frac{U}{u_\tau} = f\left(\frac{yu_\tau}{\nu}\right)$$

which is known as the law of the wall. Similarly, well away from the wall, von Kármán suggested that viscosity would be less important and the boundary layer thickness, δ , would enter as the length scale. Dimensional analysis then gives

$$\frac{U_e - U}{u_\tau} = g\left(\frac{y}{\delta}\right)$$

which is known as the defect law. Matching the velocity and velocity gradients of these two laws in the region where they overlap yields

$$\frac{U}{u_\tau} = \frac{1}{\kappa} \ln\left(\frac{yu_\tau}{\nu}\right) + C$$

for the law of the wall, where $\kappa = 0.40$ and $C = 5.10$, and

$$\frac{U_e - U}{u_\tau} = -\frac{1}{\kappa} \ln\left(\frac{y}{\delta}\right) + C'$$

for the defect law, where in both cases the constants are possibly Reynolds number dependent. The appearance of δ in the defect law is unfortunate as it is difficult to obtain accurately from experiments. It is preferable to follow Rotta and use a weighted integral thickness Δ , where

$$\Delta = \frac{\delta^* U_e}{u_\tau},$$

where δ^* is the displacement thickness, so that the defect law becomes

$$\frac{U_e - U}{u_\tau} = g'\left(\frac{y}{\Delta}\right)$$

Fernholz & Finley have shown that if this is expressed as

$$\frac{U_e - U}{u_\tau} = -M \ln\left(\frac{y}{\Delta}\right) - N$$

where $M = 4.70$ and $N = 6.74$ then in combination with the law of the wall we have an effective universal mean velocity profile, in the overlap region, over the complete Reynolds number range of $0.5 < R_\theta \times 10^{-3} < 220$. Now,

of course, the Reynolds number dependence is implicit in Δ and u_τ .

So finally we have the very useful result that to be consistent with the experimental data any LES must produce this mean flow profile.

Although the defect law given above has been generally accepted by most researchers Barenblatt [9] and George *et al* [69] have argued that u_τ is not the correct velocity scale for the outer flow. Instead they use U_e . As a result both the law of the wall and the defect law assume power law rather than logarithmic forms. Fortunately in practice the two forms are not very different except at very high Reynolds numbers.

7.2.2 Turbulence Data

The success of the inner and outer scalings for the mean velocity naturally encourages the search for similar scalings for the turbulence quantities. That is close to the wall, when suitably normalised by u_τ , do quantities become unique functions of $y^+ = (\frac{yu_\tau}{\nu})$? Whilst away from the wall are they functions of y/Δ ?

The following sections give Fernholz & Finley's conclusions to these questions for turbulence profiles in the range $2.5 \leq R_\theta \times 10^{-3} \leq 60$.

Reynolds Stresses

Dealing first with the Reynolds normal stress ($\overline{\rho u'^2}$) this is observed to exhibit similarity when plotted against y^+ in the viscous sub-layer and the buffer layer ($y^+ < \approx 30$). In outer variables the data collapse well for $y/\Delta > 0.04$ ($y/\delta > 0.1$) for $R_\theta > 5000$ that is in the logarithmic layer and the outer region.

The normal stress ($\overline{\rho v'^2}$) which is associated with fluctuations normal to the wall shows no evidence of similarity in inner variables. In outer variables similarity is once more evident. The y^+ location of the peak value of ($\overline{v'^2}/u_\tau^2$) moves away from the wall with increasing R_θ . This trend can be approximated by

$$y_{(\overline{v'^2})_{max}}^+ = 0.071 R_\theta.$$

The results for the third normal stress, ($\overline{\rho w'^2}$) are similar in that no similarity is found in the inner variables but similarity is present in outer variables. The location of the maximum value also appears to move away from the wall with increasing R_θ but cannot be determined with sufficient accuracy to determine a trend line.

The Reynolds shear stress ($-\overline{\rho u'v'}$) is more difficult to measure accurately very close to the wall as an X probe must be used. Nevertheless there is evidence of possible inner region similarity for $y^+, \approx 150$. Similarity in the outer layer, $y/\Delta > \approx 0.09$, is observed for all the Reynolds number range. The location of the peak shear stress is again a function of R_θ with a trend described by

$$y_{(\overline{u'v'})_{max}}^+ = R_\theta^{0.61}.$$

Skewness and Flatness Distributions

The scaled third moment of a quantity, such as $\overline{u'^3}/(\overline{u'^2})^{3/2}$, describes the skewness $S_{u'}$ or asymmetry of the probability distribution of u' . The function is symmetric about the origin, $S_{u'} = 0$, if $\overline{u'^3} = 0$. A positive value of $S_{u'}$ implies that large positive values of u' are more frequent than large negative values. For a Gaussian distribution, $S_{u'} = 0$. The fourth moment or flatness, $F_{u'}$, of the u' distribution is given by $\overline{u'^4}$ scaled by $(\sqrt{\overline{u'^2}})^4$, and is a measure of the frequency of occurrence of events far from the axis. If these are relatively frequent, $F_{u'}$ will take values greater than the Gaussian value of 3.

Fernholz & Finley found that in inner variables independence of Reynolds number is apparent for $S_{u'}$ in the viscous sub layer and for both $S_{u'}$ and $F_{u'}$ in the log law region with $S_{u'} \approx 0$ and $F_{u'} \approx 2.80$. Both $S_{u'}$ and $F_{u'}$ exhibit similarity when plotted against y/Δ .

The skewness $S_{w'}$ of the spanwise component w' is zero for a two dimensional layer. The flatness $F_{w'}$ exhibits similarity in both inner and outer scalings.

For the wall normal component, v' , the flatness factor $F_{v'}$ is approximately constant (≈ 3.4) over the log law region and so independent of R_θ . Once again both skewness and flatness exhibit similarity in outer scaling.

Although not as satisfying as the complete similarity produced for the mean flow, the range of similarities detected for the turbulence quantities still provide important validation criteria for the results of any Large Eddy Simulations.

7.2.3 Experimental Data

Rather than attempt to seek agreement with any particular experiment it is recommended that simulations should be checked against the similarity laws outlined above. A set of data at an R_θ of 1438 is incidentally available at the first measuring station of TBL30, and collection of mean and fluctuation profiles in the range $Re_\theta \times 10^{-3} = 4 - 13$ is included as TBL00.

7.2.4 Numerical Data

The numerical requirements for the simulation of turbulent boundary layers are more strict than those for free shear flows or for wall-bounded parallel flows, such as pipes or channels. A true simulation of a turbulent boundary layer would include its development from some forward stagnation point, its transition region, either natural or tripped, and its spatial growth to a reasonably high Reynolds number. Such a direct numerical simulation does not exist at present. The closest equivalent is Spalart's simulation in [198] in which the boundary layer is simulated in a streamwise periodic box, but where the effect of streamwise growth is simulated by including extra terms derived from a multiple-scale analysis. The resulting equations are accurate to $O(c_f)$. Four Reynolds numbers were originally computed for this flow, of which the two intermediate ones, at $Re_\theta = 300$ and 670 , are included in the data base as TBL01. The two extreme ones, although needed to esti-

mate the slow growth terms used in the simulation, are now believed to suffer from slight numerical inaccuracies. The two included data sets are now considered standard results for low to moderate Reynolds numbers. Another simulation of a pressure driven boundary layer using a similar numerical method is [197].

The lowest of the two Reynolds numbers is actually below the threshold for which self-sustained turbulence has traditionally been assumed to exist [171], and should probably not be used as a reference set by itself. It has, for example, only a marginally developed logarithmic law. It should however be useful as inlet condition for simulations of developing boundary layers, in which an initially low Reynolds number may not be too important. A method for doing so is described in [155], where it was used to simulate the separation bubble in TBL21. Full flow fields for the two Re_θ are included for this purpose.

7.3 Adverse pressure gradients

7.3.1 Experimental Data Sets

Once again a very large volume of data exists, much of which is documented in the Stanford and ERCOFTAC data bases. Here we concentrate on more recent data which either includes spectra, as in the case of the Marusic & Perry experiment, [142], TBL10, or naturally merits inclusion as it was specifically designed to complement DNS data, as in the case of the Spalart & Watmuff experiment, [201, 220] TBL12.

7.3.2 Numerical Data Sets

One numerical data set included in this section, TBL11, which was originally designed as a reference case for RANS, describes an attached turbulent boundary layer subject to an adverse pressure gradient. It contains both the numerical simulation [201] and experimental data especially compiled for the occasion [220]. Both experiment and simulation agree closely, but the experimental data extend over a longer distance than the simulation, and both are included. The numerical simulation uses a "fringe" method in which extra terms similar to those used in TBL01 to model the streamwise growth have been confined to narrow bands near the ends of the computational domain, making the overall flow spatially periodic even if the boundary layer is left to thicken naturally over most of the computational box. In this sense it is a more "natural" flow than TBL01, but still has an artificial recycling of the inlet flow that makes it roughly equivalent to a tripped layer. An initial region of favourable pressure gradient was included both in the experiment and in the computation to minimise memory effects from the trip. The inlet Reynolds number and numerical resolution are comparable to those in the higher Reynolds number case of TBL01, and were thoroughly checked in the original papers [198, 201].

7.4 Separation

7.4.1 Experimental Data Sets

The measurement of flows involving separation from a smooth surface presents extreme difficulties for the experimenter. Non-intrusive instrumentation is essential so that reliable data sets had to await the development of the Laser Doppler Anemometer. Maintaining two dimensional or axisymmetric flow is also particularly difficult and usually involves much ‘cut and try’ development. The experiment by Simpson *et al.*, [192, 193, 190] for which the majority of the data (with the exception of the transverse velocity measurements) is available from the Stanford database, is a possible testcase but is an open separation and would require inflow boundary conditions downstream. Fortunately the data of Alving & Fernholz, [3], TBL20, has recently become available. Here a turbulent boundary layer on a smooth, axisymmetric body is exposed to an adverse pressure gradient of sufficient strength to cause a short region of mean reverse flow (‘separation’). The pressure distribution is tailored such that the boundary layer reattaches and then develops in a nominally zero pressure gradient.

7.4.2 Numerical Data Sets

The two data sets [155, 199] represent roughly the same flow, an initially turbulent boundary layer subject to an adverse pressure gradient strong enough to induce separation, and immediately followed by a favourable gradient that closes the separation bubble. Beyond that they are quite different numerically and aerodynamically. The numerical scheme in TBL22 [199] is the fringe method used in TBL11, while TBL21 [155] uses actual inflow and outflow conditions in which the inflow is provided by a slightly manipulated version of the $Re_\theta = 300$ zero-pressure-gradient boundary layer in TBL01. The inlet Reynolds number in TBL22 is lower, $Re_\theta \approx 230$, and the settling length allowed to the layer before the adverse pressure gradient is applied is also shorter than in the other case. As a consequence the incoming boundary layer never becomes fully turbulent before separating and, in particular, never develops a logarithmic region. The separation bubble in TBL22 is smaller than in TBL21, and the region beyond reattachment is not long enough to allow for significant recovery of the turbulent profiles. TBL21 was designed for aeroacoustics studies, and it was run for an exceptionally long time to compile spatio-temporal pressure information. A side effect is that the averaging time for the statistics is also exceptionally long, which is an important consideration given the long characteristic times inherent to recirculation regions. In all these respects TBL21 should be used as a test case in preference to TBL22. The latter is however interesting in that it is one of the few simulations of separated flows which include a heated wall, showing highly counter-intuitive heat transfer effects in the separation bubble.

The numerical resolution in both cases is nominally similar, and of the same order as in the two other simulations mentioned above. However, while TBL22 uses the same spectral method as in the previous cases [200], TBL21 uses a second-order-accurate finite difference scheme, for which the resolution requirements should be about 50% larger than for spectral methods before dealiasing. Grid

refinement studies in [198], in which resolution was purposely degraded by a factor of two, showed significant effects on the skin friction, and the possibility that there may be marginal resolution problems in TBL21 should be kept in mind. The numerical resolution in both cases is however measured in wall units based on the point of highest skin friction in the domain, which is near the inlet. As the boundary layer thickens downstream the skin friction decreases and the effective resolution improves. Near the separation region it appears likely that the resolution of both simulations is more than adequate.

7.5 Surface curvature

Streamwise surface curvature produces significant changes in the turbulence structure within the boundary layer. Concave curvature is destabilizing (i.e. turbulent mixing is enhanced) whilst convex curvature is stabilising. These effects become significant when the ratio of boundary layer thickness to surface radius of curvature is of order 0.01, an order of magnitude earlier than curvature effects are significant in laminar flows.

The experiment by Johnson & Johnston, [98], TBL30, chosen here is an extension of another experiment using the same apparatus by Barlow & Johnston [10].

7.6 Relaxing flow

The difficulty of predicting turbulence relaxation from a major perturbation is often noted. The rate of relaxation varies with eddy size which requires skilful modelling of the turbulence. Since the success of large-eddy simulation depends on the proper representation of the interaction between the subgrid scales and the larger scales, relaxing flows can be a significant test of the calculations.

The numerous investigations of perturbed flows prior to 1985 were reviewed in Smits & Wood [196]. Since then other investigations have been conducted such as the Basaran, Smits & Joubert [14, 15] experiments on the flow over a hill. The particular needs of turbulence simulators have been recognized increasingly in recent years, particularly the need for well-established boundary and initial conditions and for flows which can be used to examine the capabilities of simulations without so much complexity that the detailed dynamics cannot be understood. One such experiment selected for this database, TBL31, is that of Webster, DeGraaff & Eaton [221] which examined the flow over a smooth bump large enough to perturb the turbulence, but just gentle enough to avoid flow separation. The experiment was designed with LES in mind and coordinated with one such effort. The flow is similar in some ways to the flow over an airfoil but without the complications of laminar/turbulent transition and stagnation points.

7.7 SUMMARY OF BOUNDARY LAYER FLOWS

ZERO PRESSURE GRADIENT.

TBL00	Basic flat plate	E	Smith and Smits [194]	pg. 161
TBL01	Pseudo-zero pressure gradient	N	Spalart & Cantwell [198]	pg. 163

ADVERSE PRESSURE GRADIENT.

TBL10	APG	E	Marusic & Perry [142]	pg. 165
TBL11	APG	N	Spalart & Watmuff [201]	pg. 167
TBL12	APG	E	Watmuff [220]	pg. 169

SEPARATION.

TBL20	Closed separation bubble	E	Alving & Fernholz [3]	pg. 171
TBL21	Closed separation bubble	N	Na & Moin. [155]	pg. 173
TBL22	Small heated separation bubble	N	Spalart & Coleman [199]	pg. 177

NON-TRIVIAL GEOMETRIES.

TBL30	Curved plate	E	Johnson & Johnston [10]	pg. 179
TBL31	Mild bump	E	Webster <i>et al</i> [221]	pg. 181

E: experimental cases. N: numerical ones. Consult individual data sheets for more details

Chapter 8: Complex Flows

L. Patrick Purtell

Office of Naval Research
Arlington, VA 22217-5660 USA

and

Robert D. Moser

Department of Theoretical and Applied Mechanics
University of Illinois at Urbana-Champaign
Urbana, IL 61801, USA

and

Wolfgang Rodi

Institute for Hydromechanics
University of Karlsruhe
D-76128 Karlsruhe, Germany

8.1 Introduction

As advances in numerics and in computer power provide faster and more accurate simulations, the flow configurations selected for examination will tend toward the more challenging geometries and conditions. Thus a group of more complex flows has been selected for inclusion in this database: Flow in a square duct; the wake of circular and square cylinders; and the backward facing step. Each has its own particular difficulties, such as secondary flows, thin shear layers, and vortex formation.

Complexity in turbulent flow has been the subject of inquiry for several decades. The categorization of flows, particularly for modelling purposes, based on rational notions of flow properties was addressed by Bradshaw [24]. He distinguished among complex flows by the type of shear flows, their interactions, and the magnitude of a perturbation, such as a backstep. More recent reviews include [196] and [172]. Many, if not most, of the complex flows described in the reviews are beyond the capabilities of present large-eddy simulations, though advances continue to expand their number. The flow configurations discussed in this chapter (summarized in Table 1.) were selected to be addressable at present or in the very near future at lower Reynolds numbers, but at higher Reynolds number they should remain challenging for some time to come.

8.2 Flow in a square duct

Fully developed turbulent flow in non-circular ducts has long been an intriguing flow configuration because of its transverse (secondary) mean motion. At first glance, there is no apparent reason why the transverse motion should occur, and indeed in fully developed laminar flow it is not generated; its source is the turbulence alone. This flow is thus of particular interest to those pursuing turbulence modelling or simulation, because if the turbulence is not represented properly in their calculations, the errors will be readily apparent in both the turbulence quantities and in the mean secondary flow.

The investigation of corner flow, with its obvious applica-

bility to practical configurations, has a long history. This record prior to 1984 has been reviewed thoroughly by Demuren and Rodi [48], denoted herein as D&R, which will thus be merely summarized. Prandtl developed a classification of secondary flows including those of the "second kind" generated by turbulence alone, but it was not until 1960 that the first actual measurements of the secondary motion were reported. As with all duct and pipe experiments, an important question is whether full development of the flow has been achieved. D&R notes that this "cannot be answered with certainty in most cases." This difficulty with inflow conditions is one reason why direct numerical simulations are so attractive to modellers, even considering their other limitations such as low Reynolds numbers. The data of Gessner and Emery [70] is considered by D&R and Huser and Biringen [86] to be adequately developed. That data was at very high Reynolds number, however, and must be scaled with the local friction velocity for comparison with other data and calculations. Recently experiments by Hirota's group, Nagoya University, at lower Reynolds numbers have been reported and are the data included here.

8.2.1 Experiments

Improvements in the quality of data measured in this difficult flow have followed the development of enhanced measurement techniques. Rotation of single element hot-wires was replaced by use of multi-wire probes together with advanced data acquisition and processing techniques to reduce measurement error, particularly in the turbulence quantities. Thus the data of Hirota's group [227] [64], which reflects these improvements, has been selected for this data base (data set CMP00). The measurements were conducted at 90 hydraulic diameters from the entrance and thus do not suffer from incomplete development. This is confirmed by global quantities such as mean resistance which agree with established values. Furthermore, remarkably good symmetry is noted in both the contours of mean velocity and, more importantly, in the turbulence quantities including the difficult differences in the important cross-planar normal stresses.

8.2.2 Simulations

The difficulties in measuring certain turbulence quantities, such as $\overline{u_2 u_3}$ and the fluctuating vorticity, and in establishing fully developed conditions for this configuration make direct numerical simulation (DNS) of the turbulence attractive for addressing questions of physics and for development of large-eddy simulation techniques. Such simulations are necessarily limited to low Reynolds numbers, but within this constraint they can provide information on any and all variables of interest. Advances in this field have led to criteria for simulations of adequate resolution and accuracy and have produced a wealth of information on a variety of flow configurations.

Thus the results of a DNS "numerical experiment" on the flow in a square duct is included in this database. There are two notable simulations of this configuration: Gavrilakis [66] and Huser & Biringen [86], Huser *et al* [87]. The simulation of [86] [87] was at twice the Reynolds number of [66] and was thus selected for this compilation (data set CMP01). Two calculations are described in the reference, but only the higher resolution data are included here.

8.3 Flow around a circular cylinder

The flow around a circular cylinder is perhaps the paradigm of complex flows. It is simple in geometry yet remarkably complex in flow features, including thin separating shear layers and large scale unsteadiness in the vortex formation and shedding. Both of these features are difficult to capture in large-eddy simulations so that this flow remains a challenge to all new computational formulations. There have been numerous experiments on cylinder flows of many kinds including the simple infinite cylinder normal to the flow, cylinders at angles, cylinders of short aspect ratios, and tapered cylinders among others. Experiments, however, which recorded time-resolved data at Reynolds numbers large enough for a turbulent wake, are difficult and rare. Thus only one dataset, CMP10, is included here, that of the experiments of Cantwell and Coles [31] which addressed the flow around a long, constant-diameter cylinder normal to the flow.

8.3.1 Experiment

The vortex shedding from the circular cylinder presents difficulties for measuring the mean statistics of the flow and turbulence. There is regularity in the shedding, but there is also a level of irregularity which must be addressed. Today, global measurement techniques, such as particle image velocimetry, can capture a flow field at an instant to display the spatial variations in velocity, but temporal statistics are still a challenge in that many such images must be recorded and analyzed. A point measurement technique, in particular hot-wire anemometry, is able to record time records, but cannot easily address spatial variations such as the vortex shedding without averaging out these important structures. Also, hot-wire anemometers cannot normally be used in reversing flow. Innovative techniques are required to capture such complex flows and record detailed data on their structure and turbulence.

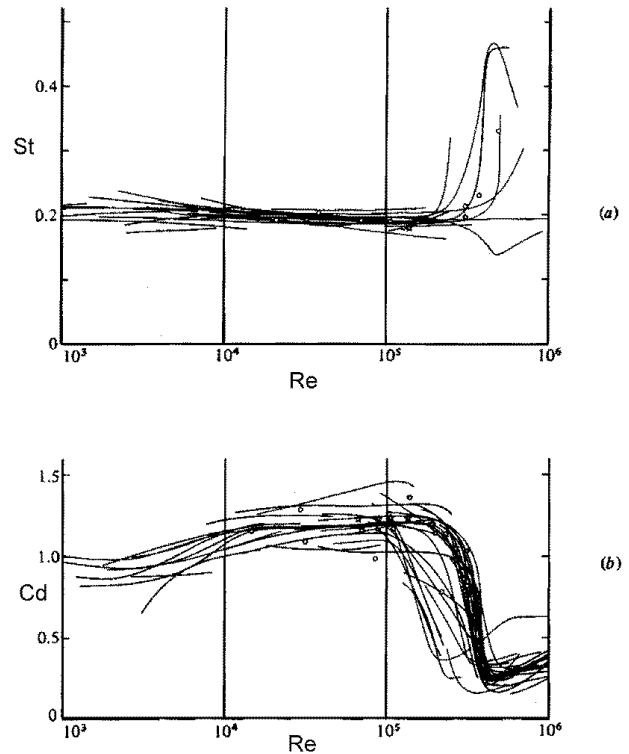


Figure 1: (a) Strouhal number and, (b) drag coefficient for the flow around a circular cylinder from [31], shown as open stars, compared with data from other sources (reprinted from [31]; see their table 1 for sources of lines).

The near wake of a circular cylinder at a Reynolds number (here 140,000) large enough to create a fully turbulent wake but laminar separation (subcritical) generates turbulent vortices in a nearly periodic fashion. If the cylinder is smooth and long (compared to its diameter), if end-plates are used, and if it is placed normal to a steady flow of low turbulence, then the regularity and two-dimensionality of the vortices will be maximized. There will still be variations in the phase of the shedding, but it will be small enough that it can be accommodated with appropriate measurement techniques. A 'flying hot-wire' and a pressure-based sampling method were employed in this experiment as described below. Any point measurement of velocity in this flow raises questions about distinguishing between 'jitter' and turbulence, but these are presumably of less importance to the large-eddy simulations than to RANS predictions. However, the computation of statistical properties should use methods appropriate for the measurements conducted in the dataset being used for evaluation.

Measurements of the Strouhal number and drag coefficient against Reynolds number in the data included here from Cantwell and Coles [31, set CMP10] compare favourably with other experiments (see figures 1 and 2). There is a somewhat surprising variation in the values reported for both quantities.

8.4 Flow around a square cylinder

The flow around a square cylinder is an important case for testing calculation procedures for complex turbulent flows

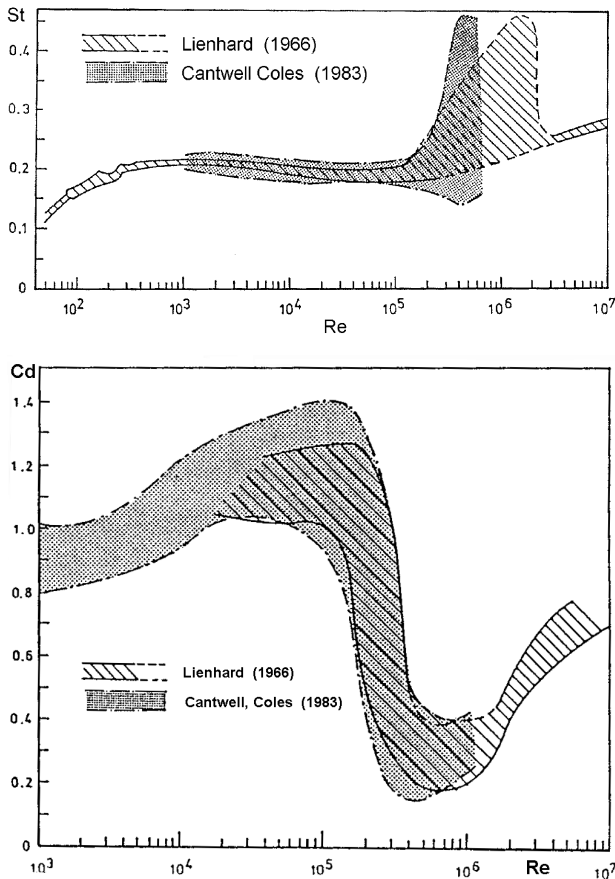


Figure 2: Summary of Strouhal numbers and drag coefficients for circular cylinders from [31] compared to those from [129].

because it has a simple geometry but involves complex physical phenomena such as vortex shedding and also transition at higher Reynolds numbers. The important difference from the circular cylinder case is that the separation point is fixed at the front corner of the cylinder.

Vortex shedding is found for Reynolds numbers higher than about 70 and remains laminar and approximately 2D up to a Reynolds number of about 600 [52]. At higher Reynolds numbers the separated shear layers over the side walls of the cylinder undergo transition, and this occurs closer to the front corner as the Reynolds number increases. At the rear corners quasi-periodic alternate vortex shedding occurs which induces the separated shear layer along the side walls to flap. The shed vortices are convected downstream and they are eventually broken up and diffused by the turbulent motion. The wake past the square cylinder is about 30% wider than that past the circular cylinder and the drag coefficient is higher by a factor of 1.7.

There are considerably fewer experimental studies on the flow past a square cylinder than for the flow past a circular one. Okajima [159] and Davis & Moore [42] have measured the influence of the Reynolds number on the dimensionless shedding frequency (Strouhal number). In the intermediate Reynolds number range, they are quite different (see figure 3); Okajima carried out his measurements with various cylinders and in various fluids so that his re-

sults appear to have a broader and more secure basis. Some numerical studies (unsteady 2D calculations without turbulence models) have been carried out at low Reynolds numbers and show a fairly wide scatter, especially when the Reynolds number is around 200 to 300. Lift and drag coefficients and Strouhal numbers have been measured by various experimenters in the Reynolds number range $2 \times 10^4 - 1.7 \times 10^5$. They found little influence of the Reynolds number on the Strouhal number (St about 0.13) and also on the mean drag coefficient (C_D about 2.1). There appears to be no drag crisis as in the case of the circular cylinder. The first more detailed measurements providing profiles of mean velocities and stresses due to fluctuations have been reported by Durao *et al* [51] for a Reynolds number of 14000 (see Fig. 5). Both blockage (13%) and free-stream turbulence level (6%) were quite high. Owing to their measurement technique, Durao *et al.* did not obtain phase-resolved results but only mean averages.

The only experiment with phase-resolved results is that due to Lyn & Rodi [133] and Lyn *et al.* [134] who provided detailed measurements of the flow past a square cylinder at $Re = 22,000$ obtained with a laser doppler velocimeter. In the first paper, single-component measurements are provided for the shear layer and reverse-flow region on the cylinder side wall, and in the second paper, two-component measurements of velocities in the wake. These measurements were chosen to be included in the data base, CMP20. The measured relatively slow recovery of the centre-line velocity in the wake, see figure 4, was sometimes considered doubtful (and is difficult to simulate by calculation methods), but it appears realistic because of the strong individual vortices that are sustained quite far downstream in this case. No DNS studies are known for this case.

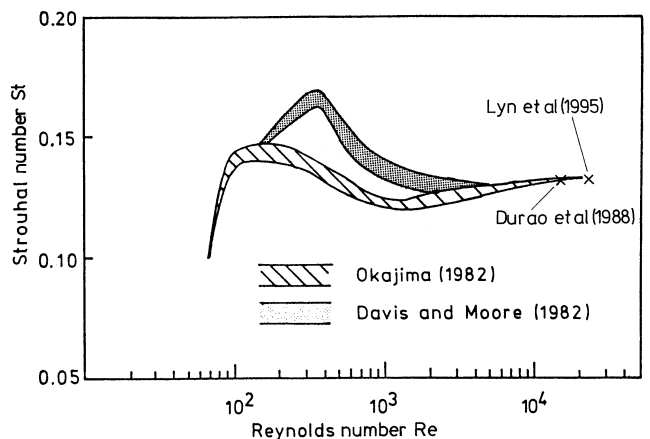


Figure 3: Strouhal number variation with Reynolds number for square cylinders; from data in [159] and [42], compared with [134] and [51].

8.4.1 Experiment

As with the circular cylinder, experiments which provide details of the flow around a square cylinder are difficult, and it was not until the development of instrumentation which could handle the reversed flow region that such data became available. Even then the separations off the front

corners complicate the measurements; the flying hot-wire, used so successfully for the circular cylinder wake, cannot be used easily in these locations. The laser velocimeter, rigged for directional discrimination, is ideal for this type of problem, however, and has been applied to the square cylinder of Lyn & Rodi [133] and Lyn et al. [134] (data set CMP20).

Measurements of time-averaged quantities compare favourably with the (scarce) available data. See figure 4 for a comparison of streamwise variations of the streamwise component of velocity, its r.m.s. value, and the r.m.s. value of the transverse velocity component. Note that some of the data is for a circular cylinder for reference only.

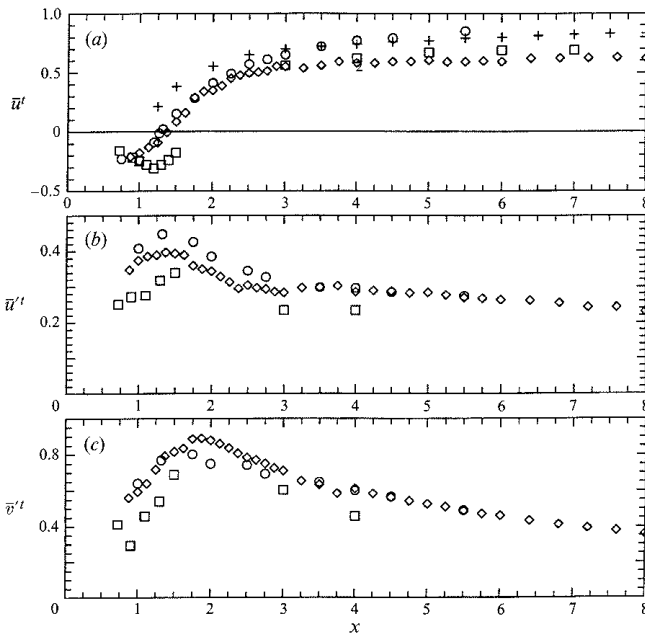


Figure 4: Streamwise variation of time-averaged (a) streamwise velocity, (b) r.m.s. streamwise velocity, and (c) r.m.s. transverse velocity in cylinder wakes, from data of: \diamond , [134]; \circ , [51]; $+$, [31], and \square , [143] (reprinted from [134].)

8.5 Incompressible flow over a backward facing step

The flow over a backward facing step has become a canonical flow for testing prediction codes. The simple geometry of the walls and the known separation point, together with the challenges of the reversing vortical flow and reattachment zone, provide well-defined conditions and adequate flow complexities to be both addressable and useful to experimentalists and computationalists. Thus there is available high quality data from both experiments and direct numerical simulations. The development of laser velocimeter systems which can capture reversing flow over a wide dynamic range has permitted documenting the details of the flow field beyond previous measurements of quantities such as the reattachment point and the outer, unidirectional flow. Likewise advances in DNS have made feasible the simulation of flows beyond the simple channel, and the backward facing step was among the first of these.

It is often noted that this flow is sensitive to small changes in geometry. For this reason it is imperative that the boundary geometry and the inflow and outflow conditions be duplicated carefully. Also, a common difficulty in the prediction of this flow lies in the details of the recovery region, and those should be a particular target of any large-eddy simulation.

8.5.1 Simulations

The backward facing step was among the first geometries with strong changes in the streamwise direction and fully turbulent flow to be addressed by DNS. The work by Le & Moin [115] established the capability of DNS to handle such flows accurately. Data from those simulations are included in this database (data set CMP30) and match the conditions from the experiments of Jovic & Driver [99] [100]. A comparison of measured [99] and computed [115] skin friction is shown in figure 5. Details of the simulations are included in the data set.

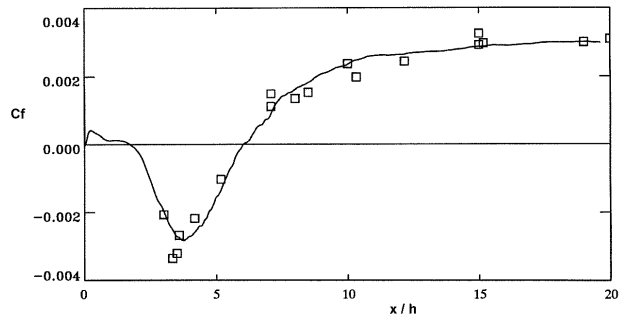


Figure 5: Comparison between the wall friction in a backwards-facing step, from: —, the simulations in [115, CMP30] and \square , the experiment in [99] (reprinted from [99]).

8.5.2 Experiments

Because of the attractive characteristics of the backward facing step for testing prediction methods, there have been many experimental studies of it. Advances in instrumentation have produced increasingly useful results over a range of Reynolds numbers, so two experiments are included in this database.

The experiment of Jovic and Driver [99] [100] (data set CMP31) was specifically designed for comparison with a DNS. A low Reynolds number was thus selected to provide data for direct comparison to the simulations, but this also presents some difficulties for the experimentalist so that the data should be utilized carefully. The low velocities increase the uncertainties in the measurements which are thus estimated to be somewhat elevated. In addition, the inflow boundary layer may still retain some history of the tripping technique. Thus additional care should be taken in the selection of inflow and boundary conditions. The work was never published except in a report and thus has not been subjected to outside scrutiny. The DNS of Le and Moin [115] (discussed above) did not uncover problems with the data, however, which increases confidence that the flow can be used for evaluation of simulations in general.

The second experiment, that of Driver and Seegmiller [50] (data set CMP32), was intended for evaluation of RANS codes and is at a higher Reynolds number. Redundant measurements and careful analysis of the data yielded a highly regarded dataset which should prove useful for evaluation of simulations, especially as they approach the more useful (higher) Reynolds numbers.

8.6 SUMMARY OF COMPLEX FLOWS

SQUARE DUCT				
CMP00	$UD/\nu = 6.5 \times 10^4$	E	Yokosawa <i>et al.</i> [64]	pg. 185
CMP01	$u_\tau D/\nu = 600$	N	Huser & Biringen [86]	pg. 187
CIRCULAR CYLINDER				
CMP10	$Re_D = 140,000$	E	Cantwell & Coles [31]	pg. 189
SQUARE CYLINDER				
CMP20	$Re_D = 22,000$	E	Lyn <i>et al</i> [134]	pg. 191
BACKWARDS FACING STEP				
CMP30	$Re_h = 5,100$	N	Le & Moin [115]	pg. 193
CMP31	$Re_h = 5,000$	E	Jovic & Driver [99, 100]	pg. 195
CMP32	$Re_h = 37,500$	E	Driver & Seegmiller [50]	pg. 197

E: experimental cases. N: numerical ones. Consult individual data sheets for more details

REFERENCES

- [1] ABRAMOVICH, G.N. 1963 *The theory of turbulent jets*. MIT Press.
- [2] ALEM, D. 1995 Analyse expérimentale d'une turbulence homogène en écoulement supersonique soumise à un choc droit. *Thesis* Univ. Poitiers.
- [3] ALVING, AMY E. & FERNHOLZ, H. H. 1996 Turbulence measurements around a mild separation bubble and downstream of reattachment. *J. Fluid Mech.* **322**, 297-328.
- [4] ANDERSSON, H.I. & KRISTOFFERSEN, R. 1994 Turbulence statistics of rotating channel flow. In *Proc. 9th Symposium Turbulent Shear Flow, Tokyo*.
- [5] ANSELMET, F., GAGNE, Y., HOPFINGER, E.J. & ANTONIA, R.A. 1984 High-order structure functions in turbulent shear flow, *J. Fluid Mech.* **140**, 63-89.
- [6] BATT, R.G. 1975 Some Measurements on the Effects of Tripping the Two-Dimensional Shear Layer, *AIAA J.* **13**, 245 – 247.
- [7] BALARAS, E., BENOCCI, C. & PIOMELLI, U. 1987 Two-layer approximate boundary conditions for large-eddy simulations. *J. Fluid Mech.* **177**, 133.
- [8] BARDINA, J., FERZIGER, J.H. & REYNOLDS, W.C. 1983 Improved subgrid-scale models based on large eddy simulation of homogeneous, incompressible, turbulent flows, *Rep. TF-19*, Dept. Mech. Engg, Stanford, CA.
- [9] BARENBLATT, G.I. 1993. Scaling laws for fully developed turbulent shear flows. Parts 1 & 2. *J. Fluid Mech.* **248**, 513–529.
- [10] BARLOW, R.S. & JOHNSTON, J.P. 1988 Structure of a turbulent boundary layer on a concave surface. *J. Fluid Mech.* **191**, 137-176.
- [11] BARRE S., QUINE C. & DUSSAUGE J.P. 1994 Compressibility effects on the structure of supersonic mixing layers: experimental results. *J. Fluid Mech.* **259**, 47–78.
- [12] BARRE, S., BRAUD, P., CHAMBRES, O. & BONNET, J.P. 1997 Influence of inlet pressure conditions on supersonic turbulent mixing layers. *Exp. Thermal and Fluid Science*.
- [13] BARRE, S., ALEM, D. & BONNET, J.P. 1996 Experimental study of normal shock/homogeneous turbulence interaction. *AIAA J.* **34**, 968-974.
- [14] BASKARAN, V., SMITS, A.J. & JOUBERT, P.N. 1987 A Turbulent Flow Over a Curved Hill. Part 1. Growth of an Internal Boundary Layer. *J. Fluid Mech.* **182**, 47-83.
- [15] BASKARAN, V., SMITS, A.J. & JOUBERT, P.N. 1992 A Turbulent Flow Over a Curved Hill. Part 2. Effects of Streamline Curvature and Streamwise Pressure Gradient, *J. Fluid Mech.* **232**, 377-402.
- [16] BATCHELOR, G.K. 1953 *The theory of homogeneous turbulence*. Cambridge University Press.
- [17] BATCHELOR, G.K. & TOWNSEND, A.A. 1949 The nature of turbulent motion at large wave numbers. *Proc. Roy. Soc. London A* **199**, 238-255.
- [18] BELL, J.H. & METHA, R.D. 1990 Development of a two-stream mixing layer from tripped and untripped boundary layers. *AIAA J.* **28**, 2034-2042.
- [19] BIRCH S.F. & EGGERS M. 1972 A critical review of the experimental data for developed free turbulent shear layers. *NASA Tech. Rep.* SP-321.
- [20] BLIN, E. 1993 Etude expérimentale de l'interaction entre une turbulence libre et une onde de choc. *Thesis* Univ. Paris 6.
- [21] BOGDANOFF D.W. 1983 Compressibility effects in turbulent shear layers. *AIAA J.* **21**, 926-927.
- [22] BRADBURY, L.J.S. 1965 The structure of self-preserving turbulent plane jet, *J. Fluid Mech.* **23**, 31-64.
- [23] BRADSHAW, P. 1969 The analogy between stream curvature and buoyancy in turbulent shear flow. *J. Fluid Mech.* **36**, 177.
- [24] BRADSHAW, P. 1971 Variations on a theme of Prandtl. *AGARD-CP-93*.
- [25] BRIASSULIS, G., AGUI, J., ANDREOPOULOS, J. & WATKINS, C. 1996 The new shock tube research facility at CCNY for high speed turbulence research. *AIAA Paper* 96-0849.
- [26] BRIASSULIS, G. & ANDREOPOULOS, J. 1996 High resolution measurements of isotropic turbulence interacting with shock waves. *AIAA Paper* 96-0042.
- [27] BRIASSULIS, G. & ANDREOPOULOS, J. 1996 Compressible effects in grid generated turbulence. *AIAA Paper* 96-2055.
- [28] BROWAND, F.K. & LATIGO, B.O. 1979 The growth of the two-dimensional mixing layer from a turbulent and non-turbulent boundary layer. *Phys. Fluids* **92**, 1011–1019.
- [29] BROWN, G.L. & ROSHKO, A. 1974 On density effects and large scale structure in turbulent mixing layers. *J. Fluid Mech.*, **64**, 775-816.
- [30] BRUUN H.H. 1995 *Hot-Wire Anemometry. Principles and Signal Analysis*. Oxford University Press.

- [31] CANTWELL, B. & COLES, D. 1983 An Experimental Study of Entrainment and Transport in the Turbulent Near Wake of a Circular Cylinder. *J. Fluid Mech.* **136**, 321.
- [32] CHAMPAGNE, F.H., HARRIS, V.G. & CORRSIN, S. 1970 Experiments on nearly homogeneous turbulent shear flow. *J. Fluid Mech.* **41**, 81-131.
- [33] CHEBBI, B., HOLLOWAY, A.G.L. & TAVOULARIS, S. 1997 The response of sheared turbulence to changes in curvature. To appear *J. Fluid Mech.*
- [34] CHEN, S.-Y. & SHAN, X. 1992 High resolution turbulent simulations using the Connection Machine-2. *Computers in Fluids* **6**, 643-646.
- [35] CLARK, R.A., FERZIGER, J.H. & REYNOLDS, W.C. 1979 Evaluation of subgrid-scale models using an accurately simulated turbulent flow, *J. Fluid Mech.* **91**, 1-16.
- [36] COLEMAN, H.W. & STEELE, W.G. 1995 Engineering application of experimental uncertainty analysis. *AIAA J.* **33**, 1888-1896.
- [37] COLEMAN, H.W., STEELE, W.G. & TAYLOR, R.P. 1995 Implications of correlated bias uncertainties in single and comparative tests. *J. Fluids Eng.* **117**, 552-556.
- [38] COLES, D. 1962 The turbulent boundary layer in a compressible fluid *Report R-403-PR*, The Rand Corporation, Santa Monica, CA.
- [39] COMTE-BELLOT, G. 1965 Ecoulement turbulent entre deux parois paralleles. Publications Scientifiques et Techniques du Ministere de l'Air no. 419.
- [40] COMTE-BELLOT, G. & CORRSIN, S. 1966 The use of a contraction to improve the isotropy of grid-generated turbulence. *J. Fluid Mech.* **25**, 657-682.
- [41] COMTE-BELLOT, G. & CORRSIN, S. 1971 Simple Eulerian time correlations of full and narrow-band velocity signals in grid-generated isotropic turbulence. *J. Fluid Mech.* **48**, 273-337.
- [42] DAVIS, R.W. & MOORE, E.F. 1982 A numerical study of vortex shedding from rectangles. *J. Fluid Mech.* **116**, 475.
- [43] DE SOUZA, F.A., NGUYEN, V.D. & TAVOULARIS, S. 1995 The structure of highly sheared turbulence. *J. Fluid Mech.* **303**, 155-167.
- [44] DEARDORFF, W. 1970 A numerical study of three-dimensional turbulent channel flow at large Reynolds numbers, *J. Fluid Mech.* **41**, 453-480.
- [45] DEBISSCHOP, J.R., CHAMBRES, O. & BONNET, J.P. 1994 Velocity field characteristics in supersonic mixing layers, *Exp. Thermal and Fluid Science* **9**, 147-155.
- [46] DELVILLE, J. 1995. La décomposition orthogonale aux valeurs propres et l'analyse de l'organisation tridimensionnelle des écoulements turbulents cisailés libres. *Thèse Doctorat*, Université de Poitiers.
- [47] DELVILLE, J., BELLIN, S., GAREM, J.H. & BONNET, J.P. 1988 Analysis of structures in a turbulent a turbulent plane mixing layer by use of a pseudo-flow visualization method based hot-wire anemometry. *Advances in Turbulence II*, Fernholz and Fiedler eds., Springer, pp 251.
- [48] DEMUREN, A. & RODI, W. 1984 Calculation of turbulence-driven secondary motion in non-circular ducts. *J. Fluid Mech.* **140**, 189.
- [49] DIMOTAKIS, P.E. 1991 Turbulent Free Shear Layer Mixing and Combustion. *Progress in Astronautics and Aeronautics* **137**.
- [50] DRIVER, D.M. & SEEGMILLER, H.L. 1985 Features of a Reattaching Turbulent Shear Layer in Divergent Channel Flow. *AIAA J.* **23**, 163.
- [51] DURAO, D.F.G., HEITOR, M.V. & PEREIRA, J.C.F. 1988 Measurements of Turbulent and Periodic Flows Around a Square Cross-section Cylinder. *Exper. Fluids* **6**, 298.
- [52] DURAO, D.F.G., HEITOR, M.V. & PEREIRA, J.C.F. 1990 Experiments on the Flow Past a Square Cylinder at Low Reynolds Numbers. *Report Instituto Superior Technico, Mech. Engr. Dept.*, Lisbon, Portugal.
- [53] DURBIN, P.A. 1995 Separated flow computations with the $k-\epsilon-v^2$ model. *AIAA J.* **33**, 659-664.
- [54] DURST, F., JOVANOVIĆ, J. & SENDER, J. 1995 LDA measurements in the near-wall region of a turbulent pipe flow. *J. Fluid Mech.* **295**, 305-335.
- [55] ECKELMANN, H. 1974 The structure of the viscous sublayer and the adjacent wall region in a turbulent channel flow. *J. Fluid Mech.* **65**, 439-459.
- [56] EGGELS, J.G.M., UNGER, F., WEISS, M.H., WESTERWEEEL, J., ADRIAN, R.J., FRIEDRICH, R. & NIEUWSTADT, F.T.M. 1994 Fully developed turbulent pipe flow: a comparison between direct numerical simulation and experiment. *J. Fluid Mech.* **268**, 175-209.
- [57] ELENA, M. 1989 Laser Doppler anemometry in supersonic flows: problems of seeding and angular bias. *AGARDograph 315*, Chapter 7.
- [58] ELLIOTT, G.S. & SAMIMY, M. 1990 Compressibility effects in free shear layer, *Phys. Fluids A*, **2**, 1231-1240.
- [59] FERCHICHI, M. & TAVOULARIS, S. 1997 Manuscript in preparation.

- [60] FERNHOLZ, H. H. & FINLEY, P. J. 1996 The incompressible zero pressure gradient turbulent boundary layer: An assessment of the data. *Prog. Aerospace Sci.* **32**, 245-311.
- [61] FERZIGER, J.H. 1996 Large Eddy Simulation, in *Simulation and modelling of turbulent flows* (Gatski, T.B., Hussaini, M. Y. & Lumley, J.L. eds.), Oxford Univ. Press.
- [62] FIEDLER, H.E., DZIOMBA, B., MENSING, P. & RÖSGEN, T. 1980. Initiation, evolution and global consequences of coherent structures in turbulent shear flows. *The role of coherent structures in modeling turbulence and mixing* (J. Jim'enez ed.), Vol. 136 of *Lecture Notes in Physics*, Springer.
- [63] FRIEDRICH, R. & BERTOLOTTI, F. 1997 Compressibility effects due to turbulent fluctuations. To appear in *Applied Scientific Research*
- [64] FUJITA, H., HIROTA, M. & YOKOSAWA, H. 1990 Experiments on turbulent flow in a square duct with a rough wall. *Memoirs of Faculty of Engr., Nagoya U.* **41**, 280.
- [65] GAVIGLIO, J. 1987 Reynolds analogies and experimental study of heat transfer in the supersonic boundary layer. *Intr. J. Heat Mass Transfer* **30**, 911-926
- [66] GAVRILAKIS, S. 1992 Numerical simulation of low-Reynolds-number turbulent flow through a straight square duct. *J. Fluid Mech.* **244**, 101.
- [67] GENGE, J.N. & MATHIEU, J. 1979 On the application of successive plane strains to grid-generated turbulence. *J. Fluid Mech.* **93**, 501-513.
- [68] GENGE, J.N. & MATHIEU, J. 1980 The return to isotropy of an homogeneous turbulence having been submitted to two successive plane strains. *J. Fluid Mech.* **101**, 555-566.
- [69] GEORGE, W. K., KNECHT, P. & CASTILLO, L. 1992 The zero pressure gradient turbulent boundary layer revisited. In: *Proceedings of the Thirteenth Biennial Symposium on Turbulence*.
- [70] GESSNER, F.B. & EMERY, A.F. 1981 The numerical prediction of developing turbulent flow in rectangular ducts, *Trans. ASME I: J. Fluids Engr.* **103**, 445.
- [71] GHOSAL, S. 1996 An analysis of numerical errors in large-eddy simulation of turbulence. *J. Comput. Phys.* **125**, 187-206.
- [72] GUTMARK, E. & WYGNANSKI, I. 1976 The planar turbulent jet. *J. Fluid Mech.* **73**, 465-495.
- [73] HANNAPPEL, R. & FRIEDRICH, R. 1995 Interaction of isotropic turbulence with a normal shock-wave. *Appl. Sci. Res.* **54**, 205-221.
- [74] HARRIS, V.G., GRAHAM, J.H.A. & CORRSIN, S. 1977 Further experiments on nearly homogeneous turbulent shear flow. *J. Fluid Mech.* **81**, 657-687.
- [75] HÄRTEL, C. 1996 Turbulent flows: direct numerical simulation and large-eddy simulation, in *Handbook of Comput. Fluid Mech.* (R. Peyret, ed.), Academic. pp. 284-338.
- [76] HEENAN, A.F., MORRISON, J.F., IUSO, G. & ONORATO, M. 1994 Evolution of two-scale, shearless grid turbulence. *II International Conference on Experimental Fluid Mechanics*, July 1994, Torino, Italy.
- [77] HERWEIJER, J. & VAN DER WATER, W. 1995 Universal shape of scaling functions in turbulence. *Phys. Rev. Lett.* **74**, 4651-4654.
- [78] HESKESTAD, G. 1965 Hot-wire measurements in a plane turbulent jet, *J. Applied Mech.* **32**, 1.
- [79] HESSELINK, L. & STURTEVANT, B. 1988 Propagation of weak shocks through a random medium, *J. Fluid Mech.* **196**, 513-553.
- [80] HO, C.M. & HUERRE, P. 1984 Perturbed shear layers, *Annual Review of Fluid Mechanics* **16**, 365-424.
- [81] HOLLOWAY, A.G.L. 1997 Personal communication.
- [82] HOLLOWAY, A.G.L. & TAVOULARIS, S. 1992 The effects of curvature on sheared turbulence. *J. Fluid Mech.* **237**, 569-603.
- [83] HOLLOWAY, A.G.L. & TAVOULARIS, S. 1993 Scaling and Structure of Turbulent Eddies in Curved Sheared Flows. *Turbulent Shear Flows 8*, F. Durst *et al.* (editors), 383-401, Springer.
- [84] HONKAN, A. & ANDREOPOULOS, J. 1990 Experiments in a shock wave/homogeneous turbulence interaction. *AIAA Paper* 90-1647.
- [85] HUANG, L.S. & HO, C.M. 1990 Small-scale transition in a plane mixing layer, *J. Fluid Mech.* **210**, 175-500.
- [86] HUSER, A. & BIRINGEN, S. 1993 Direct numerical simulation of turbulent flow in a square duct. *J. Fluid Mech.* **257**, 65.
- [87] HUSER, A., BIRINGEN, S. & HATAY, F. 1994 Direct simulation of turbulent flow in a square duct: Reynolds-stress budgets. *Phys Fluids* **6**, 65.
- [88] HUSSAIN, A.K.M.F. & ZEDAN, M.F. 1978 Effects of the initial condition on the axisymmetric free shear layer: a flow visualization study. *Phys. Fluids* **21**, 1100
- [89] HUSSAIN, A.K.M.F. & ZEDAN 1978 *Phys. Fluids* **21**, 1475

- [90] HUSSEIN, H.J., CAPP, S.P. & GEORGE, W.K. 1994 Velocity measurements in a high-Reynolds-number, momentum-conserving, axisymmetric, turbulent jet. *J. Fluid Mech.* **258**, 31-75.
- [91] JACQUIN, L., BLIN, E. & GEFFROY, P. 1993 An experiment on free turbulence/shock wave interaction, in *Turbulent Shear Flows 8* (Eds. Durst et al.) Springer, pp.229-248
- [92] JACQUIN, L. LEUCHTER, O., CAMBON, C. & MATHIEU, J. 1990 Homogeneous turbulence in the presence of rotation. *J. Fluid Mech.* **220**, 1-52.
- [93] JIMÉNEZ, J. & WRAY, A.A. 1994 On the dynamics of small-scale vorticity in isotropic turbulence. In *Annual Res. Briefs*, Centre for Turbulence Research, Stanford CA, pp. 287-312.
- [94] JIMÉNEZ, J., WRAY, A.A., SAFFMAN, P.G. & ROGALLO, R.S. 1993 The structure of intense vorticity in isotropic turbulence. *J. Fluid Mech.* **255**, 65-90.
- [95] JOHANSSON, A.V. & ALFREDSSON, P.H. 1983 On the structure of turbulent channel flow. *J. Fluid Mech.* **137**, 409-421.
- [96] JOHNSON, D.A. 1989 Laser Doppler anemometry. *AGARDograph 315*, Chapter 6
- [97] JOHNSTON, J.P., HALLEEN, R.M. & LEZIUS, D. 1969 Effect of spanwise rotation on the structure of two-dimensional fully developed turbulent channel flow. *J. Fluid Mech.* **56**, 533.
- [98] JOHNSON, P.L. & JOHNSTON, J.P. 1989 The effects of grid-generated turbulence on flat and concave turbulent boundary layers. *Report MD-53*, Dept. of Mech. Eng. Stanford University.
- [99] JOVIC, S. & DRIVER, D. 1994 Backward-facing Step Measurements at Low Reynolds Number, $Re_h = 5000$. *NASA Tech Memo 108807*.
- [100] JOVIC, S. & DRIVER, D. 1995 Reynolds Number Effect on the Skin Friction in Separated Flows Behind a Backward-facing Step. *Exper. Fluids* **18**, 464.
- [101] KAILASNATH, P., SREENIVASAN, K.R. & STOLOVITZKY, G. 1992 Probability density of velocity increments in turbulent flows. *Phys. Rev. Lett.* **68**, 2766-2769.
- [102] KARASSO, P.S. & MUNGAL, M.G. 1996 Scalar mixing and reaction in plane liquid shear layers. *J. Fluid Mech.* **323**, 23-63.
- [103] KARNIK, U. & TAVOULARIS, S. 1987 Generation and manipulation of uniform shear with the use of screens. *Exper. Fluids* **5**, 247-254.
- [104] KASAGI, N., TOMITA, Y. & KURODA, A. 1992 Direct numerical simulation of passive scalar field in a turbulent channel flow. *Trans. ASME* **114**, 598-606.
- [105] KELLER, J. & MERZKIRCH, W. 1990 Interaction of a normal shock wave with a compressible turbulent flow, *Experiments in Fluids* **8**, 241-248
- [106] KIDA, S. & ORSZAG, S.A. 1992 Energy and spectral dynamics in decaying compressible turbulence. *J. Sci. Comput.* **7**, 1-34.
- [107] KIM, J. 1983 The effect of rotation on turbulent structure. In *Proc. 4th Symposium Turbulent Shear Flow, Karlsruhe*.
- [108] KIM, J., MOIN, P. & MOSER, R.D. 1987 Turbulence statistics in fully developed channel flow at low Reynolds number. *J. Fluid Mech.* **177**, 133-166.
- [109] KOLMOGOROV, A.N 1941 The local structure of turbulence in incompressible viscous fluids a very large Reynolds numbers. *Dokl. Nauk. SSSR* **30**, 301-305.
- [110] KOLMOGOROV, A. N. 1962 A refinement of previous hypotheses concerning the local structure of turbulence in a viscous incompressible fluid at high Reynolds number. *J. Fluid Mech.* **13**, 82-85.
- [111] KRAVCHENKO, A.G. & MOIN, P. 1997 On the effect of numerical errors in the large-eddy simulations of turbulent flows. *J. Comput. Phys.* **131**, 310-332.
- [112] KREPLIN, H.P. & ECKELMANN, H. 1979 Behaviour of the three fluctuating velocity components in the wall region of a turbulent channel flow. *Phys. Fluids* **22**, 1233-1239.
- [113] KRISTOFFERSEN, R. & ANDERSSON, H. 1993 Direct simulations of low-Reynolds-number turbulent flow in a rotating channel. *J. Fluid Mech.* **256**, 163.
- [114] LAUFER, J. 1950 Investigation of turbulent flow in a two-dimensional channel. Tech. Note TN-2123, NACA.
- [115] LE, H. AND MOIN, P. 1994 Direct numerical simulation of turbulent flow over a backward facing step, *Technical Report No. TF-58*, Department of Mechanical Engineering, Stanford University.
- [116] LE PENVEN, L., GENGE, J.N. & COMTE-BELLOT, G. 1985 On the approach to isotropy of homogeneous turbulence: effect of the partition of kinetic energy among the velocity components. In *Frontiers in Fluid Mechanics*, S.H. Davis & J.L. Lumley (editors), Springer-Verlag.
- [117] LEE, M.J., KIM, J. & MOIN, P. 1990 Structure of turbulence at high shear rates. *J. Fluid Mech.* **216**, 561-583.
- [118] LEE, S., LELE, S. K. & MOIN, P. 1997 Interaction of isotropic turbulence with shock waves: effect of shock strength. *J. Fluid Mech.* **340**, 225-247.

- [119] LEE, S., MOIN, P. & LELE, S.K. 1992 *Interaction of isotropic turbulence with a shock wave*. Report **TF-52**, Thermosciences Division, Dept. Mechanical Engg., Stanford University
- [120] LELE S. 1994. Compressibility Effects on Turbulence. *Ann. Rev. Fluid Mech.*, **26**, 211–254.
- [121] LEONARD, A. 1974 Energy cascade in large-eddy simulations of turbulent fluid flows, *Advances in Geophys.* **18A**, 237-248.
- [122] LESIEUR, M. & METAIS, O. 1996 New trends in large-eddy simulations of turbulence. *Ann. Rev. Fluid Mech.* **28**, 45–82.
- [123] LEUCHTER, O., AMRAM, K. & THOMAS, P. 1992 Etude théorique et expérimentale du comportement des particules à la traversée d'une onde de choc. *3ème Congrès francophone de Vélocimétrie Laser*, Toulouse. (ONERA TP 1992-233)
- [124] LEUCHTER, O. & BENOIT, J.P. 1991 Study of coupled effects of plane strain and rotation on homogeneous turbulence. *Proc. 8th Symp. Turb. Shear Flows*, 16.3.
- [125] LEUCHTER, O., BENOIT, J.P., BERTOGLIO, J.P. & MATHIEU, J. 1991 Experimental and theoretical investigation of a homogeneous turbulent shear flow. *Adv. Turb.* **3**, 435-444.
- [126] LEUCHTER, O., BENOIT, J.P. & CAMBON, C. 1993 Homogeneous turbulence subjected to rotation-dominated plane distortion. *Appl. Sci. Res.* **51**, 197-202.
- [127] LEUCHTER, O. & BERTOGLIO, J.P. 1995 Non-linear spectral approach to rotating turbulence in the presence of strain. *Proc. 10th Symp. Turb. Shear Flows*.
- [128] LEUCHTER, O. & DUPEUBLE, A. 1993 Rotating homogeneous turbulence subjected to axisymmetric contraction. *Proc. 9th Symp. Turb. Shear Flows*, 24-2.
- [129] LIENHARD, J.H. 1966 Synopsis of lift, drag, and vortex frequency data for rigid circular cylinders. *Bulletin 300*, Washington State Univ.
- [130] LIEPMANN, H.W. & LAUFER, J. 1947 Investigations of free turbulent mixing, *NACA TN-1257*.
- [131] LINDGREN, E.R. 1969 Propagation velocity of turbulence slugs and streaks in transition pipe flow. *Phys. Fluids* **12**, 418–425.
- [132] LOULOU, P., MOSER, R., MANSOUR, N. & CANTWELL, B. 1997 Direct simulation of incompressible pipe flow using a B-spline spectral method. Technical Report TM-110436, NASA.
- [133] LYN, D.A. & RODI, W. 1994 The Flapping Shear Layer Formed by the flow Separation from the Forward Corner of a Square Cylinder. *J. Fluid Mech.* **267**, 353.
- [134] LYN, D.A., EINAV, S., RODI, W. & PARK, J.H. 1995 A Laser-Doppler Velocimeter Study of Ensemble Averaged Characteristics of the Turbulent Near Wake of a Square Cylinder. *J. Fluid Mech.* **304**, 285.
- [135] LYONS, S.L., HANRATTY, T.J. & MCLAUGHLIN, J.B. 1991 Large-scale computer simulation of fully-developed turbulent channel flow with heat transfer. *Int. J. Num. Meth. Fluids* **13**, 999–1028.
- [136] MACPHAIL, D.C. 1944 Turbulence changes in contracting and distorting passages. *Royal Aircraft Establishment Aero Rept.* no. 1928.
- [137] MAHESH, K., LEE, S., LELE, S. K. & MOIN, P. 1995 The interaction of an isotropic field of acoustic waves with a shock wave. *J. Fluid Mech.* **300**, 383-407.
- [138] MAHESH, K., LELE, S. K. & MOIN, P. 1997 The influence of entropy fluctuations on the interaction of turbulence with a shock wave. *J. Fluid Mech.* **334**, 353-379.
- [139] MANSOUR, N.N., MOSER, R.D. & KIM, J. 1996 Reynolds number effects in low Reynolds number turbulent channels. in preparation.
- [140] MANSOUR, N.N., SHIH, T-H. & REYNOLDS, W.C. 1991 The effects of rotation on initially anisotropic homogeneous flows. *Phys. Fluids A* **3**, 2421-2425.
- [141] MANSOUR, N.N. & WRAY, A.A. 1994 Decay of isotropic turbulence at low Reynolds numbers. *Phys. Fluids* **6**, 808-814.
- [142] MARUSIC, I. & PERRY, A.E. 1995 A wall-wake model for the turbulence structure of boundary layers. Part 2. Further experimental support. *J. Fluid Mech.* **298**, 389-407.
- [143] MCKILLOP, A. & DURST, F. 1986 A laser anemometer study of separated flow behind a circular cylinder. In *Laser Anemometry in Fluid Mechanics II* (ed.R. J. Adrian, et al.) LADOAN-IST, Lisbon Portugal.
- [144] MEHTA, R.D. 1991 Effect of velocity ratio on plane mixing layer development: Influence of the splitter plate wake. *Experiments in Fluids* **10**, 194-204.
- [145] MENEVEAU, C. 1994 Statistics of turbulence subgrid-scale stresses: necessary conditions and experimental tests. *Phys. Fluids* **6**, 815–833.
- [146] MICHARD, Y.J. & BERTOGLIO, J.P. 1994 Experimental study of shearless turbulence mixing layer subjected to solid body rotation. in *Advances in Turbulence V*. Kluwer, pp. 580–585.

- [147] MOIN, P. 1997 Progress in large eddy simulation of turbulent flows. *AIAA Paper* 97-0749.
- [148] MOIN, P. & JIMÉNEZ, J. 1993 Large eddy simulation of complex turbulent flows. *AIAA Paper* 93-3099.
- [149] MOIN, P. & KIM, J. 1982 Numerical investigation of turbulent channel flow. *J. Fluid Mech.* **118**, 341–377.
- [150] MORKOVIN M.V. 1962 Effect of compressibility on turbulent flows *Colloque sur la mécanique de la turbulence*, Colloques Internationaux du CNRS **108**.
- [151] MOULIN, V., LEUCHTER, O & GEFFROY, P. 1989 Experimental study of homogeneous turbulence in the presence of transverse shear. *Proc. 7th Symp. Turb. Shear Flows*, 27-5.
- [152] MOSER, R.D. 1996 Vortices in turbulent mixing layers, in *Proceedings of the 19th International Congress of Theoretical and Applied Mechanics*, August 25-31, 1996, Kyoto.
- [153] MIYAKE, Y. & KAJISHIMA, T. 1986 Numerical simulation of the effects of the coriolis force on the structure of the turbulence. *Bull. JSME* **29**, 3341.
- [154] MYDLARSKI, L. & WARHAFT, Z. 1996 On the onset of high-Reynolds-number grid-generated wind tunnel turbulence. *J. Fluid Mech.* **320**, 331-368.
- [155] NA, Y. & MOIN, P. 1996 Direct numerical simulation of turbulent boundary layers with adverse pressure gradient and separation. *Report TF-68*, Thermosciences Division, Dept. of Mech. Engg., Stanford University.
- [156] NAKABAYASHI, K. & KITO, O. 1996 Low Reynolds number fully developed two-dimensional turbulent channel flow with system rotation. *J. Fluid Mech.* **315**, 1.
- [157] NIEDERSCHULTE, M.A. 1988 *Turbulent Flow Through a Rectangular Channel*. Ph. D. thesis, Department of Chemical Engineering, University of Illinois at Urbana-Champaign.
- [158] NIEDERSCHULTE, M.A., ADRIAN, R.J. & HANRATTY, T.J. 1990 Measurements of turbulent flow in a channel at low Reynolds number. *Exp. in Fluids* **9**, 222–230.
- [159] OKAJIMA, A. 1982 Strouhal Numbers of Rectangular Cylinders. *J. Fluid Mech.* **123**, 379.
- [160] ORLANDI, P. & FATICA, M. 1997 Direct simulation of a turbulent pipe rotating along the axis. *J. Fluid Mech.* **343**, 43–72..
- [161] OSTER D. & WYGNANSKI I. 1982 The forced mixing layer between parallel streams, *J. Fluid Mech.* **123**, 91–130.
- [162] PANCHAPAKESAN, N.R. & LUMLEY, J.L. 1993. Turbulence measurements in axisymmetric jets of air and helium. Part I. Air jet, *J. Fluid Mech.* **246**, 197-223.
- [163] PAPAMOSCHOU D. & ROSHKO A. 1988 The compressible turbulent shear layer: An experimental study. *J. Fluid Mech.*, **197**, 453-477.
- [164] PAPAVALASSIOU, D.V. 1996 *Structure and Transport in Wall Turbulence*. Ph. D. thesis, Dept. of Chemical Engineering, University of Illinois, Urbana-Champaign.
- [165] PATEL R.P. 1978 Effects of stream turbulence on free shear flows. *Aeronautical Quarterly* **29**, 33-43.
- [166] PERRY, A.E., HENBEST, S.M. & CHONG, M.S. 1986 A theoretical and experimental study of wall turbulence. *J. Fluid Mech.* **165**, 163–199.
- [167] PIOMELLI, U. 1993 High Reynolds number calculations using the dynamic subgrid-scale stress model. *Phys. Fluids A* **5**, 1484–1490.
- [168] PIOMELLI, U. & LIU, J. 1995 Large-eddy simulation of rotating turbulence using a localized dynamic model. *Phys. Fluids* **7**, 839.
- [169] PIOMELLI, U., MOIN, P. & FERZIGER, J.H. 1988 Model consistency in large eddy simulation of turbulent channel flows. *Phys. Fluids* **31**, 1884–1891.
- [170] PORTER, D., POUQUET, A. & WOODWARD, P. 1995 Compressible flows and vortex stretching. In *Small scale structures in three dimensional hydrodynamic and magnetohydrodynamic turbulence* (Meneguzzi, M., Pouquet, A. and Sulem, P-L., eds.) Springer. pp. 51-58.
- [171] PRESTON, J.H. 1957 The minimum Reynolds number for a turbulent boundary layer and the selection of a transition device. *J. Fluid Mech.* **3**, 373-384.
- [172] PURTELL, L.P. 1992 Turbulence in complex flows. *AIAA* 92-0435.
- [173] PUI, N.K. & GARTSHORE, I.S. 1979 Measurements of the growth rate and structure in plane turbulent mixing layers. *J. Fluid Mech.* **91**, 111-130.
- [174] PURTELL, L.P., KLEBANOFF, P.S. & BUCKLEY, F.T. 1981 Turbulent boundary layers at low Reynolds numbers. *Phys. Fluids* **24**, 802–811.
- [175] RODI, W. 1975 A review of experimental data of uniform-density free turbulent boundary layers, in *Studies in Convection*, Vol. 1, ed. B.E. Launder. Academic.
- [176] ROGALLO, R.S. 1981 Numerical experiments in homogeneous turbulence. *NASA Tech. Memo.* 81315.

- [177] RO GALLO, R.S. & MOIN, P. 1984 Numerical simulations of turbulent flows. *Ann. Rev. Fluid Mech.* **16**, 99–137.
- [178] ROGERS, M.M. & MOIN, P. 1987 The structure of the vorticity field in homogeneous turbulent flows. *J. Fluid Mech.* **176**, 33–66.
- [179] ROGERS, M.M. & MOSER, R.D. 1992 The three-dimensional evolution of a plane mixing layer: the Kelvin-Helmholtz rollup. *J. Fluid. Mech.* **243**, 183–226.
- [180] D. ROTMAN 1991 Shock wave effect on a turbulent flow. *Phys. Fluids* **A3** (7), 1792–1806.
- [181] RUETSCH, G.R. & MAXEY, M.R. 1991 Small scale features of vorticity and passive scalar fields in homogeneous isotropic turbulence. *Phys. Fluids* **A 3**, 1587–1597.
- [182] RUTLEDGE, J. & SLEICHER, C.A. 1993 Direct simulation of turbulent flow and heat transfer in a channel. part i: Smooth walls. *Int. J. Num. Meth. Fluids* **16**, 1051–1078.
- [183] SABIN C.M. 1965. An analytic and experimental study of a plane, incompressible, turbulent shear layer with arbitrary velocity ratio and pressure gradient. *Trans. ASME J. Basic Engg.* **87**, 421–428.
- [184] SAMIMY M. & LELE S.K. 1991 Motion of particles with inertia in a compressible free shear layer. *Phys. Fluids*, **3** A, 1915–1923.
- [185] SAMIMY, M., REEDER, M.F. & ELLIOTT, G.S. 1992. Compressibility effects on large structures in free shear flows, *Phys. Fluids* **4** A, 1251–1258.
- [186] SARIC, W. S. (ED.) 1996. Turbulent boundary Layers in subsonic and supersonic flow. *AGARDO-GRAPH* **335**.
- [187] SARKAR, S. 1995 The stabilising effect of compressibility in turbulent shear flow. *J. Fluid Mech.* **282**, 163–186.
- [188] SCHUMANN, U. 1975 Subgrid-scale model for the finite-difference simulations of turbulent flows in plane channels and annuli, *J. Comput. Phys.* **18**, 376–404.
- [189] SCHUMANN, U. & FRIEDRICH, R. 1987 On direct and large-eddy simulation of turbulence, in *Advances in turbulence* (G. Comte-Bellot & J. Mathieu, eds.), Springer. pp. 88–104.
- [190] SHILOH, K., SHIVAPRASAD, B. G. & SIMPSON, R. L. 1981c The structure of a separating turbulent boundary layer. Part 3. Transverse velocity measurements. *J. Fluid Mech.* **113**, 75–90.
- [191] SIMMONS, L.F.G. & SALTER, C. 1934 Experimental investigation and analysis of the velocity variations in turbulent flow. *Proc. Roy. Soc. A* **145**, 212–234.
- [192] SIMPSON, R.L., CHEW, Y.T. & SHIVAPRASAD, B.G. 1981a The structure of a separating turbulent boundary layer. Part 1. Mean flow and Reynolds stresses. *J. Fluid Mech.* **113**, 23–52.
- [193] SIMPSON, R.L., CHEW, Y.T. & SHIVAPRASAD, B.G. 1981 The structure of a separating turbulent boundary layer. Part 2. Higher-order turbulence results. *J. Fluid Mech.* **113**, 53–74.
- [194] SMITH, R. W. 1994 *Effect of Reynolds Number on the Structure of Turbulent Boundary Layers*. Ph. D. thesis, Dept. of Aerospace and Mech. Engg, Princeton University, Ref. number 1984-T.
- [195] SMITS, A.J. & DUSSAUGE, J.P. 1996. Turbulent shear layers in supersonic flows. *AIP Press, NY*.
- [196] SMITS, A.J. & WOOD, D.H. 1985 The Response of Boundary Layers to Sudden Perturbations, *Ann. Rev. Fluid Mech.* **17**, 321–358.
- [197] SPALART, P.R. 1986 Numerical study of sink-flow boundary layers. *J. Fluid Mech.* **172**, 307–328.
- [198] SPALART, P.R. 1988 Direct numerical study of a turbulent boundary layer up to $Re_\theta = 1410$. *J. Fluid Mech.* **187**, 61–98.
- [199] SPALART, P.R. & COLEMAN, G.N. 1997 Numerical study of a separation bubble with heat transfer. *Europ. J. Mech. B* **16**, 169–189.
- [200] SPALART, P.R., MOSER, R.D. & ROGERS, M.M. 1991 Spectral methods for the Navier-Stokes equations with one infinite and two periodic directions, *J. Comp. Phys.* **96**, 297–324.
- [201] SPALART, P.R. & WATMUFF, J.H. 1993 Experimental and numerical investigation of a turbulent boundary layer with pressure gradients. *J. Fluid Mech.* **249**, 337–371.
- [202] SPEZIALE, C.G. & BERNARD, P.S 1992 The energy decay in self-preserving isotropic turbulence revisited. *J. Fluid Mech.* **241**, 645–667.
- [203] SQUIRE, K.D. & PIOMELLI, U. 1993 Large-eddy simulation of rotating turbulence using the dynamic model. In *Proc. 9th Symposium Turbulent Shear Flow, Tokyo*.
- [204] SREENIVASAN, K.R. 1985 The effect of contraction on a homogeneous turbulent shear flow. *J. Fluid Mech.* **154**, 187–213.
- [205] TAFTI, D.K. & VANKA, S.P. 1991 A numerical study of the effects of spanwise rotation on turbulence channel flow. *Phys. Fluids A* **3**, 642.
- [206] TAVOULARIS, S., BENNETT, J.C. & CORRISIN, S. 1978 Velocity-derivative skewness in small Reynolds number, nearly isotropic turbulence. *J. Fluid Mech.* **88**, 63–69.

- [207] TAVOULARIS, S. & CORRSIN, S. 1981a Experiments in a nearly homogeneous shear flow with a uniform mean temperature gradient. Part 1. *J. Fluid Mech.* **104**, 311-347.
- [208] TAVOULARIS, S. & CORRSIN, S. 1981b Experiments in a nearly homogeneous shear flow with a uniform mean temperature gradient. Part 2. The fine structure. *J. Fluid Mech.* **104**, 349-367.
- [209] TAVOULARIS, S. & CORRSIN, S. 1987. The structure of a turbulent shear layer embedded in turbulence *Phys. Fluids* **30**, 3025-3033.
- [210] TAVOULARIS, S. & KARNIK, U. 1989 Further experiments on the evolution of turbulent stresses and scales in uniformly sheared turbulence. *J. Fluid Mech.* **204**, 457-478.
- [211] TEISSEDE, C. & DANG, K. 1988 128^3 harmonics direct numerical simulation of homogeneous rotated turbulence. *2nd. Europ. Turbulence Conf* Berlin. *ONERA Rep.* **1990-7**.
- [212] THOMAS, P., BÜTEFISCH, K.-A. & SAUERLAND, K. 1993 On the motion of particles in a fluid under the influence of a large velocity gradient. *Experiments in Fluids* **14**, 42-48.
- [213] TOONDER, J.M.J. 1995 *Drag reduction by polymer additives in a turbulent pipe flow: laboratory and numerical results*. Ph. D. thesis, Delft University of Technology.
- [214] TOWNSEND, A.A. 1954 The uniform distortion of homogeneous turbulence. *Quart. J. Mech. Appl. Math.* **7**, 104-127.
- [215] TRITTON, D.J. 1992 Stabilization and destabilization of turbulent shear flow in a rotating fluid. *J. Fluid Mech.* **241**, 503.
- [216] TUCKER, H.J. & REYNOLDS, A.J. 1968 The distortion of turbulence by irrotational plane strain. *J. Fluid Mech.* **32**, 657-673.
- [217] VEERAVALLI, S. & WARHAFT, Z. 1989. The shearless turbulence mixing layer. *J. Fluid Mech.* **207**, 191-229.
- [218] VEERAVALLI, S. & WARHAFT, Z. 1990 Thermal dispersion from a line source in the shearless turbulence mixing layer. *J. Fluid Mech.* **216**, 35-70.
- [219] VINCENT, A. & MENEGUZZI, M. 1991 The spatial structure and statistical properties of homogeneous turbulence. *J. Fluid Mech.* **225**, 1-25.
- [220] WATMUFF, J.H. 1990 An experimental investigation of a low Reynolds number turbulent boundary layer subject to an adverse pressure gradient. *1989 Ann. Res. Briefs*, CTR, Stanford, pp. 37-49.
- [221] WEBSTER, D.R., DEGRAAFF, D.B. & EATON, J.K. 1996 Turbulence Characteristics of a Boundary Layer Over a Two-Dimensional Bump, *J. Fluid Mech.* **320**, 53-69.
- [222] WEI, T. & WILLMARTH, W.W. 1989 Reynolds-number effects on the structure of a turbulent channel flow. *J. Fluid Mech.* **204**, 57-95.
- [223] WIGELAND, R.J. & NAGIB, H.M. 1978 Grid generated turbulence with and without rotation about the streamwise direction. *ITT Fluids & Heat transfer Rep.* R. 78-1, Illinois Institute of Technology.
- [224] WYGNANSKI, I. & CHAMPAGNE, F.H. 1973 On transition in a pipe: Part I. The origin of puffs and slugs and the flow in a turbulent slug. *J. Fluid Mech.* **59**, 281-335.
- [225] WYGNANSKI, I. & FIEDLER, H.E. 1969. Some measurements in the self-preserving jet. *J. Fluid Mech.* **38**, 577-612.
- [226] WYGNANSKI, I. & FIEDLER, H.E. 1970. The two-dimensional mixing region, *J. Fluid Mech.* **41**, 327-361.
- [227] YOKOSAWA, H., FUJITA, H., HIROTA, M. & IWATA, S. 1989 Measurement of turbulent flow in a square duct with roughened walls on two opposite sides. *Intl. J. Heat and Fluid Flow* **10** no. 2, 125.
- [228] ZAGAROLA, M. 1996 *Mean-flow scaling of turbulent pipe flow*. Ph. D. thesis, Department of Aerospace and Mechanical Engineering, Princeton University, Reference number 2053-T.

Data Sheets for:
Chapter 3.- Homogeneous Flows

HOM00: Decaying Grid Turbulence

Comte-Bellot & Corrsin

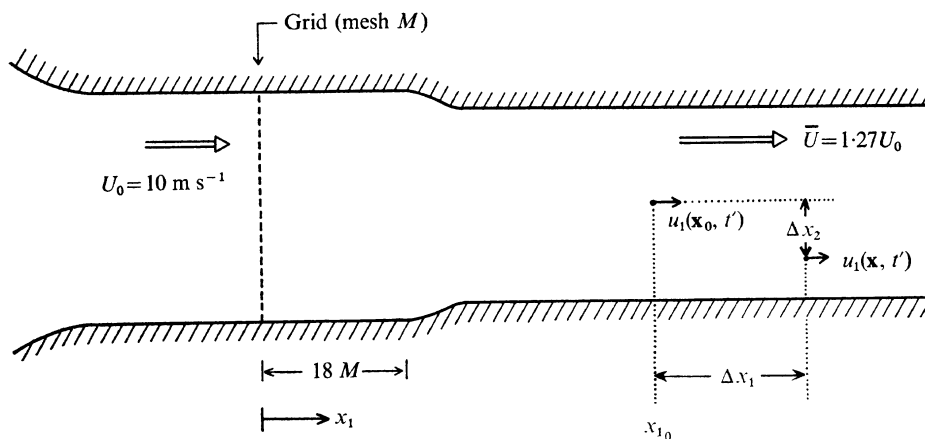
1. Description of the flow

Decaying, nearly isotropic, turbulent flow downstream of a grid.

2. Geometry

The grids were periodic arrays of square rods, in a biplanar arrangement, and had a square mesh with a solidity of 0.34. The grid was inserted across a rectangular (1.37 m × 1.03 m) section, followed by a 1.27:1 contraction (to improve the isotropy of the turbulence) and a rectangular (1.22 m × 0.915 m) measurement section.

3. Original sketch



4. Flow characteristics

The mean speed across the wind tunnel was uniform. The turbulence was very nearly isotropic, with the ratio of streamwise, u_1' , and transverse, u_2' , r.m.s. velocities in the range 0.97 to 0.98. The decay of both mean square components could be well described by a power law.

5. Flow parameters

Grid mesh size $M = 50.8 \text{ mm}$ or 25.4 mm . Mean speed $U_0 = 10.0 \text{ m/s}$ near the grid, increasing to 12.7 m/s after the contraction. Grid Reynolds number $R_M = U_0 M / \nu = 34,000$ or $17,000$.

6. Inflow and outflow boundary and initial conditions

Free stream turbulence level (without the grid) was about 0.05%.

7. Measurements

(a) Measurement procedures

All measurements were made with hot-wires and analog instrumentation. A narrow-band filter was used for measuring spectra. An analog tape recorder was used for measuring autocorrelations.

(b) Measured quantities

Streamwise and transverse r.m.s. velocities along the test section. Autocorrelation functions of the velocity; two-point transverse correlations; space-time correlations. Narrow-band autocorrelation functions in a convected frame. Spectrally local characteristic times. Frequency spectra, from which one-dimensional and three-dimensional (wave-number) energy spectra are estimated.

(c) **Measurement errors**

Spectral measurements were corrected for noise. Spectral uncertainty is difficult to estimate because of the analog methods used. Estimated uncertainty is a few percent at the lower and intermediate frequencies, increasing at the highest frequencies. The latter range should be treated with some caution, as it is known to lead to unrealistically large velocity derivative skewness (GEORGE, W.K. 1992, *Phys. Fluids A* **4**, 1492- 1509).

8. **Available variables**

One-dimensional, wave-number spectra of streamwise velocity for the $M = 50.8mm$ grid at three stations with $tU_o/M = 42, 98$ and 171 . At these locations, $R_\lambda = 71.6, 65.3$ and 60.7 .

9. **Storage size required and present format of the data**

One small file in ASCII format.

10. **Contact person**

Professor Geneviève Comte-Bellot
Centre Acoustique, Ecole Centrale de Lyon, B.P. 163, 69131 Ecully Cedex, France
tel: 3304 72186010
fax: 3304 72189143
e-mail: gcb@mecaflu.ec-lyon.fr

11. **Main references**

COMTE-BELLOT, G. & CORRISIN, S. 1966 The use of a contraction to improve the isotropy of grid-generated turbulence *J. Fluid Mech.* **25**, 657-682.

COMTE-BELLOT, G. & CORRISIN, S. 1971 Simple Eulerian time correlations of full and narrow-band velocity signals in grid-generated isotropic turbulence, *J. Fluid Mech.* **48**, 273-337.

HOM01: Decaying Grid Turbulence

Ferchichi & Tavoularis

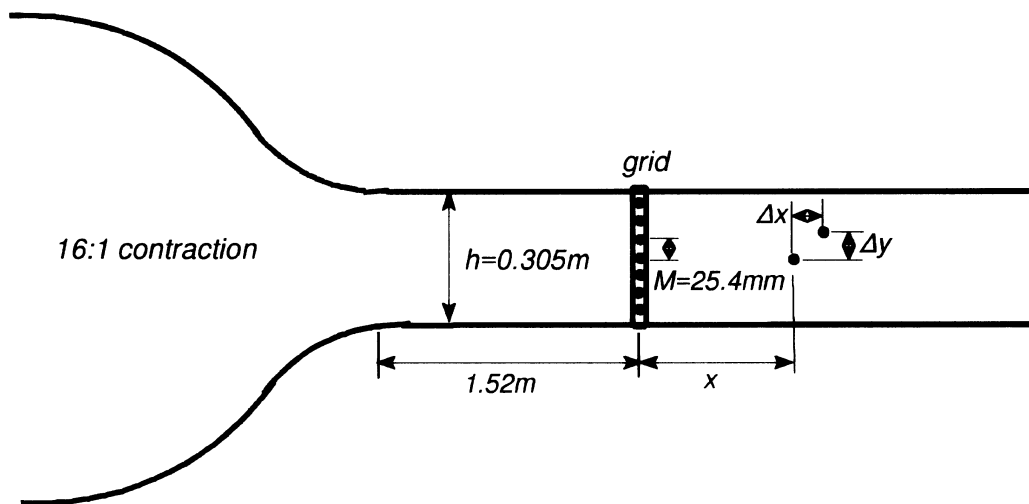
1. Description of the flow

Decaying, nearly isotropic, turbulent flow downstream of a grid.

2. Geometry

The grid consisted of 11 horizontal and parallel cylindrical rods and had a solidity of 0.34. It was placed in a rectangular (305 mm x 457 mm) test section, 1.52 m downstream of a 16:1 contraction.

3. Original sketch



4. Flow characteristics

The mean speed across the tunnel was uniform. The turbulence was nearly isotropic, with the ratio of the streamwise, u' , and the transverse, v' , r.m.s. velocities about 95%. The decay of the turbulence intensity was described by a power law with an exponent of -1.21.

5. Flow parameters

The grid mesh size was $M = 25.4\text{mm}$. The mean speed along the centreline was $\bar{U} = 10.5\text{m/s}$. The grid Reynolds number was $Re_M = \bar{U}M/\nu = 17335$.

6. Inflow and outflow boundary and initial conditions

Turbulence intensity in the unobstructed flow was less than 0.05%.

7. Measurements

(a) Measurement procedure

Two sets of hot-wire measurements were performed, the first with a cross-wire probe and the second with a parallel wire probe. Spectra were measured with a single wire probe.

(b) Measured quantities

Probability density functions of streamwise and transverse velocity differences, $\Delta u(\Delta x)$, $\Delta v(\Delta x)$ and $\Delta u(\Delta y)$ at a position with $x/M = 47.2$, where $u' = 0.320\text{m/s}$, $L = 38\text{mm}$, $\lambda = 4.1\text{mm}$, $Re_\lambda = u'\lambda/\nu = 84$ and $\eta = 0.23\text{mm}$. Energy spectra of the streamwise velocity.

(c) **Measurement errors** Because of the large volume of data used, the uncertainty of the pdf would be very small, at least for the inertial range data.

8. **Available variables**

Pdf of velocity differences at different probe spacings. Energy spectrum of the streamwise velocity.

9. **Storage size and present format of data**

Small files in ASCII format.

10. **Contact person**

Professor Stavros Tavoularis
Department of Mechanical Engineering, University of Ottawa
Ottawa, Ontario, Canada K1N 6N5
tel/fax: (613) 562 5800 ext. 6271
e-mail: tav@eng.uottawa.ca

11. **Main reference**

FERCHICHI, M. & TAVOULARIS, S. 1997 Unpublished measurements.

HOM02: Decaying Isotropic Turbulence

Wray

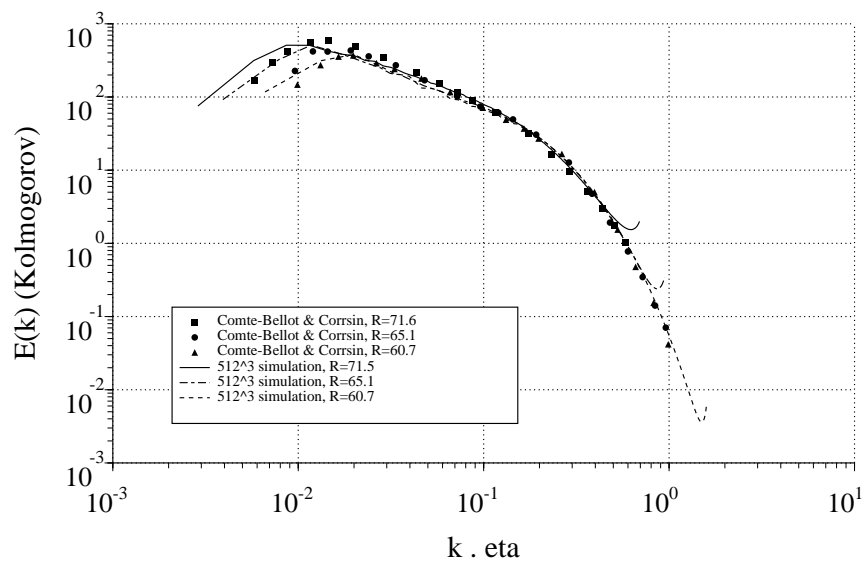
1. Description of the flow

Simulation of incompressible decaying isotropic turbulence.

2. Geometry

Triply periodic mesh.

3. Sketch



4. Flow characteristics

Time-decaying homogeneous analog of the grid-turbulence experiments of Comte-Bellot & Corrsin (1971).

5. Flow parameters

$$58.32 \leq Re_\lambda \leq 104.5$$

6. **Numerical methods and resolution:** Numerical scheme as in (Rogallo, 1981). 512^3 collocation points. Largest computational wavenumber, $k_{max} = 241$.

7. Boundary and initial conditions

Periodic boundary conditions in all three spatial directions. The initial field has a spectrum peaked at $k = 6$ (where the lowest mode is $k = 1$), and random phases, at $Re_\lambda = 952$.

8. Averaging procedures and resulting uncertainties

Statistics post-processed using the same spectral basis functions used to advance the Navier–Stokes equations in time.

9. Available variables

Filtered velocity field in physical space at $Re_\lambda = 104.5$, derived from the full 512^3 field by sharp truncation in k -space to 128^3 .

Time history of total energy, enstrophy, integral-scale, and velocity-derivative skewness.

3-d energy and transfer spectra and 1-d energy spectra at 26 times in the given Re_λ range.

Pdf of velocity differences at $Re_\lambda = 70.45, 65.11, 60.41$

10. Storage size required and present format of the data

25 Mbytes of IEEE binary, single precision floating point data for the restart file. A few Kbytes ASCII data for the statistics.

11. Contact person

Dr. A.A. Wray
NASA Ames Research Centre, Moffett Field, Ca. 94035, USA.
E-mail: wray@nas.nasa.gov

12. Main references

COMTE-BELLOT, G. & CORRISIN, S. 1971 Simple Eulerian time correlations of full and narrow-band velocity signals in grid-generated isotropic turbulence, *J. Fluid Mech.* **48**, 273-337.

ROGALLO, R.S. 1981 Numerical experiments in homogeneous turbulence. *NASA Tech. Memo.* 81315.

HOM03: Forced Isotropic Turbulence

Jiménez, Wray, Saffman & Rogallo

1. Description of the flow

Direct numerical simulations of forced isotropic turbulence in a periodic cubic box.

2. Geometry

Triply periodic box.

3. Original sketch: Not applicable.

4. Flow characteristics

Forced at low wave-numbers $k \leq 2.5$. Fully resolved $k_{max}\eta \approx 2$.

5. Flow parameters

Re_λ	N	L_ϵ	L_ϵ/λ	L_ϵ/η	L/L_ϵ	t/T	$-F_3$
37	64	1.8	2.3	27	1.09	54.2	0.49
62	128	2.2	4.2	65	0.80	9.3	0.50
95	256	2.0	6.3	120	0.72	8.2	0.52
142	384	2.4	9.5	222	0.73	5.9	0.52
168	512	2.4	11.2	286	0.69	5.1	0.52

t/T is the total run time in eddy turnover units, F_3 is the skewness coefficient of the velocity derivatives, L is the integral scale and $L_\epsilon = u'^3/\epsilon$ is the eddy dissipation scale. The size of the computational box is 2π .

6. Numerical methods and resolution

The numerical method is fully spectral, using primitive variables \mathbf{u} , p , with dealiasing achieved by spherical wave-space truncation and phase shifting (Rogallo 1981). The resolution N given in the table above reflects the number of real Fourier modes in each direction before dealiasing. The largest computational wavenumber is $k_{max} = \sqrt{2}N/3$. The time stepping is a second order Runge-Kutta for the nonlinear terms and an analytic integrating factor for the viscous ones. The time step is automatically controlled to satisfy the numerical stability condition. All fields are forced to achieve a statistically steady state by introducing a negative viscosity coefficient for all the modes with wave numbers $k = |\mathbf{k}| \leq 2.5$. The Fourier expansion functions are $\exp(\pm i k_j x_j)$, $k_j = 0, 1, \dots, K = N/2$, so that the length of the box side is always 2π . The magnitude of the negative viscosity is adjusted every few time steps so as to keep constant the product $K\eta$, where η is the Kolmogorov scale, and the instantaneous energy dissipation rate, ϵ , is computed in terms of the energy spectrum.

7. Boundary and initial conditions

Periodic boundary conditions in all three spatial directions. Initial conditions are not relevant, since the flow is driven to statistically steady state.

8. Averaging procedures and resulting uncertainties

Statistics post-processed using the same spectral basis functions used to advance the Navier–Stokes equations in time.

Numerical errors are less than 2%, checked by grid refinement at the lower Reynolds numbers. Statistical convergence errors are about $\pm 5\%$ for large scale quantities, but grow to half an order of magnitude for the extreme tails of the pdf of the gradients.

9. Available variables

3-d and 1-d energy spectra.

Pdf of longitudinal and transverse velocity-differences at the five Reynolds numbers, for separations in the inertial range. Pdf for flow fields filtered with several Gaussian filters, at $Re_\lambda = 142$.

Pdf of velocity gradients, enstrophy, total strain and vorticity stretching.

One restart field at $Re_\lambda = 96$, spectrally truncated to 32^3 resolution.

10. **Storage size required and present format of the data:** About 400 Kb of binary data for the restart file, and 400 Kbytes as ASCII data for the statistics.

11. **Contact person**

Javier Jiménez

School of Aeronautics, U. Politécnica, 28040 Madrid, Spain.

E-mail: jimenez@torroja.dmt.upm.es

12. **Main references**

JIMÉNEZ, J., WRAY, A.A., SAFFMAN, P.G. & RO GALLO, R.S. 1993 The structure of intense vorticity in isotropic turbulence, *J. Fluid Mech.* **255**, 65-90.

JIMÉNEZ, J. & WRAY, A.A. 1994 On the dynamics of small-scale vorticity in isotropic turbulence, in *Annual Res. Briefs*, Centre for Turbulence Research, Stanford CA, pp. 287-312.

RO GALLO, R.S. 1981 Numerical experiments in homogeneous turbulence. *NASA Tech. Memo.* 81315.

HOM04: Grid Turbulence with Plane Strain

Tucker & Reynolds

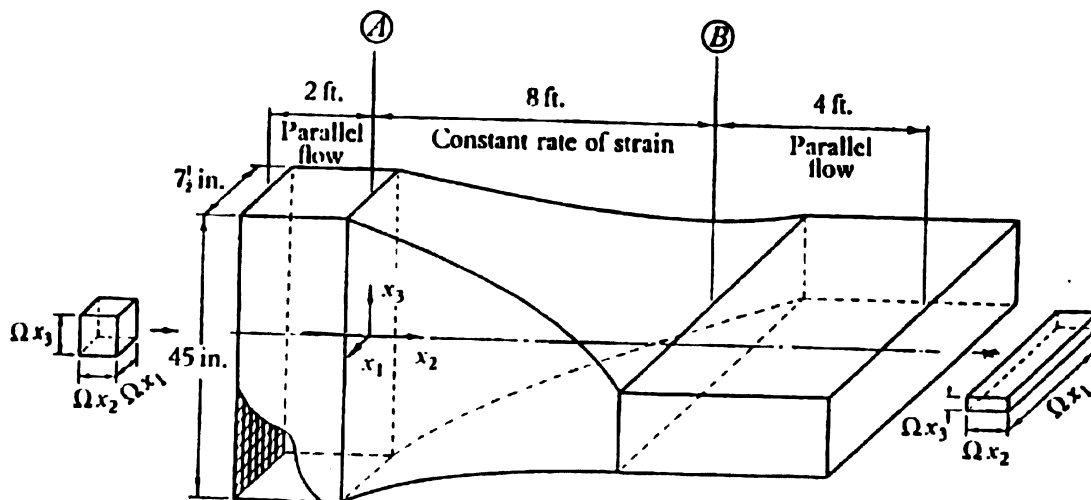
1. Description of the flow

Grid-generated, nearly isotropic turbulence is subjected to uniform strain by passing through a distorting duct.

2. Geometry

The facility used was a suction wind-tunnel with a rectangular cross-section of varying shape but constant cross-sectional area. A perforated metal plate with a square mesh was used as a grid. The flow entered, through the grid, into a parallel section, from which it passed successively into a distorting section and, finally, into another parallel section, where the strained turbulence relaxed towards isotropy.

3. Original sketch



4. Flow characteristics

The turbulence entering the distorting section contained considerable anisotropy, with the streamwise mean square velocity having 42% of the total turbulent kinetic energy.

5. Flow parameters

The grid mesh size was $M = 17.5\text{mm}$ and the solidity was $\sigma = 0.36$. The mean speed in the uniform section was $U_o = 6.1\text{ m/s}$.

6. Inflow and outflow boundary and initial conditions

Without the grid, the free stream turbulence level was 0.2%. The distorting duct was positioned at a distance of $35M$ from the grid.

7. Measurements

(a) Measurement procedures

The streamwise velocity was measured with a single hot-wire, normal to the flow. The transverse velocities were measured with a single hot-wire, slanted at 45° with respect to the flow direction.

(b) Measured quantities

Mean squared velocities in the streamwise, transverse and lateral directions.

(c) **Measurement errors** Possible uncertainty (95% confidence level) of 2% for the mean velocity, 4% for the streamwise Reynolds stress and 8% for the transverse and lateral Reynolds stresses.

8. **Available variables** Mean squared velocities in the streamwise, transverse and lateral directions.
9. **Storage size required and present format of the data**
Small ASCII file. Notice that x_2 is the streamwise direction.
10. **Contact person**
Not available.
11. **Main reference**
TUCKER, H.J. & REYNOLDS, A.J. 1968 The distortion of turbulence by irrotational plane strain *J. Fluid Mech.* **32**, 657-673.

HOM05: Grid Turbulence with Transverse Strain

Leuchter & Benoit

1. Flow description

Transverse strain at constant rate D is created in planes perpendicular to the flow direction. The flow is defined (in the laboratory axes) by the following non-zero elements of the strain rate matrix:

$$\frac{\partial U_2}{\partial x_3} = \frac{\partial U_3}{\partial x_2} = D \quad (1)$$

With this definition, the principal axes are inclined by 45 deg. with respect to the laboratory frame in which the measurements are performed. Note that in the principal axes the flow would be defined by:

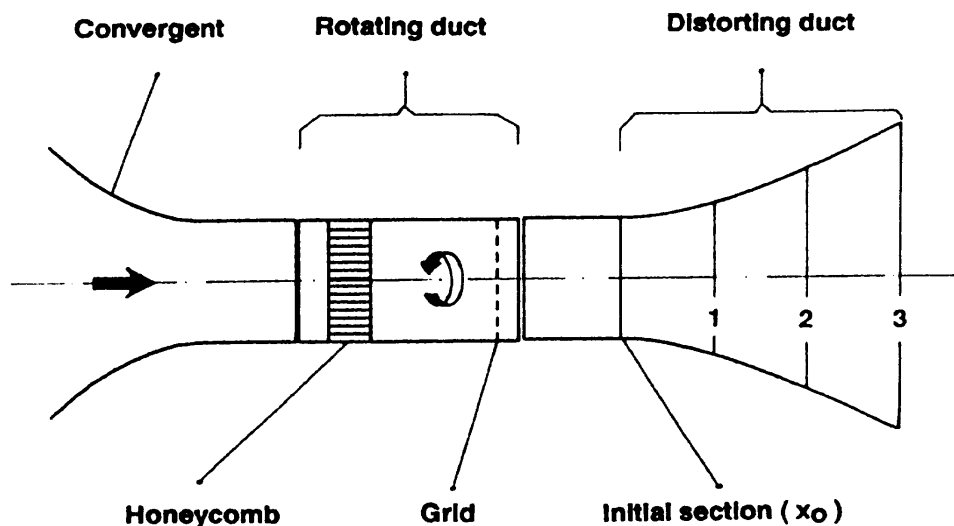
$$\frac{\partial U_2}{\partial x_2} = -\frac{\partial U_3}{\partial x_3} = D \quad (2)$$

with the other gradients zero. Satisfactory homogeneity conditions are achieved in this flow.

2. Geometry

The flow enters through a cylindrical duct of 0.3 m diameter into the distorting duct. The grid turbulence generator (of 1.5 cm mesh size) is located in the cylindrical duct 0.25 m upstream of the distorting duct. The distorting duct has elliptical cross sections of constant area with continuously increasing eccentricity and fixed orientation (of 45 deg. with respect to the laboratory axes). The maximum value of the aspect ratio a/b of the elliptical sections is 8.0 in the exit plane of the duct, corresponding to a non-dimensional time Dt of 1.04. The length of the distorting duct is $L = 0.66$ m.

3. Original sketch



4. Flow characteristics

The flow is initially homogeneous and slightly anisotropic (see below). The axial velocity remains constant during the straining process and transverse homogeneity is conserved in the central part of the flow remote from the walls. The turbulence becomes progressively anisotropic under the effect of the strain. The anisotropization is represented here by the growth of the transverse correlation coefficient $\overline{v'w'}/v'w'$, close to that observed in the transverse-shear flow (test case HOM20).

5. Flow parameters

- * Axial velocity: $U = 10 \text{ m/s}$,
- * Strain rate: $D = 15.8 \text{ s}^{-1}$.

6. Inflow conditions

”Nominal” initial conditions (at $x = 0$ and for $U = 10 \text{ m/s}$) are:

- * kinetic energy: $q^2/2 = 0.283 \text{ m}^2/\text{s}^2$,
- * anisotropy: $(\overline{u^2} - \frac{1}{2}(\overline{v^2} + \overline{w^2}))/q^2 = 0.155$,
- * dissipation rate: $\epsilon = 17.5 \text{ m}^2/\text{s}^3$,
- * longitudinal integral lengthscale: $L_u = 6.4 \times 10^{-3} \text{ m}$,
- * transverse integral lengthscale: $L_v = 2.4 \times 10^{-3} \text{ m}$,
- * Taylor microscale: $\lambda = \sqrt{5\nu q^2/\epsilon} = 1.55 \times 10^{-3} \text{ m}$,
- * Kolmogorov lengthscale: $\eta = (\nu^3/\epsilon)^{1/4} = 0.12 \times 10^{-3} \text{ m}$,
- * microscale Reynolds number: $Re_\lambda = \sqrt{q^2/3} \lambda/\nu = 45.2$.

The initial section $x = 0$ is located 0.25 m downstream of the turbulence grid.

7. Measured data

(a) Measurement procedure

Hot-wire methods using DISA (DANTEC) anemometers 55M01 and crossed-wire probes of type P61. Digital data processing of 100×2048 simultaneous samples for both velocity components. Four angular positions of the probe are considered to resolve the four non-zero Reynolds-stress components.

The measurements are made in 13 equidistant positions on the axis of the duct between the initial section $x = 0$ and the exit section $x = L = 0.66 \text{ m}$.

(b) Measured quantities

- axial mean velocity component U ,
- transverse mean velocity components V and W (negligible compared to U),
- Reynolds stresses $\overline{u^2}$, $\overline{v^2}$, $\overline{w^2}$, \overline{vw} ,
- spectra of the three velocity components,
- lengthscales $L_u (= L_{11,1})$, $L_v (= L_{22,1})$ and $L_w (= L_{33,1})$, deduced from the corresponding spectra.

(c) Measurement errors

Estimated to be of the order of one percent for the mean velocities and about a few percent for the turbulence quantities.

8. Available measurements

The results are displayed in a table with 11 columns corresponding to the following quantities:

- longitudinal position x (m),
- non-dimensional time Dt ,
- axial mean velocity component U (m/s),
- Reynolds stresses $\overline{u^2}$, $\overline{v^2}$, $\overline{w^2}$, \overline{vw} (m^2/s^2),
- dissipation rate ϵ (m^2/s^3), evaluated from $\epsilon = -D\overline{vw} - \frac{1}{2}U[dq^2/dx]$.
- lengthscales $L_u (= L_{11,1})$, $L_v (= L_{22,1})$ and $L_w (= L_{33,1})$ (m).

9. Size and present format of data

Small ASCII file.

10. Contact person

O. Leuchter
ONERA
8 rue des Vertugadins
F 92190 Meudon, France
e-mail: leuchter@onera.fr

11. Main references

LEUCHTER, O. & BENOIT, J.P. 1991 Study of coupled effects of plane strain and rotation on homogeneous turbulence *Eighth Symposium on Turbulent Shear Flows*, Munich.

LEUCHTER, O. 1993 Turbulence homogène soumise à des effets couplés de rotation et de déformation plane ou axisymétrique *Internal ONERA Report 15/1145AY*.

HOM06: Grid Turbulence with Successive Plane Strains

Gence & Mathieu

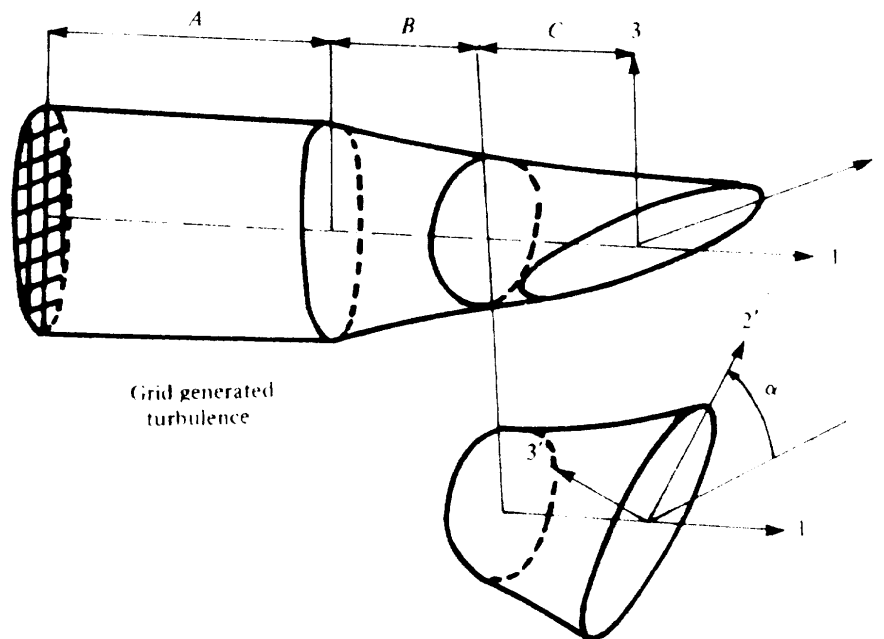
1. Description of the flow

Grid turbulence was first subjected to plane strain until its principal Reynolds stresses were aligned with the principal strain rate and then it was subjected to another plane strain but with a different orientation of principal axes.

2. Geometry

Uniform flow passed through a grid with a square mesh size, $M = 35$ mm, in an elliptical duct with axes lengths $0.3m$ and $0.075m$ and a length $x_1/M = 40$. Then, it entered a first distorting duct section, with a length of 0.4 m and an elliptical cross-section whose axis ratio diminished monotonically until it reached unity (circular shape). Finally, the flow entered a second distorting section, also with an elliptical cross-section and a length of $0.4m$, which, starting from a circular shape, ended-up to a shape identical to that at the entrance of the previous section. The final section could be rotated about the streamwise axis; results are reported for angles $\alpha = 0$ (corresponding to final section axes normal to those in the previous section, thus resulting in pure plane strain throughout both distorting sections), $\pi/8$, $\pi/4$, $3\pi/8$ and $\pi/2$.

3. Original sketch



4. Flow characteristics

The mean velocity and the magnitude of the mean strain rate were approximately maintained constant throughout the test section. The turbulence kinetic energy decayed in the first distorting section but, depending on the value of the angle α , it decayed ($\alpha = 3\pi/8$ and π) or grew ($\alpha = 0$, $\pi/8$ and $\pi/4$) in the second section. At the exit of the first distorting section, the principal axes of the Reynolds stress tensor became aligned with those of the local mean strain rate tensor and then evolved, depending on the orientation of the final section, without, however, reaching perfect alignment with the local mean strain axes at the duct's exit.

5. Flow parameters

The mean velocity was 18.6 m s^{-1} . The mean strain rate was 32.2 s^{-1} .

6. Inflow and outflow boundary and initial conditions

The trace of the Reynolds stress tensor at the entrance of the distorting duct was $\overline{q_o^2} = 0.43 \text{ m}^2 \text{ s}^{-2}$.

7. Measurements

(a) Measurement procedures

The mean velocity and the Reynolds stresses were measured with hot-wire anemometers. Shear stresses on transverse planes were measured by rotating single wires at different orientations with respect to the flow direction.

(b) Measured quantities

Apparently all Reynolds stresses were measured, but reported are only the evolutions of the turbulent kinetic energy, the main anisotropies and the principal stress angles.

(c) Measurement errors

Typical uncertainty (95% confidence level) is estimated to be $\pm 2\%$ for the mean velocity, $\pm 4\%$ for the streamwise normal stress and $\pm 8\%$ for the other stresses.

8. Available variables

All tabulated data have been presented vs. the dimensionless streamwise distance x_1/L ($L = 0.8m$ is the length of the entire distorting section), for different values of the angle α . Available variables are $\overline{q^2}/\overline{q_o^2}$, the anisotropies b_{22} and b_{33} , the invariant $b_{ik}b_{ki}$ and the angle, ϕ , between the principal axes of the Reynolds stress tensor and the strain rate tensor.

9. Storage size required and present format of the data

Small files in ASCII format.

10. Contact person

Professor J.N. Gence
Ecole Centrale de Lyon
B.P. 163, 69131 Ecully Cedex, France

11. Main reference

GENCE, J.N. & MATHIEU, J. 1979 On the application of successive plane strains to grid-generated turbulence *J. Fluid Mech.* **93**, 501-513.

HOM07: Return to Isotropy of Strained Grid Turbulence

Le Penven, Gence & Comte-Bellot

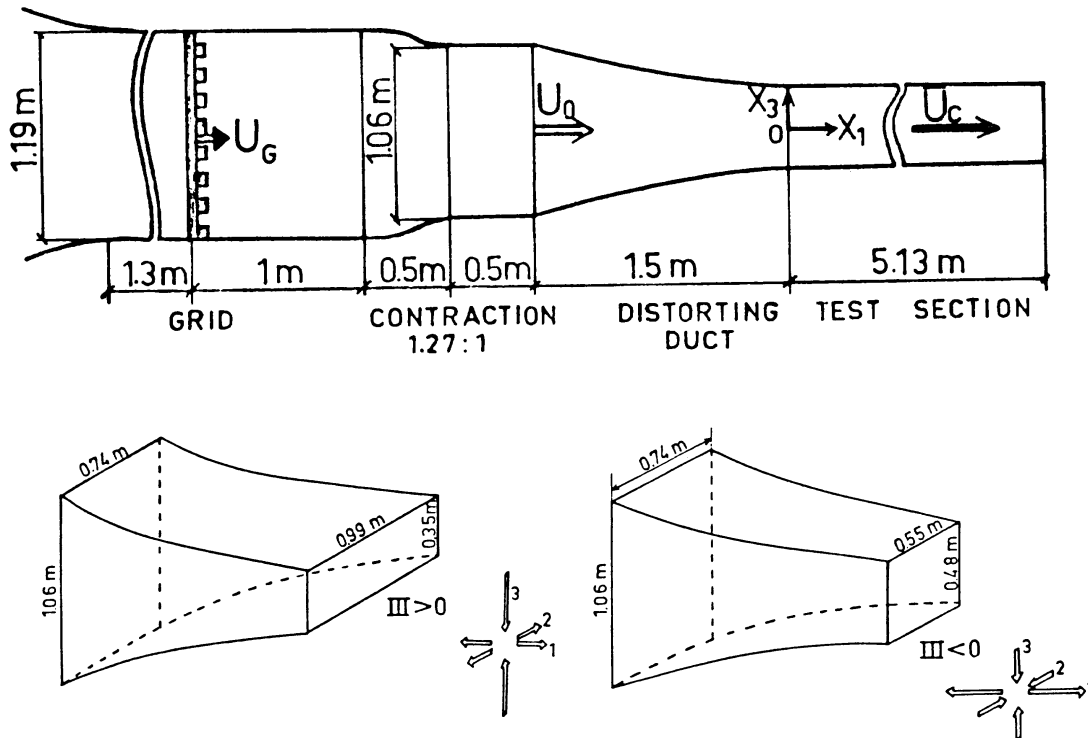
1. Description of the flow

Grid turbulence was first subjected to three-dimensional strain and then let to relax towards isotropy.

2. Geometry

Nearly isotropic turbulence was produced by a biplane grid with a square mesh size $M = 50.8\text{mm}$ and a solidity 0.33, followed by a 1.27:1 contraction. This flow entered one of two interchangeable distorting ducts, each with a length of 1.5m and a rectangular-shaped cross-section but both height and width changing continuously, so that a three-dimensional strain was imposed on the turbulence. Finally, the strained turbulence was let to relax back towards isotropy in a 5.13m long section with a uniform rectangular cross-section.

3. Original sketches



4. Flow characteristics

The objective of the experiment was to determine the rate of return towards isotropy of anisotropic turbulence, and particularly its dependence on the initial partition of the turbulence kinetic energy into its three components. The second and third invariants of the Reynolds stress anisotropy tensor, $b_{ij} = \overline{u_i u_j} / \overline{u_k u_k} - 1/3 \delta_{ij}$, are defined, respectively, as $II = b_{ij} b_{ij}$ and $III = b_{ik} b_{kj} b_{ji}$. The two distorting ducts were designed to give approximately equal values of II but opposite values of III at their exits. Because of the streamwise acceleration, both cases exhibited a streamwise Reynolds stress that was smaller than the two transverse ones. When $III > 0$, one of the transverse stresses was substantially larger than the other one, while, when $III < 0$, the two transverse stresses had comparable magnitudes. The rate of return of the turbulence structure towards isotropy was found to be larger when $III < 0$ than in the other case.

5. Flow parameters

The mean velocity at the entrance to the distorting duct was $U_o = 6.06\text{ms}^{-1}$ for $III > 0$ and 7.2ms^{-1} for $III < 0$. In both ducts the mean flow accelerated downstream.

6. Inflow and outflow boundary and initial conditions

The values of the Reynolds stresses and the turbulence kinetic energy at the entrance to the final straight duct have been provided in the data files.

7. Measurements

(a) Measurement procedures

The mean velocity and the Reynolds stresses were measured with standard cross-wire, hot-wire anemometers.

(b) Measured quantities

The three normal Reynolds stresses were measured, from which the turbulence kinetic energy and the second invariant were calculated.

(c) Measurement errors

Typical uncertainty (95% confidence level) is estimated to be $\pm 2\%$ for the mean velocity, $\pm 4\%$ for the streamwise normal stress and $\pm 8\%$ for the other stresses.

8. Available variables

The mean velocity in the distorting ducts has been presented vs. streamwise distance from the entrance. The three normal stresses in the final straight duct, the turbulence kinetic energy and the invariant II have been presented vs the elapsed time $t = \int 1/(\bar{U}_1)dx_1$, measured from some effective origin.

9. Storage size required and present format of the data

Small files in ASCII format.

10. Contact person

Professor J.N. Gence
Ecole Centrale de Lyon, B.P. 163, 69131 Ecully Cedex, France

11. Main reference

LE PENVEN, L., GENGE, J.N. & COMTE-BELLOT, G. 1985 On the approach to isotropy of homogeneous turbulence: effect of the partition of kinetic energy among the velocity components in *Frontiers in Fluid Mechanics*, S.H. Davis & J.L. Lumley (editors), Springer-Verlag.

HOM10: Rotating Decaying Turbulence

Jacquin, Leuchter, Cambon & Mathieu

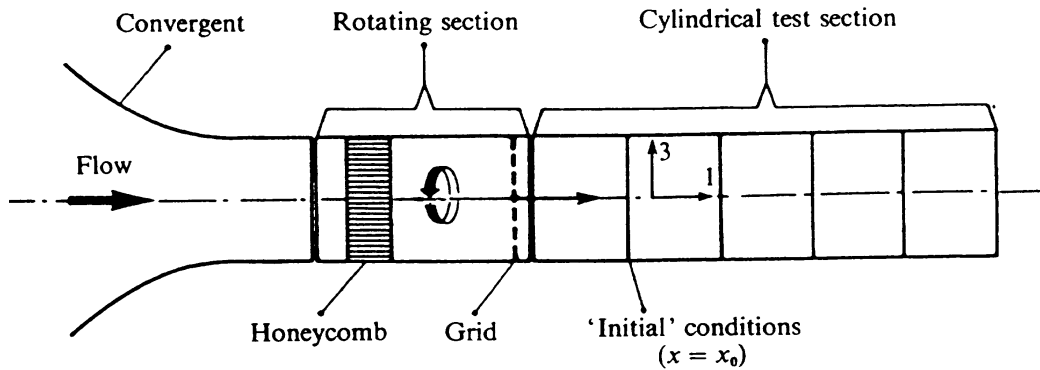
1. Flow description

Freely decaying homogeneous turbulence in solid-body rotation.

2. Geometry

Solid-body rotation is created by means of a rotating duct of 0.3 m in diameter equipped with a fine-mesh honeycomb and a grid turbulence generator. The nominal mesh size of the turbulence generator is 1.5 cm, but different mesh sizes (1 cm and 2 cm) have also been used. The flow is explored in a (fixed) cylindrical pipe of 0.3 m diameter and of 0.88 m length. The initial section is located 0.25 m downstream of the turbulence grid.

3. Original sketch



4. Flow characteristics

Homogeneous turbulence is subjected to solid-body rotation. The rotation slightly reduces the turbulent energy decay, compared to the non-rotating reference case (also included in the data). Rotation mainly affects the components normal to the rotation axis and produces a distinct anisotropization of the integral lengthscales.

5. Flow parameters

- * Axial velocity: 10 m/s,
- * Rotation rate: $\Omega = 0$ and 62.8 rd/s,
- * Rossby number $Ro = 2\epsilon/(\Omega q^2)$: ranging from 1.3 (upstream) to 0.13 (downstream).
- * Mesh size of the turbulence generator:
 - case A: $M = 1.0$ cm
 - case B: $M = 1.5$ cm
 - case C: $M = 2.0$ cm

6. Inflow conditions

'Nominal' initial conditions (at $x = 0$ and for $U = 10$ m/s, $\Omega = 0$) are given in table 1 for flow cases A, B and C. The initial section $x = 0$ is located 0.25 m downstream of the turbulence grid. The following parameters are considered in table 1:

- * kinetic energy: $q^2/2$,
- * anisotropy: $A/q^2 = (\overline{u^2} - \overline{v^2})/q^2$,
- * dissipation rate: ϵ ,
- * longitudinal integral lengthscale: L_u ,
- * transverse integral lengthscale: L_v ,

- * Taylor microscale: $\lambda = \sqrt{5\nu q^2/\epsilon}$,
- * Kolmogorov lengthscale: $\eta = (\nu^3/\epsilon)^{1/4}$,
- * microscale Reynolds number: $Re_\lambda = \sqrt{q^2/3}\lambda/\nu$.

Table 1: Inflow conditions

flow case	A	B	C
M (m)	0.01	0.015	0.02
$q^2/2$ (m^2/s^2)	0.149	0.264	0.466
A/q^2	0.04	0.17	0.17
ϵ (m^2/s^3)	11.6	16.1	31.7
L_u (m)	5.6×10^{-3}	6.4×10^{-3}	6.1×10^{-3}
L_v (m)	2.3×10^{-3}	2.4×10^{-3}	2.4×10^{-3}
λ (m)	1.4×10^{-3}	1.6×10^{-3}	1.5×10^{-3}
η (m)	0.13×10^{-3}	0.12×10^{-3}	0.10×10^{-3}
Re_λ	29.1	43.3	55.2

7. Measured data

(a) Measurement procedure

Hot-wire methods using DISA (DANTEC) anemometers 55M01 and crossed-wire probes of type P61. Digital data processing of 100×2048 simultaneous samples for both velocity components. Four-wire probes were also used.

The measurements are made in 10 positions on the axis of the duct between the initial section $x = 0$ and the exit section $x = L = 0.88$ m.

(b) Measured quantities

- axial mean velocity component U ,
- transverse mean velocity component V (negligible compared to U),
- Reynolds stresses $\overline{u^2}$ and $\overline{v^2}$,
- spectra of the three velocity components,
- lengthscales $L_u (= L_{11,1})$ and $L_v (= L_{22,1})$, deduced from the corresponding spectra.

(c) Measurement errors:

Estimated to be of the order of one percent for the mean velocities and about a few percent for the turbulence quantities.

8. Available measurements

The results are disposed in six tables with 8 columns corresponding to the following quantities:

- longitudinal position x (m),
- axial mean velocity component U (m/s),
- Reynolds stresses $\overline{u^2}$, $\overline{v^2}$, (m^2/s^2),
- trace of the Reynolds stress tensor q^2 (m^2/s^2), evaluated from $q^2 = \overline{u^2} + 2\overline{v^2}$,
- dissipation rate ϵ (m^2/s^3), evaluated from $\epsilon = -\frac{1}{2}U[dq^2/dx]$.
- lengthscales $L_u (= L_{11,1})$ and $L_v (= L_{22,1})$ (m).

The tables 1 to 6 correspond to the following cases:

- **Table 1:** Flow case A, $\Omega = 0$
- **Table 2:** Flow case A, $\Omega = 62.8$ rd/s
- **Table 3:** Flow case B, $\Omega = 0$
- **Table 4:** Flow case B, $\Omega = 62.8$ rd/s
- **Table 5:** Flow case C, $\Omega = 0$
- **Table 6:** Flow case C, $\Omega = 62.8$ rd/s

9. Size and present format of data

Small ASCII files.

10. Contact person

O. Leuchter
ONERA
8 rue des Vertugadins
F 92190 Meudon, France
e-mail: leuchter@onera.fr

11. Main references

LEUCHTER, O., JACQUIN, L. & GEFFROY, P. 1989 Etude expérimentale de la turbulence homogène en rotation. Confrontation avec un modèle EDQNM. *Internal ONERA Report 11/1145AY*.

JACQUIN, L., LEUCHTER, O., CAMBON, C. & MATHIEU, J. 1990 Homogeneous turbulence in the presence of rotation. *J. Fluid Mech.* **220**, 1-52.

HOM12: Rotating Turbulence with Axisymmetric Strain

Leuchter & Dupeuple

1. Flow description

Homogeneous turbulent flow in solid-body rotation is subjected to axisymmetric contraction with a constant strain rate. The flow distortion is defined by the following strain rate matrix:

$$\left(\frac{\partial U_i}{\partial x_j} \right) = \begin{pmatrix} D & 0 & 0 \\ 0 & -D/2 & -\Omega \\ 0 & \Omega & -D/2 \end{pmatrix} \quad (1)$$

where D is the strain rate and Ω the rotation rate which varies with time according to

$$\frac{\Omega}{\Omega_0} = e^{Dt} = \frac{U}{U_0} \quad (2)$$

Ω_0 is the initial rotation rate before the strain is applied (at time $t=0$), and U_0 the corresponding axial velocity.

2. Geometry

Solid-body rotation is created by means of a rotating duct of 0.3 m diameter equipped with a fine-mesh honeycomb and a grid turbulence generator of 1.5 cm mesh size. The geometry of the contracting duct is defined by:

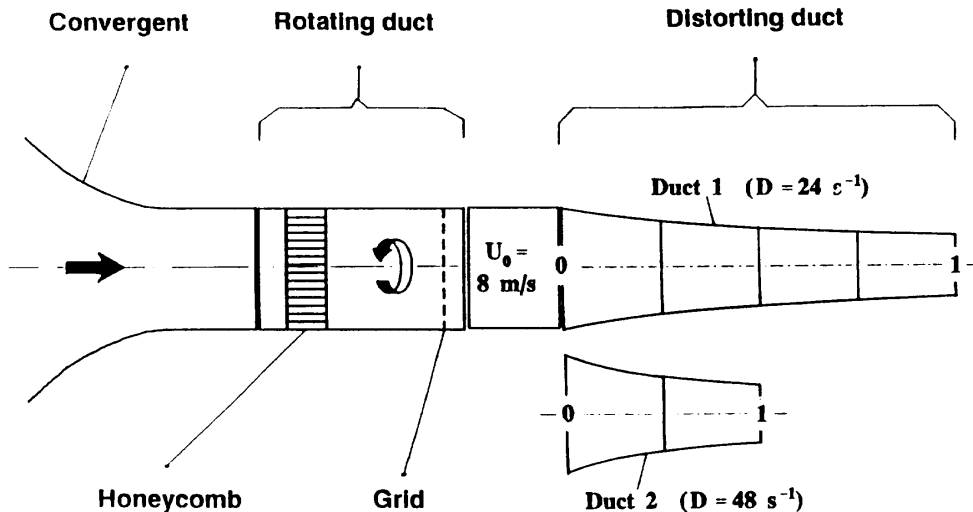
$$\frac{R(x)}{R_0} = \left(1 + \frac{Dx}{U_0} \right)^{-\frac{1}{2}} \quad (3)$$

ensuring constant D . $R(x)$ is the radius of the duct at position x and R_0 its initial value ($R_0 = 0.15 \text{ m}$); x is the axial distance from the initial section where the straining process begins.

Two contracting ducts of different length L , but with the same total contraction $C = [R_0/R(L)]^2$ have been used in the experiments:

- duct 1 of length $L=1 \text{ m}$,
- duct 2 of length $L=0.5 \text{ m}$.

3. Original sketch



4. Flow characteristics

The flow is initially in solid-body rotation and the turbulence is homogeneous. Transverse homogeneity is conserved near the axis during the straining process. The initial axial velocity is $U_0 = 8 \text{ m/s}$. The corresponding maximum initial rotation rate is $\Omega_0 = 48 \text{ rd/s}$ and the corresponding strain rate is $D = 24 \text{ s}^{-1}$ for duct 1 and $D = 48 \text{ s}^{-1}$ for duct 2. The case of pure axisymmetric strain ($\Omega_0 = 0$) is considered as the reference case and is also included in the data. During the distortion, rotation noticeably reduces the anisotropy of the Reynolds-stresses produced by the strain, and simultaneously increases the level of the rapid pressure-strain correlations. This specific rotation effect is not reproduced by the classical Reynolds-stress models.

5. Flow parameters

The flow configurations are the following:

Table 1: Flow parameters

configuration	duct	$U_0 \text{ (m/s)}$	$D \text{ (s}^{-1}\text{)}$	$\Omega_0/D = \omega_0$
1	1	8	24	0
2	1	8	24	2
3	2	8	48	0
4	2	8	48	1

6. Inflow conditions

“Nominal” initial conditions (at $x = 0$ and for $U_0 = 8 \text{ m/s}$, $\omega_0 = 0$) are:

- * kinetic energy: $q^2/2 = 0.16 \text{ m}^2/\text{s}^2$,
- * anisotropy: $(\overline{u^2} - \overline{v^2})/q^2 = 0.12$,
- * dissipation rate: $\epsilon = 8.2 \text{ m}^2/\text{s}^3$,
- * longitudinal integral lengthscale: $L_u = 5.8 \times 10^{-3} \text{ m}$,
- * transverse integral lengthscale: $L_v = 2.5 \times 10^{-3} \text{ m}$,
- * Taylor microscale: $\lambda = \sqrt{5\nu q^2/\epsilon} = 1.7 \times 10^{-3} \text{ m}$,
- * Kolmogorov lengthscale: $\eta = (\nu^3/\epsilon)^{1/4} = 0.14 \times 10^{-3} \text{ m}$,
- * microscale Reynolds number: $Re_\lambda = \sqrt{q^2/3}\lambda/\nu = 37$.

The initial section $x = 0$ is located 0.25 m downstream of the turbulence grid.

7. Measured data

(a) Measurement procedure

Hot-wire methods using DISA (DANTEC) anemometers 55M01 and crossed-wire probes of type P61. Digital data processing of 100×2048 simultaneous samples for both velocity components.

The flow is explored on the axis of the duct between the longitudinal positions $x/L = 0$ and $x/L = 1$ for duct 1 ($L = 1 \text{ m}$) and between $x/L = -0.25$ and $x/L = 1.25$ for duct 2 ($L = 0.5 \text{ m}$). The axial distance between successive measurement points is $\Delta x = L/16$, yielding a total number of 17 measurement points for duct 1 and 25 measurement points for duct 2.

(b) Measured quantities

- axial mean velocity component U ,
- transverse mean velocity component V (negligible compared to U),
- variance of the fluctuating axial velocity component $\overline{u^2}$,
- variance of the fluctuating transverse velocity component $\overline{v^2}$,
- spectra of both velocity components,
- lengthscales $L_u (= L_{11,1})$ and $L_v (= L_{22,1})$ deduced from the corresponding spectra.

(c) Measurement errors

Estimated to be of the order of one percent for the mean velocities and about a few percent for the turbulence quantities

8. Available measurements

The results are disposed in four data sets corresponding to the nominal conditions indicated in Table 1. All the quantities are given in physical dimensions. Each data set has 8 columns corresponding to the following quantities:

- longitudinal position x (m),
- local strain rate D (s^{-1}), evaluated from $D = \partial U / \partial x$,
- local rotation rate Ω (s^{-1}), evaluated from $\Omega = \Omega_0 U / U_0$,
- axial mean velocity component U (m/s),
- variance of the fluctuating axial velocity component $\overline{u^2}$ (m^2/s^2),
- variance of the fluctuating transverse velocity component $\overline{v^2}$ (m^2/s^2),
- trace of the Reynolds stress tensor q^2 (m^2/s^2), evaluated from $q^2 = \overline{u^2} + 2\overline{v^2}$,
- dissipation rate ϵ (m^2/s^3), evaluated from $\epsilon = -D(\overline{u^2} - \overline{v^2}) - \frac{1}{2}U[dq^2/dx]$.

9. Size and present format of data

Small ASCII files.

10. Contact person

O. Leuchter
ONERA
8 rue des Vertugadins
F 92190 Meudon, France
e-mail: leuchter@onera.fr

11. Main references

LEUCHTER, O. & DUPEUBLE, A. 1993 Rotating homogeneous turbulence subjected to axisymmetric contraction *Ninth Symposium on Turbulent Shear Flows*, Kyoto.

LEUCHTER, O. 1993 Turbulence homogène soumise a des effets couplés de rotation et de déformation plane ou axisymétrique *Internal ONERA Report 15/1145AY*.

LEUCHTER, O. & BERTOGLIO, J.P. 1995 Non-linear spectral approach to rotating turbulence in the presence of strain *Tenth Symposium on Turbulent Shear Flows*, The Pennsylvania State University.

HOM14: Rotating Turbulence with Plane Strain

Leuchter, Benoit & Cambon

1. Flow description

Homogeneous turbulent flow in solid-body rotation with a rotation rate Ω is subjected to plane strain with a strain rate $D < \Omega$ (elliptical flow regime). The mean flow distortion is defined by the following strain rate matrix:

$$\left(\frac{\partial U_i}{\partial x_j} \right) = \begin{pmatrix} 0 & 0 & 0 \\ 0 & 0 & D - \Omega \\ 0 & D + \Omega & 0 \end{pmatrix} \quad (1)$$

where D and Ω are constant. The distortion is restricted to planes normal to the axial direction. Eq.(1) is written in the laboratory coordinate system, in which the experimental results will be given. The laboratory frame is rotated by $\pi/4$ with respect to the principal directions of the plane strain, for which eq.(1) reads:

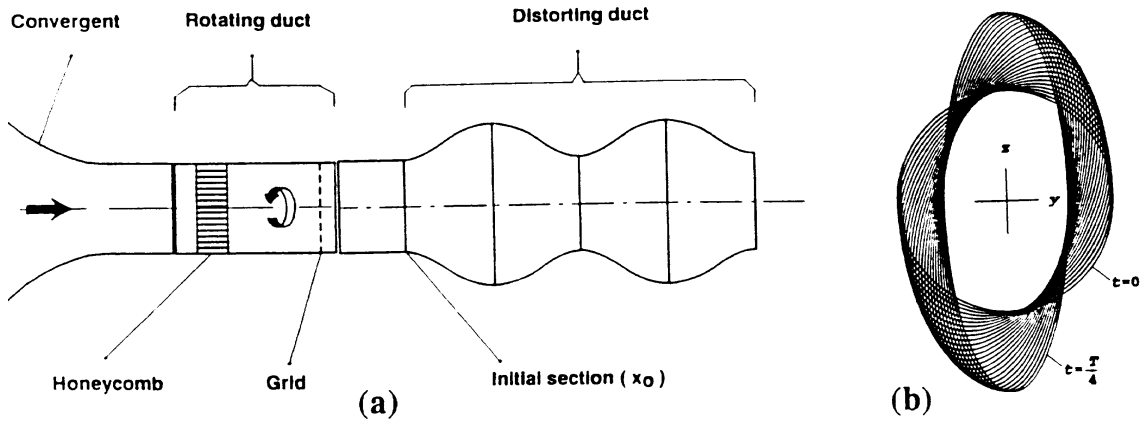
$$\left(\frac{\partial U_i}{\partial x_j} \right) = \begin{pmatrix} 0 & 0 & 0 \\ 0 & D & -\Omega \\ 0 & \Omega & -D \end{pmatrix} \quad (2)$$

Due to the condition $\Omega > D$ the basic flow becomes periodic and the turbulence parameters exhibit undulating features.

2. Geometry

Solid-body rotation is created by means of a rotating duct of 0.3 m diameter equipped with a fine-mesh honeycomb and a grid turbulence generator of 1.5 cm mesh size. The distorting duct has elliptical cross sections of constant area and periodically varying eccentricity and orientation of the main axes. For an axial velocity of 10 m/s and for $\Omega = 2D = 20\pi$, a whole period of flow is completed with a length of 1.16 m.

3. Original sketch



4. Flow characteristics

The flow is initially in solid-body rotation and the turbulence is homogeneous. According to eq.(1), the axial velocity remains constant during the distortion and transverse homogeneity is conserved in the central part of the duct. The initial axial velocity is $U = 10 \text{ m/s}$. The specific features are the undulating variations of the anisotropy parameters, confirmed by spectral modelling. Classical Reynolds-stress models do not predict correctly this behaviour.

5. Flow parameters

- * Axial velocity: 10 m/s ,
- * Strain rate: $D = 31.4 \text{ s}^{-1}$,
- * Rotation rate: $\Omega = 62.4 \text{ s}^{-1}$.

6. Inflow conditions

”Nominal“ initial conditions (at $x = 0$ and for $U = 10 \text{ m/s}$) are:

- * kinetic energy: $q^2/2 = 0.269 \text{ m}^2/\text{s}^2$,
- * anisotropy: $(\overline{u^2} - \frac{1}{2}(\overline{v^2} + \overline{w^2}))/q^2 = 0.125$,
- * dissipation rate: $\epsilon = 16.2 \text{ m}^2/\text{s}^3$,
- * longitudinal integral lengthscale: $L_u = 6.8 \times 10^{-3} \text{ m}$,
- * transverse integral lengthscale: $L_v = 3.2 \times 10^{-3} \text{ m}$,
- * Taylor microscale: $\lambda = \sqrt{5\nu q^2/\epsilon} = 1.6 \times 10^{-3} \text{ m}$,
- * Kolmogorov lengthscale: $\eta = (\nu^3/\epsilon)^{1/4} = 0.12 \times 10^{-3} \text{ m}$,
- * microscale Reynolds number: $Re_\lambda = \sqrt{q^2/3} \lambda/\nu = 45$.

The initial section $x = 0$ is located 0.25 m downstream of the turbulence grid.

7. Measured data

(a) Measurement procedure

Hot-wire methods using DISA (DANTEC) anemometers 55M01 and crossed-wire probes of type P61. Digital data processing of 100×2048 simultaneous samples for both velocity components. Four angular positions of the probe are considered to resolve the four non-zero Reynolds-stress components.

The measurements are made in 22 positions on the axis of the duct between the longitudinal positions $x = 0$ and $x = L = 1.16 \text{ m}$.

(b) Measured quantities

- axial mean velocity component U ,
- transverse mean velocity components V and W (negligible compared to U),
- Reynolds stresses $\overline{u^2}$, $\overline{v^2}$, $\overline{w^2}$, \overline{vw} ,
- spectra of the three velocity components,
- lengthscales $L_u (= L_{11,1})$, $L_v (= L_{22,1})$ and $L_w (= L_{33,1})$, deduced from the corresponding spectra.

(c) Measurement errors

Estimated to be of the order of one percent for the mean velocities and about a few percent for the turbulence quantities.

8. Available measurements

The results are disposed in a table of 11 columns corresponding to the following quantities:

- longitudinal position $x \text{ (m)}$,
- relative position $\xi = x/L$,
- axial mean velocity component $U \text{ (m/s)}$,
- Reynolds stresses $\overline{u^2}$, $\overline{v^2}$, $\overline{w^2}$, $\overline{vw} \text{ (m}^2/\text{s}^2)$,
- dissipation rate $\epsilon \text{ (m}^2/\text{s}^3)$, evaluated from $\epsilon = -2D\overline{vw} - \frac{1}{2}U[dq^2/dx]$.
- lengthscales $L_u (= L_{11,1})$, $L_v (= L_{22,1})$ and $L_w (= L_{33,1}) \text{ (m)}$.

9. Size and present format of data

Small ASCII file.

10. Contact person

O. Leuchter
ONERA
8 rue des Vertugadins
F 92190 Meudon, France
e-mail: leuchter@onera.fr

11. Main references

LEUCHTER, O. & BENOIT, J.P. 1991 Study of coupled effects of plane strain and rotation on homogeneous turbulence *Eighth Symposium on Turbulent Shear Flows*, Munich.

LEUCHTER, O., BENOIT, J.P. & CAMBON, C. 1992 Homogeneous turbulence subjected to rotation-dominated plane distortion *Fourth European Turbulence Conference*, Delft.

LEUCHTER, O. 1993 Turbulence homogène soumise a des effets couplés de rotation et de déformation plane ou axisymétrique *Internal ONERA Report 15/1145AY*.

HOM20: Transversely Sheared Flow

Leuchter *et al.*

1. Flow description

Homogeneous transverse shear is created by the superposition of solid-body rotation at rate Ω and plane strain at rate D , with $D = \Omega$, resulting in a uniform shear flow at rate $S = D + \Omega$ in planes perpendicular to the flow direction:

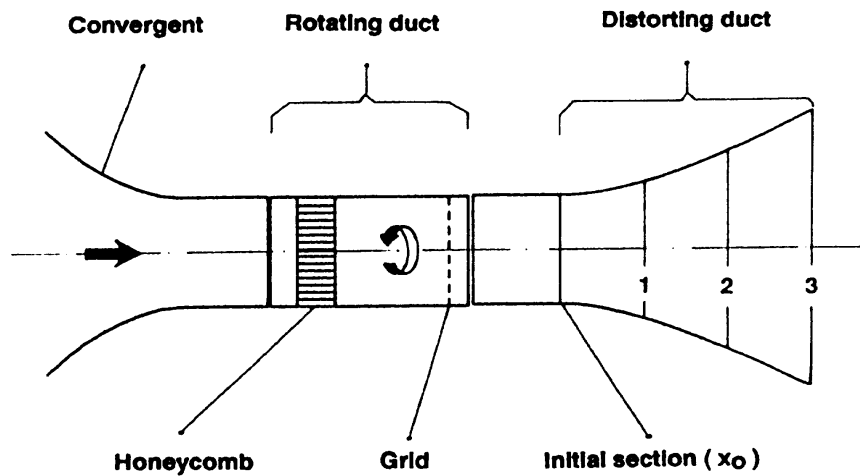
$$\left(\frac{\partial U_3}{\partial x_2}\right) = D + \Omega = S \quad (1)$$

Satisfactory homogeneity conditions are thus achieved.

2. Geometry

Solid-body rotation is created by means of a rotating duct of 0.3 m diameter equipped with a fine-mesh honeycomb and a grid turbulence generator of 1.5 cm mesh size. The distorting duct has elliptical cross sections of constant area with continuously increasing eccentricity and varying orientation of the main axes. The maximum value of the aspect ratio a/b of the elliptical section is 6.92 in the exit plane of the duct, corresponding to a non-dimensional time St of 2.25. The length of the distorting duct is $L = 0.66$ m.

3. Original sketch



4. Flow characteristics

The flow is initially in solid-body rotation and the turbulence is homogeneous. The axial velocity remains constant during the straining process and transverse homogeneity is conserved in the central part of the flow. The turbulence becomes progressively anisotropic under the effect of shear; the growing of the transverse shear stress correlation coefficient is very similar to that observed in flows with longitudinal shear.

5. Flow parameters

- * Axial velocity: 10 m/s,
- * Strain rate: $D = 17$ s⁻¹,
- * Rotation rate: $\Omega = 17$ s⁻¹,
- * Shear rate: $S = 34$ s⁻¹.

6. Inflow conditions

'Nominal' initial conditions (at $x = 0$ and for $U = 10$ m/s) are:

- * kinetic energy: $q^2/2 = 0.262 \text{ m}^2/\text{s}^2$,
- * anisotropy: $(\overline{u^2} - \frac{1}{2}(\overline{v^2} + \overline{w^2}))/q^2 = 0.159$,
- * dissipation rate: $\epsilon = 16.2 \text{ m}^2/\text{s}^3$,
- * longitudinal integral lengthscale: $L_u = 6.6 \times 10^{-3} \text{ m}$,
- * transverse integral lengthscale: $L_v = 2.7 \times 10^{-3} \text{ m}$,
- * Taylor microscale: $\lambda = \sqrt{5\nu q^2/\epsilon} = 1.56 \times 10^{-3} \text{ m}$,
- * Kolmogorov lengthscale: $\eta = (\nu^3/\epsilon)^{1/4} = 0.12 \times 10^{-3} \text{ m}$,
- * microscale Reynolds number: $Re_\lambda = \sqrt{q^2/3} \lambda/\nu = 43.5$.

The initial section $x = 0$ is located 0.25 m downstream of the turbulence grid.

7. Measured data

(a) Measurement procedure

Hot-wire methods using DISA (DANTEC) anemometers 55M01 and crossed-wire probes of type P61. Digital data processing of 100×2048 simultaneous samples for both velocity components. Four angular positions of the probe are considered to resolve the four non-zero Reynolds-stress components. Four-wire probes were also used.

The measurements are made in 13 equidistant positions on the axis of the duct between the initial section $x = 0$ and the exit section $x = L = 0.66 \text{ m}$.

(b) Measured quantities

- axial mean velocity component U ,
- transverse mean velocity components V and W (negligeable compared to U),
- Reynolds stresses $\overline{u^2}$, $\overline{v^2}$, $\overline{w^2}$, \overline{vw} ,
- spectra of the three velocity components,
- lengthscales $L_u (= L_{11,1})$, $L_v (= L_{22,1})$ and $L_w (= L_{33,1})$, deduced from the corresponding spectra.

(c) **Measurement errors** Estimated to be of the order of one percent for the mean velocities and about a few percent for the turbulence quantities.

8. Available measurements

The results are disposed in a table with 11 columns corresponding to the following quantities:

- longitudinal position x (m),
- non-dimensional time St ,
- axial mean velocity component U (m/s),
- Reynolds stresses $\overline{u^2}$, $\overline{v^2}$, $\overline{w^2}$, \overline{vw} (m^2/s^2),
- dissipation rate ϵ (m^2/s^3), evaluated from $\epsilon = -S\overline{vw} - \frac{1}{2}U[dq^2/dx]$.
- lengthscales $L_u (= L_{11,1})$, $L_v (= L_{22,1})$ and $L_w (= L_{33,1})$ (m).

9. Size and present format of data

Small ASCII file.

10. Contact person

O. Leuchter
ONERA
8 rue des Vertugadins
F 92190 Meudon, France
e-mail: leuchter@onera.fr

11. Main references

- MOULIN, V., LEUCHTER, O. & GEFFROY, P. 1989 Experimental study of homogeneous turbulence in the presence of transverse shear *Seventh Symposium on Turbulent Shear Flows*, Stanford.
- LEUCHTER, O. & GEFFROY, P. 1989 Etude expérimentale de la turbulence homogène en rotation et déformation *Internal ONERA Report 12/1145AY*.
- LEUCHTER, O., BENOIT, J.P., BERTOGLIO, J.P. & MATHIEU, J. 1990 Experimental and theoretical investigation of a homogeneous turbulent shear flow *Third European Turbulence Conference*, Stockholm.
- LEUCHTER, O., BENOIT, J.P. & GEFFROY, P. 1991 Turbulence homogène en rotation soumise à des effets de déformation. Cas particulier du cisaillement *Internal ONERA Report 13/1145AY*.

HOM21: Uniformly Sheared Flow

Tavoularis & Corrsin

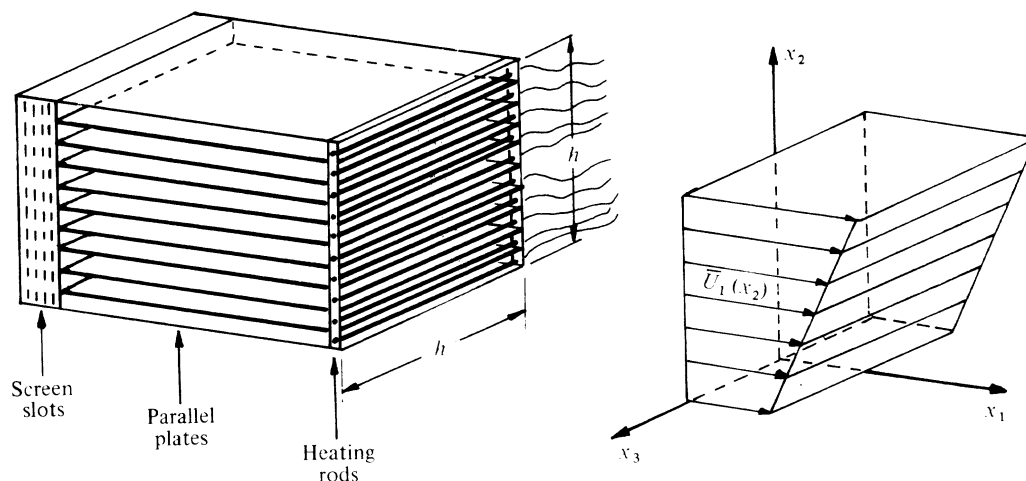
1. Description of the flow

Uniformly sheared turbulent flow, with near transverse homogeneity and with stresses growing exponentially downstream.

2. Geometry

The mean shear was produced by a shear-turbulence generator, consisting of a set of ten parallel channels, each having a mean speed adjusted by means of a different set of screens posing resistance to the flow. Circular rods positioned across the exit of each channel produced a relatively high initial turbulence level and could also be heated electrically for the generation of a temperature field. The same set of channels acted as a flow separator, enforcing an initial uniformity of length scales, comparable to the channel height.

3. Original sketch



4. Flow characteristics

The side walls of the nearly square test section were slightly diverging to produce a nearly constant mean pressure throughout the test section. Following an initial development length, in which the initial turbulence decayed, a fully developed, quasi-self-similar region was established. In this region, mean shear was, by far, the main production mechanism and the turbulence attained a reasonable transverse homogeneity and reached constant asymptotic values of the Reynolds stress anisotropies and the production-to-dissipation ratio. All Reynolds stresses and the turbulence kinetic energy grew at the same exponential rates.

5. Flow parameters

Initial channel spacing, $M = 30.8\text{mm}$. Test section height, $h = 305\text{mm}$. Centreline mean speed, $U_c = 12.4\text{m.s}^{-1}$. Mean shear, $d\bar{U}_1/dx_2 = 46.8\text{s}^{-1}$.

6. Inflow and outflow boundary and initial conditions

Because the turbulence at the exit of the shear generator was not produced by the mean shear, and, therefore, had an irrelevant structure, one should avoid using measurements too close to the origin (e.g. for $x_1/h < 4.5$).

7. Measurements

(a) Measurement procedures

All measurements were taken with standard, single- and cross-wire, hot wire anemometers. Auto-correlations were based on Taylor's frozen flow approximation and two-point correlations were measured by traversing two probes with a precision device.

(b) **Measured quantities** Means, Reynolds stresses, triple and fourth-order moments, auto-correlations and two-point correlations, space-time correlations, integral length scales in different directions, Taylor microscales, frequency spectra of the streamwise and transverse velocities and the shear stress, and single-point pdf and joint pdf.

(c) **Measurement errors**

Estimated uncertainty (95% confidence level) is 2% for the mean velocity, 5% for the mean shear, 4% for the normal turbulent stress and 8% for the other stresses.

8. **Available variables**

Normal and shear Reynolds stresses, integral length scales and Taylor microscales along the tunnel centreline have been tabulated vs. downstream distance. Two-point correlations vs. separation distance.

9. **Storage size required and present format of the data**

Small ASCII files.

10. **Contact person**

Professor Stavros Tavoularis
Department of Mechanical Engineering, University of Ottawa
Ottawa, Ontario, Canada K1N 6N5
tel/fax: (613) 562 5800 ext. 6271
e-mail: tav@eng.uottawa.ca

11. **Main references**

TAVOULARIS, S. & CORRSIN, S. 1981a Experiments in a nearly homogeneous shear flow with a uniform mean temperature gradient. Part 1 *J. Fluid Mech.* **104**, 311-347.

TAVOULARIS, S. & CORRSIN, S. 1981b Experiments in a nearly homogeneous shear flow with a uniform mean temperature gradient. Part 2. The fine structure *J. Fluid Mech.* **104**, 349-367.

HOM22: Uniformly Sheared Flow

Tavoularis, Karnik & Ferchichi

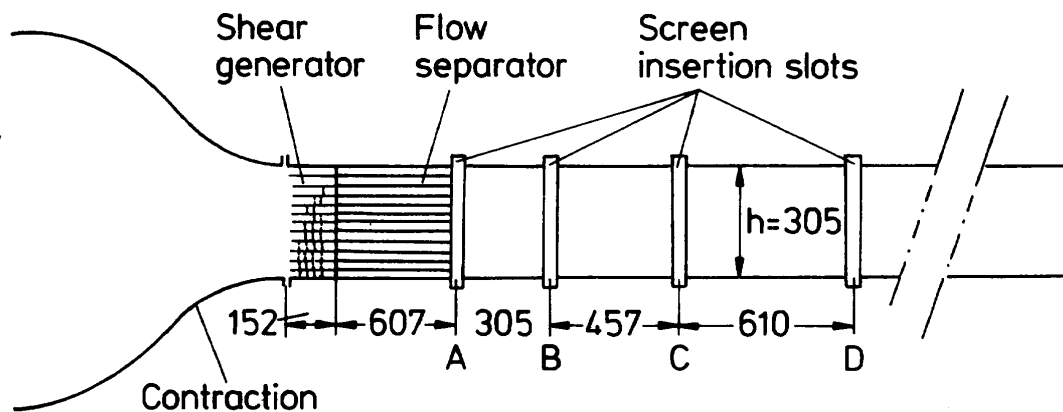
1. Description of the flow

Uniformly sheared turbulent flow, with near transverse homogeneity and with stresses growing exponentially downstream.

2. Geometry

The mean shear was produced by a shear generator, posing variable resistance to the flow. A flow separator, consisting of a set of parallel channels, enforced an initial uniformity of length scales, comparable to the channel height, M . When desired, the mean shear magnitude was reduced by the insertion of one or more uniform grids or screens in the flow development region.

3. Original sketch



4. Flow characteristics

Following an initial development region, the turbulence attained a reasonable transverse homogeneity and reached asymptotic values of the Reynolds stress anisotropies. All Reynolds stresses grew at the same exponential rates.

5. Flow parameters

Initial channel spacing, $M = 25.4$ mm. Cross section height, $h = 305$ mm (all references). Centerline mean speed: $\overline{U}_c = 13.0$ m/s (Tavoularis & Karnik 1989, TK89); $\overline{U}_c = 8.9$ m/s (Ferchichi & Tavoularis 1997, FT97.) Shear rate: maximum 84.0 m/s, reduced by the insertion of grid(s) or by lowering the tunnel speed (TK89); 63.5 m/s (FT97).

6. Inflow and outflow boundary and initial conditions

Because the turbulence at the exit of the shear generator was not produced by the mean shear, and, therefore, had an irrelevant structure, one should avoid using measurements too close to the origin (e.g. for $x_1/h < 4.5$).

7. Measurements

(a) Measurement procedures

All measurements taken with standard single- and cross-wire, hot-wire anemometers.

(b) Measured quantities

Means, Reynolds stresses, integral length scales and Taylor microscales (TK89, Holloway & Tavoularis 1992). Pdf of streamwise and transverse velocity differences (FT97). Energy spectra (Holloway & Tavoularis 1993.)

(c) **Measurement errors**

Estimated uncertainty (95% confidence level) is 2% for the mean velocity, 5% for the mean shear, 4% for the normal turbulent stress and 8% for the other stresses.

8. **Available variables**

From Ref. 5: Reynolds stresses and integral length scales along the centreline vs. streamwise distance for four different mean shear rates.

From Ref. 1: Probability density functions of streamwise and transverse velocity differences ($\Delta u_1(x_1)$, $\Delta u_2(x_1)$, $\Delta u_1(x_2)$) at a position with $x_1/h = 7.83$, where $\overline{U_c} = 8.9$ m/s, $u'_1 = 0.724$ m/s, $\lambda = 4.6$ mm, $L = 30$ mm, $Re_\lambda = 212$ and $\eta = 0.16$ mm. Energy spectrum of the streamwise velocity.

9. **Storage size required and present format of the data**

Small ASCII files.

10. **Contact person**

Professor Stavros Tavoularis
Department of Mechanical Engineering, University of Ottawa
Ottawa, Ontario, Canada K1N 6N5
tel/fax: (613) 562 5800 ext. 6271
e-mail: tav@eng.uottawa.ca

11. **Main references**

FERCHICHI, M. & TAVOULARIS, S. 1997 Unpublished measurements.

HOLLOWAY, A.G.L. & TAVOULARIS, S. 1992 The effects of curvature on sheared turbulence *J. Fluid Mech.* **237**, 569-603.

HOLLOWAY, A.G.L. & TAVOULARIS, S. 1993 Scaling and Structure of Turbulent Eddies in Curved Sheared Flows *Turbulent Shear Flows 8*, F. Durst *et al* (editors), 383-401, Springer.

KARNIK, U. & TAVOULARIS, S. 1987 Generation and manipulation of uniform shear with the use of screens *Exper. Fluids* **5**, 247-254.

TAVOULARIS, S. & KARNIK, U. 1989 Further experiments on the evolution of turbulent stresses and scales in uniformly sheared turbulence *J. Fluid Mech.* **204**, 457-478.

HOM23: Homogeneous Shear Flow

Rogers & Moin

1. Description of the flow

Incompressible homogeneous turbulent shear flow. Passive scalar evolution in the presence of a mean scalar gradient also included.

2. Geometry

Fully periodic domain, with computational grid following the mean shear between remeshings. Orthogonal grid at multiples of $St = 2$, where $S = \partial U / \partial y$ is the mean shear rate and t is time.

3. Original sketch: Not applicable.

4. Flow characteristics

Homogeneous turbulence with no irrotational interfaces or walls. Size of large-scale eddies determined by initial energy spectrum.

5. Flow parameters

Six $128 \times 128 \times 128$ simulations containing four different hydrodynamic fields and two additional cases with scalars of different Schmidt numbers. Box size $9.97 \times 4.99 \times 4.99$.

	C128R	C128S	C128U	C128W	C128X
Mean shear rate S	28.284	28.284	28.284	56.568	14.142
Kinematic viscosity	0.010	0.010	0.010	0.020	0.005
Schmidt number Sc	1.0	0.2	0.7	2.0	0.7
Mean scalar gradient	2.5	2.5	2.5	2.5	2.5
St	16	16	16	28	14

Once the flows reach the developed state, Sq^2/ϵ ranges from about 10 to 15, $q^4/(\epsilon\nu)$ ranges from about 500 to 2000, and the microscale Reynolds number $u'\lambda_1/\nu$ ranges from about 70 to 100.

6. Numerical methods and resolution: Spectral numerical scheme as in (Rogallo 1981), on a 128^3 collocation grid. The grid is distorted by the shear, and is periodically re-interpolated to orthogonal (at $S\Delta t = 2$).

7. Boundary and initial conditions

Periodic boundary conditions in all three coordinate directions. Initial top-hat energy and scalar spectrum over wavenumbers $16 < k < 32$.

8. Averaging procedures and resulting uncertainties:

Statistics post-processed using the same spectral basis functions used to advance the Navier–Stokes equations in time. Statistics are compiled over individual data fields, and uncertainties are correspondingly high.

9. Available variables

Time history of single-point second-order velocity statistics, integral length scales, and dissipation.

Short-range two-point correlation tensor, up to $\Delta N_x = \Delta N_y = \Delta N_z = 16$ for $\overline{u'v'}$, $\overline{u'^2}$, $\overline{v'^2}$, $\overline{w'^2}$, $\overline{c'u'}$, $\overline{c'v'}$, $\overline{c'^2}$, at all times with orthogonal grids, for each case.

10. Storage size required and present format of the data

About 46 Mb of IEEE single precision floating point data, plus short ASCII files.

11. Contact person

Dr. M.M. Rogers
NASA Ames Research Centre, Moffett Field, Ca. 94035, USA.
E-mail: mrogers@nas.nasa.gov

12. Main references

ROGALLO, R.S. 1981 Numerical experiments in homogeneous turbulence. *NASA Tech. Memo.* 81315.

ROGERS, M.M., MOIN, P. & REYNOLDS, W.C. 1986 The Structure and Modelling of the Hydrodynamic and Passive Scalar Fields in Homogeneous Turbulent Shear Flow, *Dept. Mech. Eng. Report No. TF-25*. Stanford University, Stanford, California.

ROGERS, M.M. & MOIN, P. 1987 The structure of the vorticity field in homogeneous turbulent flows *J. Fluid Mech.* **176**, 33-66.

ROGERS, M.M., MANSOUR, N.N. & REYNOLDS, W.C. 1989 An algebraic model for the turbulent flux of a passive scalar *J. Fluid Mech.* **203**, 77-101.

HOM24: Homogeneous Shear Flow

Sarkar

1. Description of the flow:

Uniform shear flow (DNS).

2. Geometry:

Triply periodic mesh, plus shear. Nondimensional length of the computational domain is 2π in each direction. This length is ‘much’ larger than the integral length scale and ideally does not determine the evolution of the statistics.

3. Original sketch: Not applicable.

4. Flow characteristics:

A uniform mean shear, $S = dU/dy$, is imposed on an initial isotropic perturbation field \mathbf{u} . The evolution of the flow field as a function of nondimensional time, St , is of interest. The flow is nonlinearly unstable and the asymptotic state is exponential growth of turbulent kinetic energy, K , and turbulent dissipation rate, ϵ . It should be noted that, since, R_λ and the integral length scales increase with time in uniformly sheared flow, the simulation has to be eventually stopped when the resolution of large or small scales becomes inadequate.

5. Flow parameters

For a given initial spectral shape of the isotropic velocity perturbations, the subsequent evolution of the flow as a function of nondimensional time St depends on the initial values of shear number SK/ϵ and the microscale Reynolds number $R_\lambda = u\lambda/\nu$. Here, u is the r.m.s. of a velocity component and λ is defined by $\epsilon = 15\nu u^2/\lambda^2$. The initial values of the parameters are $SK/\epsilon = 2.6$, $R_\lambda = 24.3$.

6. Numerical method and resolution:

The incompressible Navier-Stokes equations are simulated in a frame moving with the mean velocity as in Rogallo (1981). Remeshing is performed at regular intervals to minimize errors due to the skewed grid coordinates. Fourier collocation is used to compute spatial derivatives and a third-order, Runge-Kutta method is used for time advancement.

Volume averages and spectra were obtained at integral St when the computational grid is orthogonal. The computational domain is a cube of size 2π with a 128^3 spatial grid.

7. Boundary and initial conditions

Periodic boundary conditions in a frame moving with the mean velocity. Initial velocity perturbations are isotropic with an energy spectrum, $E(k) \propto k^4 \exp(-2k^2/k_m^2)$, with $k_m = 18$.

8. Averaging procedures and resulting uncertainties

Statistics are compiled during the run for individual flow fields.

9. Available variables

Time history of single-point second-order velocity statistics, integral length scales, and dissipation.

Short-range correlations for $\overline{u'_1 u'_1}$, $\overline{u'_2 u'_2}$, $\overline{u'_3 u'_3}$, $\overline{u'_1 u'_2}$, and $\overline{p' p'}$ that span a cube of side 16 points, at $St = 7, 11$ and 15.

Three-dimensional energy spectra at times $St = 0, 3$ (2) 15.

10. Storage size required and present format of the data

Approximately 2 MB of binary, plus short ASCII statistics.

11. Contact person

Sutanu Sarkar
Department of AMES, 0411, 9500 Gilman Drive
University of California at San Diego

La Jolla, CA 92093

Email: sarkar@ames.ucsd.edu

Tel: (619)-534-8243 Fax: (619)-534-7599

12. Main references

SARKAR, S. 1995 The Stabilizing Effect of Compressibility in Turbulent Shear Flow *J. Fluid Mech.*, **282**, 163-186.

SARKAR, S., ERLEBACHER, G. & HUSSAINI, M. Y. 1991 Direct Simulation of Compressible Turbulence in a Shear Flow *Theor. Comput. Fluid Dynamics*, **2**, 291-305.

HOM25: Homogeneous Shear Flow (High Shear)

Lee, Kim & Moin

1. **Description:** Homogeneous turbulent shear flow, at high shear rates.
2. **Flow geometry:** Uniform shear flow with linear mean velocity profile.
3. **Original sketch:** Not applicable.
4. **Flow characteristics**

The flow is subject to high shear rate ($S^* = Sq^2/\epsilon \approx 35$, where $S = dU/dy$ is the shear rate, q^2 is twice the turbulent kinetic energy and ϵ is the dissipation rate of $q^2/2$) and the streaky structures similar to those found in the sublayer ($y^+ < 10$) of wall-bounded flows (where $S^* \approx 35$) develop at around $St = 8$ and beyond, indicating that the (dimensionless) shear rate is the controlling parameter that determines the organized structures in turbulent shear flows. Comparison of turbulence statistics with channel flow also shows remarkable similarity.

5. **Flow parameters**

Mean flow has uniform shear (and hence linear velocity profile, $U = Sy$). The turbulence Reynolds number $Re_T = q^4/(\nu\epsilon)$ ranged from 300–2400 for $St = 0$ –16 and the Reynolds number $Re_\lambda = q\lambda/\nu$ based on the longitudinal Taylor microscale $\lambda = (\overline{u^2}/\overline{u_{,x}^2})^{1/2}$ ranged from 40 to 400.

6. **Numerical methods and resolution**

Pseudo-spectral method was used to solve the Navier–Stokes equations with $512 \times 128 \times 128$ Fourier modes in the (x, y, z) -directions. Time-marching was done with the second-order Runge–Kutta method. Alias removal is carried out by combination of phase shift and truncation. (Rogallo 1981). Grid spacing was uniform in all three directions: $\Delta \approx 4(\nu/S)^{1/2}$.

7. **Boundary and initial conditions**

Computational domain: $(B_x, B_y, B_z) = (8\pi, 2\pi, 2\pi)$, periodic in all three directions

The initial condition for the present data set was obtained by an isotropic-decay run which gave an isotropic field with realistic statistics including velocity-derivative skewness $S_{u,x} \approx -0.47$.

8. **Averaging procedures and resulting uncertainties**

Averaged is done over individual fields.

9. **Available variables**

Time histories of one-point statistics: R_{ij} , dR_{ij}/dt , Reynolds-stress transport budget terms (P_{ij} , T_{ij} , D_{ij}), integral length scales, Taylor microscales, as well equivalent quantities for the vorticity.

10. **Storage size required and file format:** Short ASCII file.

11. **Contact person**

Moon J. Lee

Department of Mechanical Engineering, Pohang University of Science and Technology
Hyoja-dong San 31, Pohang 790–784, Korea

E-mail: mjlee@vision.postech.ac.kr

Phone: 82–562–279–2178

FAX: 82–562–279–5567 or 3199

12. **Main references**

LEE, M.J., KIM, J. & MOIN, P. 1990 Structure of turbulence at high shear rate, *J. Fluid Mech.* **216**, 561–583.

HOM26: Uniformly Sheared Flow with Streamwise Plane Strain

Sreenivasan

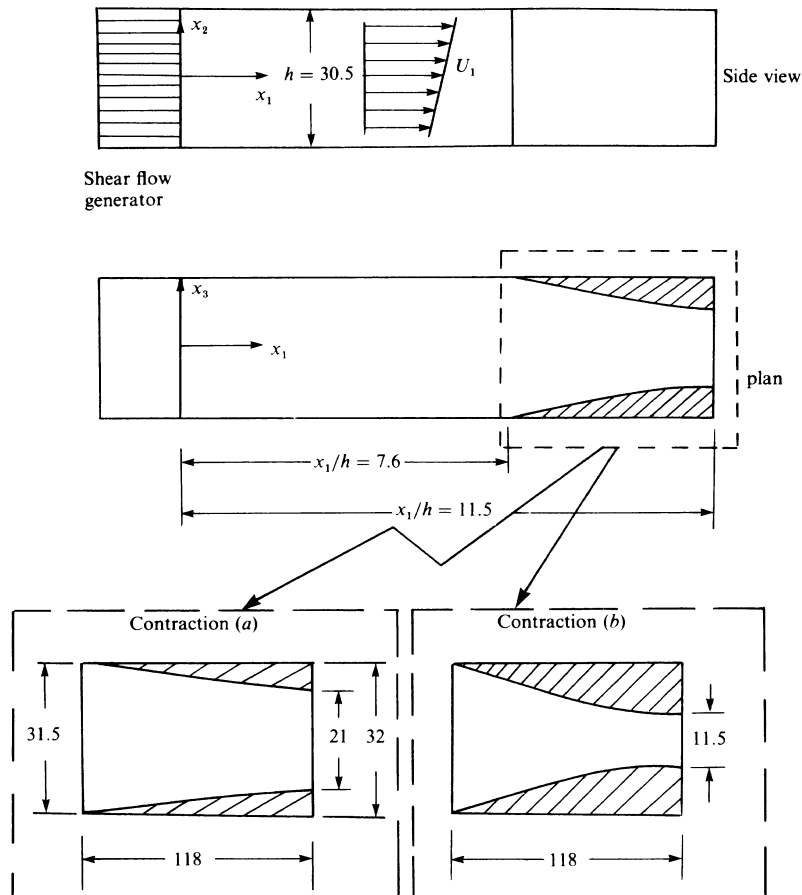
1. Description of the flow

Uniformly sheared turbulence was let to develop to an asymptotic state and then passed through a two-dimensional contraction, perpendicular to the mean shear.

2. Geometry

The flow was generated by the usual means of a shear generator/flow separator device, with a uniform channel spacing, essentially the same as the Harris, Graham and Corrsin (1977) and the Tavoularis and Corrsin (1981) setup (see case HOM21). The wind tunnel height, h , in the direction of mean shear, was kept constant throughout the experiment. The contractions were made of polished wood and inserted symmetrically at a position $7.6h$ downstream of the shear generator, where the sheared turbulence had reached its asymptotic structure. Two contractions, denoted as a and b, were used, with final contraction ratios equal to 1.4 and 2.6, respectively.

3. Original sketch



4. Flow characteristics

The additional losses due to the contraction caused a decrease in the upstream centreline mean speed and mean shear, compared to those in the undisturbed shear flow; these decreases were stronger for the larger contraction ratio. Through the contraction, the centreline mean speed increased monotonically, while the mean shear decreased monotonically, while remaining approximately uniform on the transverse plane. The turbulence also remained approximately transversely homogeneous.

5. Flow parameters

The important parameter characterizing the effects of contraction is the ratio of the mean strain rates in the transverse and streamwise directions. This ratio was approximately 0.12 for case a and 1 for case b. The turbulence structure is characterized by the structural parameters $K_o = -\overline{u_1 u_2} / \overline{u_k u_k}$, $K_1 = (\overline{u_1^2} - \overline{u_2^2}) / (\overline{u_1^2} + \overline{u_2^2})$ and $K_2 = (\overline{u_1^2} - \overline{u_3^2}) / (\overline{u_1^2} + \overline{u_3^2})$, following Townsend's (1954) notation.

6. Inflow and outflow boundary and initial conditions

At the entrance to the contraction, the mean centreline velocity was $U_{co} = 10.86 \text{ m s}^{-1}$ (a), or 10.31 m s^{-1} (b); the mean shear was $(dU_1/dx_2)_o = 39 \text{ s}^{-1}$ (a), or 36 s^{-1} (b).

7. Measurements

(a) Measurement procedures

Cross-wire anemometry was used for the measurements.

(b) Measured quantities

Mean velocity profiles and the dominant Reynolds stresses were measured at different downstream stations, upstream and through the contractions. These results were used to compute the evolutions of the structural parameters and other dimensionless groups. Some inconsistencies have been noticed in the published plots of the shear stress. It would be better to disregard Figure 5 of the paper.

(c) Measurement errors

Estimated uncertainty (95% confidence level) is 2% for the mean velocity, 5% for the mean shear, 4% for the normal turbulent stress and 8% for the other stresses.

8. Available variables

Centreline evolution of the mean velocity, the mean shear and the Reynolds stresses for cases a and b.

9. Storage size required and present format of the data

Small ASCII files.

10. Contact person

Professor K.R. Sreenivasan
Department of Mechanical Engineering, Yale University
New Haven, Conn. 06520, USA
tel: (203) 432 4345
fax: (203) 432 7654
e-mail: krs@kolmogorov.eng.yale.edu

11. Main reference

SREENIVASAN, K.R. 1985 The effect of contraction on a homogeneous turbulent shear flow *J. Fluid Mech.* **154**, 187-213.

HOM27: Uniformly Sheared Flow with Uniform Curvature

Holloway & Tavoularis

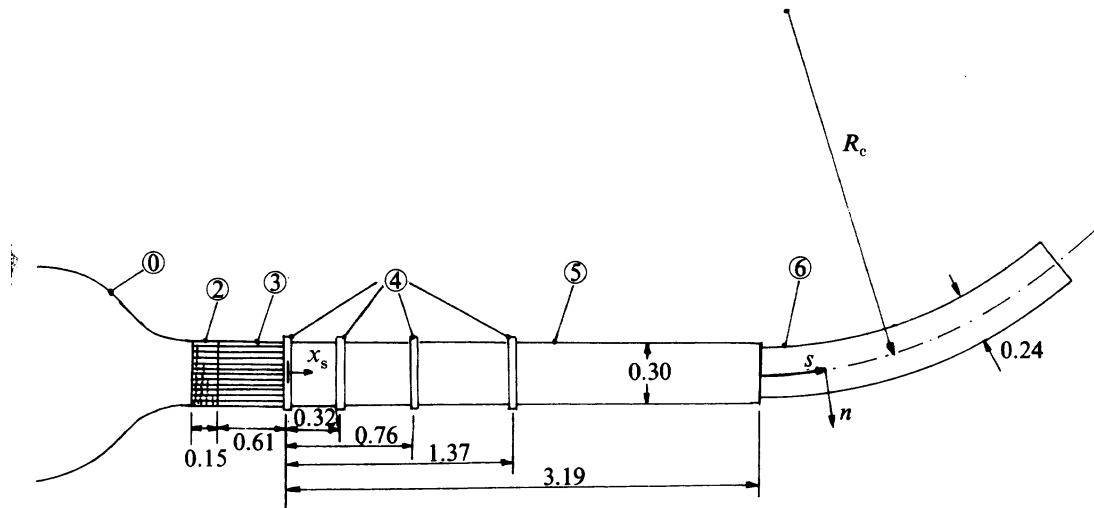
1. Description of the flow

Uniformly sheared turbulence was let to develop to an asymptotic, quasi-self-similar state in a rectilinear section and then passed through a curved section with a uniform curvature on the same plane as the mean velocity gradient.

2. Geometry

The flow was generated by a shear generator/flow separator, with a uniform channel spacing, $M = 25.4 \text{ mm}$, as in the Tavoularis and Karnik (1989) setup. The curved section was inserted at a position $10.5h_s$ downstream of the shear generator. When desired, the mean shear was reduced by the insertion of uniform grids upstream of the curved section. Two curved sections with different radii of curvature and several mean shear values were used in these experiments. The relative orientation of curvature with respect to the mean shear direction could be reversed by inverting the shear generator.

3. Original sketch



All dimensions are in meters.

4. Flow characteristics

The boundary layers were essentially removed at the entrance to the curved section, where the rectilinear shear flow had developed to its asymptotic, self-similar state, at least for the high shear cases. The wind tunnel width was gradually increased in the curved section, to partly compensate for boundary layer growth. Reasonable uniformity of the mean shear and transverse homogeneity of the turbulence were observed in all cases. The curvature enhanced or suppressed the turbulence kinetic energy and shear stress, compared to those in rectilinear shear flow subjected to the same total strain, depending on whether the *curvature parameter* $S = (U_c/R_c)/(dU/dn)$ was negative ("destabilized flow", analogous to a boundary layer over a concave wall) or positive ("stabilized flow", analogous to a boundary layer over a convex wall).

5. Flow parameters

The upstream, straight section had a height of $h_s = 305 \text{ mm}$ and a length of 3.2 m . The curved sections had a height of 240 mm and centreline radii of curvature, R_c , either 5 m (mild curvature) or 2 m (strong curvature). Ten different combinations of mean shear and radius of curvature were generated, grouped in two sets of five cases each, according to the sign of the curvature parameter S . The evolution of the various parameter is presented in terms of the *total strain* $\tau - \tau_o = (s/U_c)/(dU/dn)$, where s is the distance along the centreline of the curved section, and τ_o is the total strain in the straight section, measured from the position of insertion of the last screen.

6. Inflow and outflow boundary and initial conditions

The values of the different turbulent parameters upstream of the curved section are specified in the data files ($\tau - \tau_o < 0$).

7. Measurements

(a) Measurement procedures

Single- and cross-wire, hot-wire anemometry was used for all measurements.

(b) Measured quantities

Reynolds stresses, integral length scales and Taylor microscales along the centreline vs. streamwise distance for different mean shear rates and relative orientations of the mean shear and curvature.

(c) Measurement errors

Estimated uncertainty (95% confidence level) is 2% for the mean velocity, 5% for the mean shear, 4% for the normal turbulent stress and 8% for the other stresses.

8. Available variables

Turbulence kinetic energy, Reynolds stress anisotropies, integral length scales and Taylor microscales along the centreline vs. the total strain, $\tau - \tau_o$, for different values of the curvature parameter, S .

9. Storage size required and present format of the data

Small ASCII files.

10. Contact person

Professor Stavros Tavoularis
Department of Mechanical Engineering, University of Ottawa
Ottawa, Ontario, Canada K1N 6N5
tel/fax: (613) 562 5800 ext. 6271
e-mail: tav@eng.uottawa.ca

11. Main references

HOLLOWAY, A.G.L. & TAVOULARIS, S. 1992 The effects of curvature on sheared turbulence, *J. Fluid Mech.***237**, 569-603.

HOLLOWAY, A.G.L. & TAVOULARIS, S. 1993 Scaling and Structure of Turbulent Eddies in Curved Sheared Flows *Turbulent Shear Flows 8*, F. Durst *et al* (editors), 383-401, Springer.

HOM28: Uniformly Sheared Flow with S-Shaped Curvature

Chebbi, Holloway & Tavoularis

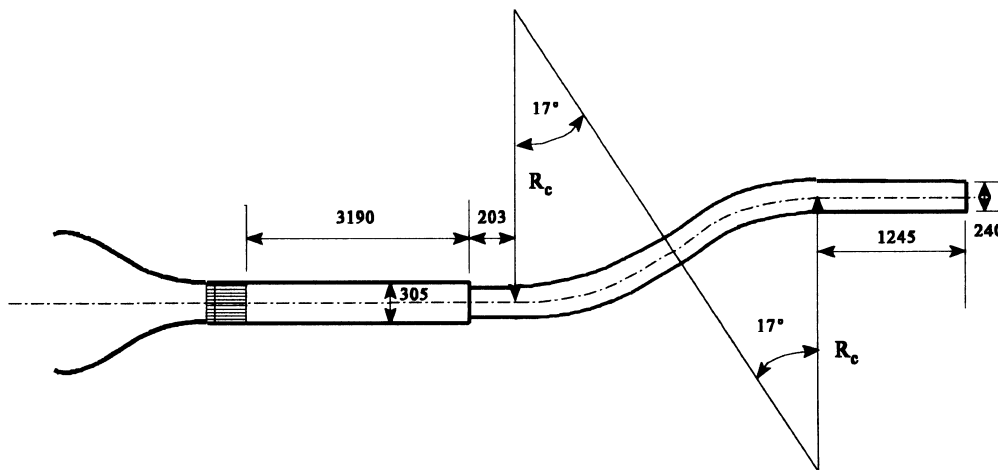
1. Description of the flow

Uniformly sheared turbulence was let to develop to an asymptotic, quasi-self-similar state in a rectilinear section and then passed through an S-shaped curved section with curvature on the same plane as the mean velocity gradient, at the end of which it relaxed in a final straight section. The specific aim of these experiments was to determine the rate at which the turbulence structure adjusts to sudden changes in curvature.

2. Geometry

The flow was generated by a shear generator/flow separator device, with a uniform channel spacing, similar to the Tavoularis and Karnik (1989) setup. The upstream, straight section had a height of $h = 305 \text{ mm}$ and a length of 3.19 m . The curved sections had a height of 240 mm and centreline radii of curvature, $R_c = 3.5 \text{ m}$. The relative orientation of curvature with respect to the mean shear direction could be reversed by inverting the shear generator.

3. Original sketch



All dimensions are in mm.

4. Flow characteristics

The boundary layers were essentially removed at the entrance to the curved section, where the rectilinear shear flow had developed to its asymptotic, self-similar. The wind tunnel width was gradually increased in the curved section, to partly compensate for boundary layer growth. The curved section was inserted far enough downstream of the shear generator for the turbulence to approach its asymptotic, self-similar structure, with nearly constant Reynolds stress anisotropies and exponentially growing stresses. Reasonable uniformity of the mean shear and transverse homogeneity of the turbulence were observed in all cases, except in the final straight section, where the boundary layers appear to be influencing the core flow. The curvature enhanced or suppressed the turbulence kinetic energy and shear stress, compared to those in rectilinear shear flow subjected to the same total strain, depending on whether the *curvature parameter* $S = (U_c/R_c)/(dU/dn)$ was negative ("destabilized flow", analogous to a boundary layer over a concave wall) or positive ("stabilized flow", analogous to a boundary layer over a convex wall).

5. Flow parameters

The incoming flow into the curved section had a curvature parameter $S \approx \pm 0.05$, depending on the orientation of the shear generator. The evolution of the various parameter is presented in terms of the dimensionless distance s/h , where s is the distance along the centreline of the curved section. Some results are presented vs. the total strain $\Delta\tau = (\Delta s/U_c)/(dU/dn)$, measured from the latest position of curvature change.

6. Inflow and outflow boundary and initial conditions

The values of the different turbulent parameters at the entrance of the curved section are specified in the data files.

7. Measurements

(a) Measurement procedures

Single- and cross-wire, hot-wire anemometry was used for all measurements.

(b) Measured quantities

Reynolds stresses, integral length scales and Taylor microscales along the centreline vs. streamwise distance for the two initial relative orientations of the mean shear and curvature.

(c) Measurement errors

Estimated uncertainty (95% confidence level) is 2% for the mean velocity, 5% for the mean shear, 4% for the normal turbulent stress and 8% for the other stresses.

8. Available variables

Turbulence kinetic energy, Reynolds stress anisotropies, integral length scales and Taylor microscales along the centreline vs. s/h , for the two initial relative orientations of the mean shear and curvature.

9. Storage size required and present format of the data

Relatively small ASCII files.

10. Contact person

Professor Stavros Tavoularis
Department of Mechanical Engineering, University of Ottawa
Ottawa, Ontario, Canada K1N 6N5
tel/fax: (613) 562 5800 ext. 6271
e-mail: tav@eng.uottawa.ca

11. Main references

CHEBBI, B., HOLLOWAY, A.G.L. & TAVOULARIS, S. 1997 The response of sheared turbulence to changes in curvature *J. Fluid Mech.* (to appear).

Data Sheets for:

Chapter 4.-Shock-wave/ grid-turbulence interaction

SHW00: Homogeneous Turbulence Interacting with a Normal Shock

Jacquin, Blin & Geffroy

- Description of the flow:** Grid-generated homogeneous turbulence in supersonic flow interacts with a normal shock-wave. The grid is located at the entrance of a supersonic wind tunnel of nearly constant cross section and constitutes the sonic throat of the tunnel. The position of the shock-wave is controlled by a second throat at the downstream end of the tunnel and by boundary-layer suction at the channel wall.
- Geometry:** The dimensions of the wind tunnel section are $0.1m \times 0.12m$; the mesh width of the turbulence grid is 7 mm. The shockwave is located at a distance of 0.25 m (i.e. 35.7 mesh widths) downstream of the turbulence grid.
- Sketch:**
- Flow characteristics:** Homogeneous turbulence interacts with a normal shock-wave in a supersonic flow. The turbulent energy follows a decay law of the form $t^{-0.83}$ upstream of the shock and $t^{-1.41}$ downstream. The shock-wave does not produce any significant amplification of the turbulent kinetic energy.
- Flow parameters:** The main parameters of the flow (ahead the shock-wave) are:
 - * Mach number: $M = 1.4$
 - * Stagnation pressure: $p_s = 0.9 \text{ bar}$
 - * Stagnation temperature: $T_s = 290 \text{ K}$
 - * Turbulent kinetic energy: $q^2/2 = 101 \text{ m}^2/\text{s}^2$
 - * Mean velocity: $U = 405 \text{ m/s}$
 - * Relative turbulence intensity: $\sqrt{q^2}/U = 0.035$
- Inflow conditions:** "Nominal" initial conditions at the shock position are:
 - * Mach number: $M = 1.4$
 - * pressure: $p = 0.283 \text{ bar}$
 - * temperature: $T = 208 \text{ K}$
 - * kinetic energy: $q^2/2 = 101 \text{ m}^2/\text{s}^2$,
 - * anisotropy: $(\overline{u^2} - \overline{v^2})/q^2 = 0.03$,
 - * dissipation rate: $\epsilon = 1.55 \times 10^5 \text{ m}^2/\text{s}^3$ (estimated from the variation of $\overline{u^2}$ assuming isotropy),
 - * Taylor microscale: $\lambda = \sqrt{5\nu q^2/\epsilon} = 0.44 \times 10^{-3} \text{ m}$,
 - * Kolmogorov lengthscale: $\eta = (\nu^3/\epsilon)^{1/4} = 2.0 \times 10^{-5} \text{ m}$,
 - * microscale Reynolds number: $Re_\lambda = \sqrt{q^2/3}\lambda/\nu = 122.8$.

7. Measured data:

Measurement procedure:

- Laser-Doppler Velocimetry in standard two-colour configuration with forward scattering;
- ONERA device with DANTEC counters LD55;
- The transverse dimension of the probe volume is about 0.2 mm;
- Samples of 2000 instantaneous values are considered for the measurements.

Measured quantities:

- axial mean velocity component U ,
- transverse mean velocity component V (negligible compared to U),

- variance of the fluctuating axial velocity component $\overline{u^2}$,
- variance of the fluctuating transverse velocity component $\overline{v^2}$.

Measurement errors

Estimated to be of the order of one percent for the mean velocities and about a few percent for the turbulence quantities. Particle-drag bias is limited to a few millimeters immediately behind the shock-wave. Errors due to the relatively low signal-to-noise ratio may be important in the very downstream part of the explored domain. It is to note that a number of 2000 samples is convenient for mean velocities, but may be too small for turbulence measurements, even in the (present) case of low turbulence intensities.

8. Available measurements

The results are given in two tables, corresponding, respectively, to the shock-free flow (Table 1) and to the shock-turbulence interaction (Table 2). All the data are given in physical dimensions. Each table includes the longitudinal position, U , V , $\overline{u^2}$, $\overline{v^2}$, and the trace of the Reynolds stress tensor, evaluated as $q^2 = \overline{u^2} + 2\overline{v^2}$.

The tabulated data represent average values from eleven axial explorations made at different heights (z) in the vertical symmetry plane ($y=0$) of the wind tunnel, between $z = -0.03$ and $+0.02$ m.

9. Size and present format of data: Modest size of data (two tables, ASCII format)

10. Contact person:

L. Jacquin
ONERA
8 rue des Vertugadins
F 92190 Meudon, France
e-mail: jacquin@onera.fr

REFERENCES

- E. BLIN 1993 Etude expérimentale de l'interaction entre une turbulence libre et une onde de choc, *Thèse de doctorat*, Université Paris 6.
- L. JACQUIN, E. BLIN, P. GEFFROY 1993 An experiment on free turbulence/shock wave interaction, *Turbulent Shear Flows 8* (Eds. Durst *et al.*) Springer, pp. 229-248

SHW01: Homogeneous turbulence interacting with a normal shock

Barre, Alem & Bonnet

1. **Description of the flow:** Homogeneous turbulence in supersonic flow is generated by means of a multi-nozzle located at the entrance of a supersonic wind tunnel. The normal shock is created by the interaction of two oblique shock waves through a Mach effect.
2. **Geometry:** The dimensions of the wind tunnel section are $0.15m \times 0.15m$; the ‘mesh width’ of the multinozzle turbulence generator is 6 mm. The mesh width is defined as the square root of the ratio between the cross section of the turbulence generator and the total number of micro-nozzles. The shock wave is located at a distance of 0.46 m (i.e. 76.7 mesh widths) downstream of the turbulence grid.
3. **Sketch:**
4. **Flow characteristics:** Homogeneous turbulence convected at high supersonic speed (Mach number = 3) interacts with a normal shock-wave. The decay of the turbulent energy is characterized by a law of the form $t^{-0.79}$, similar to that found in the ONERA experiment. The shock-wave increases (as expected) the axial velocity fluctuations, in accordance with DNS results, and decreases the axial integral lengthscale.
5. **Flow parameters:** The main parameters of the flow (ahead the shock-wave) are:

- * Mach number: $M = 3.0$
- * Stagnation pressure: $p_s = 0.9 \text{ bar}$
- * Stagnation temperature: $T_s \approx 240 \text{ K}$
- * Turbulent kinetic energy: $q^2/2 = 2.02 \text{ m}^2/\text{s}^2$
- * Mean velocity: $U = 550 \text{ m/s}$
- * Relative turbulence intensity: $\sqrt{q^2}/U = 0.004$

6. **Inflow conditions:** “Nominal” initial conditions at the shock position are:

- * Mach number: $M = 3.0$
- * pressure: $p = 0.0245 \text{ bar}$
- * temperature: $T = 86 \text{ K}$
- * kinetic energy: $q^2/2 = 2.02 \text{ m}^2/\text{s}^2$,
- * anisotropy: $(\overline{u^2} - \overline{v^2})/q^2 \approx 0$,
- * dissipation rate: $\epsilon = 1.91 \times 10^3 \text{ m}^2/\text{s}^3$ (estimated from the variation of $\overline{u^2}$ assuming isotropy),
- * Taylor microscale: $\lambda = \sqrt{5\nu q^2/\epsilon} = 0.79 \times 10^{-3} \text{ m}$,
- * Kolmogorov lengthscale: $\eta = (\nu^3/\epsilon)^{1/4} = 1.0 \times 10^{-4} \text{ m}$,
- * microscale Reynolds number: $Re_\lambda = \sqrt{q^2/3}\lambda/\nu = 15.5$
- * turbulence Mach number: $u'/a = 0.006$
- * longitudinal integral scale: $L_u = 3.4 \times 10^{-3} \text{ m}$

7. **Measured data:**

Measurement procedure:

Hot-wire anemometry and Laser-Doppler velocimetry have been used:

Hot-wire anemometry: DANTEC 55M10 constant-temperature anemometer with 55M12 bridge; DANTEC 55P11 probes equipped with $2.5 \mu\text{m}$ wires (bandwidth $\leq 300 \text{ kHz}$).

Laser-Doppler velocimetry: Two-colour configuration with forward scattering; data processing with Aerometrics DSA system.

Measured quantities:

- axial mean velocity component U ,
- transverse mean velocity component V (negligible compared to U),
- variance of the fluctuating axial velocity component $\overline{u^2}$,
- variance of the fluctuating transverse velocity component $\overline{v^2}$,
- spectra of hot-wire signals (representing mass flux fluctuations),
- lengthscales $L_u (= L_{11,1})$ deduced from autocorrelations of the hot-wire signal.

Measurement errors:

Hot-wire measurements: Estimated to be of the order of one percent for the mean velocities and about a few percent for the turbulence quantities.

LDV measurements: Estimated to be of the order of 10 percent. Errors due to particle drag are estimated to be negligible downstream of 4 mm behind the shock.

8. Available measurements:

Data are given both for shock-free flow and shock/turbulence interaction:

For the shock-free case: U , $\overline{u^2}/U^2$, the longitudinal integral scale L_u , the ratio $\overline{u^2}/\overline{v^2}$, representing the anisotropy, and the correlation coefficient $R_{uv} = \overline{uv}/\sqrt{\overline{u^2}\overline{v^2}}$, as a function of the longitudinal distance from the grid;

For the case with shock: U , V , $\overline{u^2}$, $\overline{v^2}$, L_u , skewness and flatness factors for the longitudinal velocity, and the trace of the Reynolds stress tensor, evaluated as $q^2 = \overline{u^2} + 2\overline{v^2}$, as a function of the distance from the shock.

Hot-wire spectra measured upstream and downstream of the shock are also given.

9. Size and present format of data: Modest size ASCII file.**10. Contact person:**

S. Barre
LEA/CEAT
43 rue de l'Aérodrome
F 86000 Poitiers, France
e-mail: barre@univ-poitiers.fr

REFERENCES

D. ALEM 1995 Analyse expérimentale d'une turbulence homogène en écoulement supersonique soumise à un choc droit. *Thèse de doctorat*, Université de Poitiers.

S. BARRE, D. ALEM, J.P. BONNET 1996 Experimental study of normal shock/homogeneous turbulence interaction, *AIAA J.* **34**, 968-974

Data Sheets for:
Chapter 5.- Pipes and Channels

PCH00: Fully Developed Turbulent Pipe Flow Simulation

Loulou, Moser, Mansour & Cantwell

1. **Description of the flow:** The flow is a numerically simulated, pressure-gradient driven fully-turbulent, statistically stationary pipe flow.
2. **Geometry:** The flow is in a smooth cylindrical pipe with a uniform pressure gradient. The domain is formally infinite in the streamwise direction, though only a finite domain is simulated (see §7).
3. **Sketch:** None needed
4. **Flow characteristics:** Fully developed pipe flow exhibits the usual characteristics of wall-bounded turbulent flows. However, the Reynolds number in this case is low enough to produce low-Reynolds number effects. For example, turbulent kinetic energy production does not equal dissipation anywhere in the flow.
5. **Flow parameters:** Various measures of the flow Reynolds number are $Re_b = 5600$, $Re_c = 7248$, $Re_\tau = 380$ and $C_f = 9.16 \times 10^{-3}$. Reynolds numbers are based on bulk velocity, centreline velocity and friction velocity respectively, and the diameter.
6. **Numerical methods and resolution:** The numerical method uses Fourier expansions to represent the azimuthal and streamwise directions. Near-spectral resolution is achieved using b-spline (basis-spline) polynomials in the radial direction. The computation is carried out on a grid of $72 \times 160 \times 192$ (radial, azimuthal and axial) modes for a total of 2.2 million Fourier/b-spline modes with quartic b-splines. A non-uniform grid is used in the radial direction based on an exponential function. The first point away from the wall is at $r^+ = 0.39$ while near the center of the pipe $\Delta r^+ = 5.7$. A finer grid is used very close to the centre of the pipe where regularity conditions are imposed. See Loulou *et al* (1997) for details.
7. **Boundary and initial conditions:** The pipe walls are treated as no-slip boundaries. The no-slip condition is imposed exactly on the b-spline expansion. In the streamwise direction, the domain is truncated to a finite size and periodic boundary conditions are imposed. The length of the computational domain is $5D$. Since the flow is statistically stationary and has periodic boundary conditions in the streamwise direction, the initial conditions are irrelevant, and there is no need for inlet conditions.
8. **Averaging procedures and uncertainties:** Turbulence statistics are obtained by using 46 different fields approximately equispaced in time and averaged over a period of 43 time units (D/U_b). Statistical steady state is assumed to have been reached when the total shear stress reaches a linear function of radius to within a mean deviation of 0.5%. Comparisons with single-point statistics are, on the whole, excellent with the exception of higher moments of the radial velocity near the wall where some discrepancies between simulations and experiment are observed. See Loulou *et al* (1997) for extensive comparisons to experimental data (Eggels *et al*, 1994, Westerweel *et al*, 1997, Durst *et al* 1995) and other computations (Eggels *et al*, 1994, Kim *et al*, 1987).

Correlations of the velocity show that velocity fluctuations remain slightly correlated for large streamwise separations suggesting that the domain length of $5D$ may be too small to permit adequate comparisons with experiments carried out in much longer pipes. However, this uncertainty will not affect comparisons to LES simulations if the same domain size is used.
9. **Available variables:** The following data are available: 1) Mean velocity, vorticity and pressure, 2) Reynolds shear stress, 3) Skewness and Flatness, 4) Reynolds stress, kinetic energy and dissipation budgets, 5) Streamwise and azimuthal velocity spectra of all three components, 6) Streamwise and azimuthal vorticity spectra of all three components,
10. **Storage size and data format:** Format is ASCII, requiring approximately 1 MB of total storage.
11. **Contact person:**

Brian Cantwell
271 Durand, Stanford University, Stanford, CA 94305, USA
Phone: (415)-723-4825
Fax: (415)-725-3377
E-mail: cantwell@leland.stanford.edu

REFERENCES

- DURST, F., JOVANOVIĆ, J. & SENDER, J. 1995 LDA measurements in the near-wall region of a turbulent pipe flow. *J. Fluid Mech.* **295**, 305–335.
- EGGELS, J. G. M., UNGER, F., WEISS, M. H., WESTERWEEL, J., ADRIAN, R. J., FRIEDRICH, R. & NIEUWSTADT, F. T. M. 1994 Fully developed turbulent pipe flow: a comparison between direct numerical simulation and experiment. *J. Fluid Mech.* **268**, 175–209.
- KIM, J., MOIN, P. & MOSER, R. D. 1987 Turbulence statistics in fully developed channel flow at low Reynolds number. *J. Fluid Mech.* **177**, 133–166.
- LOULOU, P., MOSER, R., MANSOUR, N. & CANTWELL, B. 1997 Direct simulation of incompressible pipe flow using a b-spline spectral method. Technical Report TM 110436, NASA.
- WESTERWEEL, J., DRAAD, A. A., VAN DER HOEVEN, J. G. TH. & VAN OORD, J. 1997 Measurements of fully developed turbulent pipe flow with digital particle image velocimetry. To appear in *Exper. in Fluids*.

PCH01: Turbulent Pipe Flow Experiments

Durst, Jovanovic & Sender

1. **Description of the flow:** This case is a fully developed turbulent pipe flow at low to moderate Reynolds number.
2. **Geometry:** The flow is in a smooth cylindrical pipe with $L/D = 80$.
3. **Sketch:** None needed
4. **Flow characteristics:** Fully developed, smooth wall, turbulent pipe flow is generated in an 80 diameter long pipe. Although the L/D is marginal for attaining a fully developed flow, the required development distance is reduced somewhat by the use of a trip at the pipe entrance. The assumption of fully developed flow is not as well established for this case as for the other pipe flow cases.
5. **Flow parameters:** In this case, $Re_b = 7442, 13500$ and $20,800$. For $Re_b = 7442$, we get $Re_\tau = 500$ and $C_f = 9.03 \times 10^{-3}$. Re_b and Re_τ are based on diameter and bulk and friction velocities respectively.
6. **Inflow, outflow, boundary and initial conditions:** The flow is tripped at the pipe entrance. A screw conveyer pump, which generates very low flow rate pulsations, is used in suction mode to draw fluid through the test section.
7. **Measurement procedures:** The measurements were carried out using Laser Doppler Anemometry applied to a 50mm diameter glass pipe mounted in a rectangular viewing box. The pipe and viewing box are filled with a working fluid composed of a mixture of Diesel oils whose index of refraction is matched to the pipe. The temperature of the working fluid is controlled by heating and cooling units installed in the upstream and downstream settling chambers of the test rig. The measuring volume was measured to be 70 microns in diameter and 250 microns in length. The data is corrected for bias due to the finite size of the measuring volume. Strategies are used to minimize errors due to measuring angle misalignment and electronic noise resulting in accurate mean velocity data down to $y^+ = 0.5$ at $Re_b = 7442$. See Durst *et al*(1995) for details.

The time interval between samples was set close to the integral time scale, D/U_c , and a sample size of 40,000 was used giving a relatively low statistical uncertainty. Estimated errors are: mean $< 0.28\%$, turbulent intensities $< 1\%$, flatness $< 2.3\%$. It may be that the potential lack of fully developed flow results in larger uncertainties than these.
8. **Available variables:** The following data are available: mean, r.m.s., skewness and flatness of all three velocity components.
9. **Storage size and data format:** The data is in ASCII format and comprises less than 1 Mb of storage.
10. **Contact person:** Franz Durst
Lehrstuhl für Strömungsmechanik, Universität Erlangen-Nürnberg
Cauerstrasse 4, D-91058 Erlangen, Germany

REFERENCES

DURST, F., JOVANOVIĆ, J. & SENDER, J. 1995 LDA measurements in the near-wall region of a turbulent pipe flow. *J. Fluid Mech.* **295**, 305–335.

PCH02: Turbulent Pipe Flow Experiments

Perry, Henbest & Chong

1. **Description of the flow:** This case is a fully developed incompressible turbulent pipe flow, both smooth and rough wall data are included.

2. **Geometry:**

The apparatus consists of a long cylindrical pipe fitted with an upstream axisymmetric settling chamber and 27:1 contraction. The settling chamber consists of honeycomb flow straighteners and 4 screens.

Smooth Pipe: Precision-drawn brass tubing with an internal diameter of 0.099 m, and a length of 41.17 m. Measuring station: $L/D = 398.5$. Static pressure locations: $L/D = 49.2, 109.9, 170.5, 231.1, 291.7, 352.3$. The smooth wall flow was tripped using a sandpaper strip, 50 grit and 15 cm long.

Rough Pipe: "k-type" roughness (0.25 mm height, 2.5 mm cell size, woven fabric wedding veil glued to the inside of the pipe). Internal Diameter, 0.101 m; length, 41.14 m; measuring station, $L/D = 390.7$; static pressure locations, $L/D = 46.1, 50.3, 176.8, 206.5, 226.5, 285.7, 345.1$. Static pressure probes were used, rather than taps, 2.0 mm diameter hypodermic tubing 20 mm off the wall.

3. **Sketch:** None needed

4. **Flow characteristics:** Both smooth and rough wall cases are fully developed.

5. **Flow parameters:** In the smooth wall pipe, data is available at Reynolds numbers $Re_c = 75,000, 100,000, 125,000, 150,000, 175,000, 200,000$ which is $Re_\tau = 1610, 2080, 2550, 3010, 3420, 3900$, respectively.

In the rough wall case, the same centreline Reynolds numbers are available, which correspond to $Re_\tau = 1670, 2380, 2920, 3515, 4140, 4710$, respectively. Reynolds numbers are based on centreline or friction velocities and diameter.

6. **Inflow, outflow, boundary and initial conditions:** The apparatus consists of a long cylindrical pipe fitted with an upstream axisymmetric settling chamber and 27:1 contraction. The settling chamber consists of honeycomb flow straighteners and 4 screens. The smooth wall flow was tripped using a sandpaper strip (50 grit, 15 cm long). Flow in the pipe exits into a centrifugal fan. The pipe is expected to be fully developed at the measurement station.

7. **Measurement procedures:** All measurements were taken at approximately 400 diameters from the pipe entrance. Mean flow profiles were measured with pitot-static tubes. Pressure drop was measured along the pipe using static taps. Results were corrected for small density changes along the pipe due to compressibility effects. Wall friction was inferred from the pressure drop measurements. Turbulence measurements and spectra were measured using cross-wires. Hot-wires were calibrated using a dynamic calibration system giving very accurate turbulence intensity measurements.

For the rough wall pipe, pressure drop was measured using a static pressure probe protruded 20 mm from the wall. A normal wire (DISA normal boundary layer probe, type 55P05) was also used in addition to an in-house-built X-wire.

The pressure drop and Pitot-static tube mean flow data were monitored using a Datametric Barocell pressure transducer (model 1014A), the output voltage of which was integrated on an EAI TR-20 analogue computer. The pressure drop data was sampled for at least 15 seconds. For mean flow, 3 samples of 15 second data were ensemble averaged. The accuracy of mean flow measurements and wall shear-stress is estimated to be within 0.5%.

All hot-wire signals were processed on line using a TR-20 analogue computer together with a DEC PDP 11/10 digital computer (12 bit resolution). Reynolds stress data was averaged from 8 bursts of 8000 data points sampled at 200 Hz. The accuracy of dynamically calibrated Reynolds stresses is estimated to be within 2.5%.

The traversing mechanism was accurate to within 0.05 mm. See Henbest (1983) and Perry *et al*(1986) for details.

8. **Available variables:** Mean streamwise velocity and skin friction.

9. **Storage size and data format:** The data is in ASCII format and requires approximately 100 Kb of storage.

10. **Contact person:**

Anthony E. Perry

Department of Mechanical and Manufacturing Engineering The University of Melbourne
Parkville, Victoria, 3052, Australia.

REFERENCES

HENBEST, S. M. 1983 PhD thesis, University of Melbourne.

PERRY, A. E., HENBEST, S. M. & CHONG, M. S. 1986 A theoretical and experimental study of wall turbulence. *J. Fluid Mech.* **165**, 163–199.

PCH03: Turbulent Pipe Flow Experiment

den Toonder & Nieuwstadt

1. **Description of the flow:** This case is a fully developed turbulent flow in a smooth circular pipe at moderate Reynolds number.
2. **Geometry:** The geometry is a cylindrical pipe with a diameter of 4 cm and a total length of 34 m ($L/D = 850$).
3. **Sketch:** None needed.
4. **Flow characteristics:** Fully developed turbulent pipe flow exhibits all the usual features of wall-bounded turbulent flows.
5. **Flow parameters:** The working fluid is water at a temperature $T = 16.6C$, ($\rho = 998.9\text{kg/m}^3$ and $\nu = 1.09 \times 10^{-6}\text{m}^2/\text{sec}$). The Reynolds number is $Re_b = 24,580$ and $Re_\tau = 1382$ (based on diameter and bulk or friction velocities respectively).
6. **Inflow, outflow, boundary and initial conditions:** The flow is tripped at the pipe entry. All experimental data are taken at a position where the flow can be considered fully developed.
7. **Measurement procedures:** Measurements were carried out using a two-component laser Doppler anemometer. The authors suggest using a wall position correction of $\Delta r = -2.92 \times 10^{-5}$ m with the uncorrected data provided.
The sampling frequency was 60 Hz and measuring time per position: 300 s. Hence, typically 1800 samples per position were taken, fewer close to the wall.
Uncertainties were computed in a standard way per position and are included in the data file. Relative errors are approximately 0.4% for the mean velocity and 1% for the r.m.s. velocity.
See den Toonder (1995) for more details.
8. **Available variables:** Axial and radial components of mean and r.m.s. velocity, skewness and flatness, turbulent shear stress $\tau_t = \overline{uv}^+$, viscous shear stress $\tau_v = -dU_z^+/dr^+$, and non-dimensionalized production of turbulent energy $P_{zz} = -\tau_t dU_z^+/dr^+$ are all provided as a function of both r^+ and r/D ; as are the relative statistical errors in the mean, r.m.s. velocities, flangeless, and τ_t .
9. **Storage size and data format:** Data is in ASCII format, requiring approximately 100 kB of storage.
10. **Contact person:**
Dr. Jaap M. J. den Toonder
Philips Research Laboratories
Prof. Holstlaan 4, 5656 AA Eindhoven, The Netherlands
Phone: +31-40-2742185
Fax: +31-40-2744288
e-mail: toonder@natlab.research.philips.com

REFERENCES

DEN TOONDER, J. M. J. 1995 *Drag reduction by polymer additives in a turbulent pipe flow: laboratory and numerical results*. Ph. D. thesis, Delft University of Technology.

PCH04: Turbulent Pipe Flow Experiments (Superpipe)

Zagarola & Smits

1. **Description of the flow:** This case is a fully developed turbulent pipe flow with Reynolds number varying by 3 orders of magnitude.
2. **Geometry:** The experiments are carried out in a cylindrical aluminium pipe with a diameter of 12.7 cm and a total length of 2603.27 cm ($L/D = 205$). The wall is polished smooth over its full length to a roughness measure of approximately 0.15 micron rms.
3. **Sketch:** None needed.
4. **Flow characteristics:** Fully developed pipe flow exhibits the usual features of wall-bounded turbulent flows.
5. **Flow parameters:** The experiments were performed in a test pipe enclosed within a pressure vessel. The working fluid is air at pressures ranging from 1 to 189 atmospheres. Test Reynolds numbers range from $Re_b = 31,500$ to 35,259,000 ($Re_\tau = 1700$ to 10^6). Reynolds numbers based on diameter and bulk velocity (or friction velocity). Detailed gas property and mean flow parameter information is provided with each velocity profile.
6. **Inflow, outflow, boundary and initial conditions:** The flow at the pipe entry is free of swirl and has a relatively high turbulence level. This insures fully developed flow at the measuring stations in the absence of an entry trip.
7. **Measurement procedures:** Both the flow rate and gas density were varied to achieve the set of test Reynolds numbers. Gas temperatures remained close to ambient. Mean velocity profiles were measured by traversing a 0.9 mm diameter Pitot tube across 75% of the pipe. Static pressure measurements were taken at twenty 0.8mm diameter wall taps equally spaced over a 25 diameter long section between the secondary measuring station at 2072.67 cm and the primary measuring station at 2532.56 cm. The test air was filtered and dried to produce a water content of approximately 14 ppm. With the whole system under pressure, the flow through the pipe was generated using a vertical turbine pump driven by a variable speed motor.

Typical sampling rates for the Pitot tube were at 500 samples/sec with sampling periods of approximately 30 sec. The tabulated data is not corrected for the effects of probe displacement although several correction methods are discussed in Zagarola (1996). A complete uncertainty analysis is also given in Zagarola (1996). The uncertainty in the mean velocity is estimated to be 0.3%. The uncertainty in the friction factor is estimated at 1.1%. For more details see Zagarola (1996) and Zagarola & Smits (1997).
8. **Available variables:** The data consists of a set of mean velocity profiles at 26 Reynolds numbers. Header information for each profile includes gas properties, friction velocity and compressibility factor.
9. **Storage size and data format:** Data is in ASCII files, requiring approximately 130 Kb of storage.
10. **Contact person:** Prof. Alexander J. Smits
Director, Gasdynamics Laboratory, Department of Mechanical and Aerospace Engineering
Princeton University, Princeton, NJ 08544, USA
Tel: (609) 258 5117; Fax: (609) 258 2276
E-mail: asmits@pucc.princeton.edu
http://www.princeton.edu/gasdyn/People/Lex_Smits.html

REFERENCES

- ZAGAROLA, M. 1996 *Mean-flow scaling of turbulent pipe flow*. Ph. D. thesis, Department of Aerospace and Mechanical Engineering, Princeton University, Reference number 2053-T.
- ZAGAROLA, M. V. & SMITS, A. J. 1997 Experiments in high Reynolds number turbulent pipe flow, *Phys. Rev. Lett.* **78**.

PCH05: Rotating Turbulent Pipe Flow Simulation

Orlandi & Fatica

1. **Description of the flow:** The flow is a direct simulation at low Reynolds number of smooth wall pipe flow with the pipe rotating about its centreline axis.
2. **Geometry:** The flow is in a smooth cylindrical pipe with a uniform pressure gradient. The domain is formally infinite in the streamwise direction, though only a finite domain is simulated (see §7).
3. **Sketch:** None needed.
4. **Flow characteristics:** Fully developed pipe flow exhibits the usual features of wall-bounded turbulence. When the pipe rotates a drag reduction is achieved and for high rotation rates the mean streamwise velocity tends to the parabolic laminar Poiseuille profile.
5. **Flow parameters:** The Reynolds number is $Re_b = 4900$ and data for four rotation numbers are provided, $Ro_b = 0, 0.5, 1$ and 2 , where $Ro_b = D\Omega/U_b$.
6. **Numerical methods and resolution:** The N-S equations, in primitive variables and in cylindrical coordinates, are solved by a second-order finite difference method on a staggered grid. For the details of the numerical method see Verzicco & Orlandi (1996) The resolution used is $128 \times 96 \times 257$ points (in the azimuthal, radial and axial direction) for a pipe of length $L = 7.5D$.
7. **Boundary and initial conditions:** The pipe walls are treated as no-slip boundaries. In the streamwise direction, the domain is truncated to a finite size and periodic boundary conditions are imposed. The length of the computational domain is $7.5D$.
Since the flow is statistically stationary and has periodic boundary conditions in the streamwise direction, the initial conditions are irrelevant, and there is no need for inlet conditions.
8. **Averaging procedures and resulting uncertainties:** Averaging is performed once the mean profile reaches a steady-state. Averages are done as a post-processing procedure on fields separated by a $\Delta t = 2D/U_b$ dimensionless time units. For $N=0$, 25 fields are sufficient. For $N=2$ the number of fields increases up to 65. The physical reasons for a larger number of fields is related to the elongated helical structures in the central region of the pipe.
9. **Available variables:** Mean axial, radial, tangential velocities and pressure. Turbulent statistics profiles, such as second order one-point velocity and vorticity correlations, skewness, flatness, enstrophy, helicity and Lamb vector components.
10. **Storage size and data format:** Data is in ASCII format requiring approximately 1Mb of storage.
11. **Contact person:** Prof. Paolo Orlandi
Dip. Meccanica e Aeronautica, Univ. di Roma "La Sapienza"
e-mail: orlandi@orlandisun.ing.uniroma1.it

REFERENCES

- ORLANDI, P. 1997 Helicity fluctuations and turbulent energy production in rotating and non-rotating pipes, *Phys. Fluids* **9**, To appear.
- ORLANDI, P. & FATICA, M. 1997 Direct simulation of a turbulent pipe rotating along the axis. *J. Fluid Mech.* **343**, 43–72.
- VERZICCO & ORLANDI, P. 1996 A finite-difference scheme for three-dimensional incompressible flows in cylindrical coordinates, *J. Comp. Phys.* **123**, 402.

PCH10: Fully Developed Turbulent Channel Flow Simulations

Mansour, Moser & Kim

1. **Description of the flow:** The flow is a numerically simulated, pressure-gradient driven, fully-turbulent, statistically stationary channel flow.
2. **Geometry:** The channel flow is the flow between two parallel walls separated by a distance 2δ . It is driven by a uniform streamwise pressure-gradient, which is varied in time to maintain a constant mass flux. The streamwise and spanwise directions are formally infinite, though only a finite domain is simulated (see §7).
3. **Sketch:** None needed.
4. **Flow characteristics:** The flows exhibit all the usual characteristics of wall bounded turbulent flows. The Reynolds numbers are sufficiently high for a small region to exist where the production and dissipation rate of turbulent kinetic energy are almost equal.
5. **Flow parameters:** The only relevant parameter in this flow is the Reynolds number. In the two cases, $Re_\tau = 395$ and 590 ($Re_b = 6875$ and 10935), where the Reynolds numbers are based on half-width and friction (or bulk) velocity. The lower Reynolds number case ($Re_\tau = 395$) was computed by Kim (1990, unpublished). The data were used in Rodi & Mansour (1993), and are reported along with the high Reynolds number ($Re_\tau = 590$) data in Mansour et al. (1997).
6. **Numerical methods and resolution:** The direct numerical simulations were performed using the spectral numerical method of Kim, Moin & Moser (1987). The method makes use of Fourier expansions in the streamwise and spanwise directions and a Chebychev representation in the wall-normal direction. The incompressible Navier-Stokes equations are formulated using a toroidal/poloidal decomposition, in which the pressure is eliminated and incompressibility is imposed exactly. See Kim *et al* (1987) for details.

The number of Fourier/Chebychev modes used in each simulation are shown in table 1, along with the resulting streamwise and spanwise grid spacing in plus units (the Nyquist grid spacing associated with the highest wavenumber Fourier mode). Also shown in table 1 is the equivalent grid spacing (an effective Nyquist spacing) in the y direction at the centre of the channel. An estimate of the y resolution as a function of y location is given by $\Delta y^+(y) \approx \Delta y_c^+ \sqrt{1 - y^2}$, where y goes from -1 at one wall to 1 at the other.

7. **Boundary and initial conditions:** The two walls of the channel are treated as no-slip boundaries. The no-slip condition is imposed exactly on the Chebychev expansion. In the streamwise and spanwise directions the domain is truncated to a finite size and periodic boundary conditions are imposed. The domain sizes are shown in table 1.

Since the flow is statistically stationary and has periodic boundary conditions in the streamwise direction, the initial conditions are irrelevant, and there is no need for inlet conditions.

8. **Averaging procedures and resulting uncertainties:** All the data provided from these simulations are obtained by computing the appropriate quantities from the simulated velocity fields and averaging in the homogeneous spatial directions x and z and time. The averages in time are taken over approximately 50 widely spaced velocity fields in each case.

There are three potential sources of uncertainties in this data. First is the numerical discretization errors introduced in the numerical simulations. These uncertainties should be negligible. The second uncertainty is statistical, which arises from computing the averages over a finite domain size and a finite time. An estimate of the magnitude of this error can be obtained by realizing that the ideal profiles will be either even or odd in y , depending on the quantity. Departure from this ideal behaviour provides an estimate of the error. In particular, if the profile of a quantity q should be even (for example), then the magnitude of the odd part $((q(y) - q(-y))/2)$ relative to the even part $((q(y) + q(-y))/2)$ is an estimate of the relative error due to limited statistical sampling. Such estimates can be computed from the data provided. The third source of errors is due to the finite domain size of the numerical simulation, though the domain sizes were selected to ensure that this uncertainty is small. This is an error only if one takes the view that the simulations are a model for an ideal flow in a streamwise and spanwise infinite domain. However, if an LES is done in the same domain with the same periodic boundary conditions, than a comparison can be made without error due to the domain size.

Re_τ	L_x	L_z	$N_x \times N_y \times N_z$	Δx^+	Δz^+	Δy_c^+
395	$2\pi\delta$	$\pi\delta$	$256 \times 193 \times 192$	10.0	6.5	6.5
590	$2\pi\delta$	$\pi\delta$	$384 \times 257 \times 384$	9.7	4.8	7.2

Table 1: Simulation parameters for the two channel direct numerical simulations. The Reynolds number Re_τ is based on the friction velocity u_τ and δ .

9. **Available variables:** For both cases, profiles of the mean velocity $U(y)$, the velocity variances ($\overline{u^2}$, $\overline{v^2}$, $\overline{w^2}$), and Reynolds stress \overline{uv} as well as dissipation (ϵ). In addition, the triple velocity correlations appearing in the Reynolds stress balance equations are provided. Furthermore, streamwise and spanwise one-dimensional spectra of the three velocity components are provided at several y locations. Note that all of these data are computed from unfiltered velocity fields, so care must be exercised when comparing these data directly to LES results. In addition, higher order moments such as triple correlations are more sensitive to finite statistical samples, so the uncertainties in these quantities are larger. Finally, the small separation velocity-velocity two-point correlation required to compute filtered versions of the second order statistical profiles as described in Chapter 3 in the database document are provided.
10. **Storage size and data format:** There are four profile files containing mean velocity, velocity variance dissipation and triple correlation data in ASCII (270 Kb). In addition, there is a binary file containing the small-separation two-point correlations needed to compute filtered quantities. Total data size: 23 Mbytes.

11. **Contact person:**

Nagi N. Mansour
 NASA Ames-Research Center, Moffett Field, CA 94035, USA
 Phone: (415)-604-6420
 E-mail: nmansour@mail.arc.nasa.gov

or

Robert D. Moser
 Dept. Theoretical and Applied Mechanics, University of Illinois
 104 S. Wright St., Urbana, IL 61801 USA
 Phone: (217)-244-7728
 E-mail: r-moser@uiuc.edu

REFERENCES

- KIM, J., MOIN, P. & MOSER, R. D. 1987 Turbulence statistics in fully developed channel flow at low Reynolds number, *J. Fluid Mech.* **177**, 133–166.
- MANSOUR, N. N., MOSER, R. D. & KIM, J. 1997 Reynolds number effects in low Reynolds number turbulent channels, in preparation.
- RODI, W. & MANSOUR, N. N. 1993 Low Reynolds number $k-\epsilon$ modeling with the aid of direct simulation data, *J. Fluid Mech.* **250**, 509.

PCH11: Fully Developed Turbulent Channel Flow Experiment

Niederschulte, Adrian & Hanratty

1. **Description of the flow:** The flow is a fully developed turbulent flow in rectangular channel.
2. **Geometry:** The channel is rectangular with aspect ratio 12:1 (24 inches by 2 inches). The measurement station was located 394δ (394 inches) down stream of the channel inlet and trip, and in the centre of the span of the channel, see Niederschulte (1988) and Niederschulte, Adrian & Hanratty (1990) for details.
3. **Sketch:** None needed.
4. **Flow characteristics:** The flow exhibits all the usual characteristics of wall bounded turbulent flows.
5. **Flow parameters:** The only relevant parameter in this flow is the Reynolds number, which is $Re_b = 18,339$ or $Re_\tau = 921$. The working fluid is water at 25°C .
6. **Inflow, outflow, boundary and initial conditions:** The top and side walls of the channel are rigid and conform to the design dimensions to within 0.01%. The boundary layers at the inlet of the channel are tripped, and the development length of 394δ is sufficiently long for the channel to be fully developed.
7. **Measurement procedures:** The velocity was measured using a 2-component LDV system with a measuring volume that is 35 microns in diameter and 300 microns long. The configuration was designed to permit accurate measurement of the velocity profile near the wall, without correction for the size of the measurement volume. Water in the channel was filtered and seeded with 0.5 micron particles such that there would be an insignificant probability of more than one particle appearing in the measurement volume, while still providing a near continuous signal. The data were taken with a very high sample rate (500 Hz) to eliminate all questions of velocity biasing associated with low data density in LDV measurements. See Niederschulte (1988) and Niederschulte *et al*(1990) for further details of the measurement procedures.

In the near-wall region ($y^+ < 20$) there is an apparent increase in the rms velocity due to noise caused by optical flare from the wall. Data below $y^+ = 20$ should not be considered valid.
8. **Available variables:** The streamwise and cross stream velocities were measured. Mean, r.m.s. velocity, Reynolds stress and skewness and flatness profiles at selected y locations are included.
9. **Storage size and data format:** There is a single ASCII data file containing the profile data. Total data size: 5kb.
10. **Contact person:** Prof. Ron Adrian
Dept. Theoretical and Applied Mechanics, University of Illinois
104 S. Wright St., Urbana, IL 61801 USA
Phone: (217)-333-1793
E-mail: r-adrian@uiuc.edu

REFERENCES

- NIEDERSCHULTE, M. A., ADRIAN, R. J. & HANRATTY, T. J. 1990 Measurements of turbulent flow in a channel at low Reynolds number. *Exp. in Fluids* **9**, 222–230.
- NIEDERSCHULTE, M. A. 1988 *Turbulent Flow Through a Rectangular Channel*. Ph. D. thesis, Department of Chemical Engineering, University of Illinois at Urbana-Champaign.

PCH12: Fully Developed Turbulent Channel Flow Experiments

Wei & Willmarth

1. **Description of the flow:** The flow is a fully developed turbulent flow in rectangular channel.
2. **Geometry:** The channel is rectangular with aspect ratio 11.9:1 (30.48 cm by 2.572 cm). The measurement station was located 173δ down stream of the channel inlet, and in the centre of the span of the channel, see Wei & Willmarth (1989) for details.
3. **Sketch:** None needed.
4. **Flow characteristics:** The flow exhibits all the usual characteristics of wall bounded turbulent flows.
5. **Flow parameters:** The only relevant parameter in this flow is the Reynolds number, which for the three cases included here is $Re_c = 14914, 22776$ and 39580 , $Re_b = 13145, 20197$ and 35353 , or $Re_\tau = 708, 1017$ and 1655 . Reynolds numbers are based on half-width (δ) and centreline, bulk or friction velocities respectively. The working fluid is water.
6. **Inflow, outflow, boundary and initial conditions:** The top and side walls of the channel are rigid and conform to the design dimensions to within 0.25%, and the development length was 173δ from the channel inlet. This should be sufficiently long for the channel to be fully developed.
7. **Measurement procedures:** Velocities were measured using a high spatial and temporal resolution two colour, two component LDA Wei & Willmarth (1989). The LDA measurement volume was formed by crossing four laser beams, two green and two blue, within a 50 micrometer diameter sphere. This translates to a spatial resolutions of 2.76, 3.94, and 6.43 viscous units for the three Reynolds numbers, respectively. The flow was seeded using 3 micrometer diameter titanium dioxide particles. Statistically long, time resolved data records were taken at a number of distances from the wall for each Reynolds number.

The LDA data rates were sufficiently high to provide smooth, time resolved velocity measurements, which enabled the computation of fluctuating velocity spectra. This also eliminates the possibility of velocity biasing due to low data rates. For all Reynolds numbers, the highest data rates were obtained between $y^+ \approx 15$ and $y^+ \approx 500$. Data rates tended to be uniformly high throughout this region. The lowest data rates occurred very close to the wall and at the channel centreline. Data was not taken with data rates less than 300 Hz. At all three Reynolds numbers, the two v' measurements closest to the wall appear to be affected by low data rates. The two closest data points to the wall are thus less reliable than the rest of the data.
8. **Available variables:** The streamwise and cross stream velocities were measured. Mean, rms velocity and Reynolds stress profiles are included.
9. **Storage size and data format:** There are three ASCII data files containing the profile data for the three Reynolds numbers. Total data size: 14kb.
10. **Contact person:** Prof. Timothy Wei
Dept. Mechanical and Aeronautical Engineering, Rutgers University
PO Box 909, Piscataway NJ, USA
Phone: (908)-445-2718
twei@jove.rutgers.edu

REFERENCES

WEI, T. & WILLMARTH, W. W. 1989 Reynolds-number effects on the structure of a turbulent channel flow. *J. Fluid Mech.* **204**, 57–95.

PCH13: High Reynolds Number Channel Flow Experiment

Comte-Bellot

1. **Description of the flow:** The flow is a fully developed turbulent flow in rectangular channel.
2. **Geometry:** The channel is rectangular with aspect ratio 13.3:1 (2.4 m by 18 cm). The measurement station was located 122δ down stream of the channel inlet, and in the centre of the span of the channel, see Comte-Bellot (1965) for details.
3. **Sketch:** None needed.
4. **Flow characteristics:** The flow exhibits all the usual characteristics of wall bounded turbulent flows.
5. **Flow parameters:** The only relevant parameter in this flow is the Reynolds number, which for the three cases included here is $Re_b = 57000$, 120000 and 230000 , or $Re_\tau = 2340$, 4800 and 8160 . Reynolds numbers are based on half-width (δ) and bulk or friction velocities respectively. The working fluid is air.
6. **Inflow, outflow, boundary and initial conditions:** The top and side walls of the channel are rigid and conform to the design width 0.1 mm, and the development length was 122δ from the channel inlet.
7. **Measurement procedures:** Mean velocity measurements were made with pito probes except very close to the wall (less than 3 mm). Constant current X-wire anemometers with analog linearization were used to measure second order moments. The linearization makes higher order moments suspect, so they are not included. The wire lengths are 3 mm and the wires were 2 mm apart. The wire length is thus between 78 and 270 wall units, which is rather large, especially near the wall. For this reason, near-wall data in not included. Comte-Bellot estimates the uncertainties in the mean velocities away from the wall to be approximately 1% , and 6% for the velocity variance away from the wall. See Comte-Bellot (1965) for more details.
8. **Available variables:** The streamwise, cross stream and spanwise velocities were measured. Mean, rms velocity and Reynolds stress profiles are included.
9. **Storage size and data format:** There are nine ASCII data files containing the profile data for the three Reynolds numbers. Total data size: 14 kb.
10. **Contact person:** Prof. Genevieve Comte-Bellot
Ecole Centrale de Lyon
36 Avenue Guy de Collongue
BP 163-69131 Ecully Cedex, France
Phone: 33 4 72 18 60 10
gcb@selene.mecaflu.ec-lyon.fr

REFERENCES

COMTE-BELLOT, G. 1965 Ecoulement turbulent entre deux parois paralleles. Publications Scientifiques et Techniques du Ministere de l'Air no. 419.

PCH20: Fully Developed Rotating Channel Flow

Johnston, Halleen & Lezius

1. **Description of the flow:** A small water channel was rotated at a constant rate about an axis perpendicular to the flow direction to generate a Coriolis effect on the channel flow. The resulting asymmetry in the flow was explored, including the effects on the turbulence.
2. **Geometry:** Water was pumped through a channel rotating about an axis parallel to the mean (transverse) vorticity in the channel flow. The channel was 1.5 m long, 0.04 m high and 0.28 m wide. Measurements were performed in a region 10δ long.
3. **Sketch:** None needed.
4. **Flow characteristics:** On the centreline, mean velocity measurements, at zero rotation, indicate the flow to be fully developed. However, computed values of the mixing length indicated the flow was still developing. Existence of a two-dimensional region, free of the influence of the side walls, was verified. Rotation acts to suppress turbulence on one side of the channel and enhance it on the other.
5. **Flow parameters:** Tests were performed for a range of Reynolds and Rotation numbers, and data is available at

$$Re_b = 5500 \quad Ro \leq 0.21$$

$$Re_b = 17,500 \quad Ro \leq 0.081$$

where Re_b is the Reynolds number based on half-width and bulk velocity, and $Ro = 2\delta\Omega/U_b$ is the rotation number.

6. **Inflow, outflow, boundary and initial conditions:** The flow entered the channel from a plenum with flow straighteners. Mean velocity measurements with no rotation indicated fully developed channel flow at the measurement region 58 and 68 channel widths from the entrance. However, mixing length profiles indicated that the flow was not quite fully developed. The outflow, beyond the measurement region, was through a perforated plate across which the pressure drop was used to calculate the flow rate.
7. **Measurement procedures:** Mean velocity profiles were measured by pressure probes using a special iterative procedure to deduce the velocity. Flow visualization was employed to infer the state of the flow and the near wall turbulent structure.

Velocity profiles are available for two combinations of Reynolds number and rotation rate:

(a) Measured quantities:

Mean primary flow velocity, U_1

Local wall shear stress, τ_w (inferred from the velocity measurements)

(b) Measurement Uncertainties: A recent re-analysis of the data by the authors suggests an uncertainty in the mean velocities of $\pm 1.5\%$, and an uncertainty in the wall shear stress of $\pm 2.5\%$. The authors also suggest that these may be low estimates (see the README associated with this data in the database).

8. **Available variables:** Mean velocity profiles and wall shear stress. In addition, extensive qualitative observations are noted from flow visualization.
9. **Storage size and data format:** There are three ASCII data files, containing profiles; two for the two Reynolds numbers studied, and one containing the relative values of the wall friction velocity. Total data size: 15Kb.
10. **Contact person:**

REFERENCES

JOHNSTON, J. P., HALLEEN, R. M. & LEZIUS, D. 1969 Effect of spanwise rotation on the structure of two-dimensional fully developed turbulent channel flow. *J. Fluid Mech.* **56**, 533.

PCH21: Fully Developed Rotating Channel Flow Simulations

Piomelli & Liu

1. **Description of the flow:** The rotating channel flow is obtained by imposing a spanwise rotation on a 2D fully-developed turbulent plane channel. To attain a fully developed flow, the simulation was allowed to develop until a statistical steady state was reached, and statistics were then accumulated. This DNS was part of a larger study on the computation of this flow by large-eddy simulation.
2. **Geometry:** The computational domain was $4\pi\delta \times 2\delta \times 4\pi\delta/3$ in the streamwise, wall-normal and spanwise directions, respectively.
3. **Sketch:** None needed.
4. **Flow characteristics:** The flow characteristics evident in the simulations of Kristoffersen & Andersson (1993) were also noted in this study. See previous section for a description. Filtered data are available from this study which are not available for Kristoffersen & Andersson (1993).
5. **Flow parameters:** The parameters for this flow are the Reynolds number and the rotation number. The Reynolds number for this flow is $Re_\tau = 177$ (based on u_τ and δ , the shear velocity and channel half-width) or $Re_b = 2850$ (based on bulk velocity U_b and δ). The rotation number, $Ro_b = 2\delta\Omega/U_b = 0.144$, and based on u_τ and δ it was 1.166.
6. **Numerical methods and resolution:** The Navier-Stokes equations are integrated in time using a Fourier-Chebyshev pseudospectral collocation scheme. The skew-symmetric form of the momentum equation is employed, and the time advancement is performed by a fractional time step method with a semi-implicit scheme. The wall-normal diffusion term is advanced using the Crank-Nicolson scheme, and the remaining terms by a low-storage third-order Runge-Kutta scheme. Periodic boundary conditions are applied in the streamwise and spanwise directions, and no-slip conditions at the solid walls. $96 \times 97 \times 128$ grid points were used.
7. **Boundary and initial conditions:** (a) Domain size and truncations : Size: $4\pi\delta \times 2\delta \times 4\pi\delta/3$ in the streamwise, wall-normal and spanwise directions with a grid of: $96 \times 97 \times 128$.
(b) Boundary conditions : No slip on the walls; periodic in the streamwise and the transverse directions.
(c) Inlet or initial conditions : Results from an equilibrium (no rotation) simulation were used as the initial condition. After rotation was applied, a new steady state was reached, and the statistics were obtained.
8. **Averaging procedures and resulting uncertainties:** Averaging was performed over 4 dimensionless time units, tu_τ/δ . The total shear stress deviated from the expected linear variation by less than 0.5%.
9. **Available variables:** Time- and plane-averaged data available include all the velocity moments up to the flatness. Skewness and flatness were computed using only the restart files, while first and second moments were calculated on the fly, and are, therefore, substantially smoother. Several flow realizations, either on the original grid or on a finer mesh ($128 \times 129 \times 128$ grid points) are available from the contact.
10. **Storage size and data format:** There is a single ASCII data file, containing profiles of mean velocity, velocity variance and Reynolds shear stress. Total data size: 21kb.
11. **Contact person:** Prof. Ugo Piomelli
Dept. Mech. Engr., Univ. of Maryland
College Park, MD 20742, USA
Phone: (301) 405-5254
E-mail: ugo@glue.umd.edu

REFERENCES

- KRISTOFFERSEN, R. & ANDERSSON, H. 1993 Direct simulations of low-Reynolds-number turbulent flow in a rotating channel. *J. Fluid Mech.* **256**, 163.
- PIOMELLI, U. & LIU, J. 1995 Large-eddy simulation of rotating turbulence using a localized dynamic model. *Phys. Fluids* **7**, 839.

PCH22: Fully Developed Rotating Channel Flow Simulations

Andersson & Kristoffersen

1. **Description of the flow:** The rotating channel flow is obtained by imposing a spanwise rotation on a 2D fully-developed turbulent plane channel. To attain a fully developed flow, the simulation was allowed to develop until a statistical steady state was reached, and statistics were then accumulated.
2. **Geometry:** The channel flow between parallel walls was simulated in a computational domain of : $4\pi\delta \times 2\delta \times 2\pi\delta$ (where 2δ is the channel height).
3. **Sketch:** None needed.
4. **Flow characteristics:** With increasing rotation the velocity becomes more asymmetric and contains a linear region of slope $dU/dy \simeq 2\Omega$ in the centre of the channel. The wall-layer on the unstable side becomes thinner and the turbulence is enhanced, then levels off around $Ro_b = 0.10$; a significant drop is noticed at $Ro_b = 0.5$. On the stable side the wall-layer becomes thicker, and the turbulence level is reduced, without attaining a full relaminarization.

An interesting observation is the tendency towards isotropy of the turbulence on the unstable side, due to the augmentation of v^2 and the saturation of u^2 . On the stable side, however, the anisotropy increases with Ro . Another important finding is the existence of regions of negative energy production, already hypothesized on the basis of the experiments (Andersson & Kristoffersen, 1994). The region arises when the position of zero turbulent stress does not coincide with the maximum of the mean velocity. Negative energy production leads to energy being extracted from the turbulence and could be an interesting test for models.

The Taylor-Görtler rolls are observed but are found unsteady, apart from the case $Ro_b = 0.15$. Therefore, no attempt was made to separate large scale structures from the turbulence for statistical purposes. Qualitative description of flow patterns can be found in Kristoffersen & Andersson (1993).

5. **Flow parameters:** The parameters in this flow are the Reynolds number, $Re_\tau = 194$, and the rotation number, Ro_b which varied from 0 to 0.5.
6. **Numerical methods and resolution:** The computational grid is $128 \times 128 \times 128$. The mesh spacing is constant in x and z at 19 and 9.5 wall units, and is stretched in y following a tanh-distribution to obtain a minimum spacing of .5 wall units at the grid point next to the wall. Spatial derivatives are discretized by a 2nd order central-difference approximation, and the solution is marched in time with a second-order explicit Adams-Bashforth scheme.
7. **Boundary and initial conditions:** Periodic boundary conditions are imposed for the x and z , directions, requiring a forcing term corresponding to an imposed mean pressure gradient in x

$$dp/dx = 1$$

The equations are solved within a computational domain of : $4\pi\delta \times 2\delta \times 2\pi\delta$

(a) Domain size and truncations: The formally infinite domain in the streamwise (x) and spanwise (z) directions are truncated to domain of $4\pi\delta \times 2\delta \times 2\pi\delta$

(b) Boundary conditions: No slip is imposed on the walls and periodic conditions are imposed in the streamwise and spanwise directions.

(c) Inlet or initial conditions: The simulation was started from a random initial field. When the total shear stress was linear across the channel, statistically steady turbulence was assumed. The simulation was then continued for several large-eddy turnover times, δ/u_τ . As rotation was increased, the previous results were used as the starting field.

8. **Averaging procedures and resulting uncertainties:** Though several large-eddy turnover times were used for averaging, as mentioned above, the authors feel this may have been only marginally adequate for some cases. The critical friction velocities are estimated to be accurate to within 3% for all but the highest rotation rate. A simulation at zero rotation rate was performed which agreed well with previous, accepted simulations.

9. **Available variables:** A variety of mean statistical data are compiled for this study including skin-friction as a function of rotation rate, profiles of mean velocity, Reynolds stress, and turbulent kinetic energy, as well as various terms in the Reynolds stress transport budget. The individual quantities are defined in Andersson & Kristoffersen (1994).

Filtered data for direct use in evaluating LES is not available for this simulation.

10. **Storage size and data format:** There are eleven subdirectories of data, each with an index file describing the contents. These are identified with corresponding figures in Andersson & Kristoffersen (1994). All of the files are ASCII and total about 285kb.
11. **Contact person:** Prof. Helge Andersson
Dept. Appl. Mech., Mech. Engr., Norwegian Inst. of Tech.
Trondheim, Norway
E-mail: tonera@tv81.termo.unit.no

REFERENCES

- ANDERSSON, H. I. & KRISTOFFERSEN, R. 1994 Turbulence statistics of rotating channel flow. In *Proc. 9th Symposium Turbulent Shear Flow, Tokyo*.
- KRISTOFFERSEN, R. & ANDERSSON, H. 1993 Direct simulations of low-Reynolds-number turbulent flow in a rotating channel. *J. Fluid Mech.* **256**, 163.

PCH23: Fully Developed Rotating Channel Flow Experiment

Nakabayashi & Kitoh

1. **Description of the flow:** A small wind tunnel (channel) was rotated at a constant rate about an axis perpendicular to the flow direction to generate a Coriolis effect on the channel flow. The resulting asymmetry in the flow was explored, including the effects of Reynolds number and rotation on the turbulence. The Reynolds number range was lower than that of Johnston et al., and the data (primarily hot-wire) are much more detailed and extensive.
2. **Geometry:** Air was blown through a channel rotating about an axis parallel to the mean (transverse) vorticity in the channel flow. The channel was 2.0m long, 0.010 m high and 0.080 m wide. Measurements were performed at a station 361 channel half-heights from the entrance, where the turbulence was fully developed.
3. **Sketch:** None needed.
4. **Flow characteristics:**
5. **Flow parameters:** The Reynolds number Re_b ranged from 850 to 5000 and rotation number $R_\Omega = 4D^2\Omega/\nu$ ranged from 0 to 0.0547.
6. **Inflow, outflow, boundary and initial conditions:** Because of the very long channel, the effective inflow and outflow conditions are those of fully developed channel flow, keeping in mind the Reynolds number effects.
7. **Measurement procedures:** Velocity and turbulence profiles were measured by hot-wire anemometry. A special curve-fitting technique is used to infer the wall shear stress. Both single and x-wires were employed. Not all of the following variables are available for all conditions. Estimated uncertainties are 2% for mean velocity and 5% for wall shear stress.
8. **Available variables:** The following data are available: mean streamwise flow velocity profiles, U_1 , normal stresses, $\langle u_{11} \rangle$, $\langle u_{22} \rangle$, turbulent stress, $\langle u_1 u_2 \rangle$, local wall shear stress, τ_w (inferred from velocity measurements) and surface pressures.
9. **Storage size and data format:** The data are stored in a series of ascii files organized into directories by the Reynolds number of the run. For each Reynolds number there are several files for different rotation numbers, and for mean and fluctuation quantities. Total data size: 85 kbytes
10. **Contact person:**

REFERENCES

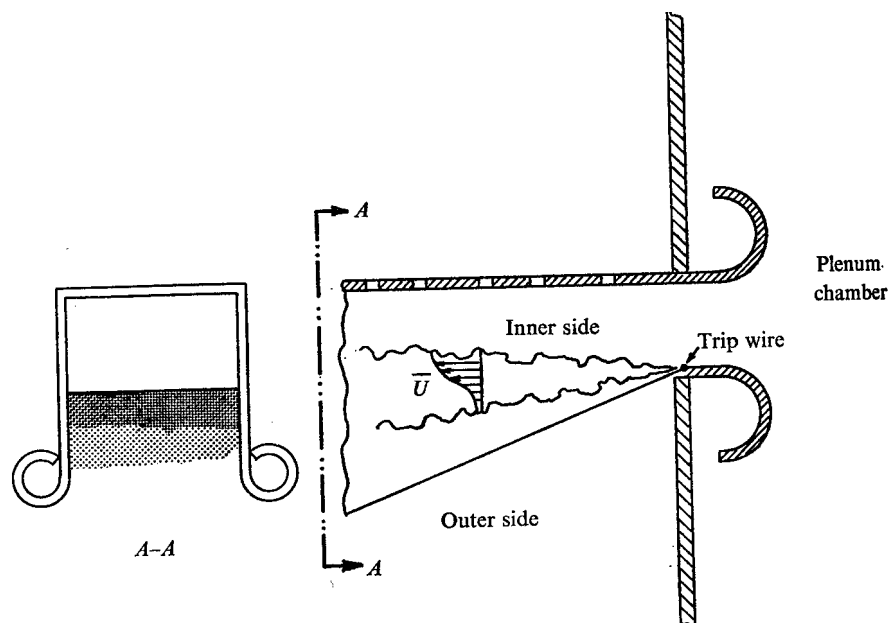
NAKABAYASHI, K. & KITOH, O. 1996 Low Reynolds number fully developed two-dimensional turbulent channel flow with system rotation. *J. Fluid Mech.* **315**, 1.

Data Sheets for:
Chapter 6.- Free Shear Flows

SHL00: Single Stream Plane, Incompressible Turbulent Mixing Layer

Wynanski & Fiedler

1. **Description of the flow:** Single stream, plane mixing layer. One side at rest. The boundary layers can be either turbulent (tripped, supposed to be fully developed, based on Log plot analysis) or laminar (aspiration is used). Only self preservation region results are available. Self preservation accepted from $Re \simeq 3 \times 10^5$.
2. **Geometry:** Rectangular exit, 18 cm x 51 cm Total length available: 80 cm. Contraction 1:28. Trailing edge with tripping wire.
3. **Original sketch**



4. **Flow characteristics:** One stream mixing layer. Mean velocity 12 m/s. $\lambda = 1$.
5. **Flow parameters:** Mixing layer: Spreading rate $\sigma_0 = 9$.
6. **Inflow/Outflow/Boundary and Initial Conditions:** Free stream turbulence 0.1% in long. velocity. Tripped boundary layer.
7. **Measurement procedure:** Mean and fluctuating longitudinal velocities are measured. Hot Wire Anemometry - X wire. Linearity assumed. Analog measurements.
8. **Available variables:** Mixing layer data: growth rates, velocities: \overline{U}/U_∞ ; $\overline{u^2}$; $\overline{v^2}$; $\overline{w^2}$; \overline{uv} ; $\overline{vu^2}$; $\overline{vw^2}$; $\overline{uw^2}$; $\overline{uv^2}$; $\overline{u^3}$; $\overline{v^3}$; $\overline{w^3}$ (+ skewness, flatness) Dissipation terms $\overline{\left(\frac{\partial u_i}{\partial x_j}\right)^2}$ for $i = 1, 2, 3$ and $j = 1, 2$. + Micro scales. Turbulent kinetic energy balance. One dimensional spectra and two point correlations (R_{uu} : space (x and y) and time, R_{uv} : time), intermittency functions. Measurement locations: 29 to 80 cm.
9. **Storage size and data format:** Format is ASCII. Data are tabulated from printed forms. 70 Kb.
10. **Contact persons:**
Prof. H. Fiedler
TU Berlin, Hermann- Föttinger-Institut

Strasse des 17 juni 135, D-1000 Berlin 12, Germany.

Phone: (49) 30 314 23359

Fax: (49) 30 314 21101

E-mail: hfiedler@hobo.pi.TU-berlin.de

or

Prof. I. Wagnanski

AME dept. Tucson, AZ 85721, USA,

Phone: (602) 621 6089

Fax: (602) 621 8191

E-mail: wygy@bigdog.engr.arizona.edu

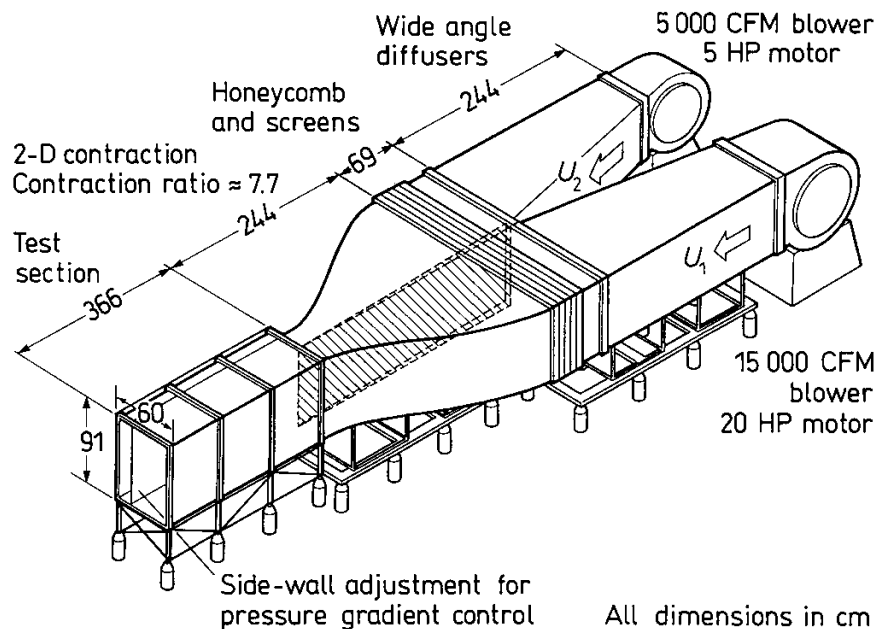
REFERENCES

WYGNANSKI, I. & FIEDLER, H. E. 1970 The two-dimensional mixing region. *J. Fluid Mech.* **41**, part 2, 327–361.

SHL01: Plane, Incompressible Turbulent Mixing Layer. Influence of initial conditions. Vel. ratio 0.6

Bell & Mehta

- Flow description:** Two stream, plane mixing layer. The boundary layers can be either turbulent (tripped, fully developed, based on shape factor) or laminar. The development of the ML is given.
- Geometry:** Rectangular exit, 36 x 91 cm². Total length available: 366 cm. Useful length: 250 cm. Splitter plate trailing edge: 1° wedge. Edge thickness 0.25 mm.
- Original Sketch:**



- Flow characteristics:** Two streams mixing layer. Mean velocities 15 m/s; 9 m/s. $\lambda = 0.25$
- Flow parameters:** Boundary layers: Laminar BL: $\delta = 0.4/0.44$ mm; $\theta = 0.53/0.61$ mm; $H = 2.52/2.24$; $C_f = 0.72/0.91 \times 10^{-3}$; $R_\theta = 525/362$. Turbulent BL: $\delta = 7.6/8.5$ mm; $\theta = 0.82/0.94$ mm; $H = 1.5/1.5$; $C_f = 5.3/4.86 \times 10^{-3}$; $R_\theta = 804/567$. Mixing layer: Spreading rates $d\delta_w/dx$ (from *erf* function)= untripped: 0.023; tripped: 0.019.
- Inflow, outflow, boundary and initial conditions:** Free stream turbulence 0.15% in longitudinal velocity and 0.05% in transverse vel. Initial boundary conditions are either natural (probably pre-transitional) or tripped by means of thin wires 15 cm upstream of the trailing edge. Only global BL parameter are given.
- Measurement procedure:** Hot Wire Anemometry - X wire. A/D measurements (low frequency recording). Plenum chamber calibration. Mean and fluctuating velocities U, V and W are measured. Spanwise variations from 40% to 4%, depending on distance and tripping. Spanwise averaged.
- Available variables:** Boundary Layer data: $\bar{U}_e, C_f, \delta, \theta$.
Mixing layer data: $\bar{U}/U_\infty; \overline{u^2}, \overline{v^2}, \overline{w^2}, \overline{uv}, \overline{uv^2}$.
Streamwise mixing layer growth; Streamwise development of max. primary turbulent stresses ($\overline{uv}, \overline{u^2}, \overline{v^2}, \overline{w^2}$).
8 measurement locations (cm): 7.8, 16.7, 57.3, 77.6, 108.1, 128.4, 189.4, 250.3

9. **Storage size and data format:** The data are in ASCII format. 70 Kb.

10. **Contact Person**

Dr. R. D. Mehta

Fluid Dynamics Laboratory, NASA Ames Research Center
Moffett Field, CA 94305, USA.

Tel: (650) 604 4114; Fax: (650) 604 4511

E-mail: rmehta@mail.arc.nasa.gov

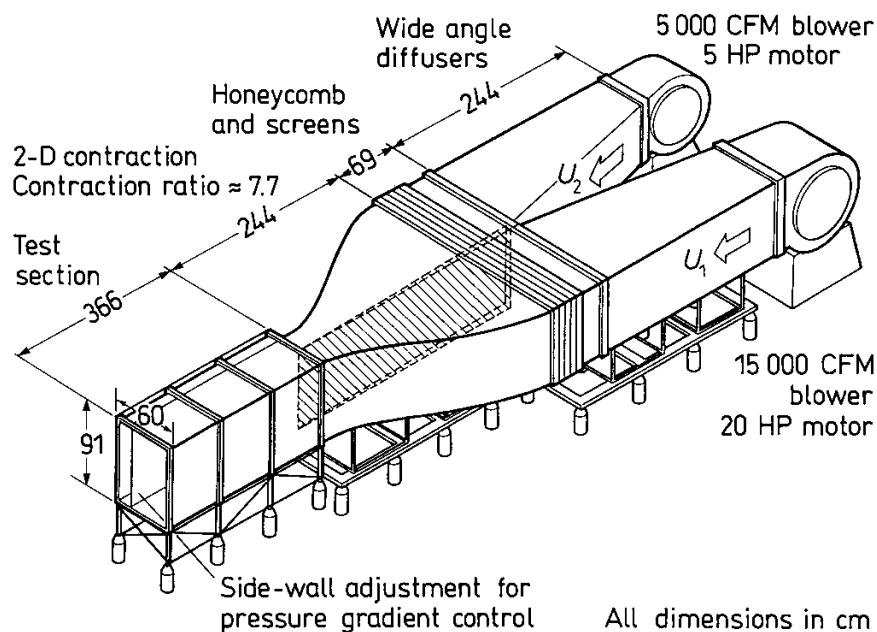
REFERENCES

BELL, J.H. & MEHTAR.D. 1990 Development of a Two-Stream Mixing Layer from Tripped and Untripped Boundary Layers. *AIAA J.* 28, No 12, 2034–2042.

SHL02: Plane, Incompressible Turbulent Mixing Layer. Influence of Near Plate Wake.

Mehta

- Flow description:** Two streams, plane mixing layer. The boundary layers are turbulent (tripped, fully developed, based on shape factor). Depending on the velocity ratio, the wake of the plate can be present. The velocity ratio ranges from 0.5 to 0.9. The development of the ML is given.
- Geometry:** Rectangular exit, 36 x 91 cm². Total length available: 366 cm. Useful length: 250 cm. Splitter plate trailing edge: 1° wedge. Edge thickness 0.25 mm.
- Original sketch:**



- Flow characteristics:** Two streams mixing layer. Mean velocities: high speed side: 21 m/s, low vel. side: 10.5-18.9 m/s. $0.0526 \leq \lambda \leq 0.333$.
- Flow parameters:** Boundary layers: Tripped BL (second values correspond to the different low speed side according to the vel. ratio): $\delta = 7.6/8.5$ mm; $\theta = 0.96/0.83-0.87$ mm; $H \approx 1.5$; $C_f = 4./4.4-4.7 \times 10^{-3}$; $R_\theta = 1,300/686-1,114$.
Mixing layer: Spreading rates $d\delta_w/dX$: from 0.0073 to 0.0318.
- Inflow, outflow, boundary and initial conditions:** Free stream turbulence 0.15% in longitudinal velocity and 0.05% in transverse vel. Initial boundary conditions are tripped by means of thin wires 15 cm upstream of the trailing edge. Only global BL parameter are given. The velocity ratio are 0.5, 0.6, 0.7, 0.8, 0.9.
- Measurement procedure:** Hot Wire Anemometry - X wire. A/D measurements (low frequency recording). Plenum chamber calibration.
Mean and fluctuating velocities: U, V and W are measured Spanwise variations from 40% to 4%, depending on distance and tripping. Spanwise averaged data.

8. **Available variables:** Boundary Layer data: $\overline{U}_e, C_f, \delta, \theta$.

Mixing layer data: $\overline{U}/U_\infty, \overline{u^2}/U_\infty^2, \overline{v^2}/U_\infty^2, \overline{uv}/U_\infty^2, \overline{u^2v}/U_\infty^3, \overline{uv^2}/U_\infty^3$.

Global parameters: Mixing layer growth. Streamwise development of maximum primary stresses ($\overline{uv}, \overline{u^2}, \overline{v^2}$). Streamwise development of velocity defect: $(U_{min} - U_2)/(U_1 - U_2)$. Variation of the growth rate versus the velocity ratio.

8 measurement locations (cm): 12, 32, 73, 111, 144, 205, 236, 267

NB: The triple products were not given in the original paper.

9. **Storage size and data format:** The data are in ASCII format. 260 Kb.

10. **Contact person:** Dr. R. D. Mehta

Fluid Dynamics Laboratory, NASA Ames Research Center
Moffett Field, CA 94305-100, USA.

Phone: (650) 604 4114

Fax: (650) 604 4511

E-mail: rmehta@mail.arc.nasa.gov

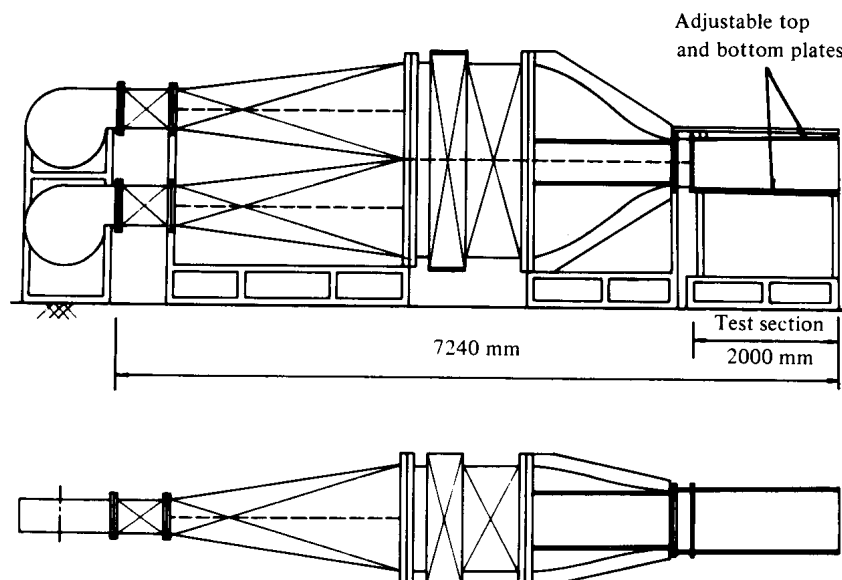
REFERENCES

MEHTA, R.D. 1991 Effect of velocity ratio on plane mixing layer development: Influence of the splitter plate wake. Experiments in Fluids 10, 194–204.

SHL03: Plane, Incompressible Turbulent Mixing Layer. Natural and Forced.

Oster & Wygnanski

1. **Flow description:** Two streams, plane mixing layer. Two different blowers are used. The velocity ratio ranges from 0.3 to 0.6. Main results are available at 0.3 and, mainly, 0.6.
2. **Geometry:** Rectangular exit $0.5 \times 0.6 \text{ m}^2$. Total length available: 2. m. Contraction 1:7.3 Splitter plate trailing edge: 3° wedge. Edge thickness (flap) 0.5 mm.
3. **Original sketch:**



4. **Flow characteristics:** Two streams mixing layer. Mean velocity of the high speed side: 13.5 m/s. (low speed adjustable from 0 to 13.5 m/s). $0.25 \leq \lambda \leq 0.54$
5. **Flow parameters:** The boundary layers are not examined. Detailed data are available at $X = 100 \text{ mm}$ downstream of TE (considered as initial conditions). Reynolds number based on velocity difference and momentum thickness: 10^4 .
6. **Inflow, outflow, boundary and initial conditions:** Free stream turbulence : 0.2%. Homogeneity of mean velocity better than 1 %. Initial conditions are given at 100 mm downstream of the TE.
7. **Measurement procedure:** Hot Wire Anemometry CTA - X wires. (10 kHz). Sampling 4kHz. Detailed calibration. Measured quantities: Mean and fluctuating velocity U . Measurement errors 1% on U and 2% on V .
8. **Available variables:** 'Initial conditions': for $r = 0.6$ ($X = 100 \text{ mm}$): $\bar{U}/\Delta U$, $u'/\Delta U$, $v'/\Delta U$.
Mixing layer data: Integral quantities θ ; b ; spreading rates for $r = 0.3, .4, .5, .6$.
Mixing layer velocity data:
 - (a) $r = 0.3, 0.4, 0.5, 0.6$: $\bar{U}/\Delta U$, $u'/\Delta U$ for $X = 20., 40., 60., 80., 100., 120., 140., 160. \text{ cm}$. (add 10 cm for the 3 last cases).
 - (b) $r = 0.6$: $v'/\Delta U$, $\overline{uv}/\Delta U^2$ for $X = 30., 50., 70., 90., 110., 130., 150., 170. \text{ cm}$.

NB Detailed data with trailing edge flapping are available: Mean and fluctuating data (u' , v' , w' , $u'v'$ and total turbulent energy) for $r = 0.3, 0.4, 0.5, 0.6$. Combination of 4 frequencies (30, 40, 50 and 50 Hz) and 3 amplitudes ($A = 0.5, 1., 1.5$ and 2 mm).

9. **Storage size and data format:** The data are in ASCII format. Data are tabulated from printed forms. 120 Kb.
10. **Contact person:** Prof. I. Wygnanski, AME Dept. Tucson, AZ 85721, USA
Phone: (602) 621 6089
Fax: (602) 621 8191
E-mail: wygy@bigdog.engr.arizona.edu

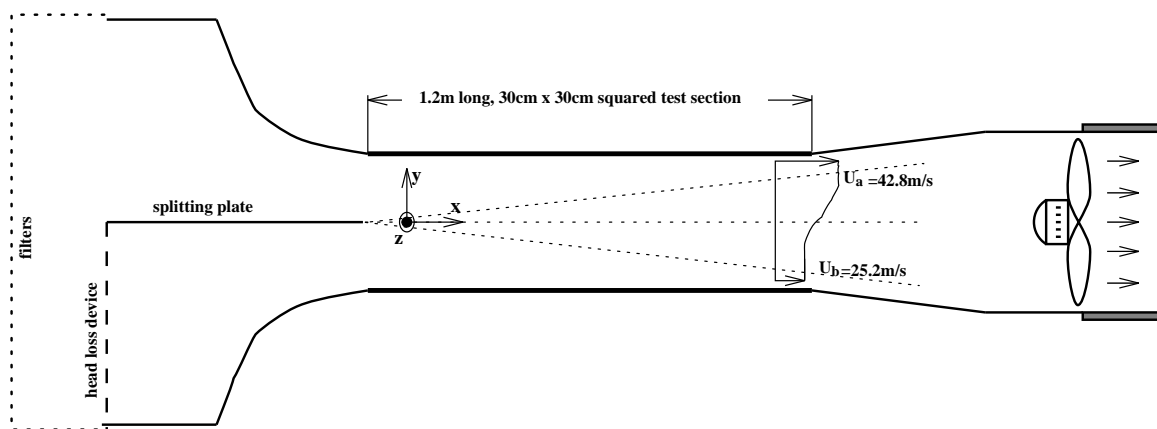
REFERENCES

OSTER, D. & WYGNANSKI, I. 1982 The forced mixing layer between parallel streams. *J. Fluid Mech.* **123**, 91–130.

SHL04: Plane, Incompressible Turbulent Mixing Layer. Vel. ratio 0.54

Delville, Garem & Bonnet

- Flow description:** Two stream, plane mixing layer. The boundary layers are turbulent (fully developed, based on spectra, Log plot, etc. analysis). Development of the ML is given
- Geometry:** Rectangular exit, 30 cm x 30 cm. Total length available: 120 cm. Useful X range 100 cm. Contraction 1:16. Splitter plate: 1 m long, 3° wedge on 50 mm. Thickness at TE: 0.3 mm.
- Original sketch**



- Flow Characteristics** Two stream mixing layer. Mean velocities 41.54 and 22.40 m/s. $\lambda = 0.3$
- Flow parameters:** Boundary layers: $\delta = 9.6/6.3$ mm; $\theta = 1.0/0.73$ mm; $H = 1.35/1.37$; $R_\theta = 2900/1200$.
Mixing layer: Spreading rates equivalent $\sigma_0 = 10.6$; $d\delta_\omega/dx = 0.05$.
- Inflow, outflow, boundary and initial conditions:** Free stream turbulence level: 0.3 % in longitudinal velocity. Tripped boundary layers.
- Measurement procedure:** Hot Wire Anemometry—X wires. Rakes (up to 48 wires). Non-linearized calibration laws. Analog Mean and rms coupled with simultaneous sampling at 50 kHz.
Mean and fluctuating velocities are measured for the 3 components.
- Available variables:** Boundary layer data: \overline{U} ; $\overline{u^2}$
Mixing layer data: \overline{U}/U_∞ ; $\overline{u^2}$; $\overline{v^2}$; $\overline{w^2}$; \overline{uv}
 $\overline{vu^2}$; $\overline{vw^2}$; $\overline{uw^2}$; $\overline{uv^2}$; $\overline{u^3}$; $\overline{v^3}$; $\overline{w^3}$ (+ skewness, flatness)
Dissipation terms from spectra. Turbulent kinetic energy balance. Spectra and two point correlations.
Single wire measurements at 24 downstream locations, from 3 cm up to 100 cm.
Probability Density Functions of 2 components of velocity at $X = 600$ mm. P.d.f. of **velocity differences**, 2 components, at $X = 600$ mm, for 3 reference positions (on the axis, in the middle and outside of the ML). The difference are determined for transverse (y) separation **and** for time separations (on the axis only).
- Storage size and data format:** The data are in ASCII format. 17 Mb.
A detailed report is included in the present database in Postscript (PDF) format, including drawings and discussions.
Not provided here, but available, huge size for raw data, see ERCOFTAC data base (typically between 20 and 100Mb).

10. **Contact person:** Dr J. Delville
LEA-CEAT, University of Poitiers, 43 rue de l' Aérodrome, F-86036 Poitiers cedex France
Phone: (33) 05 49 53 70 57
Fax: (33) 05 49 53 70 01
E-mail: delville@univ-poitiers.fr

REFERENCES

- DELVILLE, J. 1995 La décomposition orthogonale aux valeurs propres et l'analyse de l'organisation tridimensionnelle des écoulements turbulents cisailés libres. Thèse, Univ. Poitiers
- DELVILLE, J., BELLIN, S., GAREM, J.H. & BONNET J.P. 1988 Analysis of structures in a turbulent a turbulent plane mixing layer by use of a pseudo-flow visualization method based hot-wire anemometry. *Advances in Turbulence II*, Fernholz and Fiedler eds., Springer, pp 251.

SHL05: Time Developing Turbulent Mixing Layer Simulations

Rogers & Moser

1. **Description of the flow:** The flow is a fully turbulent time-developing mixing layer. Initial conditions are taken from two realizations of a parallel turbulent boundary layer. Three cases are included that differ in the details of their initial conditions (see §7).
2. **Geometry:** The time-developing mixing layer is spatially homogeneous in the streamwise and spanwise directions and develops in an infinite domain in the cross-stream direction, with the layer thickness growing in time without bound.
3. **Sketch:** None needed
4. **Flow characteristics:** The simulated turbulent mixing layers evolve through a “transition” period in which the boundary layers turbulence provided as an initial condition is changed to turbulence characteristic of a mixing layer. There is clear evidence (Rogers & Moser, 1994) that during this transition, the layer undergoes Kelvin-Helmholtz rollup, though the rollers are far from two-dimensional in some cases. As the layer grows, so do the rollers, which have been observed to pair, at least locally. Depending on the case the rollers may or may not persist throughout the simulated development (see Rogers & Moser, 1994). All except Case 3 evolve through a period of self-similar growth (see table 5).
5. **Flow parameters:** The only relevant parameter in this flow is the Reynolds number. Flow quantities are nondimensionalized by the initial momentum thickness δ_m^0 and the velocity difference between the two-streams of the mixing layer ΔU . In these units the Reynolds number of all three cases is 800. The Reynolds number based on the (evolving) momentum thickness grows to be as large as 2420.
6. **Numerical methods and resolution:** The numerical method used in these simulations is that of Spalart, Moser & Rogers (1991). It is a spectral method in which the streamwise and spanwise spatial variations are represented using Fourier series, and the cross-stream dependence is represented with a mapped polynomial expansion based on Jacobi polynomials. The formally infinite cross-stream (y) direction was mapped to the interval $\eta \in (-1, 1)$ by the mapping $\eta = \tanh(y/y_0)$. See Spalart *et al* (1991) for details.
Both the mapping parameter, y_0 , and the number of Fourier and Jacobi polynomial modes in the representation (N_x , N_y and N_z , where x and z and the streamwise and cross-stream directions respectively) were varied through each simulation as the Reynolds number increased. The variation is shown in table 6.
7. **Boundary and initial conditions:** The formally infinite homogeneous streamwise and spanwise directions are truncated to a finite size and periodic boundary conditions are imposed. The domain sizes are $125\delta_m^0$ and $31.25\delta_m^0$ in the streamwise and spanwise directions respectively, where δ_m^0 is the initial momentum thickness of the layer (see Rogers & Moser, 1994). In the cross stream direction, the conditions are that $u(y) \rightarrow \pm 1/2\Delta U$ as $y \rightarrow \pm\infty$, where u is the streamwise velocity component and all other velocity components go to zero. ΔU is the free-stream velocity difference.

The initial conditions for the simulations were constructed using two realizations of an incompressible turbulent boundary layer computed by Spalart (1988). The momentum thickness Reynolds number Re_θ of the boundary layer was 300, and in the units of the mixing layer simulations $\theta = \frac{3}{4}\delta_m^0$. If the two boundary layer velocity vector fields are written $\mathbf{u}_1(x, y, z)$ and $\mathbf{u}_2(x, y, z)$, where $0 \leq y \leq \infty$, $-L_x/2 \leq x \leq L_x/2$, and the wall is at $y = 0$. Then the basic initial condition field $\mathbf{u}^1(x, y, z)$ (for case 1) is given by

$$\mathbf{u}^1(x, y, z) = \begin{cases} \mathbf{u}_1(x, y, z) & y \geq 0 \\ \mathcal{R}\mathbf{u}_2(-x, -y, z) & y < 0 \end{cases} \quad (1)$$

where \mathcal{R} is a reflection operator that changes the sign of the x and y components of a vector, leaving the z component unchanged.

The initial condition fields for cases 2 and 3 (\mathbf{u}^2 and \mathbf{u}^3 respectively) are constructed from those of case 1 by

$$\mathbf{u}_x^j(x, y, z) = u_x^1(x, y, z) + \frac{\gamma_j}{L_z} \int_0^{L_z} \mathbf{u}_x^1(x, y, z) dz$$

	γ	Self-Similar Period	$d\delta_m/dt$
Case 1	0	$105 < t < 150$	0.014
Case 2	4	$100 < t < 150$	0.014
Case 3	19	$(80 < t < 125)$	(0.017)

Table 1: Case information for the mixing layer simulations. Initial condition parameter γ is defined in §7. The growth rate $d\delta_m/dt$ is for the self similar period. In Case 3, there is no convincing self-similar period, the growth rate and period shown are for an approximate similarity period as discussed in Rogers & Moser (1994).

	Time	$N_x \times N_y \times N_z$	y_0
Case 1	0-34.9	$256 \times 120 \times 128$	4.0
	34.9-87.3	$512 \times 180 \times 128$	4.0
	87.3-104.2	$512 \times 120 \times 192$	4.0
	104.2-150.0	$512 \times 180 \times 192$	6.0
	150.0-187.5	$512 \times 210 \times 192$	6.0
	187.5-250.0	$384 \times 180 \times 128$	8.0
Case 2	0-77.9	$256 \times 120 \times 128$	4.0
	77.9-150.0	$256 \times 180 \times 128$	6.0
Case 3	0-17.3	$256 \times 120 \times 128$	4.0
	17.3-85.4	$384 \times 120 \times 128$	6.0
	85.4-175.0	$384 \times 160 \times 128$	8.0
	175.0-250.0	$384 \times 220 \times 128$	11.0

Table 2: Specification of numerical parameters for time developing turbulent mixing layer simulations from Rogers & Moser (1994).

$$\mathbf{u}_y^j(x, y, z) = u_y^1(x, y, z) + \frac{\gamma_j}{L_z} \int_0^{L_z} \mathbf{u}_y^1(x, y, z) dz$$

$$\mathbf{u}_z^j(x, y, z) = u_z^1(x, y, z)$$

where $\gamma_j = 4$ and 19 for $j = 2$ and 3 respectively. The initial condition fields provided with this data base include boundary layer realizations similar to those used for initial conditions here.

- Averaging procedures and uncertainties:** All the data provided from these simulations is obtained by computing the appropriate quantities from the simulated velocity fields and averaging in the homogeneous spatial directions x and z . There are three sources of uncertainty in this data. First are the numerical discretization errors introduced in the numerical simulations. The simulations were done with great care to ensure that the discretization errors are negligible (Rogers & Moser, 1994).

The second source of uncertainty is statistical, which arises from computing the averages over a finite domain size for a single realization. An estimate of the magnitude of this error can be obtained by realizing that the ideal profiles will be either even or odd in y , depending on the quantity. Departure from this ideal behavior provides an estimate of the error. In particular, if the profile of a quantity q should be even (for example), then the magnitude of the odd part $((q(y) - q(-y))/2)$ relative to the even part $((q(y) + q(-y))/2)$ is an estimate of the relative error due to limited statistical sampling. Such estimates can be computed from the data provided. Also, if the measured quantities are considered to represent the evolution of this particular flow, with these particular initial conditions, then there is no statistical error. However, it is not clear how comparisons to LES can be made in this sense, since LES is only expected to be valid statistically.

The third source of uncertainty is due to the finite domain size of the numerical simulation. However, if an LES is done in the same domain with the same periodic boundary conditions, then a comparison can be made without error due to the domain size.

- Available variables:** For each of the three cases, data is provided at several times through the evolution of the flow, as indicated in table 1. Given are the mean velocity $U(y)$, the velocity variances $(\overline{u^2}, \overline{v^2}, \overline{w^2})$, and the Reynolds stress \overline{uv} .

In addition to this data at discrete times, the time evolution of the momentum and vorticity thickness is provided.

10. **Storage size and data format:** The data is in ASCII files, organized into directories according to initial conditions. Total data size: approximately 1 Mbyte of total storage.

11. **Contact person:**

Michael M. Rogers
NASA Ames-Research Center, Moffett Field, CA 94035, USA
Phone: (415)-604-4732
E-mail: mrogers@nas.nasa.gov

or

Robert D. Moser
Dept. Theoretical and Applied Mechanics, University of Illinois
104 S. Wright St., Urbana, IL 61801 USA
Phone: (217)-244-7728
E-mail: r-moser@uiuc.edu.

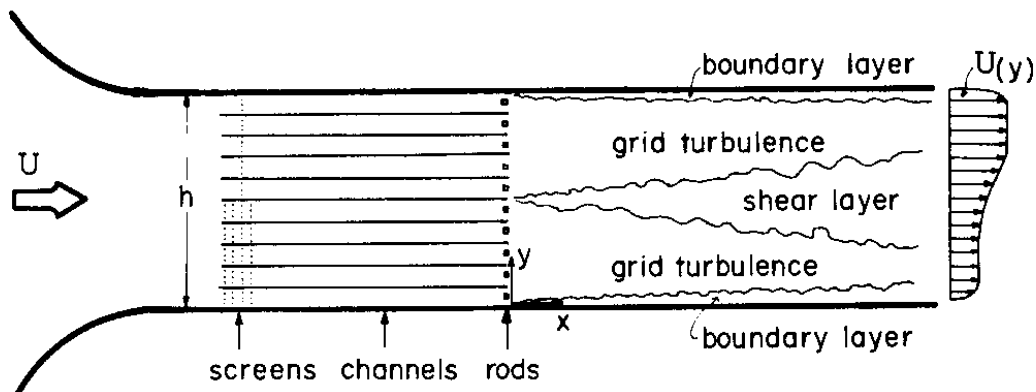
REFERENCES

- ROGERS, M. M. & MOSER, R. D. 1994 Direct simulation of a self-similar turbulent mixing layer. *Phys. Fluids* **6**, 903–923.
- SPALART, P.R. 1988 Direct numerical study of a turbulent boundary layer up to $Re_\theta = 1410$. *J. Fluid Mech.* **187**, 61–98.
- SPALART, P.R., MOSER, R.D. & ROGERS, M.M. 1991 Spectral methods for the Navier-Stokes equations with one infinite and two periodic directions, *J. Comp. Phys.* **96**, 297–324.

SHL06: Plane, Incompressible Turbulent Mixing Layer. Influence of External Turbulence.

Tavoularis & Corrsin

1. **Flow description:** Two-stream, plane mixing layer. The mixing layer develops within a significant turbulence level. The development of the ML is given.
2. **Geometry:** Square test section, $30.5 \times 30.5 \text{ cm}^2$. Total length available: 330 cm. Contraction 9:1 before the channels and turbulence generators. Each of the two streams originated at the outlets of five parallel channels, equipped with fine-mesh screens at their upstream ends and turbulence enhancing rods at their downstream ends. The solidities and numbers of the screens were adjusted to produce the desired mean velocity ratio.
3. **Original sketch**



4. **Flow characteristics:** Two-stream mixing layer. Mean velocities 10 m/s; 21.4 m/s. $\lambda = 0.36$. The flow outside the mixing layer resembled grid-generated turbulence, with near zero shear stress and nearly equal, decaying normal stresses. Although integral length scales in the “grid turbulence” regions have not been reported, one may roughly estimate their initial values by half the channel size (15 mm).
5. **Flow parameters:** Reynolds number based on vorticity thickness: from 45 to $83 \cdot 10^3$. Mixing layer spreading rate: $\sigma = 32$.
6. **Inflow, outflow, boundary and initial conditions:** Typical turbulence levels: 4% of local mean velocity, isotropic (resp. 2.5 % and 5 % in term of conv. vel. 15.7 m/s).
7. **Measurement procedure:** Hot Wire Anemometry CTA, $5\mu\text{m}$ - single and X wires. Two single wires for space correlations with 0.1 mm accuracy in space. No information on calibration procedure. Measured quantities: Mean velocities U. Turbulent data: 2 components. Space correlations for 3 directions.
8. **Available variables:** Near the origin (no splitter plate), $x = 30 \text{ cm}$: $U \text{ (m/s)}, u'/U_c, v'/U_c; \overline{u'v'}/u'v'$.
 Mixing layer development: $\overline{U}/\Delta U, u'/\Delta U, v'/\Delta U, \overline{uv}/\Delta U^2$
 Three detailed measurement locations (cm): 76.2 (2.5 h); 122 (4); 168(5.5)
 Autocorrelations for some y locations (axis, intermed. and edge) for $x = 76 \text{ cm}$. longitudinal, transverse and shear stress components.
 Two-point correlations: for some y locations (axis, intermed. and edge) for $x = 76 \text{ cm}$. longitudinal, transverse and shear stress components, with separations in x, y and z directions.

9. **Storage size and data format:** The data are in ASCII format. 40 Kb.

10. **Contact person:** Prof. S. Tavoularis
Department of Mechanical Engineering. University of Ottawa, 770 King Edward Avenue
Ottawa, Ontario K1N 6N5, Canada.
Phone: (613) 5625800 ext. 6271
Fax: (613) 562 5177
E-mail: tav@eng.uottawa.ca

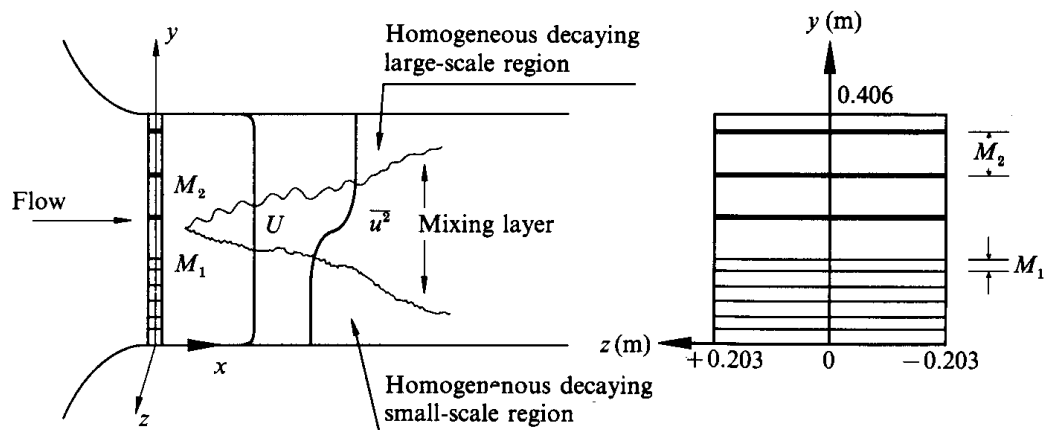
REFERENCES

TAVOULARIS, S. & CORRSIN, S. 1987 The Structure of a Turbulent Shear Layer Embedded in Turbulence. *Phys. Fluids* **30** (10), 3025–3033

SHL10: No-shear Turbulence Mixing. (Vel. ratio 1.)

Veeravalli & Warhaft

1. **Flow description:** Mixing between two turbulent streams of same velocity but different characteristics. The flow is created by two sets of grids (or perforated plates) with same solidity but different spacings. The mixing layer develops within a significant turbulence level (0.1% to 2%). The development of the ML is given.
2. **Geometry:** Square test section, $40.6 \times 40.6 \text{ cm}^2$. Total length available: 425 cm (Useful length: 253 or 168 cm). Three grids or perforated plates: 3.3:1; 8.9:1 and 3:1 (solidity 0.3). No splitter plate.
3. **Original sketch:**



4. **Flow Characteristics** 'Turbulence' mixing layer. Mean velocity 6 m/s
5. **Flow parameters:** Three sets of turbulence data are available. Reynolds numbers: mean (Grids size): from 1744 to 15 539; Turbulence (Taylor microscale): from 18 to 96.5.
6. **Inflow, outflow, boundary and initial conditions:** Turbulence levels from 0.1% to 2%
7. **Measurement procedure:** Hot Wire Anemometry CTA, $3\mu\text{m}$ - X wires. Sampling 45 kHz. Measured quantities: Mean velocities U. Turbulent data: 3 components. The homogeneity is better than 5% (average 2%) outside of the ML.
8. **Available variables:**
Global Flow parameters are given at the first downstream location: k , ϵ , integral lengths, R_e numbers etc. Decay rates and evolution of half width thickness. Evolution of the integral time scales. Mean velocity profiles. Production/dissipation ratio. RMS of the three velocity components for 3 downstream locations. Observations on approx. 60 cm (of order of 50 meshes). Higher orders moments (3 and 4) for the three velocity components and three locations.
9. **Storage size and data format:** The data are in ASCII format. Data are tabulated from printed forms. 60 Kb.

10. **Contact person:** Prof. Z. Warhaft
Cornell Univ., Sibley School of Mech. Engg., 244 Upson Hall
Ithaca, NY 14853-7501 USA.
Phone: (607) 255 3898
Fax: (607) 255 1222
E-mail: zw16@cornell.edu

REFERENCES

- VEERAVALLI, S. & WARHAFT, Z. 1989 The Shearless Turbulence Mixing Layer, *J. Fluid Mech.* **207**, 191–229
- VEERAVALLI, S. & WARHAFT, Z. 1990 Thermal Dispersion from a Line Source in the Shearless Turbulence Mixing Layer, *J. Fluid Mech.* **216**, 35–70

SHL20: Supersonic Plane Turbulent Mixing Layer, $M_c = 0.62$

Barre, Quine, Mena & Dussauge

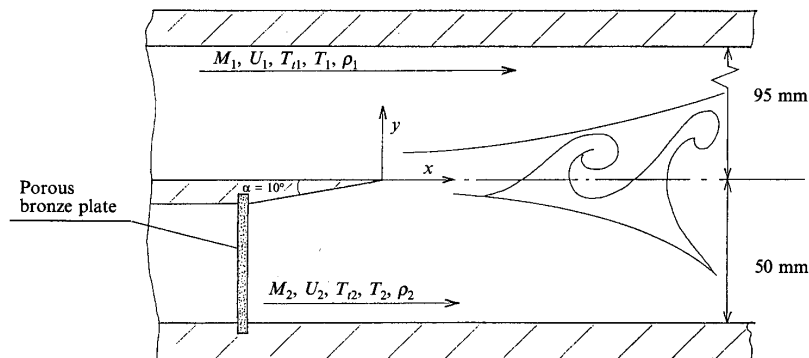
1. **Flow description:** Two stream supersonic/subsonic, plane mixing layer. The boundary layer in the supersonic stream is turbulent (fully developed, based on spectra, Log plot, etc. analysis). Development of the ML is given.

Two set of data are provided. They correspond to two slight different arrangements of a wind tunnel. The results obtained for the common data are comparable but not exactly identical. The data provided are complementary. The user then should consider the two sets of results as independent flows, unless some averaging process (not provided by the authors) can be used to collapse the data.

2. **Geometry:** Rectangular exit, 15 cm x 14 cm.

Thickness at TE: $\simeq 0.1$ mm.

3. **Original sketch:**



4. **Flow characteristics:** Two stream mixing layer, one side supersonic, the other subsonic. Mach numbers, supersonic side: 1.79; Subsonic side: 0.3. Convective Mach Number: 0.62

5. **Flow parameters:** Low pressure settling chamber ($0.6 \times 10^5 Pa$). Turbulent boundary layer in the supersonic stream: $\delta = 9.7mm$; $\theta = .78mm$; $C_f = 2.02 \times 10^{-3}$; $R_\theta = 1.57 \times 10^4$. (Very thin boundary layer on the subsonic side, typically less than 1 mm)

6. **Inflow, outflow, boundary and initial conditions:** Free stream turbulence level: supersonic side $\sigma_u/(U_1 - U_2) \simeq 0.3\%$, subsonic side $\sigma_u/(U_1 - U_2) \simeq 1\%$

7. **Measurement procedure:** Pitot tube, temperature probe. Constant Current Anemometry, single wire. Mode separation through Morkovin's (1956) fluctuation diagram (14 overheat ratios). Measured quantities: Mean and fluctuating longitudinal velocities. uv component through mean momentum balance. The turbulent heat flux is also provided through the integration of the mean total enthalpy equation. Temperature fluctuations and velocity/temperature correlations.

8. **Available variables:** Boundary layer data, 5 mm upstream of the TE in the supersonic side and Mixing layer data : Mean values, (dimensional data) P/P_0 , \bar{T} , \bar{U} , $\bar{\rho}$, $\bar{\rho u}$, Re, Entropy, Viscosity.

Fluctuations: (dimensionless data) $\overline{T'_t/T_t}$; $\overline{(\rho u)^{t2}/(\rho u)}$; $\overline{u'^2}$; $\overline{T'^2/T^2}$; $\overline{T'u'/TU}$; R_{uT} ; $\overline{\rho u'v'}$ (indirect). The Strong Reynolds Analogy (Morkovin 1962) $((\gamma - 1)M^2(u'/U))/(T'/T)$ is also tested.

Measurement locations: -5; 1; 8; 16; 32; 64; 80; 100; 120; 140; 160; 180; 200 mm.
N.B. Two-point statistics will be available under request to the contact person.

9. **Storage size and data format:** The data are in ASCII format. 180 Kb.
10. **Contact person:** Dr. J.P. Dussauge
IRPHE, 12 av. Général Leclerc, F-13003 Marseille France
Phone: (33) 04 91 50 54 39
Fax: 04 91 41 96 20
E-mail: dussauge@marius.univ-mrs.fr

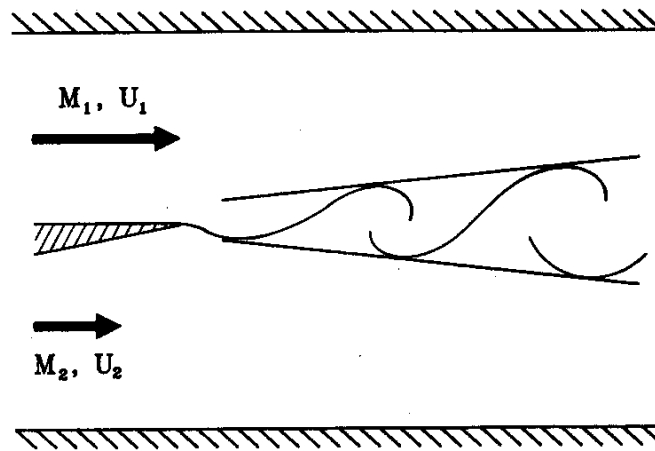
REFERENCES

- BARRE, S., QUINE, C. & DUSSAUGE, J.P 1994 Compressibility Effects on the Structure of Supersonic Mixing Layers: Experimental Results. *J. Fluid Mech.* **259**, 47–78.
- MENAA, M. 1997 Etude expérimentale d'une couche de mélange turbulente supersonique et analyse des propriétés de similitude. PhD Thesis, Université de Provence.
- MORKOVIN M.V. 1956 Fluctuations and Hot-Wire Anemometry in Compressible Fluid. *AGARDograph* **24**, NATO, June 1956.
- MORKOVIN M.V. 1962 Effect of compressibility on turbulent flows *Colloque sur la mécanique de la turbulence*, Colloques Internationaux du CNRS **108**.

SHL21: Supersonic/Subsonic Plane Turbulent Mixing Layer. $M_c = 0.51-0.86$

Samimy & Elliott

1. **Flow description:** Two stream supersonic/subsonic, plane mixing layer. The boundary layer in the supersonic stream is turbulent (fully developed, based on spectra, Log plot, etc. analysis). Development of the ML is given.
2. **Geometry:** Rectangular exit, 15 cm x 15 cm.
Thickness at TE: $\simeq 0.5$ mm.
3. **Original sketch:**



4. **Flow characteristics:** Two stream mixing layer, one side supersonic, the other subsonic. Mach numbers, supersonic side: 1.8; 2.; 3. Subsonic side: 0.45. Convective Mach Number: 0.51; 0.64; 0.86
5. **Flow parameters:** High pressure settling chamber (2.65×10^5 Pa). Turbulent boundary layers in the supersonic stream (Mach 3; $M_c = 0.86$): $\delta = 9.2\text{mm}$; $\theta = 0.75\text{mm}$; $R_\theta = 4.0 \times 10^4$. (Mach 1.8, $M_c = 0.54$): $\delta = 8\text{mm}$; $\theta = 0.5$; $R_\theta = 2.15 \times 10^4$.
The boundary layers in the subsonic stream are very thin (typically less than 1mm).
6. **Inflow, outflow, boundary and initial conditions:** Free stream turbulence level: supersonic side $\sigma_u/(U_1 - U_2) < 1\%$, subsonic side $\sigma_u/(U_1 - U_2) < 0.5\%$.
7. **Measurement procedure:** 2D LDV 2048 samples. Measured quantities: Mean and fluctuating velocities U and V.
8. **Available variables:** Boundary layer data, supersonic side for $M_c = 0.51$ and 0.86. Mixing layer data: $Y_{0.5}$; $Y_{0.1}$; $Y_{0.9}$; Temperature; Mach, Reynolds, δ ; δ_ω ; σ ; etc...
 \bar{U}/U_∞ , $\overline{u^2}$; $\overline{v^2}$; \overline{uv} ; $\overline{u^3}$; \overline{uvv} ; $\overline{u^4}$; $\overline{v^4}$; (metric and non-dimensionalized).
Measurement locations: 60; 120; 150; 180; 210 mm. for $M_c = 0.51$. X= 120; 150; 165; 180 mm for $M_c = 0.64$. X= 180; 210; 250 mm for $M_c = 0.86$.
9. **Storage size and data format:** The data are in ASCII format. 80 Kb.
10. **Contact person:** Prof. M. Samimy
Dept. Mech. Engg., The Ohio State Univ. 206 West 18th av.
Columbus, OH 43210-1107, USA.
Phone: (614) 292 6988
Fax: (614) 292 3163
E-mail: samimy.1@osu.edu

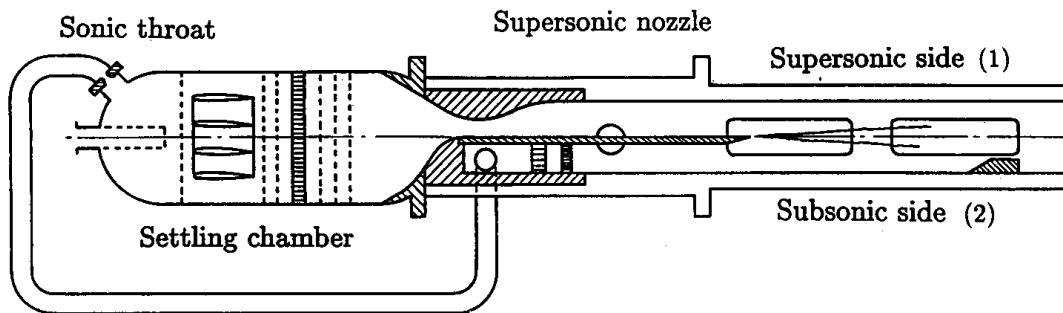
REFERENCES

- ELLIOTT, G.S. & SAMIMY, M. 1990 Compressibility Effects in Free Shear Layer. *Phys. Fluids A* **2**(7), 1231–1240.
- SAMIMY, M. & ELLIOTT, G.S. 1990 Effects of Compressibility on the Characteristics of Free Shear Layers. *AIAA J.* **28**, 439–445.
- SAMIMY, M., REEDER, M.F. & ELLIOTT G.S. 1992 Compressibility effects on large structures in free shear flows. M. Samimy, *Phys. Fluids* **4**, N. 6, 1251–1258.

SHL22: Supersonic Plane Turbulent Mixing Layer, $M_c = 0.525-1.04$

Bonnet, Barre & Debisschop

- Flow description:** Two-stream supersonic/subsonic, plane mixing layer. The boundary layer in the supersonic stream is turbulent (fully developed, based on spectra, Log plot, etc. analysis). Development of the ML is given. **N.B.** A full set of experiments are obtained at convective Mach number 1.04, with a pressure drop, see last reference. Data not provided here but available upon request.
- Geometry:** Rectangular exit, 15 cm x 15 cm Total length available: 50 cm.
Splitter plate: 80 cm long, 5° thickness at TE: $\simeq 0.3$ mm.
- Original sketch:**



- Flow characteristics:** Two stream mixing layer, one side supersonic, the other subsonic. Mach numbers, supersonic side: 1.48; 1.65; 1.76; 2.; 3.2. Subsonic side: 0.2–0.4 Convective Mach Numbers: 0.525; 0.535; 0.58; 0.64; 1.04.
- Flow parameters:** High pressure settling chamber (4×10^5 to $12 \times 10^5 Pa$). Turbulent boundary layers in the supersonic stream: $\delta = 12mm$; $\theta = .97; .96; .96; .76; .66mm$; $R_\theta = 6.8; 8.64; 8.64; 6.8; 6.3 \times 10^4$. The boundary layers in the subsonic side are very thin (typically less than 1mm).
Mixing layer: Spreading rates depends on convective Mach number.
- Inflow, outflow boundary and initial conditions:** Free stream turbulence level: supersonic and subsonic sides $\simeq 0.4/(U_1 - U_2)\%$.
- Measurement procedure:** Laser Doppler velocimetry: ONERA System and Aerometrics system. SiO_2 seeding. Measured quantities: Mean and fluctuating velocities (2 components). Measurement errors are estimated to 1 % in mean and 4 % in rms.
- Available variables:** Boundary layer data, supersonic side for $M = 3$ ($M_c = 1.04$): \overline{U} ; $\overline{u^2}$; $\overline{v^2}$; \overline{uv} .
Mixing layer data: $Y_{0.5}; Y_{0.1}; Y_{0.9}$; Temperature; Mach, Reynolds, δ ; δ_ω ; $\delta_{Stanford}$; σ ; etc...
 \overline{U} , $\overline{u^2}$; $\overline{v^2}$, \overline{uv} ; $\overline{vu^2}$; $\overline{uv^2}$; $\overline{u^3}$; $\overline{v^3}$; (+ skewness, flatness)
Measurement locations: 2; 10; 70; 125; 150; 180; 210; 240; 265; 295; 320 mm.
- Storage size and data format:** The data is in ASCII format. 300 Kb.
- Contact persons:** Dr J.P. Bonnet
LEA-CEAT, University of Poitiers, 43 rue de l'Aérodrome, F-86036 Poitiers cedex France
Phone: (33) 05 49 53 70 31
Fax: (33) 05 49 53 70 01
E-mail: bonnet@univ-poitiers.fr

Dr S. Barre
LEA-CEAT, University of Poitiers, 43 rue de l' Aérodrome, F-86036 Poitiers cedex France
Phone: (33) 05 49 53 70 05
Fax: (33) 05 49 53 70 01
E-mail barre@univ-poitiers.fr

REFERENCES

- DEBISSCHOP, J.R., CHAMBRES, O. & BONNET, J.P. 1994 Velocity field characteristics in supersonic mixing layers. *Exp. Thermal and Fluid Science* **9**, 147–155.
- BARRE, S., BRAUD, P., CHAMBRES, O. & BONNET, J.P. 1997 Influence of inlet pressure conditions on supersonic turbulent mixing layers. *Exp. Thermal and Fluid Science* **14**, N. 1, 68–74.

SHL30: Round turbulent jet

Hussein, Capp & George

1. **Description of the flow:** Axisymmetric jet discharging from a circular orifice into a large room with stagnant air. Only the self-preserving far-field is of interest here.

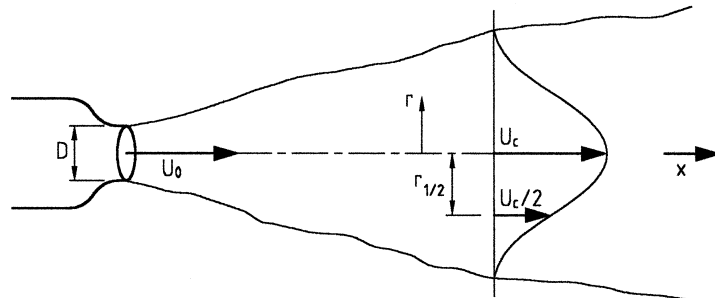


Figure 1: Flow configuration

2. **Geometry:** The only geometrical parameter of interest in the case of an axisymmetric jet issuing into nominally infinite surroundings is the exit diameter $D = 1$ inch ($= 2.54$ cm).

In reality, the room into which the jet discharges is of finite size but the enclosure was kept large and designed to minimize the backflow momentum (Fig. 2). It should be noted that the jet does not issue from an orifice in the wall but the exit is 34 ft from the end wall. The enclosure has a 16×16 ft cross-section and is 82 ft long.

3. **Original sketch**

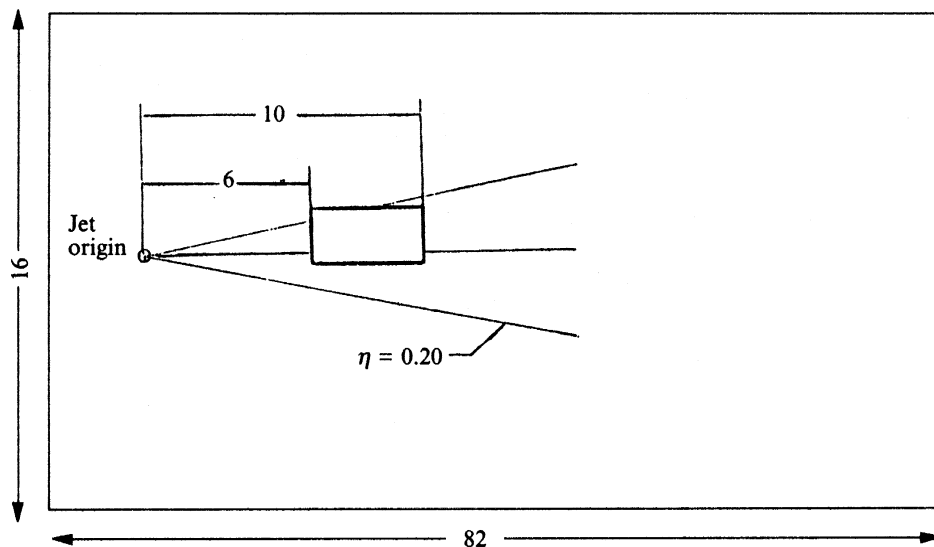


Figure 2: Layout of jet facility (dimensions in feet)

4. **Flow characteristics:** After an initial development region, the flow develops self-preserving behaviour: the jet spreads linearly with x , i.e.

$$dr_{1/2}/dx = \text{const.} = 0.094,$$

where $r_{1/2}$ is the jet half-width defined in Fig. 1, and the velocity on the centre-line U_c decays as

$$(U_0/U_c) = \frac{1}{B_u}(x/D - x_0/D) \quad (\text{here } B_u = 5.8)$$

where x_0 is the virtual origin of the jet (here $x_0/D \approx 4$). In the self-preserving region, lateral profiles of all quantities at various x collapse when made dimensionless with the local centre-line velocity U_c and the downstream distance from the virtual origin, $x - x_0$, or alternatively the local jet half-width $r_{1/2}$. Hence, only similarity profiles, the spreading rate $dr_{1/2}/dx$ and the decay constant B_u need to be given to define the jet behaviour in the self-preserving region. The mean velocity U was found to be self-similar for $x/D > 30$; profiles of the turbulence quantities measured at $x/D = 70$ and 100 were found to be self-similar (measurements at $x/D = 70$ are presented).

5. **Flow parameters:** The Reynolds number based on the exit velocity U_0 and the exit diameter D is $Re = U_0 D / \nu = 9.55 \times 10^4$. The exit velocity is $U_0 = 56.2$ m/s and the turbulence level in the exit flow is 0.58%.
6. **Inflow/Outflow/Boundary and Initial Conditions:** The mean velocity and turbulence intensity across the jet exit was measured with a hot-wire probe. The boundary layer at the jet lip was laminar with a thickness $\delta_{95} = 0.7$ mm so that the exit profile was near top hat. The momentum flux in the self-preserving portion of the jet is 85% of the momentum flux at the exit.

In any case, the self-preserving state of the jet should be independent of the inflow conditions.

7. **Measurement procedures:** Velocity measurements were carried out with stationary hot-wires, flying hot-wire and a burst-mode Laser-Doppler anemometer (LDA). The hot-wire-anemometer voltages were digitized and processed on a computer. The stationary hot-wire has limitations in this flow since the local turbulence intensity ranges from 30% at the centre-line to a value above 100% towards the edge. The flying hot-wire is moved with a velocity of 7.5 m/s so that the effective turbulence intensity seen by the wire is less than 12% at all locations. A two-channel LDA was used working in the back-scatter mode with frequency shift. The signals were processed with a counter using the resident time weighting technique. The results obtained with the flying hot-wire and the LDA are very similar but distinctly different from those obtained with a stationary hot-wire. Because of the problems of stationary hot-wires in high-intensity flows, only the former results will be included here. The quantities measured are the mean velocity, the Reynolds-stress components, the triple correlations (second-order moments) and the dissipation rate on the assumption of the turbulence being locally axisymmetric. Balances of the turbulent kinetic energy and of the individual Reynolds-stress components were constructed from these measurements.

No explicit information is given on the measurement errors and uncertainties for the various quantities. The measured shear-stress distribution agrees well with the distribution calculated from the mean velocity and the spreading rate, giving confidence in the measurements of the second moments. The stresses are generally higher than measured previously with stationary hot-wires and in the outer region they are also higher than the measurements obtained by Panchapakesan and Lumley (1993) with a moving hot-wire, but in a jet whose Reynolds number was smaller by a factor of 10. There are some uncertainties about the measurements of the dissipation rate leading to a fairly large pressure-diffusion term near the axis so that the balances presented are considered less reliable and are not included in the data provided. They can be obtained from the original paper.

8. **Available variables:** Spreading rate $dr_{1/2}/dx = 0.094$, decay constant for centre-line velocity $B_u = 5.8$, similarity profiles in analytical form of U/U_c , $\overline{u'^2}^{1/2}/U_c$, $\overline{v'^2}^{1/2}/U_c$, $\overline{w'^2}^{1/2}/U_c$, $\overline{u'v'}/U_c$ versus $\eta = y/(x - x_0)$
9. **Storage size and data format:** Format is ASCII.
10. **Contact person:** Prof. W.K. George
University of Buffalo, SUNY, 339 Engg East, 14260 Buffalo, NY, USA
E-mail: trlbill@eng.buffalo.edu

REFERENCES

- HUSSEIN, H.J., CAPP, S.P. AND GEORGE, W.K. 1994 Velocity measurements in a high-Reynolds-number, momentum-conserving, axisymmetric, turbulent jet, *J. Fluid Mech.* **258**, 31–75.
- PANCHAPAKESAN, N.R. AND LUMLEY, J.L. 1993 Turbulence measurements in axisymmetric jets of air and helium. Part I. Air jet, *J. Fluid Mech.* **246**, 197–223.

SHL31: Plane turbulent jet

Gutmark & Wygnanski

1. **Flow description with sketch:** Two-dimensional plane jet discharging from a rectangular orifice (slot) into stagnant ambient. Only the self-preserving far-field is of interest here.

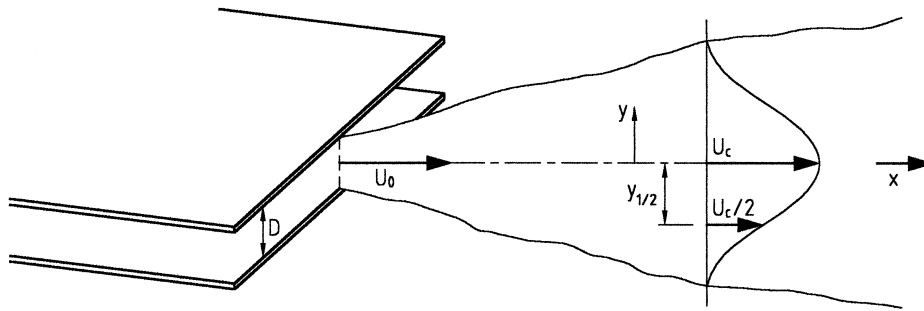


Figure 1: Flow configuration

2. **Geometry:** The only geometrical parameter of interest in the case of a $2D$ plane jet issuing into nominally infinite surroundings is the slot width which was $D = 1.3$ cm.

However, the finite size of the room into which the jet discharges may influence the jet development and hence information on the size of this room is given in Fig. 2. The orifice was 1.3 cm wide and 50 cm long. The jet developed between two walls of 200×200 cm size forming top and bottom, and screens were installed to eliminate most room draughts.

3. **Original sketch**

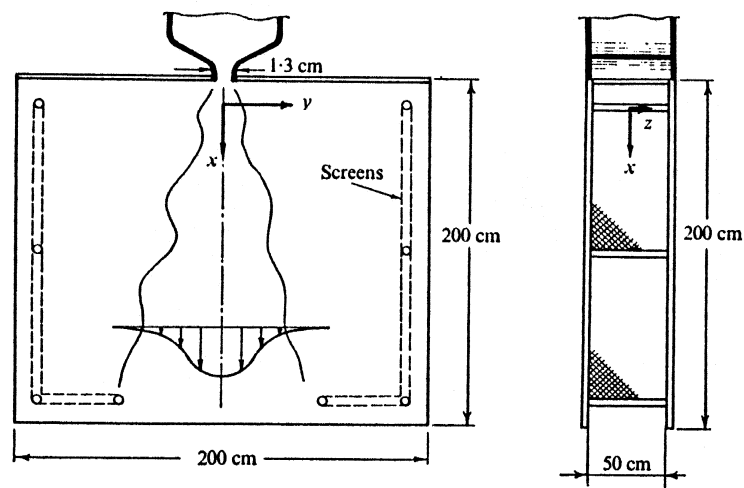


Figure 2: Schematic diagram of experimental apparatus.

4. **Flow characteristics:** After an initial development region, the flow develops self-preserving behaviour: the jet spreads linearly with x , i.e.

$$dy_{1/2}/dx = \text{const.} = 0.1,$$

where $y_{1/2}$ is the jet half-width defined in Fig. 1, and the velocity on the centre-line U_c decays as

$$(U_0/U_c)^2 = \frac{1}{A_u}(x/D - x_0/D) \quad (\text{here } A_u = 5.32)$$

where x_0 is the virtual origin of the jet (here $x_0/D \approx 3$). In the self-preserving region, lateral profiles of all quantities at various x collapse when made dimensionless with the local centre-line velocity U_c and the downstream distance from the virtual origin, $x - x_0$, or alternatively the local jet half-width $y_{1/2}$. Hence, only similarity profiles, the spreading rate $dy_{1/2}/dx$ and the decay constant A_u need to be given to define the jet behaviour in the self-preserving region. The authors state that the flow was found to be self-preserving beyond $x/D > 40$, but some of the profiles of turbulence quantities indicate that self-preservation occurred only beyond $x/D \approx 100$.

5. **Flow parameters:** The Reynolds number based on the exit velocity U_0 and slot width D is $Re = U_0 D / \nu = 3 \times 10^4$. The turbulence level in the exit flow is 0.2%.
6. **Inflow/Outflow/Boundary and Initial Conditions:** The jet exits from a slot in the wall. Detailed measurements are not provided at the jet exit. A top-hat velocity profile was aimed at by using a strong nozzle contraction. That this was nearly achieved is indicated by the fact that the momentum flux in the jet is 89% of the momentum flux at the exit, assuming a top-hat profile.

In any case, the self-preserving state of the jet should be independent of the inflow conditions.

7. **Measurement procedures:** The mean-velocity profile was measured with a Pitot tube and a single hot-wire probe. The latter was also used to measure the longitudinal fluctuations while the other two fluctuating components were measured with x-wires and single inclined wires (constant temperature anemometer with linearizers). Further quantities measured are the intermittency factor, the Reynolds stresses with averaging performed only over the turbulent zones, two-point velocity correlations, dissipation terms and microscales, triple correlations. The turbulent kinetic energy balance was constructed by assuming local isotropy for determining the viscous dissipation.

No direct information is given on the measurement errors. However, the measured shear-stress distribution agrees fairly well with the distribution calculated from the mean-velocity profile and the spreading rate, giving some confidence in the measurements of the second moments. The normal stresses are in reasonable agreement with the measurements of Heskestad (1965), and for the v - and w -components this is true also for other measurements reviewed in Rodi (1975), but the latter show up to 20% smaller values for $\overline{u'^2}^{1/2}/U_c$. Hence, strangely, there is some uncertainty about this quantity. There are even greater uncertainties about the measurements of higher moments and the terms in the kinetic energy balance so that these are not included in the data provided. They can be obtained from the original paper.

8. **Available variables:** Spreading rate $dy_{1/2}/dx = 0.1$, decay constant for centre-line velocity $A_u = 5.32$, similarity profiles of U/U_c , $\overline{u'^2}^{1/2}/U_c$, $\overline{v'^2}^{1/2}/U_c$, $\overline{w'^2}^{1/2}/U_c$, $\overline{u'v'}/U_c$ versus $y/y_{1/2}$ (and the corresponding $\eta = y/(x - x_0)$)
9. **Storage size and data format:** Format is ASCII.
10. **Contact person:** Prof. I. Wygnanski
AME dept. Tucson, AZ 85721, USA,
Phone: (602) 621 6089
Fax: (602) 621 8191
E-mail: wygy@bigdog.engr.arizona.edu

REFERENCES

- GUTMARK, E. AND WYGNANSKI, I. 1976 The planar turbulent jet, *J. Fluid Mech.***73**, 465–495.
- HESKESTAD, G. 1965 Hot-wire measurements in a plane turbulent jet, *J. Appl. Mech.***32**, pp. 1.
- RODI, W. 1975 A review of experimental data of uniform-density free turbulent boundary layers, in *Studies in Convection*, Vol. 1, ed. B.E. Launder, Academic Press, London.

Data Sheets for:
Chapter 7.- Turbulent Boundary Layers

TBL00: Flat plate, zero-pressure-gradient TBL

Smith & Smits

1. **Description of the flow:** Flat-plate, zero-pressure-gradient TBL.

2. **Geometry:**

The experiments were conducted in a long, subsonic, open return wind tunnel having a rectangular cross-section. Test section dimensions were 5.8 m long (streamwise), by 1.22 m wide (spanwise) by 0.15 m high (wall-normal).

3. **Sketch:** None needed.

4. **Flow characteristics**

The mean flow was approximately two-dimensional as evidenced by agreement with the momentum integral equation to within $\pm 7\%$. A settling chamber and 6:1 contraction (described below) minimized free stream turbulence levels. The outer wall, opposite the measurement wall, was contoured to minimize the streamwise pressure gradient.

5. **Flow parameters**

The working fluid was air at existing ambient temperature and pressure. Ambient conditions were monitored throughout all experiments, and the temperature did not vary by more than 0.2°C during any given run. Using an upstream pitot tube, the tunnel flow speed was set to obtain a unit Reynolds number $Re_{unit} = 2,100,000 \pm 3\%$ for all runs. The free stream flow speed was approximately 33 m/s . Mean flow measurements were obtained at ten streamwise locations, providing momentum-thickness Reynolds numbers ranging from 4,601 to 13,189. Turbulence measurements were made at two streamwise locations, at Reynolds numbers of $Re_\theta \approx 5,000$ and 13,000. The static pressure coefficient varied by less than 4% over the length of the test section.

Flow parameters for the mean flow data files

x (mm)	Re_θ	δ^+	U_∞ (m/s)	U_{ref} (m/s)	u_τ (m/s)	C_f	δ (mm)	δ^* (mm)	θ (mm)	H	Π	δ_{log}/δ
1.021	4,601	1,500	33.32	33.16	1.291	.00300	18.35	2.98	2.18	1.37	.513	.264
1.161	4,980	1,609	33.39	33.06	1.285	.00296	19.82	3.20	2.36	1.36	.513	.327
1.302	5,388	1,705	32.46	32.19	1.234	.00289	21.31	3.48	2.56	1.36	.545	.292
1.451	5,888	1,847	33.41	33.03	1.261	.00285	23.02	3.76	2.77	1.36	.543	.314
1.721	6,866	2,058	33.40	33.12	1.225	.00269	26.65	4.44	3.26	1.36	.646	.290
2.021	7,696	2,316	33.84	33.43	1.229	.00264	30.07	4.93	3.63	1.36	.642	.307
2.523	9,148	2,712	34.03	33.69	1.220	.00257	35.73	5.83	4.32	1.35	.638	.300
3.023	10,347	3,089	33.11	32.81	1.173	.00251	41.46	6.58	4.92	1.34	.640	.271
3.542	11,608	3,490	33.41	33.23	1.179	.00249	47.04	7.34	5.52	1.33	.601	.302
4.124	13,189	4,005	32.97	32.82	1.154	.00245	54.49	8.28	6.28	1.32	.578	.279

Flow parameters for the turbulence data files

x (mm)	Re_θ	δ^+	U_∞ (m/s)	U_{ref} (m/s)	u_τ (m/s)	C_f	δ (mm)	δ^* (mm)	θ (mm)	H	Π	δ_{log}/δ
1.021	5,021	1,518	32.85	32.26	1.236	.00283	19.29	3.33	2.40	1.39	.660	.310
4.124	13,052	4,087	33.04	32.27	1.170	.00251	54.98	8.13	6.22	1.31	.502	.313

6. **Inflow, outflow, boundary and initial conditions:**

Ambient air entered the tunnel through a large bell-mouth, passed through a honeycomb flow-straightener, having a grid size of 6.3 mm and a depth of 76 mm, and into a settling chamber. The settling chamber was 0.91 m long and contained a series of five screens oriented perpendicular to the flow direction. The first screen was of openness ratio 67% (mesh size 0.9 mm by 0.9 mm), and the last four screens were of openness ratio 63% (mesh size 1.3 mm by

1.3 mm). The flow exited the settling chamber, passed through a two-dimensional 6:1 contraction, and entered the test section.

Downstream, the flow leaving the test section entered a short, two-dimensional diffuser, followed by a longer, three-dimensional diffuser. In the two-dimensional diffuser, a row of vortex generators prevented separation on the outer wall. A final screen placed between the two diffuser sections helped reduce flow unsteadiness.

7. Measurement procedures:

Static pressure coefficient data were obtained from pressure taps along the centerline of the tunnel test wall. At ten streamwise locations, mean velocity profiles were measured via Pitot probe surveys.

Turbulence measurements were made using single normal-wire hot-wire probes operated in the constant temperature mode. Reynolds stresses were measured using crossed-wire probes oriented to measure u and v , and then u and w . The hot-wire anemometer circuits contained symmetrical bridges to enhance frequency response. For all runs, the frequency response was at least 65 KHz.

Maximum error in percent relative to the measured value

Re_θ	y	$\overline{u'^2}$	$\overline{v'^2}$	$\overline{w'^2}$	$-\overline{u'v'}$	$\overline{q^2}$	$\frac{-\overline{u'v'}}{u'_{rms} v'_{rms}}$	$\frac{\overline{q^2}}{-\overline{u'v'}}$	$\frac{\overline{v'^2}}{u'^2}$	$\frac{\overline{w'^2}}{u'^2}$	$\frac{\overline{v'^2}}{w'^2}$
$\approx 5,000$	$y^+ \approx 17$	15	-	-	-	-	-	-	-	-	-
	$y/\delta \approx 0.1$	5	10	5	10	6	3	-4	5	UA	5
	$y/\delta \approx 0.7$	3	5	3	5	4	1	-1	2	UA	2
$\approx 13,000$	$y^+ \approx 17$	15	-	-	-	-	-	-	-	-	-
	$y/\delta \approx 0.1$	5	7	5	7	6	1	-4	2	UA	2
	$y/\delta \approx 0.7$	3	5	3	5	4	1	-1	2	UA	2

8. Available variables

Mean flow data consist of mean velocity profiles, static pressure coefficient, and skin friction coefficient at ten Reynolds numbers. Turbulence data consist profiles of mean and mean-squared values, as well as third and fourth order moments, of the three velocity components. Profiles of the uv and uw Reynolds stresses and u^2v and wv^2 are also available. The README file accompanying the data provides full details of the available data.

9. **Storage size and data format:** Data are in ASCII files, requiring approximately 50 Kb of storage. A README file provides details about file formats.
10. **Contact person:** Prof. Alexander J. Smits
 Director, Gasdynamics Laboratory, Department of Mechanical and Aerospace Engineering
 Princeton University, Princeton, NJ 08544, USA
 Tel: (609) 258 5117; Fax: (609) 258 2276
 E-mail: asmits@pucc.princeton.edu
http://www.princeton.edu/gasdyn/People/Lex_Smits.html

REFERENCES

- SMITH, R. W. 1994 *Effect of Reynolds Number on the Structure of Turbulent Boundary Layers*. Ph. D. thesis, Department of Aerospace and Mechanical Engineering, Princeton University, Reference number 1984-T (for a full description of the data)
- DUSSAUGE, J.P., FERNHOLZ, H.H., FINLEY, J.P., SMITH, R.W., SMITS, A.J. & SPINA, E.F. 1995 *Turbulent Boundary Layers in Subsonic and Supersonic Flow*, AGARDograph 335.

TBL01: Turbulent Boundary Layer with No Pressure Gradient

Spalart

- Description of the flow:** Numerical simulation of a two-dimensional boundary layer with zero pressure gradient.
- Geometry:** Smooth flat surface, periodic spanwise and streamwise with multiple-scale corrections to model the streamwise growth. Data from two sets of simulations are included, both using the same numerical code and flow parameters. In Spalart (1988) the streamwise extent of the numerical is $L_x = 100 \delta^*$, and the spanwise extent is $L_z = 25 \delta^*$. The simulations in Chacin *et al* (1996) are run in a computational box only half as long in the streamwise direction.
- Sketch:** Not needed
- Flow characteristics:** The flow is intended to model conditions in a zero-pressure-gradient boundary layer at a given streamwise position. The computational box is short enough that the streamwise growth is not significant, and this is explicitly used in the computational scheme. Four cases were originally computed, corresponding to $Re_{\delta^*} = 250, 500, 1000, 2000$, and used to estimate the slow growth parameters of the boundary layer, which are then used in the code. Only the two middle ones are included as data sets, since they are now recognised as having the best numerical quality.
- Flow parameters:** Within classical thinking, Re_{θ} fully describes the flow. For the two sets included, $Re_{\theta} \approx 300, 670$. The free stream is nominally quiet, but the periodic boundary conditions are roughly equivalent to a “tripped” layer. Trip “memory” is clearly an issue for the first set but probably not for the second. The Reynolds number of the first data set is also marginal for fully developed turbulence, which is traditionally expected to exist only above $Re_{\theta} \approx 320$, but this case is used as inlet condition for the simulation in TBL21, and an instantaneous flow field is included here for that purpose.
- Numerical methods, resolution and resulting uncertainties:** The numerical scheme is fully spectral, Fourier in the streamwise and spanwise directions and Jacobi normal to the wall, de-aliased in the three directions by the 2/3 rule Spalart (1986; 1988). The multiple-scale procedure discussed in Spalart (1988) provides a fair approximation to the streamwise growth effects, including entrainment. The spacing between collocation points is $\Delta x^+ \approx 20$ and $\Delta z^+ \approx 7$, and the stretched grid in the y -direction is adjusted to have 10 points within the first 9 wall units. The size of the collocation grid for the lower Reynolds number case in Spalart (1988) is $(128 \times 50 \times 96)$ in the x -, y - and z -directions. For the high Reynolds number it is $(256 \times 64 \times 192)$. For the shorter computational boxes in Chacin *et al* (1996) the resolution is maintained by halving the number of streamwise modes. Grid refinement studies conducted in Spalart (1988) for the lower Reynolds number case suggest that truncation errors due to resolution should be below 2%. Time step is adjusted to a maximum local CFL of 2 (Spalart 1986).
- Boundary and initial conditions:**
 - Domain size and truncation:** Domain size is given above. Wall normal grid is mapped exponentially with a scale proportional to the displacement thickness.
 - Boundary conditions:** Periodic spanwise. No-slip at the wall and free-slip at the top of the domain, which is far in the free stream.
 - Inlet and initial conditions:** Flow is streamwise periodic with the corrections mentioned above. The simulation is run until the flow is statistically stationary.
- Averaging procedures and resulting uncertainties:** Statistics are compiled after the flow becomes statistically stationary, and accumulated during $t = 200 \delta^*/U_{\infty}$, corresponding to about two full flow-throughs at the free stream.
- Available variables:** At $Re_{\theta} = 300$ and 670, profiles from Spalart (1988) contain $y, U, \overline{u'^2}, \overline{v'^2}, \overline{w'^2}, -\overline{u'v'}$, and the budgets of $\overline{u'^2}, \overline{v'^2}, \overline{w'^2}, -\overline{u'v'}$. Viscous diffusion and dissipation are distinct, but not pressure-strain and pressure diffusion.

One instantaneous flow field is included for each Reynolds number from Chacin *et al* (1996), which is essentially a re-computation of the original flow fields.

10. **Storage size required and present format of the data:** 66 Kb, ASCII file for the profiles. 5 Mb binary files for the low Reynolds number flow field. 17 Mb for the high Reynolds number one.
11. **Contact person:** For Spalart (1988): P. R. Spalart
Boeing Commercial Airplane Group, P.O. Box 3707, Seattle, WA 98124-2207, USA
e-mail:spalart@nas.nasa.gov
For Chacin *et al* (1996): B. Cantwell
Dept. Aeronautics and Astronautics, Stanford U., Stanford, CA 94305, USA
e-mail: cantwell@leland.stanford.edu

REFERENCES

- CHACIN, J.M., CANTWELL, B.J. & KLINE, S.K. 1996 Study of turbulent boundary layer structure using the invariants of the velocity gradient tensor. To appear in *J. Exper. Thermal and Fluid Sci.*
- SPALART, P.R. 1986 Numerical simulations of boundary layers: Part 1. Weak formulation and numerical methods, NASA TM-88222.
- SPALART, P.R. 1988 Direct numerical study of a turbulent boundary layer up to $Re_\theta = 1410$, *J. Fluid Mech.* **187**, 61-98.

TBL10: Turb. B.L. in Adverse Pressure Gradient

Marusic & Perry

- Description of the flow:** Two flows, called 10APG and 30APG, with upstream velocities of 10m/s and 30 m/s. Both start in zero pressure gradient and are then acted upon by an approximately constant adverse pressure gradient.
- Geometry:** Flows develop on the 940mm wide floor of an open return blower type wind tunnel. A contraction area ratio 8.9:1 leads to a 4.3m long working section with 68 pressure tappings along the floor streamwise centre line. Pressure gradients are imposed by heavy screening at the downstream diffuser and by varying the angle of 12 adjustable louvers in part of the working section roof. The inclination of the first 1.45m of the working section roof was varied to obtain an approximately zero pressure gradient on the floor.
- Sketch:**

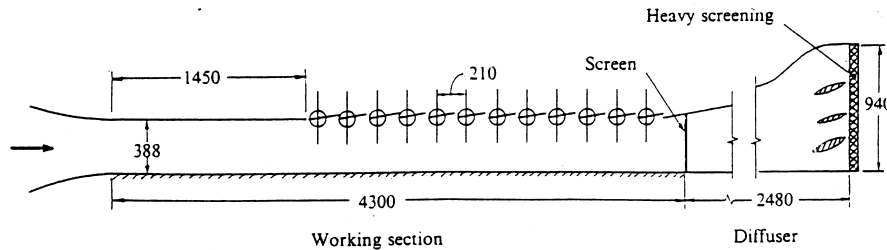


Figure 1: Details of working section (dimensions in mm).

- Flow characteristics:** Two two-dimensional adverse pressure gradient turbulent boundary layer flows far from equilibrium.
- Flow parameters:** Free stream turbulence intensity 0.3%.
Mean flow parameters, see table below.

$x(\text{mm})$	U_e/u_τ	H	R_θ
(10APG)			
1200	23.6	1.43	2206
1800	25.4	1.44	3153
2240	28.1	1.49	4155
2640	31.5	1.58	5395
2880	34.5	1.64	6395
3080	38.4	1.73	7257
(30APG)			
1200	26.4	1.40	6430
1800	28.2	1.41	8588
2240	30.1	1.44	10997
2640	32.9	1.49	14209
2880	35.2	1.54	16584
3080	38.1	1.60	19133

x is the streamwise direction; U_e is the velocity at the edge of the boundary layer; u_τ , friction velocity; R_θ , momentum thickness Reynolds number; H , shape factor.

- Inflow, outflow boundary and initial conditions:** Should be taken from initial and final profiles and imposed pressure distribution.

7. Measurement procedures:

- (a) **Measured Quantities:** Mean flow profiles, Reynolds shear stresses, all three components of the Reynolds normal stresses and measured spectra.
- (b) **Measurement Errors:** Not cited
- (c) **Other supporting information:** Mean flow profiles from pitot-static probe. Wall shear from Clauser chart and Preston tube. Turbulence quantities from stationary and flying X hot wires.

8. **Available variables:** Mean flow profiles, Reynolds shear stresses, all three components of the Reynolds normal stresses and measured spectra.

9. **Storage size required and file format:** Profiles 50 Kbytes, Spectra 6 Mbytes. ASCII files.

10. **Contact person:** I. Marusic

Department of Mechanical and Manufacturing Engineering, University of Melbourne, Parkville, Victoria 3052, Australia

e-mail:ivan@mame.mu.oz.au

REFERENCES

MARUSIC, I. & PERRY, A.E. 1995 A wall-wake model for the turbulence structure of boundary layers. Part 2. Further experimental support. *J. Fluid Mech.* **298**, 389–407.

TBL11: Turb. B.L. in Adverse Pressure Gradient; Numerical

Spalart & Watmuff

- Description of the flow:** Numerical simulation of a two-dimensional boundary layer with sequentially favourable and adverse pressure gradients. The simulation was intended to replicate experimental data, compiled especially for that purpose, and which are also included in the data set. Only the simulation is described here. For a description of the experiment, see Watmuff (1990); Spalart & Watmuff (1993).
- Flow geometry:** 3-D computational box, periodic in the streamwise, x -, and spanwise z -directions, with streamwise corrections discussed above. All lengths are expressed in meters while velocities are normalised with the free-stream velocity U_o at the inlet. The useful length of the experimental flat plate was 1.5 m, and the boundary layer was tripped at $x = 0.15$. Free-stream pressure was controlled by a contoured upper wall, convergent from $x = 0.2$ to 0.6 and divergent thereafter. The resulting pressure distribution is shown in the sketch below. The computational region extends from $x = 0.3$ to 1.1, but only the region from $x = 0.4$ to $x = 1$ is considered useful. The rest is used by the numerical “fringes” described below. The boundary layer remains attached and, at the beginning of the comparison region, is fully turbulent with thickness of the order of $\delta^* = 1.9$ mm. The spanwise extent of the computational box is $L_z = 0.09$.
- Sketch:**

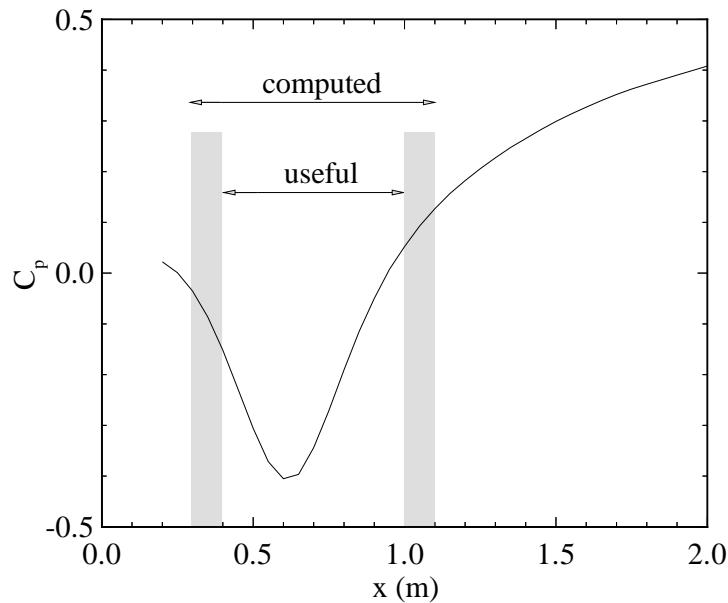


Figure 1: Computational domain and experimental pressure distribution outside the boundary layer.

- Flow characteristics:** The flow accelerates from a C_p near 0 to near -0.4 , which helps erase the memory of the trip and of the inflow condition. After that the C_p returns to about $+0.05$ in the region covered by the DNS, although the experiment went farther. The boundary layer remains attached, and thickens until it reaches $Re_\theta \approx 1750$ and $H \approx 1.6$. A zero-pressure-gradient boundary layer at the same Re_θ would be $H \approx 1.45$.
- Flow parameters:** The Reynolds number per meter is 4.28×10^5 , and Re_θ is 530 at the beginning of the comparison region. The pressure coefficients are given in the sketch. The free stream is nominally quiet and the two-dimensionality of the experiment was checked to be of the order of 1-2% over spanwise distances of 20 cm.
- Numerical methods, resolution and resulting uncertainties:** Fully spectral method, Fourier in the x - and z -directions. Jacobi polynomials in y , matched to an exponential mapping (Spalart *et al* 1991). Streamwise boundary layer growth is compensated by a “fringe” method in which an extra term is applied to the equations in $x = (0.3 - 0.4)$ and $x = (1 - 1.1)$, restoring the outgoing flow to the desired inflow condition (Spalart & Watmuff 1993). The

collocation grid is $(960 \times 82 \times 320)$. Dealiasing is done in the three directions by the $2/3$ rule. Based on the highest mean skin friction in the box, the distance between collocation points is $\Delta z^+ = 20$, $\Delta z^+ = 7.3$. The wall normal stretched grid has 10 points below $y^+ = 9$. Numerical quality parameters are discussed in Spalart & Watmuff (1993).

7. **Boundary and initial conditions:**

- (a) **Domain size and truncations:** The boundary layer is essentially fully developed as it reaches the domain numerical domain, and relaxes further due to the favourable pressure gradient. The lateral extent of the large eddies was estimated from the two-point correlation function to be of the order of 0.02 at $x = 1$, compared to the computational box size $L_z = 0.09$.
- (b) **Boundary conditions** The pressure distribution outside the boundary layer is controlled in the experiment by a contoured upper wall. In the simulation, it is controlled by tailoring the behaviour of the wall-normal velocity at boundary at large y . Velocity and stress profiles are given at inflow. Outflow is not critical.
- (c) **Inlet or initial conditions:** Generated by the fringe method described above.

8. **Averaging procedures and resulting uncertainties:** Mean values are averaged over the span, and over time. A filter of streamwise width ≈ 0.02 is also applied. The statistical sample is formed by 100 velocity fields, covering a total time of about $0.81/U_o$, or about one full flow-through.

9. **Available variables:** The simulation data are given at $x = 0.55$ to 1 by 0.05. The file has $y, U, V, C_p, \overline{u'^2}, \overline{v'^2}, \overline{w'^2}, -\overline{u'v'}$. The same data are given from an accompanying experiment from $x = 0.2$ to 2 by 0.05, in TBL12.

10. **Storage size required and file format:** 67 Kbytes, ASCII file.

11. **Contact person:** P. R. Spalart
Boeing Commercial Airplane Group
P.O. Box 3707, Seattle, WA 98124-2207, USA
e-mail:spalart@nas.nasa.gov

REFERENCES

SPALART, P. R., MOSER, R. D. AND ROGERS, M. M. 1991 Spectral methods for the Navier-Stokes equations with one infinite and two periodic directions, *J. Comp. Phys.* **96**, 297-324.

SPALART, P.R. & WATMUFF, J.H. 1993 Experimental and numerical investigation of a turbulent boundary layer with pressure gradients. *J. Fluid Mech.* **249**, 337-371.

WATMUFF, J.H. 1990 An experimental investigation of a low Reynolds number turbulent boundary layer subject to an adverse pressure gradient. *1989 Ann. Res. Briefs*, CTR, Stanford, pp. 37-49.

TBL12: Turb. B.L. in Adverse Pressure Gradient; Experimental

Watmuff

1. **Description of the flow:** Incompressible, two-dimensional, turbulent boundary-layer flow. Downstream of a trip the pressure gradient is initially favourable to allow the turbulence to mature without undue increase in Reynolds number. The pressure gradient then becomes adverse. The experiment was especially devised to match the conditions of the direct numerical simulation TBL11.
2. **Geometry:** Flow develops on the 1.0m wide 2.1m long floor of an open return blower type wind tunnel. A contraction area ratio 5:1 leads to the initially 0.24m high working section. Pressure gradients are imposed by a flexible ceiling and the test section has two Plexiglas sidewalls.
3. **Sketch:**

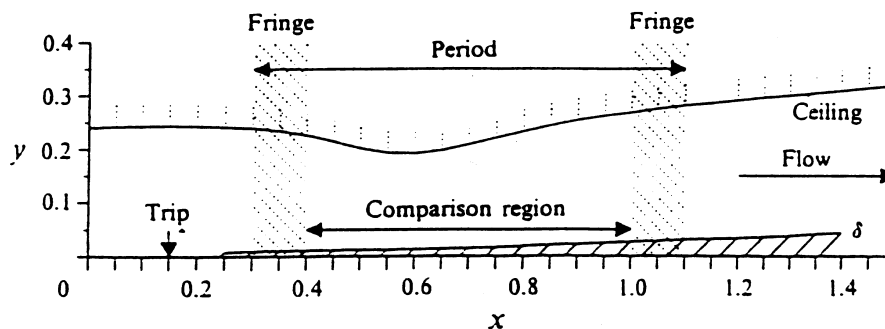


Figure 1: Flow configuration (from Spalart & Watmuff, 1993).

4. **Flow characteristics:** Two dimensional favourable and adverse pressure gradient turbulent boundary layer flow.
5. **Flow parameters:** Free stream turbulence intensity at end of contraction is 0.2%. Reference velocity U_{ref} at entrance to the test section, $x = 0$, is 6.5 m/s giving a reference unit Reynolds number of $4.28 \times 10^5 \text{ m}^{-1}$. Reynolds numbers based upon momentum thickness are below 1600, well within the range for which 'low-Reynolds-number effects' are known to occur in zero pressure gradient.
6. **Inflow, outflow boundary and initial conditions:** From initial and final profiles and imposed pressure distribution.
7. **Measurement procedures:**
 - (a) **Measured Quantities:** Wall static pressure distribution, skin friction distribution, mean flow profiles, Reynolds shear stresses, all three components of the Reynolds normal stresses. Mean flow and Reynolds stress profiles measured at 50mm intervals along tunnel centreline from $x = 0.2\text{m}$ to 2.0m , i.e. 37 profiles.
 - (b) **Measurement Errors:** Not tabulated but some discussion in references.
 - (c) **Other supporting information:** All mean velocity and turbulence data obtained from normal and X wire hot-wire probes attached to a high-speed three-dimensional computer-controlled traversing mechanism. Wall static pressure measured at 44 tapings. Skin friction from Preston tubes.
8. **Available variables:** As in Measured Quantities, above.
9. **Storage size required and present format of the data:** 65 Kbytes ASCII file.
10. **Contact person:** P. R. Spalart
Boeing Commercial Airplane Group, P.O. Box 3707, Seattle, WA 98124-2207, USA
e-mail:spalart@nas.nasa.gov

REFERENCES

SPALART, P. R. & WATMUFF, J. F. 1993 Experimental and numerical study of a turbulent boundary layer with pressure gradients, *J. Fluid Mech.* **249**, 337-371.

WATMUFF, J.H. 1990 An experimental investigation of a low Reynolds number turbulent boundary layer subject to an adverse pressure gradient. *1989 Ann. Res. Briefs*, CTR, Stanford, pp. 37-49.

TBL20: Closed Separation Bubble

Alving & Fernholz

- Description of the flow:** Turbulent boundary layer on a smooth, axisymmetric body exposed to an adverse pressure gradient of sufficient strength to cause a short region of mean reverse flow ('separation'). The pressure distribution is tailored such that the boundary layer reattaches and then develops in a nominally zero pressure gradient.
- Geometry:** The test surface was a hollow aluminium circular cylinder, 1.65m in length and 0.25m in diameter, its axis aligned with the flow and preceded by a 0.3m elliptical nose cone. The boundary layer was tripped at the nose-cone/cylinder junction. The test surface was surrounded by a concentric, perforated cylinder forming the outer wall (diameter 0.61m) and ended at a perforated end plate. This outer wall was shaped, as shown in the sketch below, to produce an adverse pressure gradient at the start of the test cylinder.
- Sketch:**

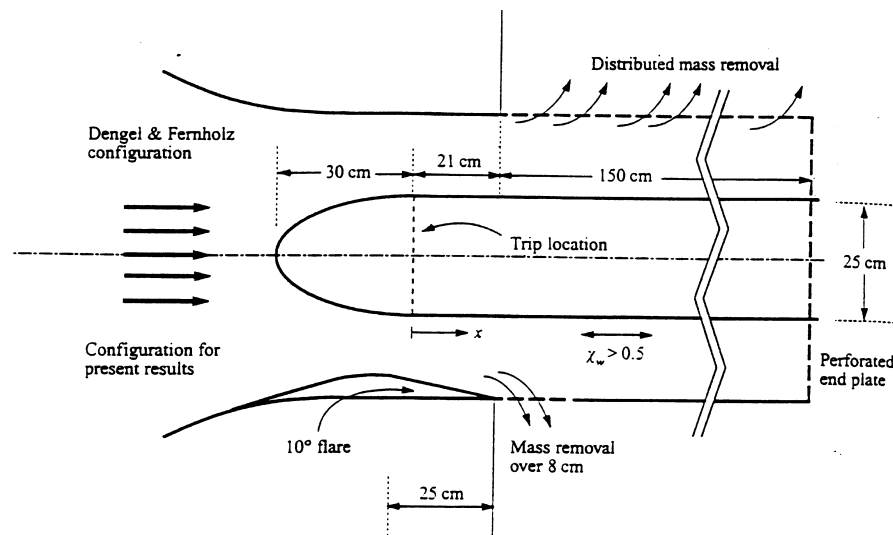


Figure 1: Sketch of the facility.

- Flow characteristics:** Flow over and downstream of an adverse pressure gradient induced separation bubble. The flow reattaches in a mild adverse pressure gradient and then develops in a nominally zero pressure gradient.
- Flow parameters:** Reference Reynolds number, $U_{throat}/\nu = 1.62 \times 10^6/m$. Free stream turbulence intensity 0.2%. Mean flow parameters, see table below.
- Inflow, outflow boundary and initial conditions** From initial and final profiles and imposed pressure distribution.
- Measurement procedures:**
 - Measured Quantities:** Mean flow profiles, Reynolds shear stresses, all three components of the Reynolds normal stresses third and fourth order moments.
 - Measurement Errors:** For pulsed wire $\overline{u^2} \pm 5\%$, $-\overline{uv} \pm 20\%$, $\overline{v^2} \pm 30\%$.
 - Other supporting information:** Mean flow profiles and turbulence quantities from single and X hot wires except in regions of reverse flow or high turbulence intensity where pulsed wires were used. Wall shear from Clauser chart and pulsed wire.
- Available variables:** Mean flow profiles, Reynolds shear stresses, all three components of the Reynolds normal stresses third and fourth order moments.
- Storage size required and file format:** 206Kbytes, ASCII file.

$x(\text{m})$	ξ	C_p	dC_p/dx	U_p/U_t	χ_w	C_{fCl}	C_{fpw}	$\delta_{99}(\text{m})$	$\theta(\text{m})$	H	Re_θ
0.175	-2.2	0.398	2.18	0.75	0.0	0.00185	0.00249	0.0149	0.0023	1.9	2850
0.275	-1.5	0.566	1.34	0.65	9.6	0.00057	0.00065	0.027	0.0046	2.2	4850
0.325	-1.2	0.595	0.58	0.61	28.0	0.00031	0.00026	0.034	0.0063	2.4	6850
0.425	-0.6	0.623	0.27	0.61	74.0		-0.00025	0.047	0.0076	3.2	7520
0.525	0.0	0.656	0.32	0.57	47.0		0.00005	0.051	(0.0078)	(2.4)	(7200)
0.625	0.7	0.679	0.19	0.57	7.0	0.00057	0.00080	0.063	0.0113	2.09	10400
0.725	1.3	0.688	0.056	0.56	0.2	0.00110	0.00151	0.066	0.0123	1.75	11200
0.825	1.9	0.690	0.036	0.56	0.0	0.00160	0.00193	0.074	0.0129	1.55	11700
0.925	2.6	0.689	-0.010	0.56	0.0	0.0020	0.0022	0.079	0.0129	1.43	11700
1.025	3.2	0.688	-0.024	0.56	0.0	0.0022	0.0024	0.079	0.0127	1.37	11400
1.225	4.4	0.6856	-0.019	0.55	0.0	0.0025	0.0026	0.090	0.0133	1.30	11900
1.475	6.1	0.685	0.000	0.56	0.0	0.0026	0.0027	0.103	0.0148	1.25	13300

Table 1: x streamwise from tripwire location; $\xi = (x - x_{reatt}) / (x_{reatt} - x_{sep})$; $x_{sep} = 0.361 \text{ m}$; $x_{reatt} = 0.518 \text{ m}$; U_p/U_t potential velocity extrapolated to wall / velocity at throat; χ_w probability of reverse flow at the wall; C_{fCl} from Clauser plot; C_{fpw} from pulsed wire; Re_θ momentum thickness Reynolds number; H shape factor.

10. **Contact person:** A.E. Alving

Aerospace Engineering & Mechanics, University of Minnesota, Minneapolis, MN 55455, USA
e-mail:alving@aem.umn.edu

REFERENCES

- ALVING, A.E. & FERNHOLZ, H.H. 1996 Turbulence measurements around a mild separation bubble and downstream of reattachment. *J. Fluid Mech.* **322**, 297-328.
- ALVING, A.E. & FERNHOLZ, H.H. 1995 Mean-velocity scaling in and around a mild, turbulent separation bubble. *Phys. Fluids* **7**, 1956-1969.

TBL21: Mild Separation Bubble

Na & Moin

1. **Description of the flow:** Numerical simulation of a turbulent boundary layer with adverse pressure gradient and a closed mild separation bubble.
2. **Flow geometry:** 3-D computational box: the streamwise extent of the domain is $350 \delta_{in}^*$, the vertical height is $64 \delta_{in}^*$ and the spanwise extent is $50 \delta_{in}^*$, where δ_{in}^* is the displacement thickness at the inlet of the computational domain (see sketch below). All values are normalised with δ_{in}^* and with the free-stream velocity U_o at the inlet.
3. **Sketch:**

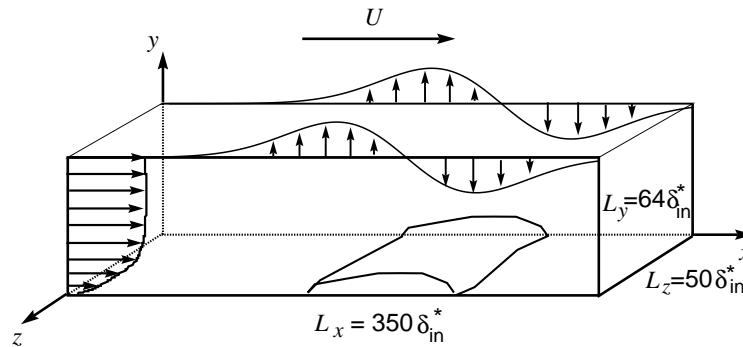


Figure 1: Computational domain of separated turbulent boundary layer.

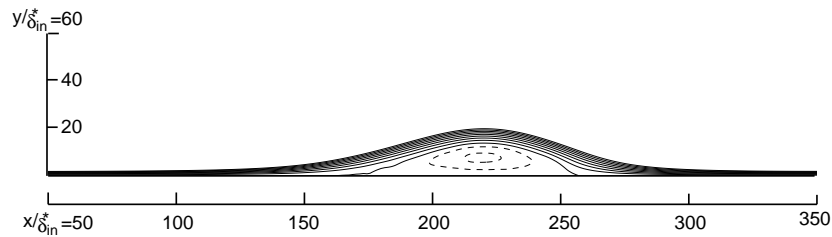


Figure 2: Mean streamlines.

4. **Flow characteristics:** A suction-blowing velocity profile was prescribed along the upper boundary of the computational domain to create an adverse-to-favourable pressure gradient that produces a closed separation bubble. Turbulent structures emanating upstream of separation move away from the wall into the shear layer in the detachment region and then turn around the bubble. Iso-surfaces of negative pressure fluctuations which correspond to the core region of the vortices show that large-scale structures grow in the shear layer and merge with one another. They then impinge on the wall and subsequently convect downstream. The characteristic Strouhal number $St = f \delta_{in}^* / U_o$ associated with this motion ranges between 0.0025 to 0.01. The locations of the maxima of wall-pressure fluctuations and Reynolds shear stress occur downstream of the reattachment zone. Contour plots of two-point correlation of wall-pressure fluctuations are highly elongated in the spanwise direction inside the separation bubble implying the presence of large 2-D roller-type structures. The convection velocity determined from the space-time correlation of pressure fluctuations is as low as $0.33U_o$ in the separated zone and increases downstream of reattachment.
5. **Flow parameters:** The Reynolds number based on inlet momentum thickness and maximum mean streamwise velocity at inlet is 300. The height of the separation bubble is about two inlet boundary layer thickness ($\approx 20 \delta_{in}$), and its length is about $75 \delta_{in}$.

6. **Numerical methods, resolution and resulting uncertainties:** The incompressible Navier-Stokes and continuity equations are integrated in time using a semi-implicit scheme with the modified fractional step procedure (Le & Moin 1991), which advances the velocity field through the Runge-Kutta substeps without satisfying the continuity equation. Continuity is only enforced at the last substep by solving a Poisson equation. A low-storage, third-order Runge-Kutta scheme (Spalart 1987; Spalart *et al* 1991) is used for treating convective terms explicitly and the second order Crank-Nicholson scheme is used for implicit treatment of viscous terms. All spatial derivatives are approximated with second-order central difference schemes. The grid spacing is uniform in the streamwise and spanwise directions. Based on the inlet wall shear velocity $\Delta x^+ \approx 18.3$ and $\Delta z^+ \approx 10.5$. In the wall-normal direction the grid spacing is minimum at the wall, $\Delta y_{min}^+ \approx 0.11$, and maximum in the free-stream, $\Delta y_{max}^+ \approx 22.7$. The number of cells in the grid is $512 \times 192 \times 130$, in x , y and z .

7. **Boundary and initial conditions:**

- (a) **Domain size and truncations:** See point 2 above
- (b) **Boundary conditions** The suction-blowing velocity profile shown in Figure 3 is prescribed along the upper boundary of the computational domain.

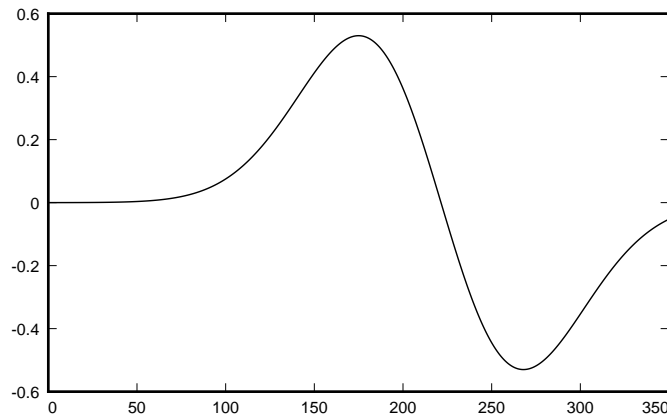


Figure 3: Suction-blowing velocity distribution along the upper boundary.

(c) **Inlet or initial conditions**

Inflow turbulence is generated by sequentially feeding at the inflow plane a frozen DNS field randomised by amplitude factors. Phase angle information is considered more important than the amplitude factor in that it is closely related to turbulence structures, and the phase angles of the frozen field are not changed during the procedure of generating inflow turbulence. The technique attempts to get physically realistic velocity fluctuations using an already validated DNS data and superposes them on a given mean velocity profile at the inflow plane. The mean velocity profile is taken from zero-pressure gradient simulation in Spalart (1988) at $Re_\theta = 300$ (see TBL01). Using a single realisation of his 3-D flow field, the three components of the velocity fluctuations $u_j'(x, y, z)$ are calculated by subtracting the mean velocity $\bar{u}_j(y)$ from the instantaneous velocity $u_j(x, y, z)$,

$$u_j'(x, y, z) = u_j(x, y, z) - \bar{u}_j(y), \quad (1)$$

From Fourier coefficients obtained by transforming u_j' in the streamwise and spanwise directions,

$$\hat{u}_j'(k_x, y, k_z) = |\hat{u}_j'| e^{i\varphi},$$

a new field is constructed by jittering $|\hat{u}_j'|$ with real random numbers α_u in the range $0.8 \leq \alpha_u \leq 1.2$,

$$(\hat{u}_j')_{new} = \alpha_u(k_x, y, k_z) |\hat{u}_j'| e^{i\varphi} \quad (2)$$

The new coefficients are transformed back to physical space to obtain a fluctuating velocity field, which is then superimposed on the long-time mean velocity profile, and fed into the computational domain using Taylor's hypothesis. In other words, the streamwise coordinate x of the input field is fed as inlet boundary condition at the time $t = x/U_c$, where U_c is a convection velocity. It was checked that changing U_c in the range $0.8U_o - U_o$ resulted in negligible differences in the statistics of a zero-pressure gradient turbulent boundary layer, and consequently $U_c = U_o$ was used throughout the present study. After the whole randomised field is fed into the inlet plane, it is recycled by using a new set of α_u in (2). At the exit of the computational box, a convective boundary condition is used.

8. Averaging procedures and resulting uncertainties:

The mean velocity components, turbulence intensities, and pressure are calculated on a staggered grid. Thus, the pressure is obtained at cell centres and velocities at the cell surfaces. Statistical averages were performed over the homogeneous spanwise direction and time and, hence, single point statistics are functions of both x and y . The data were sampled every 10 calculation time steps, at equal time intervals $\Delta t_s = 0.3\delta_{in}^*/U_0$, and the total averaging time was $2250\delta_{in}^*/U_0$, equivalent to about 7 “flow-through” times, defined as the full travel time of fluid particles outside the separation bubble.

An idea of the statistical uncertainties can be had from the r.m.s. value of the time-averaged field of the spanwise velocity w , which should vanish everywhere. The spatial average of this mean field is $\sim 10^{-6}$, but its spatial r.m.s. value is 1.5×10^{-3} , which is 5% to the r.m.s. value of the velocity itself $w' = 0.03$.

The correlation functions are averaged over 60 instantaneous fields separated by 7.5 time units. They therefore correspond to roughly one fifth of the averaging time for the mean values. Their statistical uncertainty can be estimated by comparing the zero-separation correlations with the turbulent intensities of the longer averages. The differences are,

u'	v'	w'	$u'v'$
4%	3%	8%	7%

9. **Available variables:** Two-dimensional ($x-y$) maps of mean and r.m.s fluctuations of the three velocity components and pressure, plus τ_{xy} Reynolds shear stress (Figures 4-5). Because of staggered-mesh numerical method, the velocities are known at the cell faces, while the pressure, and w in a two-dimensional projection, are known at the centres. This has been respected in the time-averaged flow fields, which are therefore separated into three files, each with its own, slightly staggered, grid. The Reynolds stresses are given interpolated at the locations of both the u and v velocities.

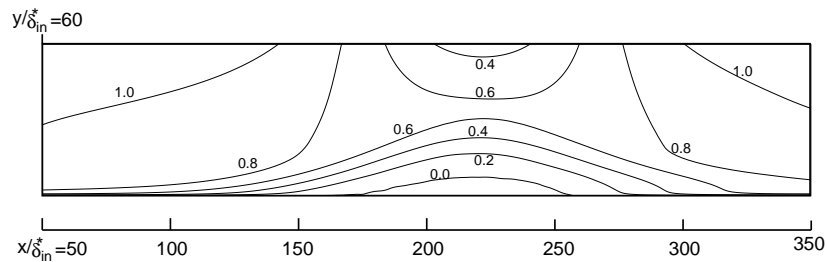


Figure 4: Contours of mean streamwise velocity.

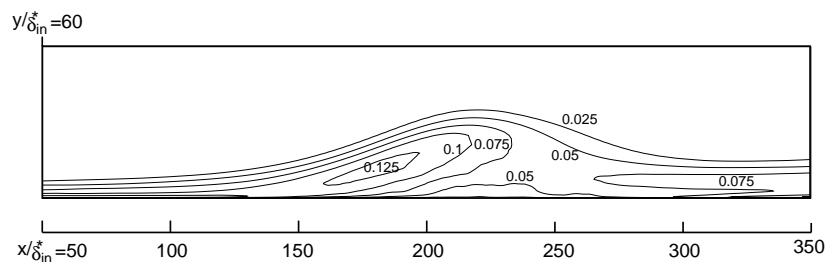


Figure 5: Contours of longitudinal turbulence intensities.

Two-point small-separation correlation functions of the $u-u$, $v-v$, $w-w$, and $u-v$ velocity components, computed for six cross-flow slabs, centred at $x = 80.5, 122.4, 160.7, 220.0, 270.2, 321.1$, and each one spanning $\Delta x \approx 7$. These locations are those for which momentum balances are computed in (Na & Moin 1996). These are full five-dimensional correlation functions in $x, x', y, y',$ and $z - z'$, as explained in chapter 2.

10. **Storage size required and file format:** Approximately 4 Mb of binary data for the averaged fields. Approximately 35 Mb of binary data for each of the six correlation slabs.

11. Contact person:

Yang Na
 U. Illinois, 104 S. Wright St., Urbana, IL 61801
 e.mail: yangna@uiuc.edu

REFERENCES

- LE, H. AND MOIN, P. 1991 An improvement of fractional step methods for the incompressible Navier-Stokes equations, *J. Comp. Phys.* **92**, 369-379.
- NA, Y. AND MOIN, P. 1996 Direct numerical simulation of turbulent boundary layers with adverse pressure gradient and separation, *Report TF-68*, Thermosciences Division, Dept. of Mech. Eng., Stanford University.
- SPALART, P. R. 1987 Hybrid RKW3 + Crank-Nicolson scheme, *private communication*.
- SPALART, P.R. 1988 Direct numerical study of a turbulent boundary layer up to $Re_\theta = 1410$, *J. Fluid Mech.* **187**, 61-98.
- SPALART, P. R., MOSER, R. D. AND ROGERS, M. M. 1991 Spectral methods for the Navier-Stokes equations with one infinite and two periodic directions, *J. Comp. Phys.* **96**, 297-324.

TBL22: Small Separation Bubble on Isothermal Wall

Spalart & Coleman

- Description of the flow:** Numerical simulation of a small two-dimensional turbulent separation bubble, with heat transfer on an isothermal wall.
- Flow geometry:** 3-D computational box, periodic in the streamwise, x -, and spanwise z -directions, with streamwise corrections discussed above. All values are normalised with the height H of the computational domain and with the free-stream velocity U_o at the inlet. The streamwise extent of the domain is $L_x = 10$ and the spanwise extent is $L_z = 1.43$, but the useful region extends only from $x = 1.3$ to 8.7 . The momentum thickness at $x = 1.3$ is $\theta = 0.0105$, and the temperature deficit thickness $\Delta_2 = 0.0119$. The boundary layer thickness, defined by the 2% spanwise vorticity isoline, is $\delta \approx 0.24$.
- Sketch:** Not available.
- Flow characteristics:** The momentum and temperature boundary layers are turbulent at the inflow and first relax in a settling region, about 7δ long. Strong adverse and then favourable pressure gradients cause separation (negative mean skin friction) and rapid reattachment on $x \approx 5.85 - 6.85$. The highest point of the separating streamline is $y/\delta \approx 0.5$. Instantaneous flow reversal occurs far upstream of mean reversal, and streaks disappear. Surprisingly, heat transfer peaks near separation. Also, negative turbulent kinetic energy production and counter-gradient heat flux are found in a small region.
- Flow parameters:** Reynolds number based on the length of the useful region is about 160,000. $R_\theta \approx 230$ at inflow. $Pr = 0.71$.
- Numerical methods, resolution and resulting uncertainties:** Fully spectral method, Fourier in the x - and z -directions. Jacobi polynomials in y , matched to an exponential mapping (Spalart *et al* 1991). Streamwise boundary layer growth is compensated by a “fringe” method in which an extra term is applied to the equations in $x < 1.3$ and $x > 8.7$, restoring the outgoing flow to the desired inflow condition (Spalart & Watmuff 1993; Spalart & Coleman 1997). The collocation grid is $(600 \times 200 \times 256)$, with 30 out of the 200 points in the y -direction above the upper boundary at $y = H$. Dealiasing is done in the three directions by the 2/3 rule. Based on the highest mean skin friction in the box, the distance between collocation points is $\Delta z^+ = 20$, $\Delta x^+ = 7.3$. The wall normal stretched grid has 10 points below $y^+ = 2.5$. Numerical quality parameters are extensively discussed in Spalart & Coleman (1997).
- Boundary and initial conditions:**
 - Domain size and truncations:** The main problems in this simulation are the short settling region for the incoming boundary layer after the inlet fringe, and the low Reynolds number. The boundary layer never attains a fully-developed profile and, in particular, never develops a logarithmic law. Also, there is no space for a proper recovery of the layer after reattachment.
 - Boundary conditions** The flow is controlled by suction and blowing through an inviscid boundary at $y = H$, given by
$$V_{top}/U_o = -\sqrt{2}V_o\xi \exp(0.5 - \xi^2), \quad \text{where } \xi = (x - x_c)/\sigma,$$
and $V_o = 0.435$, $x_c = 6.5$ and $\sigma = 1.22$. Inflow velocity, temperature and stress profiles are given. Velocity and temperature fields are turbulent at inflow. Outflow is not critical.
 - Inlet or initial conditions:** Generated through the fringe method described above.
- Averaging procedures and resulting uncertainties:** Mean values are averaged over the span, and over time. A filter of streamwise width ≈ 0.1 is also applied. The statistical sample is formed by 429 velocity and temperature fields, covering a total time of about $24H/U_o$, or about 2.4 full flow-throughs.
- Available variables:** At 12 streamwise stations, wall-normal profiles of mean $U, V, \bar{T}, \Psi, \overline{u'^2}, \overline{v'^2}, \overline{w'^2}, -\overline{u'v'}, \overline{T'^2}, -\overline{T'u'}, -\overline{T'v'}, \overline{\omega'_x}, \overline{\omega'_y}, \overline{\omega'_z}$. Also the wall C_p and C_f and Stanton numbers.
- Storage size required and file format:** About 500Kbytes, ASCII file.

11. **Contact person:** P. R. Spalart
Boeing Commercial Airplane Group, P.O. Box 3707, Seattle, WA 98124-2207, USA
e-mail:spalart@nas.nasa.gov

REFERENCES

- COLEMAN, G.N. & SPALART, P.R. 1993 Direct numerical simulation of a small separation bubble. *Int. Conf. on Near-Wall Turbulent Flows*, Mar. 15-17, ASU, Tempe, AZ. (So, Speziale & Launder, editors). Elsevier, 277-286.
- SPALART, P.R. & COLEMAN, G.N. 1997 Numerical study of a separation bubble with heat transfer. *Europ. J. Mech. B* **16**, 169-189.
- SPALART, P. R., MOSER, R. D. AND ROGERS, M. M. 1991 Spectral methods for the Navier-Stokes equations with one infinite and two periodic directions, *J. Comp. Phys.* **96**, 297-324.
- SPALART, P.R. & WATMUFF, J.H. 1993 Experimental and numerical investigation of a turbulent boundary layer with pressure gradients. *J. Fluid Mech.* **249**, 337-371.

	Station				
	Flat	15°	30°	45°	60°
x (cm)	-56.0	35.6	71.2	106.8	142.4
U_{pw} (cm/s)	15.19	15.32	15.12	15.05	15.26
u_τ (cm/s)	0.690	0.715	0.735	0.755	0.790
C_f	.00413	.00436	.00473	.00503	.00536
δ_{99} (cm)	7.98	9.29	10.19	11.62	12.51
θ (cm)	0.91	1.11	1.18	1.33	1.23
R_θ	1455	1813	1904	2121	1952
H	1.41	1.33	1.29	1.24	1.20

Table 1: x streamwise; U_{pw} potential velocity extrapolated to wall; u_τ friction velocity; R_θ momentum thickness Reynolds number; H shape factor.

- (b) **Measurement Errors:** In U less than $\pm 1\%$, in velocity fluctuations less than $\pm 3\%$. In the transport terms, $\overline{vu^2}$, $\overline{vv^2}$, and $\overline{vw^2}$, over 100% in some cases in the near wall region. For $u_\tau \pm 3\%$ and $C_f \pm 5\%$. See references for details
- (c) **Other supporting information:** Mean flow profiles and turbulence quantities from two colour, three beam, laser-Doppler anemometer. Flow visualization by coloured dye and laser induced fluorescence.
8. **Available variables:** Mean flow profiles, Reynolds shear stress, $-\overline{uv}$, all three components of the Reynolds normal stresses and third and fourth order moments.
9. **Storage size required and present format of the data:** 43Kbytes ASCII file.
10. **Contact person:** James P. Johnston, Thermosciences Division, Department of Mechanical Engineering, Stanford University, Stanford, California 94305-3030, USA. e.mail: johnston@vk.stanford.edu

REFERENCES

- BARLOW, R. S. & JOHNSTON, J. P. 1988 Structure of a turbulent boundary layer on a concave surface, *J. Fluid Mech.* **191**, 137-176.
- JOHNSON, P.L. & JOHNSTON, J. P. 1989 The effects of grid-generated turbulence on flat and concave turbulent boundary layers. *Report MD-53* Dept. of Mech. Eng. Stanford University.

TBL31: Relaxing Turbulent Boundary Layer

Webster, DeGraaff & Eaton

- Description of the flow:** The investigation was performed in a low-speed wind tunnel having the dimensions given under "Geometry" below. Since the flow did not separate, hot-wire anemometry was sufficient for measurement of the mean and fluctuating velocities. Because of the complex velocity profiles, an oil-film technique was used to measure local skin-friction. The uncertainty in the measurements is acceptably low and is summarized in the table. Measurements were made at three momentum-thickness Reynolds numbers, 1500, 2500, and 4000. These are all in the "low Reynolds number" range (ie., below 5000) but also thus in a range to be calculated by LES without an inordinate demand for computer resources. The results cannot be directly compared to other experiments because the geometry has not been duplicated elsewhere. However, the characteristics of the flow have been examined in the light of other work, such as flow over a convex or concave curvature and found to be consistent. The relative simplicity of the flow, the low measurement uncertainties, and the care in providing details needed by simulators invite consideration for use in developing LES capabilities.
- Geometry:** A flat plate boundary layer over a faired, two-dimensional bump, 305 x 20 mm, in a rectangular test section of constant cross-section, 152 x 711 mm.
- Sketch:**

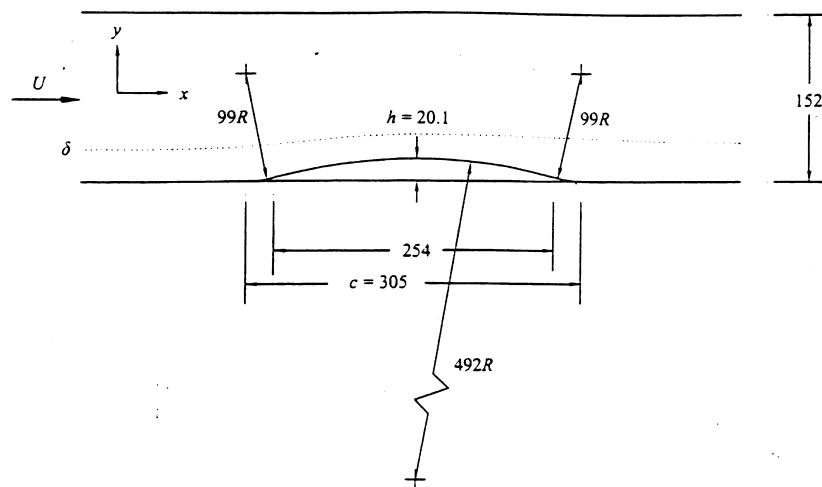


Figure 1: Sketch of test-section and bump geometry. All dimensions in mm.

- Flow characteristics:** Two-dimensional, incompressible, turbulent boundary layer, attached flow everywhere over the bump.
- Flow parameters:** Air at nominally room conditions; $R_\theta = 1500, 2500, 4000$
- Inflow, outflow boundary and initial conditions:** Inflow was standard 2-D boundary layer; outflow was nearly standard and was measured.
- Measurement procedures:**
 - Measured quantities:** All components of velocity and Reynolds stress (hot-wire), wall-pressure, and skin friction measured using an oil flow fringe imaging technique.
 - Measurement errors:** 3% in velocity; 5% in normal and 10% in skew components of Reynolds stress; 5% in skin friction.
 - Other supporting information:**

8. **Available variables:** Mean velocity, wall pressure, skin friction; all Reynolds stress components.
9. **Storage size required and present format of the data:** 274Kbytes ASCII file.
10. **Contact person:** J.K.Eaton Department of Mechanical Engineering, Stanford University, Stanford, California 94305-3030, USA. e-mail: eaton@vk.stanford.edu

REFERENCES

WEBSTER, D.R., DEGRAAFF, D.B., AND EATON, J.K. 1996 Turbulence Characteristics of a Boundary Layer Over a Two-Dimensional Bump, *J. Fluid Mech.* **320**, 53-69

Data Sheets for:
Chapter 8. Complex Flows

CMP00: Flow in a square duct – Experiments

Yokosawa, Fujita, Hirota, & Iwata

1. **Description of the flow:** These are the experiments of Yokosawa *et al* (1989). Air was blown through a flow meter and a settling chamber into a square duct. Measurements were performed 90 duct widths downstream where the flow was fully developed.
2. **Geometry:** Cross-section: $50\text{mm} \times 50\text{mm} \times 4500\text{mm}$, Bellmouth nozzle, 6:1 contraction
3. **Sketch:**

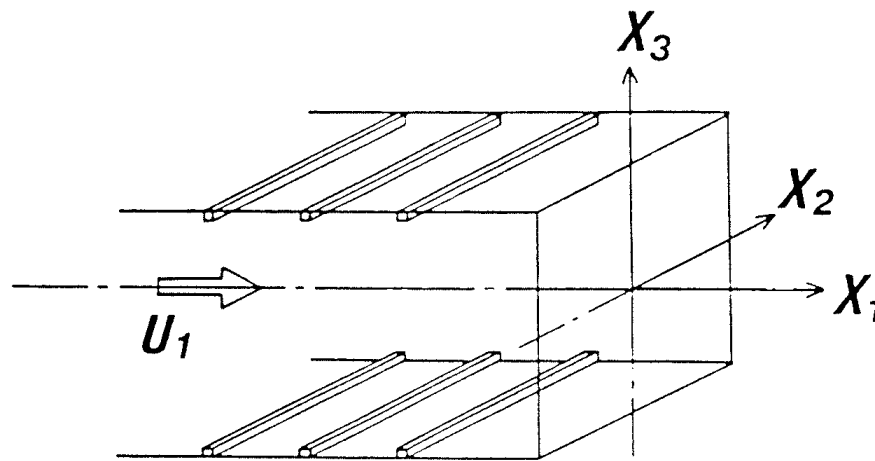


Figure 1: Geometry and coordinate system for experiments (from Fig. 1 of Yokosawa *et al*, 1989).

4. **Flow characteristics:** The fully developed flow exhibits axial vortex pairs (crossflow) in each corner. Only the data for the case of all four walls smooth is included here.
5. **Flow parameters:** Reynolds number: $UD/\nu = 6.5 \times 10^4$; U is the bulk velocity, approximately 21m/s; D is the hydraulic diameter. Mean velocity at the duct centre approximately 25 m/s.
6. **Inflow, outflow, boundary, and initial conditions:** Uniform, low-turbulence flow at entrance; flow open to atmosphere at exit; flow judged fully developed duct flow at measurement station.
7. **Measurement procedures:**

(a) Measured Quantities:

- Mean primary flow velocity, U_1
- Mean secondary flow velocities, U_2 and U_3
- Mean normal stresses, $\overline{u_i u_i}$, $i = 1, 2, 3$
- Mean turbulent stresses, $\overline{u_1 u_2}$ and $\overline{u_1 u_3}$
- Local wall shear stress, τ_w

(b) Measurement Uncertainties:

- U_1 : 1.4%; U_2 and U_3 : 6%
- $\overline{u_1 u_1}$: 2.4%; $\overline{u_2 u_2}$ and $\overline{u_3 u_3}$: 8.6%
- $\overline{u_1 u_2}$ and $\overline{u_1 u_3}$: 4.9%

8. **Available variables:** Quantities described above, measured in a quarter section of the duct.
9. **Storage Size and File Format:** The data are contained in one text file of approximately 32KB. They are in sets of columns with a descriptive header and labels.
10. **Contact person:** Prof. Masafumi Hirota
Dept. of Mech. Engr.
Nagoya University
Furo-cho, Chikusa-ku
Nagoya 464-01 Japan

REFERENCES

- YOKOSAWA, H., FUJITA, H., HIROTA, M., & IWATA, S. 1989 Measurement of turbulent flow in a square duct with roughened walls on two opposite sides. *Intl. J. Heat and Fluid Flow* **10**, 125.
- FUJITA, H., HIROTA, M., & YOKOSAWA, H. 1990 Experiments on turbulent flow in a square duct with a rough wall. *Memoirs of Faculty of Engr., Nagoya U.* **41**, 280.

CMP01: Flow in a square duct – Simulation

Huser & Biringen

1. **Description of the flow:** This is the simulation of Huser & Biringen (1993). Turbulent flow of an incompressible, constant property fluid through a straight square duct was simulated for fully developed conditions (no further evolution in the streamwise direction). Statistics were collected after the simulation reached a steady state.
2. **Geometry:** The computational domain dimensions were $1 \times 1 \times 6.4$. Periodic boundary conditions were specified in the streamwise direction.
3. **Sketch:**

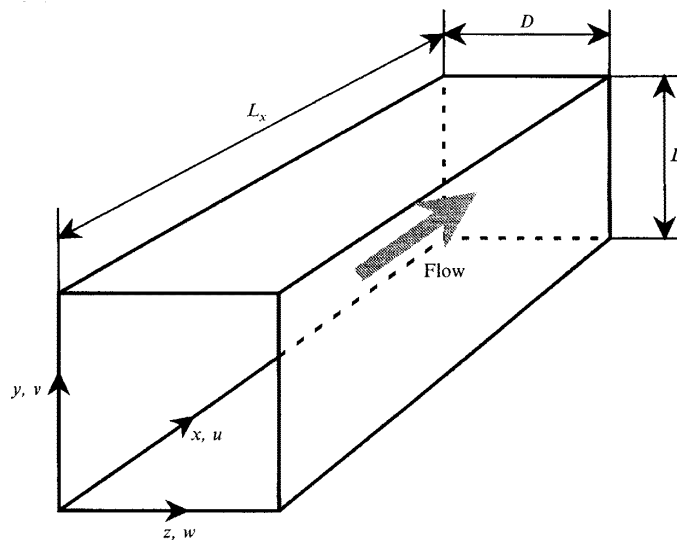


Figure 1: Geometry and coordinate system (from Fig. 1 of Huser & Biringen, 1993).

4. **Flow Characteristics:** The secondary flow is of prime importance since it is generated solely by the interaction of the turbulent stresses. Thus adequate calculation of the turbulence is crucial to an accurate overall simulation or modelling.
5. **Flow Parameters:** This deceptively simple geometry is described by one parameter only, the Reynolds number. For the simulation presented here, the Reynolds number based on the mean friction velocity and duct width was 600.
6. **Numerical Methods and Resolution:** The time-splitting method of Le & Moin (1994) was used to advance in time. A Lagrangian polynomial method was used to obtain the finite differences for first and second derivatives in the wall-normal direction on a stretched, staggered grid. Fifth order upwind-biased differences were used for the convective terms in all three directions. This will introduce artificial dissipation, which may affect spectra and correlations, but is necessary since explicit dealiasing is not possible. The momentum equations were solved by using fourth-order central differences for the viscous terms in the wall-normal direction. The pseudo-spectral Fourier method was implemented in the streamwise direction to calculate the viscous terms and to solve the pseudo-pressure equation. The pseudo-pressure equation in the wall-normal direction was discretized by fourth-order central differences. The grid for the results presented here was $101 \times 101 \times 96$.
7. **Boundary and Initial Conditions:**
 - (a) Domain size and truncations: Size: $1 \times 1 \times 6.4$
 - (b) Boundary conditions: No slip on the walls; periodic in the streamwise direction.

(c) Inlet or initial conditions: The calculations began with a laminar flow perturbed randomly, then run until a statistically steady state was obtained. This was achieved at a nondimensional time, based on friction velocity and duct width, of 60. This corresponds to a flow distance of about 1300 widths, far beyond the entrance length in experiments. It should be noted, though, that this is achieved at constant pressure gradient while experiments are run at constant mass flux. The latter converge much faster than the former which should therefore be evaluated carefully in this regard.

8. **Averaging Procedures and Uncertainties:** Long-time statistics were obtained by averaging the flow field in the homogeneous direction, over the four quadrants, and in time for a nondimensional time duration of 15. A friction factor of 0.027 was computed, slightly lower than 0.030 of experiments. A lower resolution simulation was computed, $81 \times 81 \times 64$, which gave results very similar to those included here.
9. **Available Data:** The data in this database are mean streamwise and secondary velocities, all three components of the mean vorticity, the mean pressure, and all the components of the mean strain rate tensor; all the components of the Reynolds stress tensor, the skewness and flatness of the velocity components, the pressure, and the products of velocity components; kinetic energy, dissipation rate, enstrophy, and streamwise vorticity budget terms; terms of the transport equations for mean streamwise and transverse velocities, mean streamwise and transverse velocities squared, and products of streamwise and transverse velocities.
Full, small-separation correlation functions for the velocities are also provided.
10. **Storage Size and File Format:** The data are contained in twelve text files totalling approximately 6 Mb. Each variable is presented in a group corresponding to a value in the first group which is the distance from one wall and subsequent groups for the other distances from the wall (51 groups for each variable corresponding to 51 distances from the wall). The data is given for one quadrant of the duct since averages were taken over the four quadrants. The correlations are in a single binary file (with header) of 115 Mb.
11. **Contact Person:** Prof. Sedat Biringen
Dept. of Aero. Engr.
Univ. of Colorado
Boulder, CO 80309 USA

REFERENCES

- HUSER, A., AND BIRINGEN, S. 1993 Direct numerical simulation of turbulent flow in a square duct. *J. Fluid Mech.* **257**, 65.
- LE, H. AND MOIN, P. 1994 Direct numerical simulation of turbulent flow over a backward facing step, *Technical Report No. TF-58*, Department of Mechanical Engineering, Stanford University.
- HUSER, A., BIRINGEN, S., AND HATAY, F. 1994 Direct simulation of turbulent flow in a square duct: Reynolds-stress budgets. *Phys. Fluids* **6** no. 9, 65.

CMP10: Flow Around A Circular Cylinder

Cantwell & Coles

1. **Description of the flow:** This is the experiment of Cantwell & Coles (1983), the near wake of a smooth circular cylinder.
2. **Geometry:** A cylinder 2.97m in length and 10.14 cm in diameter was mounted in a wind tunnel test section of circular cross-section. Velocity measurements were made in the first eight diameters downstream in the wake.
3. **Sketch:**

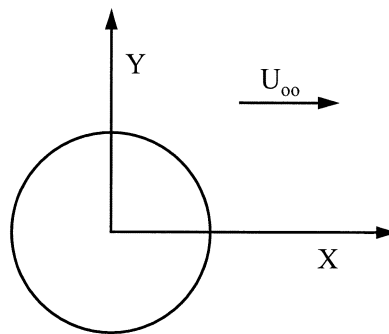


Figure 1: Geometry and coordinate system

4. **Flow characteristics:** The flow is that of a smooth circular cylinder placed normal to a uniform approaching flow at a Reynolds number of 140,000. This is large enough to create a fully turbulent wake but have laminar separation (subcritical) which generates turbulent vortices in a nearly periodic fashion.
5. **Flow Parameters:** Reynolds number: $UD/\nu = 140,000$; U is the free-stream velocity, approximately $21.2m/s$; D is the cylinder diameter. At these conditions the Strouhal number, $fD/U = 0.179$.
6. **Inflow, outflow, boundary, and initial conditions:** There was uniform, low-turbulence approach flow; the test section extended beyond the measurement range (eight diameters) downstream. The test section was 10 feet (3.05m) in diameter. There were end plates on the cylinder.
7. **Measurement procedures:** The primary instrument was a hot-wire probe, either single or crossed-wire, mounted on an arm rotating at a high speed which increases the relative velocity component along the probe axis (a "flying hot-wire"). Thus the angle of the velocity vector relative to the probe axis remains in an acceptable range.

The hot-wire signals were recorded digitally and sampled in phase with the vortex shedding detected by a fast pressure sensor on the cylinder. Ensemble averages of the data thus provide a "frozen" field of velocity as a function of phase angle. Variations from these averages are measures of the turbulence in the field, also a function of phase angle.

(a) Measured quantities:

Mean streamwise and transverse velocities: U_1 and U_2

Mean Products: $u_1^2, u_2^2, u_1u_2, u_1^2u_2, u_1u_2^2$

Third and fourth powers: $u_1^3, u_2^3, u_1^4, u_2^4$

Intermittency

Maxima and minima of these variables for each profile

(b) Measurement Uncertainties:

U_1 and U_2 : 1%

Products: 5%

Third and fourth powers: 25%

8. **Available variables:** Quantities described above.
9. **Storage Size and File Format:** Approximately 7.5 MB of data are stored in 19 text files. They are self-explanatory except that UN or $UREFN$, where $N = 1, 2, 3, \text{ or } 4$, refers to U^N or U_{REF}^N .
10. **Contact person:** Prof. Brian Cantwell
Dept. of Aero. and Astro.
Stanford University
Stanford, CA 94305 USA

REFERENCES

CANTWELL, B., AND COLES, D. 1983 An Experimental Study of Entrainment and Transport in the Turbulent Near Wake of a Circular Cylinder. *J. Fluid Mech.* **136**, 321.

CMP20: Flow Around A Square Cylinder

Lyn, Einav, Rodi & Park

1. **Description of the flow:** This is the experiment of Lyn & Rodi (1994) and Lyn et al. (1995), the flow around a long square cylinder mounted transversely to an oncoming uniform flow.
2. **Geometry:** The cylinder was 40mm in width and 392mm long mounted in the rectangular test section of a water channel 392mm by 560mm (blockage 7.1%). Velocity measurements were made above the upper surface and behind the cylinder up to eight diameters downstream.
3. **Sketch:**

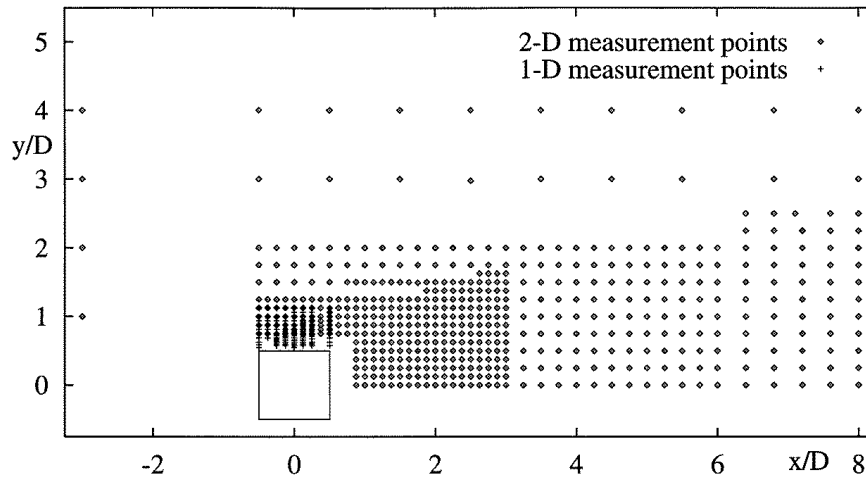


Figure 1: Coordinate system and location of measurement points.

4. **Flow characteristics:** The flow is around a long square cylinder in a water channel at Reynolds number of 22,000. At this Reynolds number the flow is approximately periodic with a Strouhal number of 0.133 ± 0.004 .
5. **Flow Parameters:** Reynolds number: $UD/\nu = 22,000$; U is the free-stream velocity, approximately 0.54m/s ; D is the cylinder width, 40mm . At these conditions the Strouhal number, $fD/U = 0.133$.
6. **Inflow, outflow, boundary, and initial conditions:** The approach flow three cylinder widths upstream had a turbulence level of about 2% and a centreline mean velocity deficit of about 5 to 10%. Though measurements of mean velocity, $\overline{u_1u_1}$, and $\overline{u_2u_2}$ are available, calculations should be started further upstream if uniform conditions are desired.
7. **Measurement procedures:** The data are compilations from single-component laser-Doppler velocimetry (LDV) and two-component LDV experiments. The single-component (streamwise) measurements are clustered just above the upper surface of the cylinder where it would be difficult to project the laser beams necessary for the second component of velocity. Bragg cells were employed to provide an offset frequency necessary to capture the reversal of flow direction in regions of separation. A low-pass filtered pressure signal from a tap on the cylinder side-wall was used to obtain a reference phase for phase-averaging the velocity measurements. Twenty phase-bins were used.

(a) Measured quantities:

Mean streamwise flow velocity, U_1

Mean transverse flow velocity, U_2

Mean normal stresses, $\overline{u_1u_1}$, $\overline{u_2u_2}$

Mean turbulent stress, $\overline{u_1u_2}$

Forward-flow-fraction of both U_1 and U_2

(b) Measurement Uncertainties:

U_1 and U_2 : 5% of approach velocity

$\overline{u_1 u_1}$ and $\overline{u_2 u_2}$: 5%

$\overline{u_1 u_2}$: 15 to 25%

8. **Available variables:** Quantities described above, measured in the upper half plane. Measurement locations are shown in the figure under Sketch.
9. **Storage Size and File Format:** The data is stored in 21 text files totalling approximately 804 KB. The first 20 files contain data from each of 20 phase angles during a period of the vortex shedding. The 21st file contains data averaged over all the phases.
10. **Contact person:** Prof. Wolfgang Rodi
Universität Karlsruhe
Kaiserstr. 12
D-76128 Karlsruhe, Germany
e-mail: rodi@bau-verm.uni-karlsruhe.de

REFERENCES

- LYN, D.A., RODI, W. 1994 The Flapping Shear Layer Formed by the flow Separation from the Forward Corner of a Square Cylinder. *J. Fluid Mech.* **267**, 353.
- LYN, D.A., EINAV, S., RODI, W., PARK, J.H. 1995 A Laser Doppler Velocimeter Study of Ensemble Averaged Characteristics of the Turbulent Near Wake of a Square Cylinder. *J. Fluid Mech.* **304**, 285.

CMP30: Backward Facing Step - Simulation

Le & Moin

1. **Description of the flow:** This simulation is that of Le & Moin (1994) matching the experiment of Jovic & Driver (1994), (1995), the flow of a fully developed turbulent boundary layer over a backward facing step. Before the step there is a short entry region over which the boundary layer develops. Beyond the step, there is a long recovery region before the flow exits the domain.
2. **Geometry:** The computational domain is shown in the sketch. For the simulation included here, the various dimensions shown on the sketch are given by $L_i = 10h$, $L_x = 30h$, $L_y = 6h$, $L_z = 4h$. The expansion ratio is 1.2.
3. **Sketch:** (See sketch under experiment of Jovic and Driver, CMP31.)
4. **Flow Characteristics:** The backstep flow results in separation of the turbulent boundary layer as it flows over the step followed by a recirculation zone under the separated boundary layer. The boundary layer reattaches at a mean distance down-stream of the step of $6.28h$. In the separated region, there is a free shear layer separating the recirculation region from the rest of the flow. This free shear layer exhibits many of the features of a mixing layer.
5. **Flow Parameters:** There are two relevant flow parameters in this flow. One is the Reynolds number $Re_h = 5100$, which is based on the inlet mean velocity at the upper (no-stress) boundary and the step height h . The other is the ratio of the inlet boundary layer thickness to the step height $\delta/h = 1.2$, where δ is the 99% thickness. The inlet boundary layer (statistics taken from the DNS of Spalart [4]) thus had a Reynolds number $Re_\delta = 6100$, a displacement thickness Reynolds number $Re^* = 1000$, and a momentum thickness Reynolds number $Re_\theta = 670$.
6. **Numerical Methods and Resolution:** The numerical method used in the simulations is a second-order staggered grid finite difference method. It is described in detail, along with the code implementing it in Le & Moin [1]. The grid spacing in the streamwise and spanwise directions was uniform with 768 and 64 grid points respectively. In the wall-normal direction 193 grid points were used. They are distributed nonuniformly, according to the following mapping:

$$y = \begin{cases} K_1 \psi_1 \left[1 - \frac{\tanh \gamma_1 (\psi_1 - \xi)}{\tanh \gamma_1 \psi_1} \right] & 0 \leq \xi \leq \eta \\ h + K_2 (\psi_2 - \eta) \left[1 - \frac{\tanh \gamma_2 (\psi_2 - \xi)}{\tanh \gamma_2 \psi_2} \right] & \eta \leq \xi \leq L_y \end{cases}$$

where $L_y = 6h$, $\eta/h = 2.1875$, $\psi_1/h = 1.1$, $\gamma_1 = 2.2$, $\psi_2/h = 6$, $\gamma_2 = 0.7963$. A uniform distribution of grid point in ξ then results in the desired point distribution in y .

7. **Boundary and Initial Conditions:** In the spanwise direction, periodic boundary conditions are used, and the lower boundaries (inlet and recovery sections, step face) are no-slip walls. The upper boundary is a no-stress boundary, with the streamwise, normal and spanwise velocities (u , v , and w respectively) satisfying

$$v = 0 \quad \text{and} \quad \frac{\partial u}{\partial y} = \frac{\partial w}{\partial y} = 0.$$

Since the flow is statistically stationary, the initial conditions are not relevant. However, the inflow conditions are very important. Inflow conditions were generated as a random process designed to match the spectra and Reynolds stresses of the boundary layer DNS of Spalart (1988). The technique is described in detail in Le & Moin (1994).

The outflow boundary condition is given by

$$\frac{\partial u}{\partial t} = U_c \frac{\partial u}{\partial t},$$

where U_c is the convection velocity, which is independent of y and z and is selected to balance the mass flow at the inlet.

8. **Averaging Procedures and Uncertainties:** All the data provided from these simulations are obtained by computing the appropriate quantities from the simulated velocity fields and averaging in the homogeneous spatial direction, z , and time. The averages in time are taken over a period of approximately $109h/U_0$, where U_0 is the velocity at the upper (no stress) boundary.

There are three potential sources of uncertainty in this data. First are the numerical discretization errors introduced in the numerical simulation. The numerical method is a second order finite difference. Further, due to computer time and memory restrictions, the grid resolution was limited, especially in the spanwise direction. The consequences of this are discussed in Chapter 5. The second uncertainty is statistical, which arises from computing the averages over a finite domain size and a finite time. The third source of uncertainty is due to the finite domain size of the numerical simulation. However, if an LES is done in the same domain with the same boundary conditions, then a comparison can be made without error due to the domain size. A related issue is the effect of the artificial inlet (and outlet) conditions, which is also discussed in Chapter 5.

9. **Available Data:** Provided are the mean velocities, nontrivial components of the Reynolds stress tensor and pressure variance as a function of x and y . Note that all of these data are computed from unfiltered velocity fields, so care must be exercised when comparing these data directly to LES results. Finally, the small separation velocity-velocity two-point correlations required to compute filtered versions of the second order statistical profiles as described in Chapter 2 are provided for several x -locations.

10. **Storage Size and File Format:** The data is provided in a total of 7 binary files, one for the one point statistics and one each for the 6 x -locations at which the small separation two-point correlation is provided. Total storage is approximately 56 Mb.

11. **Contact person:**

Prof. Robert Moser
Dept. of Theor. Appl. Mech.
University of Illinois, Urbana-Champaign
Urbana, IL 61801 USA

REFERENCES

LE, H. AND MOIN, P. 1994 Direct numerical simulation of turbulent flow over a backward facing step, *Technical Report No. TF-58*, Department of Mechanical Engineering, Stanford University.

JOVIC, S., AND DRIVER, D. 1994 Backward-facing Step Measurements at Low Reynolds Number, $Re_h = 5000$. *NASA Tech Memo 108807*.

JOVIC, S., AND DRIVER, D. 1995 Reynolds Number Effect on the Skin Friction in Separated Flows Behind a Backward-facing Step. *Exper. Fluids* **18**, 464.

SPALART, P.R. 1988 Direct simulation of a turbulent boundary layer up to $Re_\theta = 1410$. *J. Fluid Mech.* **187**, 61.

(Also see CMP31.)

CMP31: Backward Facing Step - Experiment

Jovic & Driver

1. **Description of the flow:** This is the experiment of Jovic & Driver (1994); 1995), the flow of a fully developed turbulent boundary layer over a backward facing step. The approaching boundary layer was at a Reynolds number $R_\theta = 610$.
2. **Geometry:** The flow is that of a boundary layer passing over a backstep in the wall. The test section is symmetrical in that a mirror image boundary layer and backstep is located on the wall opposite that tested (see figure), forming a double-sided expansion. The channel height upstream is 96mm and downstream 115mm. The channel aspect ratio was 31 to avoid 3D effects.
3. **Sketch:**

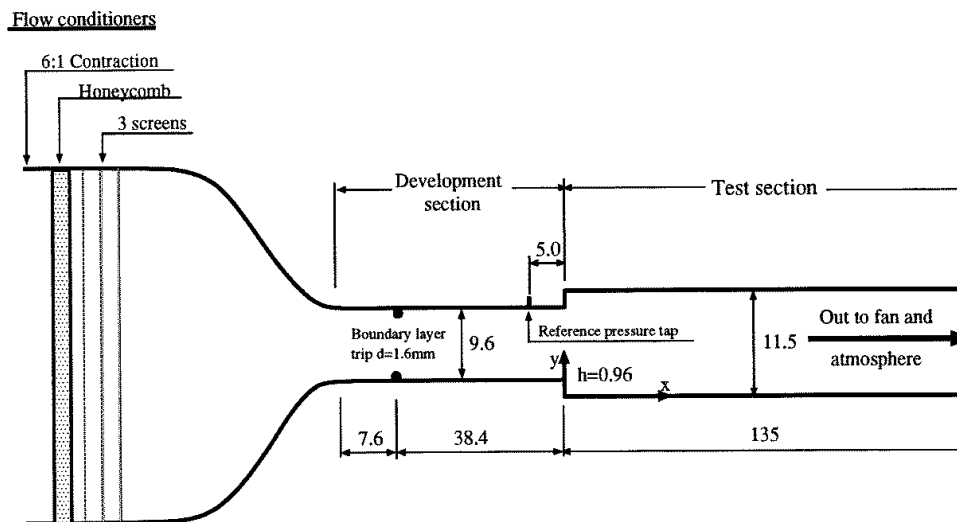


Figure 1: Geometry of experimental setup (From Jovic & Driver, 1994).

4. **Flow characteristics:** A wind tunnel with the fan at the exit was used to generate a fully developed turbulent boundary layer over a flat plate to a backward facing step. The opposite wall was a mirror image plate and step to form a plane of symmetry at the tunnel centreline and an expansion ratio of 1.2.
5. **Flow Parameters:** Reynolds number: $Uh/\nu = 5000$; U is the centreline velocity ahead of the step, approximately 7.7m/s; h is the step height.
Boundary layer ahead of step: $\delta = 11.5mm$; $\delta^* = 1.7mm$; $\theta = 1.2mm$; $H = 1.45$; $C_f = 0.0049$; $R_\theta = 610$.
6. **Inflow, outflow, boundary, and initial conditions:** Boundary layer developing along a straight duct; profiles measured. Outflow: At end of long straight duct after step.
7. **Measurement procedures:**
 - (a) Measured quantities:

Instrumentation: LDV with frequency shifting for directional resolution; laser-interferometer for oil-flow measurement of skin friction (see sketch); surface pressure taps.

Mean flow velocities, U_1 and U_2

Mean normal stresses, $\overline{u_1 u_1}$, $\overline{u_2 u_2}$

Mean turbulent stress, $\overline{u_1 u_2}$

Local wall shear stress, τ_w

Surface pressures

(b) Measurement Uncertainties:

Mean velocities: 2%

Reynolds stresses: 15%

Pressure coefficient: 0.0005

8. **Available variables:** The above quantities averaged over time.

9. **Storage Size and File Format:** Approximately 7 KB of time-averaged data are stored in one text file.

10. **Contact person:** David Driver
NASA Ames Research Center
Moffett Field, CA 94035

REFERENCES

JOVIC, S., AND DRIVER, D. 1994 Backward-facing Step Measurements at Low Reynolds Number, $Re_h = 5000$. *NASA Tech Memo 108807*.

JOVIC, S., AND DRIVER, D. 1995 Reynolds Number Effect on the Skin Friction in Separated Flows Behind a Backward-facing Step. *Exper. Fluids* **18**, 464.

CMP32: Backward Facing Step - Experiment

Driver & Seegmiller

1. **Description of the flow:** This is the experiment of Driver and Seegmiller (1985), a fully developed turbulent boundary layer over a flat plate and a backward facing step.
2. **Geometry:** The flow is that of a high Reynolds number boundary layer passing over a backstep in the wall of height, h , 12.7mm forming an expansion ratio of 1.125. The channel height upstream is $8h$, and the channel width is $12h$. The wall opposite the step was either parallel to the wall with the step or diverging at 6 deg. Only the data from the straight wall case is included here.
3. **Original Sketch:**

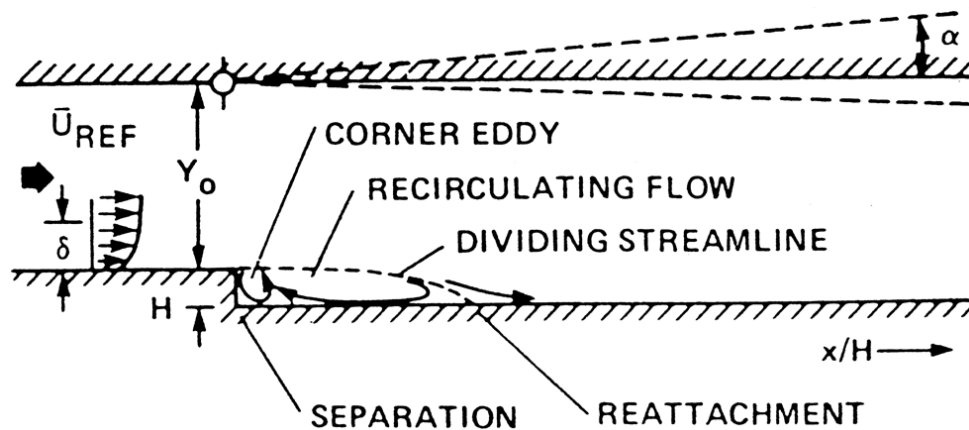


Figure 1: Geometry of experimental setup (from Driver & Seegmiller, 1985).

4. **Flow characteristics:** A low speed wind tunnel was used to generate a fully developed turbulent boundary layer over a flat plate and a backward facing step. The opposite wall was either parallel to the boundary layer wall (data reported here) or diverging at 6 deg beginning at a point opposite the step (data not reported here). The approaching boundary layer was at a Reynolds number $R_\theta = 5000$ and Mach number of 0.128.
5. **Flow Parameters:** Reynolds number: $Uh/\nu = 37500$; U is the centreline velocity ahead of the step, approximately 44.2 m/s; h is the step height.
Boundary layer $4h$ upstream of step: $\delta = 19mm$; $\delta^* = 2.7mm$; $\theta = 1.9mm$; $H = 1.42$; $C_f = 0.0029$
6. **Inflow, outflow, boundary, and initial conditions:** Inflow: Boundary layer developing along a straight duct; profiles measured. Outflow: At end of long straight duct after step.
7. **Measurement procedures:**
 - (a) Measured quantities:
 - Instrumentation: LDV with frequency shifting for directional resolution; laser-interferometer for oil-flow measurement of skin friction; surface pressure taps.
 - Mean flow velocities, U_1 and U_2
 - Mean normal stresses, $\overline{u_1 u_1}$, $\overline{u_2 u_2}$
 - Mean turbulent stress, $\overline{u_1 u_2}$
 - Local wall shear stress, τ_w
 - Surface pressures
 - (b) Measurement Uncertainties:

Mean velocities: 1.5%

Reynolds stresses: 12%

Pressure coefficient: 0.0002

8. **Available variables:** The above quantities measured in profiles along the duct.
9. **Storage Size and File Format:** Approximately 10 KB of time-averaged data are stored in one text file.
10. **Contact person:** David Driver
NASA Ames Research Center
Moffett Field, CA 94035

REFERENCES

DRIVER, D.M., AND SEEGMILLER, H.L. 1985 Features of a Reattaching Turbulent Shear Layer in Divergent Channel Flow. *AIAA J.* **23**, 163.